UNIVERSITY OF CRETE
DEPARTMENT OF MATERIALS SCIENCE AND TECHNOLOGY

Rheometric tools and protocols for materials with multi-scale response and fading mechanical memory

Thanasis Athanasiou

A DISSERTATION

submitted in partial fulfillment of

the requirements for the degree of

Doctor of Philosophy

University of Crete, April 2023

UNIVERSITY OF CRETE

DEPARTMENT OF MATERIAL SCIENCE AND TECHNOLOGY

Rheometric tools and protocols for materials with multi-scale response and fading mechanical memory

PhD Dissertation presented

by

Thanasis Athanasiou

Approved by the committee in charge:

1. Prof. **G. Petekidis** (co-advisor), University of Crete, Greece

2. Prof. **D. Vlassopoulos** (co-advisor), University of Crete, Greece

3. Prof. **G. H. McKinley**, Massachusetts Institute of Technology, USA

4. Prof. **J. Vermant**, Eidgenössische Technische Hochschule Zürich, Switzerland

5. Dr. **B. Loppinet**, Foundation for Research and Technology Hellas, Greece

6. Prof. **E. Glynos**, University of Crete, Greece

7. Prof. **E. Filippidi**, University of Crete, Greece

To Elena who inspired me to follow research

Preface and Acknowledgments

My motivation for this study is trivial. I wanted to understand the related physics and contribute to answering open questions. Now, as I approach "Ithaca" (Cavafy 1911)[++], the benefits of this trip become clearer. I realize how it shaped the way I perceive matter in general. In my pre-scientific career as a marine engineer I used to perceive materials either as solids or liquids. The basic differentiation within each category was the Young's modulus for the former and the kinematic viscosity for the latter. No molecular perspective was ever considered as the relevant length scale of my world was 10 decades larger that the nanometric length scale of the microstructured soft materials. In the former large length scales, and given no relativistic velocities are attained, classic mechanics of fluids and solids dominates and properties of interest are stress, strain, modulus, inertia, compliance, brittleness, and fatigue. Interestingly, all these properties are applicable to soft matter and are referred in this thesis, seen however from the very different perspective of mesoscopic world. The gate-way to this universe was the first system I encountered, colloidal HS spheres, as the continuum treatment utilizes familiar for me terms such as hydrodynamic interactions, particle inertia, Reynolds number and so on. Nevertheless, the subsequent destinations, the macromolecular "threads" exhibiting self-avoiding walks and the peptide based stress bearing networks were equally exciting and complemented the exotic scenery. But this would have been a dull journey if no crew were onboard. The in-lab colleagues that I refer to and feel as true friends, contributed with many little things yet, divergent integral. Coffee breaks where refreshing and also gave me the chance to ask scientific questions. Thank you Daniele, Esmaeel, Katerina, Mohan, Niko, Mano and many more. Antje and Antonis were always available to give a helping hand in measurements as well as ideas. Specific and significant contribution to this work has been made by B. Mei in Chapter1, K. Peponaki in Chapter 4, P. Roose and M. Geri in Chapter5, N. Kalafatakis in Chapter 5 and 6, and P. Edera and J. Kolhbrecher in Chapter 3. I gratefully acknowledge the Greek General Secretariat for Research and Technology (grant RCI-01612) for supporting this thesis. This research forms part of the research programme of DPI, project #837. I also can't omit the contribution of B. Loppinet with many-many

advices on scattering experiments and fruitful scientific discussions that helped me to see the big picture and demystify fancy terminology.

Nevertheless, it would have been a journey with no compass if I did not have guidance and support from my advisors D. Vlassopoulos and G. Petekidis. They showed me paths to avoid scientific "reefs" and supported me to maintain my Velocity Made Good in difficulties. At the same time they provided the vital "free volume" that allowed me to select my route of choice. Thanks to all these people that I encountered "*Ithaca* gave *me a marvelous journey*, *full of experiences".* As I am approaching the last stop of this trip, a milestone in the major journey, I feel my expectations fulfilled: I "developed tools and protocols" useful to appreciate the physics of the mesoscale cosmos and maybe beyond. Life is the major journey for which I would definitely book a window seat.

[++] C. P. Cavafy, Ithaca (1911). From collected poems, translated by E. Keeley and P. Sherrard, edited by G. Savidis, Princeton University Press, NJ 1992.

Thanasis Athanasiou

Heraklion April 2023

Affiliation

Institute of Electronic Structure & Laser, FORTH, Heraklion, 70013 Greece (athanasiou@iesl.forth.gr)

Department of Materials Science and Technology, University of Crete, Heraklion, 70013 Greece

DPI, P.O. Box 902, 5600 AX Eindhoven, the Netherlands

Table of contents

Chapter 1 : Introduction

1.1 Basic concepts and motivation

"Soft" refers to materials with constituents that can be deformed and/or set in motion with energies on the order of the thermal energy, k_BT, where k_B is the Boltzmann constant and T is the absolute temperature. These constituents are larger than the typical size of simple molecules hence, they define the ''mesoscopic'' length scale from a few nanometers to a few micrometers. They are sufficiently small to exhibit thermal fluctuations, while competing interactions (Israelachvili 2011) lead to a rich variety of static and dynamic behavior. Soft materials such as polymeric melts and solutions (Rubinstein and Colby 2003), suspensions (Lionberger and Russel 2000, Mewis and Wagner 2012) and amphiphilic self-assembling systems (Lindman and Wennerström 2006, Tanford 1980), typically exhibit a fading memory of their strain history (Coleman and Noll 1961), which is embedded in the majority of models of stress relaxation (Larson 2013, Morrison 2001). The persistence of this elastic-driven memory ranges between the two ideal limits: infinitely long (strong) for the dislocations-free solid and nonexistent for the liquid. This memory is reflected in a measurable quantity, the linear viscoelasticity, LVE (Tschoegl 2012). A common way to probe LVE macroscopically is by applying shear deformation. When perturbation is small enough (within the linear regime), the experiment does not disturb the microstructure, hence the measured quantities correspond to the quiescent state. On the other hand, the nonlinear response refers to a totally different state of the material as the experiment interferes strongly with the microstructure. The imposed large deformation or rate of deformation alters the microstructure in a reversible or irreversible way, leading to a divergence from the LVE behavior (Barnes et al. 1989). Very often, the microstructural recovery time is considerably long and this can be thought of as a "remembrance" of past nonlinear elastic or plastic deformations (Jamali and McKinley 2022). This memory is reflected in the nonlinear memory function, for example that introduced to describe the response of polyethylene melt at large deformations (Laun 1978) or the damping function when a linear memory function was utilized (Wagner 1976). In particulate thermal or jammed glasses, plastic deformation encodes structural memories (Keim et al. 2019), which are evidenced by the existence of residual stresses (Ballauff *et al.* 2013, Mohan *et al.* 2015, Sudreau *et al.* 2022) in analogy with solids (Totten 2002). This structural memory is very different from the elastic-driven memory. Obviously, the former is not linearly additive and, as we discuss in Chapter 4, it may be invisible to LVE measurements, causing complexities in data interpretation. Memory at the microscopic level is also discussed in the literature. For example, the relaxation time of a linear entangled polymer is the time required for one chain to completely erase the "memory of the

tube"(Rubinstein and Obukhov 1993). This memory is lost after a sufficient number of diffusive steps of duration that grows with the chain molecular weight. On the other hand, for "uncaged" particles dispersed in a solvent, the microscopic memory is predominantly associated with hydrodynamic interactions. The motion of a given (reference) particle induces a backflow pattern in the surrounding fluid that reacts on the same particle at later times (Hansen and McDonald 2013).

Rheometry measures the mechanical response of a soft material by controlling an imposed stress or strain. Here, we focus on *strain control* unidirectional isochoric shear deformation, where a well-defined shear strain waveform, $\gamma(t)$, excites the sample while the stress response, $\sigma(t)$, is monitored. Many soft materials are viscoelastic liquids, which means that given enough time they will eventually flow. This is why the term "simple shear flow" is used, although it refers to viscous rearrangements that may not always be present in the available experimental window. Within this context, we will adopt the term "fluid" for a viscoelastic sample in the analysis below. An elemental shear rheometer in strain-controlled mode is visualized in Figure 1.1 for two different configurations. In both cases the sample is loaded between two plates, where the upper plate translates horizontally at a velocity V and the lower is stationary. In the combined actuator-sensor configuration, the moving plate is mechanically connected to both the actuator (motor) that imposes the desired strain and the sensor that probes the sample's stress response. In practice, sensing and moving is accomplished by the same electro-mechanical component. This arrangement looks and actually is mechanically simple however, decoupling the material's true response from the tool inertia requires iterative calculations (Läuger and Stettin 2016). The separated actuator-sensor configuration is more suitable for strain-controlled experiments, since the sensing plate is stationary and therefore the effect of tool inertia on the measuring surface is negligible. On the other hand, the combined actuator-sensor configuration is more versatile. Hydrogels discussed in Chapter 3 are adequately probed up to 100 rad/s with the single-headed MCR501 rheometer (Anton Paar, Austria). The large lower plate facilitates the installation of solvent trap or sealing rim filled with PDMS to prevent evaporation. In both configurations the sensor compliance attains momentarily some finite value, which is quasi-instantly compensated by the force rebalancing mechanism of rotational rheometers (see discussion for the ARES transducer (Franck 2006, Mackay and Halley 1991)). Force rebalancing is essentially achieved by a feedback loop that constantly compensates the marginal movement of the sensor, trading-off response time. Consequently, in Chapter 2, for high frequency oscillatory measurements we utilize a double-headed rotational rheometer (MCR702) with split actuator-sensor configuration and a high frequency piezoelectric rheometer (PZR) without force rebalancing. Likewise, the normal force piezoelectric sensor of the CPP3+ fixture has no rebalancing mechanism albeit adequate stiffness, and therefore has minimal time resolution (see Chapter 6). Rotational rheometers impose the plane Couette flow of Figure 1.1 to a very good approximation by means of parallel disks (plate-plate) or cone-plate

geometries (for the present study), where strain and stress are proportional to the tool deflection angle and torque, respectively, see Chapter 5 and (Macosko 1994).

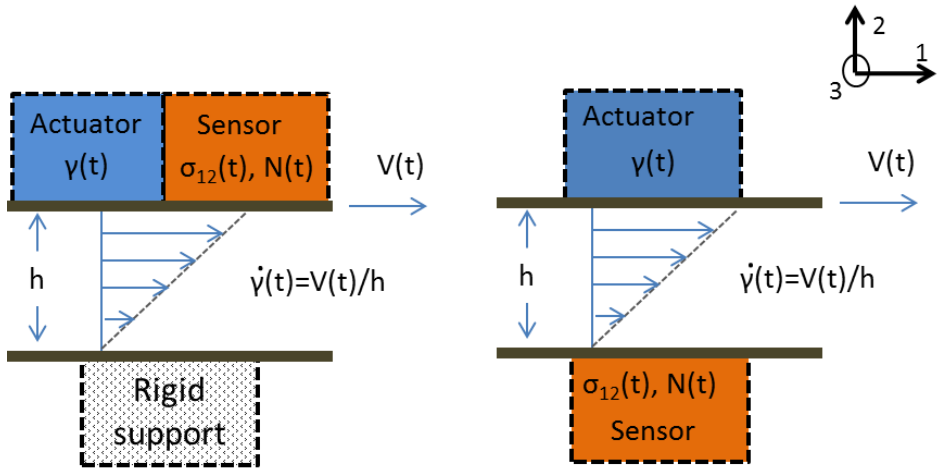

Figure 1.1: Elementary rheometric device in strain-controlled mode. Here the upper plate translates horizontally (slides) to impose the desired shear strain (in practice, the plate rotates). The lower is stationary. Two configurations are shown. Left (single headed): sensor and actuator are combined and mechanically connected to the upper plate (moving plate). Right (double headed): sensor and actuator are separated. Blue arrows indicate the deformation. The rheometric gap, h, is constant during the experiment.

In all cases the imposed shear strain is adequately described by a scalar quantity when no secondary flows or instabilities are present. In the linear limit and for isotropic samples the stress response is also described by a scalar, i.e., stress magnitude in the shear direction, $\sigma_{1,2}$ (see axis definition in Figure 1.1). However, in the nonlinear regime the tensorial character of the stress cannot be ignored as its different components provide useful information and are necessary to describe the response to flow conditions for many applications.

A brief description of stresses and viscometric functions follows, where the sample is viewed as a continuum, a reasonable assumption when the sample is homogenous. For detailed discussion on definitions, principles and tensorial notation we refer the reader to (Nomenclature and Symbols 2013) and textbooks such as (Macosko 1994, Morrison 2001).

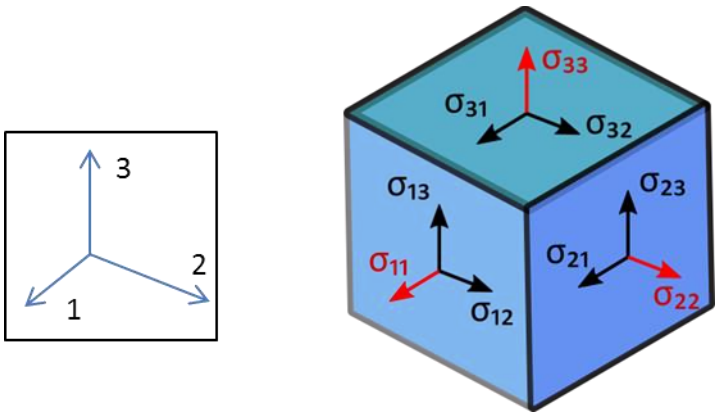

Figure 1.2 The elemental fluid cube (control volume). Red arrows denote tractions normal to the respected plane.

An elemental fluid cube is depicted in Figure 1.2 in the Cartesian coordinate frame. If we consider the 1-2 plane, direction 1 refers to shear, 2 to shear gradient and 3 to vorticity. For isotropic fluids and due to conservation of angular momentum (Larson 2013) the extra (deviatoric) stresses related to flow can be fully described by a second order symmetric tensor:

$$\underline{\sigma} = \begin{bmatrix} \sigma_{11} & \sigma_{12} & \sigma_{13} \\ \sigma_{21} & \sigma_{22} & \sigma_{23} \\ \sigma_{31} & \sigma_{32} & \sigma_{33} \end{bmatrix} \quad (1)$$

Due to symmetry, the response in shear direction (shear stress) is $\sigma_{ij} = \sigma_{ji}$ (i,j = 1,2,3 and i≠j). For simple shear flow in the 1-2 plane we have $\sigma_{21} = \sigma_{12}$, while the rest of-diagonal elements are zero (simple shear). The diagonal elements represent normal stresses. When the flow-induced microstructural distortion is negligible, $\sigma_{11} = \sigma_{22} = \sigma_{33} = 0$ and the only viscometric function usually reported is the shear viscosity $\eta = \sigma_{21}/\dot{\gamma}$. However, when the imposed shear rate distorts the microstructure, normal stresses attain non-zero values. In experiments, the stresses that act on the measuring geometries and are quantified by the sensor (or sensors) are described by the total stress tensor:

$$\underline{\Pi} = \begin{bmatrix} \sigma_{11} + P & \sigma_{12} & 0 \\ \sigma_{21} & \sigma_{22} + P & 0 \\ 0 & 0 & \sigma_{33} + P \end{bmatrix} \quad (2)$$

where the isotropic pressure P reflects the pressure excreted from the surrounding fluid. For compressible fluids, P is derived from the constitutive equation of gases. However, this is not the case for the incompressible fluids of our study, where the calculation of P is based on boundary conditions (Kundu *et al.* 2015). To this end, the viscometric functions that contain material properties related to normal stresses are defined as:

$$N_1 = (\sigma_{11} + P) - (\sigma_{22} + P) \quad \text{and} \quad N_2 = (\sigma_{22} + P) - (\sigma_{33} + P) \tag{3}$$

where N_1 and N_2 are P-independent, true material properties, the so-called normal stress differences. N_1 and N_2 are the manifestation of nonlinear elasticity and are important in polymer processing and many applications that involve flow of microstructured fluids. In Chapter 6 we discuss how N_2 affects rheometry and discuss methods to determine N1 and N_2 from a single measurement.

Given the plethora of protocols and devices (tools) available today, many technical challenges of the past have already been addressed. In particular, modern commercial rotational rheometers have excellent sensitivity (measurement resolution), temperature control and versatility, while they can be combined with structure probing techniques such as scattering, polarimetry, optical microscopy and infrared spectroscopy (Wagner 1998). The embedded electronics in modern rheometers allow the user to perform a series of experiments, here referred as intervals, in a fully automatized way, while many parameters such as temperature, shear rate and data sampling frequency are controlled and even varied simultaneously. On the other hand, automation with its many merits trades-off accessibility to data processing as the "sterilized" operator is not fully aware of how data are processed by the "smart" firmware. This might be sufficient for many applications but not when specific scientific questions challenge a scientist to "push" a rheometer to the edge of its parametric envelope, i.e., frequency, strain resolution, data sampling, shear rate and so on. In many cases, targeted rheometric experiments have to be made in order to assess the limitations and errors of applied techniques or protocols. At the same time, rheology is expanding to systems with distinct and complex features, while the more classic systems (such as polymer melts for instance) need to be investigated in extended parameter space. Few examples out of the many include: i) crosslinking polymers and aging gels require frequency sweeps with a total duration shorter than the rate by which their LVE evolves (Geri *et al.* 2018); ii) polymers with high glass transition temperature need to be measured at elevated temperatures (Parisi *et al.* 2021); iii) local interactions in colloids act at frequencies above 100 rad/s (Schroyen *et al.* 2019) calling for higher frequency measurement capabilities; iv) investigating the response of thixotropic materials requires sequences of tests (Mewis 1979) with superior time resolution and minimal tool inertia (Ewoldt *et al.* 2015); v) the study of materials with structural memory requires specific rejuvenation protocols (Choi and Rogers 2020) and methods to interpret the nonlinear measurements (Divoux *et al.* 2013); vi) edge fracture is a limiting factor in steady shear measurements, and special tools are required to isolate the measuring surfaces from the edge effects (Meissner *et al.* 1989). Obviously the list is long and becomes even longer when discussion is expanded to include extensional deformation (Kolte *et al.* 1997) and in-situ structure probing techniques (Fuller 1990, Wagner 1998). It is clear though, that an all-round rheometer, able to address all possible needs and requirements would be too complicated or even impossible to construct. This motivated many groups to develop custom devices such as rheometers (Athanasiou *et al.* 2019,

Clasen and McKinley 2004, Schroyen *et al.* 2017, Yamamoto *et al.* 1987) shear cells with optical access (Aime *et al.* 2016), rheometric tools (Chaparian *et al.* 2022, Snijkers and Vlassopoulos 2011) and rheometric protocols tailored to address specific problems (Di Dio *et al.* 2022, Donley *et al.* 2020). These are few examples out of the many. In this thesis we will address specific rheometric challenges by developing and implementing rheometric tools and protocols. By no means all protocols or tools described here are strictly new. The state-of-the-art lies in the combination of tools and protocols based on system properties in order to address specific questions, understand measurement issues and expand our current rheometric capabilities.

1.2 Rheometric protocols

The list of rheometric protocols is long (Collyer 1993, Macosko 1994) while their classification can be based on i) the nature of flow such as shear or extension; ii) the control parameter (stress, strain); iii) whether the steady state or the transient signal is of interest; iv) the deformation waveform, i.e., steady or oscillatory; v) the linear or nonlinear dependence of the response on the excitation. We focus on two categories, important for this study. Firstly, the frequency-domain linear and nonlinear protocols, that are based on oscillatory deformation and are described in Chapter 2 and 3. Notably, the raw data are acquired in the time-domain, whereas results are reported in the frequency-domain. Secondly, the time-domain protocols based on constant shear rate. These two categories are described in Chapters 5 and 4, respectively, while a broader introduction with reference to signal processing follows below.

1.2.1 Strain-control protocols: from time to frequency domain

Theoretically, any causal system can be fully characterized by its response to the unitary impulse, the delta function, as depicted in *Figure 1.3* (Oppenheim *et al.* 1997, Smith 2013). The delta function is defined by:

$$\int_{-\infty}^{\infty} \delta(t)dt = 1 \; and \; \delta(t) = 0 \; for \; t \neq 0 \tag{4}$$

When the impulse response, $y_\delta(t)$, is known then the system's response to any arbitrary excitation, $\gamma(t)$, can be extracted by convolving the latter with the impulse response :

$$\sigma(t) = y_\delta(t) * \gamma(t) = \int_{-\infty}^{t} y_\delta(t)\,\gamma(t-t')dt' \tag{5}$$

where * denotes convolution, t is the reference time and t´ is the variable in the convolution integral.

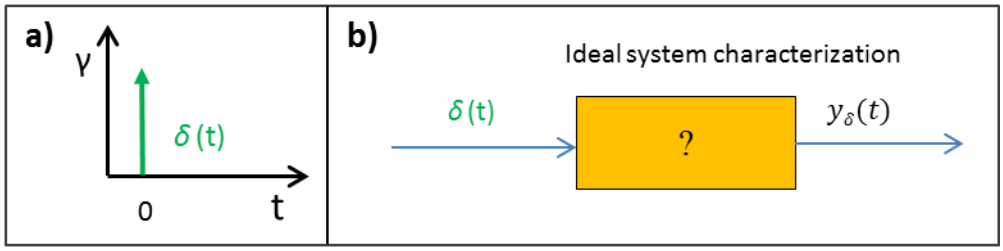

Figure 1.3 Fundamental system characterization by the unitary impulse (delta) function. Yellow rectangular denotes any arbitrary system with input and output.

Evidently from Eq.(4), the delta function is a mathematical abstraction. For strain excitation δ(t) has units of s^{-1} hence the response y(t) has also units of Pa s^{-1} consistent with Eq.(5). This excitation waveform is far from feasible in experiments as it has zero duration. It can be shown that when the superposition principle holds (discussed below), the step function can be utilized instead (Oppenheim *et al.* 1997, Tschoegl 2012). Therefore, shear step-strain (Figure 1.4) is the fundamental deformation utilized in strain-controlled experiments where shear stress is monitored as a function of time. Results are reported in the time domain, while the ratio of the stress to the applied strain, γ_0, defines $G(t)= \sigma(t)/\gamma_0$, the relaxation modulus.

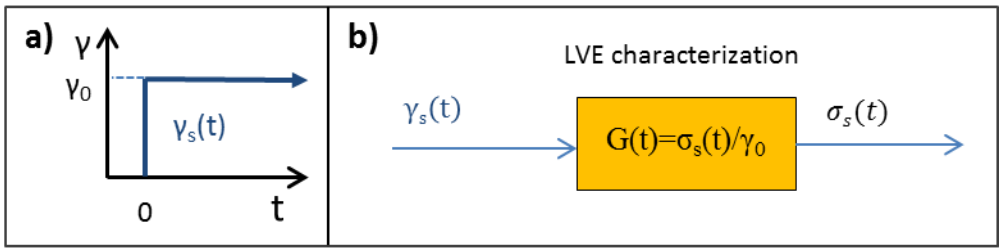

Figure 1.4 *LVE characterization by the step-strain function. The subscript s in stress response denotes the step function (excitation). Yellow rectangular denotes the viscoelastic material under test.*

However, superposition of strain history is valid only when the system is linear and time-translation invariant (called invariant, below). Suppose a system responds with waveform $\sigma_1(t)$ when excited by a waveform $\gamma_1(t)$ and with and $\sigma_2(t)$ when excited by $\gamma_1(t)$. Then conditions for homogenous, additive and invariant response are described as per in Figure *1.5* , (from top to bottom) where c_1 and c_2 are constants. Homogeneity is essentially scaling while additivity ensures that the two or more strain excitations are "processed" independently. In most cases these two properties of panels (i) and (ii) imply one another and are known in rheometry as linearity. Property of panel (iii) is related to the absence of time dependence (aging or in general, evolution of system's response with time). Hence linearity does not necessarily precondition that the system is invariant and vice-versa.

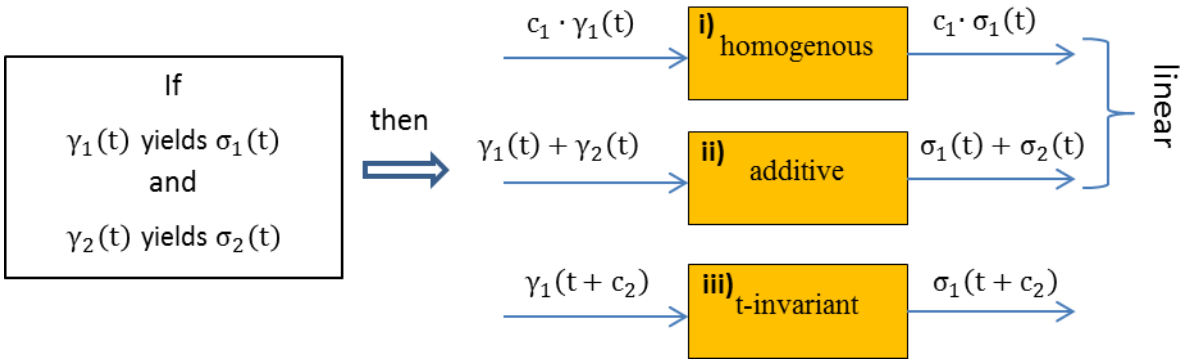

Figure 1.5 Important properties of a system under rheometric probing. The excitation quantity (input) is strain and the monitored quantity (output) is stress. The coefficients c_1, c_2 are arbitrary.

Linearity and invariance constitute the foundations of linear rheometry and are requirements for the validity of the so-called Boltzmann superposition principle expressed as (Ferry 1980, Pipkin 2012):

$$\sigma(t) = \int_{-\infty}^{t} G(t-t')\ \dot{\gamma}(t')dt' \tag{6}$$

where t denotes the time of interest. Here, stresses due to all past-time deformations are integrated up to the time of interest (causality). Eq. (6) is not valid in systems that age and violate time invariance, i.e., where G(t) becomes a function of time (Fielding *et al.* 2000). When the deformation is large enough to distort the microstructure, linearity is violated and G(t) becomes a function of time and strain (G(t,γ)). A notable case is that of systems where strain and time are separable, for instance in homopolymers. In this case the nonlinearity is expressed by the damping function h(γ) = G(t,γ)/ G(t). The relaxation modulus can be viewed as a measure of memory (Dealy *et al.* 2018), and indeed it is related to the fading memory function when modeling the stress response (Larson 2013, Morrison 2001, Wagner 1976). Each strain deformation imposed in the past gradually decays until all memory of the imposed strain is lost.

From an experimental perspective, step-strain is associated with technical limitations as the ideal step-strain cannot be achieved affecting short time stress relaxation data (Flory and McKenna 2004, Venerus and Kahvand 1994). Monitoring the relaxation at very short and long times requires adequate time resolution and sensitivity, respectively. To this end, frequency domain rheometry may offer advantages. It is a popular characterization method where the complex modulus G*(ω), the Fourier transformation of G(t), is determined. Based on the convolution theorem, the convolution of Eq. 5 becomes a simple multiplication in the frequency domain. Hence, by rearranging Eq.5 in the Fourier space we obtain:

$$G^*(\omega) = \frac{\hat{\sigma}(\omega)}{\hat{\gamma}(\omega)} \tag{7}$$

where the circumflex accent ("hat") denotes Fourier transform (FT). Notably, experimental data are discrete values (time series) and not continuous functions, therefore discrete Fourier transform is

applicable (see Chapter 5). Two important messages emanate from the above discussion. Firstly, Eq. 7 holds for any arbitrary excitation function that may contain multiple complex exponentials, i.e., the sum of phase-shifted sinusoids. Signals such as frequency-modulated sinusoids (chirps), superposition of sinusoids (multiwaves), pulses and even pseudo-random noise (Yamamoto, Nakamura and Okano 1987) can be utilized to interrogate the sample. Secondly, and as a consequence of properties illustrated in *Figure 1.5* sinusoidal fidelity is conserved, i.e., the response is a pure harmonic waveform with the same frequency of interrogation.

In a conventional Dynamic Frequency Sweep Test (DFS), the sample is excited sequentially by a few strain oscillations for every frequency point tested. Due to sinusoidal fidelity of the signal, the response of the system is a phase-shifted sinusoidal waveform of the same frequency as the excitation signal, the latter referred to as the base frequency. Phase-shifted sinusoids are conveniently represented as complex exponentials. The correlation of stress response to the imposed complex exponential strain yields the polar coordinates of G*, i.e., the magnitude |G*| and the phase angle (δ). Usually the Cartesian coordinates, i.e., the dynamic moduli, are reported, as shown in the example of *Figure 1.6*(a). This periodic experiment at angular frequency ω, is qualitatively equivalent to a transient experiment at $t=1/\omega$ under the assumption that quasi-steady state is reached within one period of oscillation (Ferry 1980). On the other hand, when a large strain amplitude is applied, linearity breaks-down and the stress response becomes a distorted sinusoid corresponding to odd harmonics. This is the case in Dynamic Strain Sweep tests (DSS) where oscillations with increasing strain amplitude at a given angular frequency are imposed (*Figure 1.6*(b)). At low strain amplitudes the response is linear, while at larger values the apparent complex modulus becomes strain amplitude dependent. Although in principle this is a linear to nonlinear transition, the complex exponential correlation is the same with DFS where usually (or often) only the base frequency is processed and all higher harmonics are rejected. This is in contrast with a typical large or medium amplitude oscillatory experiment (LAOS, MAOS) where odd harmonics are also processed under a specialized framework (Ewoldt *et al.* 2008, Swan *et al.* 2014). Eventually, under DSS the material will yield and post-yielded rheological signatures may exhibit time dependence due to structural recovery as we discuss in Chapter 3. Even harmonics are theoretically not possible, due to time odd symmetry, however they may be present as a result of noise, spectrum leakage, aging or even wall slip (Klein *et al.* 2007).

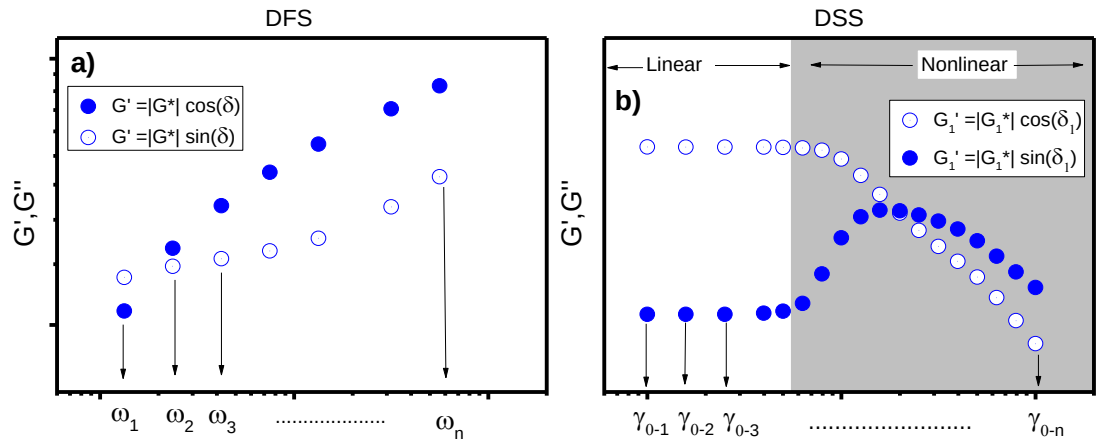

Figure 1.6 An example of data reported for two popular oscillatory tests: a) Dynamic Frequency Sweep. The tested frequencies (points) are indexed from 1 to n; b) Dynamic Strain Sweep. Discrete amplitude increments are indexed form 1 to n. Subscript 1 in the moduli (legend) denotes the base frequency. Gray area denotes the nonlinear regime.

1.2.2 Protocols based on applying a constant shear rate

In these protocols the rheometer executes a single (or a sequence of) steady shear interval(s), while the transient or the steady state signal of shear or normal stress is monitored. A typical response of a linear entangled polymeric melt in shear start-up experiment is shown in Figure 1.7. Upon shear start-up the imposed (accumulated) strain scales linearly with time, i.e., a product of time and shear rate. Initially, the material deforms linearly up to a certain strain as the microstructure is marginally distorted. As strain accumulates, the response deviates from linearity and eventually the material yields and flows, depending on its microstructure. When steady state is reached, material functions, such as shear viscosity and normal stress differences, N_1 and N_2, are usually reported as a function of shear rate. On the other hand, many studies focus on the transient part of the signal, upon flow onset or cessation, a rather important aspect of the material's response. The stress response as a function of time is monitored, upon start-up or cessation of flow, referred as shear stress growth (σ^+) or decay function (σ^-), respectively. In the former case, the rheological consequences of structural changes caused by shear are probed, while the latter captures the relaxing stresses entrapped into the material's microstructure. Usually yielding is considered at the peak stress termed static yield stress or at the steady state termed as dynamic yield stress.

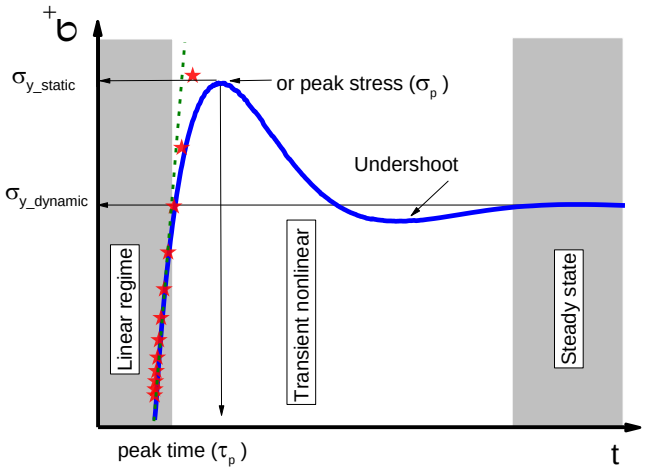

Figure 1.7 Typical stress response (stress growth function) of a linear entangled polymeric melt in shear start-up experiment. Gray shaded areas depict the linear regime and the steady state. Dashed line indicates the linear response. Star symbols denote the linear envelope and are derived from LVE data (Cox-Merz rule).

Understanding all aspects of the yielding mechanism remains a challenge in many materials (Møller *et al.* 2006), given the diversity of microscopic constituents exhibiting plastic events (Aime *et al.* 2022) or conformational changes in systems such as Brownian hard spheres (Koumakis *et al.* 2016), percolated clusters of particles (Moghimi *et al.* 2017), percolated networks (Koga *et al.* 2009) , polymer melt (Cao and Likhtman 2015) or polymeric glasses (Hasan and Boyce 1995). Protocols based on steady shear where flow is interrupted or even reversed are utilized in Chapter 4, to study yielding and thixotropic behavior of a hydrogel. In a simpler form they are utilized in Chapter 6 to probe the steady state N_1 and N_2 values of a linear entangled polymeric melt and solution.

1.3 Thesis overview

In the following Chapters we discuss rheometric tools and protocols that aim to address specific challenges; we discuss their utility as well as the associated limitations. In Chapter 2, we combine LVE measurements using conventional rotational rheometers and our home made HF piezo-rheometer, to probe local interactions in a colloidal glass. We chose sterically stabilized PMMA spheres dispersed in squalene covering a very broad range of volume fractions. We contribute to the discussion on the physics of caging in the supercooled and glassy regime by confronting the data with predictions of a microscopic Nonlinear Langevin Equation dynamical theory with highly accurate structural input. In Chapter 3 we study the rheology of an amphiphilic pentablock hydrogel which was designed and synthesized to serve as drug carrier for anticancer treatment, targeting pancreatic malignant cells. A series of linear and nonlinear tests are performed with this novel hydrogel based on amino acids. We also attempt to correlate

its structure with the nonlinear mechanical response and in particular the yielding behavior. The hydrogel exhibits thixotropic response, residual stresses and strong structural memories imprinted by past plastic deformations, and the investigation of this complex rheology is the subject of Chapter 4. We show that these memories reduce the modulus of resilience, i.e., the ability of the material to store energy elastically. Since memory encoding and probing is achieved by the same experiment, specific protocols are implemented. In Chapter 5, we combine HF rheometry and frequency-modulated strain waveforms to perform Dynamic Frequency Sweeps with a total duration of a few seconds. We show the utility of this method by probing the LVE of a curing vinilester resin. Curing kinetics are also discussed. Finally, in Chapter 6 we utilize the acquired experience with piezoelectric sensors (PZR) to develop a measurement technique for normal stresses in start-up experiments. We improve the current state-of-the-art method of N_1 and N_2 measurement (Schweizer *et al.* 2008) by embedding a piezoelectric sensor to the cone-partition plate fixture, namely CPP. Our model systems in this case are entangled linear polymer melts and solutions.

References

Aime, S., Ramos, L., Fromental, J.-M., Prevot, G., Jelinek, R., and Cipelletti, L., ‘‘A stress-controlled shear cell for small-angle light scattering and microscopy,’’ Review of Scientific Instruments 87, 123907 (2016).

Aime, S., Truzzolillo, D., Pine, D. J., Ramos, L., and Cipelletti, L., ‘‘A unified state diagram for the yielding transition of soft colloids,’’ arXiv preprint arXiv:2212.08863 (2022).

Athanasiou, T., Auernhammer, G. K., Vlassopoulos, D., and Petekidis, G., ‘‘A high-frequency piezoelectric rheometer with validation of the loss angle measuring loop: application to polymer melts and colloidal glasses,’’ Rheologica Acta 58, 619-637 (2019).

Ballauff, M., Brader, J. M., Egelhaaf, S. U., Fuchs, M., Horbach, J., Koumakis, N., Kruger, M., Laurati, M., Mutch, K. J., Petekidis, G., Siebenburger, M., Voigtmann, T., and Zausch, J., ‘‘Residual stresses in glasses,’’ Phys Rev Lett 110, 215701 (2013).

Barnes, H. A., Hutton, J. F., and Walters, K., *An introduction to rheology Vol. 3* (Elsevier, 1989).

Cao, J., and Likhtman, A. E., ‘‘Simulating startup shear of entangled polymer melts,’’ ACS Macro Letters 4, 1376-1381 (2015).

Chaparian, E., Owens, C. E., and McKinley, G. H., ‘‘Computational rheometry of yielding and viscoplastic flow in vane-and-cup rheometer fixtures,’’ Journal of Non-Newtonian Fluid Mechanics 307, 104857 (2022).

Choi, J., and Rogers, S. A., ‘‘Optimal conditions for pre-shearing thixotropic or aging soft materials,’’ Rheologica Acta 59, 921-934 (2020).

Clasen, C., and McKinley, G. H., ‘‘Gap-dependent microrheometry of complex liquids,’’ Journal of Non-Newtonian Fluid Mechanics 124, 1-10 (2004).

Coleman, B. D., and Noll, W., ‘‘Foundations of linear viscoelasticity,’’ Reviews of modern physics 33, 239 (1961).

Collyer, A. A., *Techniques in rheological measurement* (Springer, 1993).

Dealy, J. M., Read, D. J., and Larson, R. G., *Structure and rheology of molten polymers: from structure to flow behavior and back again* (Carl Hanser Verlag GmbH Co KG, 2018).

Di Dio, B. F., Khabaz, F., Bonnecaze, R. T., and Cloitre, M., ‘‘Transient dynamics of soft particle glasses in startup shear flow. Part II: Memory and aging,’’ Journal of Rheology 66, 717-730 (2022).

Divoux, T., Grenard, V., and Manneville, S., ‘‘Rheological hysteresis in soft glassy materials,’’ Physical review letters 110, 018304 (2013).

Donley, G. J., Singh, P. K., Shetty, A., and Rogers, S. A., ‘ ‘Elucidating the G ″ overshoot in soft materials with a yield transition via a time-resolved experimental strain decomposition,’ ’ Proceedings of the National Academy of Sciences 117, 21945-21952 (2020).

Ewoldt, R. H., Hosoi, A., and McKinley, G. H., ‘‘New measures for characterizing nonlinear viscoelasticity in large amplitude oscillatory shear,’’ Journal of Rheology 52, 1427-1458 (2008).

Ewoldt, R. H., Johnston, M. T., and Caretta, L. M., “Experimental challenges of shear rheology: how to avoid bad data.” *Complex fluids in biological systems* (Springer, 2015).

Ferry, J. D., *Viscoelastic properties of polymers* (John Wiley & Sons, 1980).

Fielding, S. M., Sollich, P., and Cates, M. E., ‘‘Aging and rheology in soft materials,’’ Journal of Rheology 44, 323-369 (2000).

Flory, A., and McKenna, G., ‘‘Finite step rate corrections in stress relaxation experiments: a comparison of two methods,’’ Mechanics of Time-Dependent Materials 8, 17-37 (2004).

Franck, A., ‘‘FRT transducer,’’ Rheology Brochure (2006).

Fuller, G. G., ‘‘Optical rheometry,’’ Annual review of fluid mechanics 22, 387-417 (1990).

Geri, M., Keshavarz, B., Divoux, T., Clasen, C., Curtis, D. J., and McKinley, G. H., ‘‘Time-resolved mechanical spectroscopy of soft materials via optimally windowed chirps,’’ Physical Review X 8, 041042 (2018).

Hansen, J.-P., and McDonald, I. R., *Theory of simple liquids: with applications to soft matter* (Academic press, 2013).

Hasan, O., and Boyce, M. C., ‘‘A constitutive model for the nonlinear viscoelastic viscoplastic behavior of glassy polymers,’’ Polymer Engineering & Science 35, 331-344 (1995).

Israelachvili, J. N., *Intermolecular and surface forces* (Academic press, 2011).

Jamali, S., and McKinley, G. H., ‘‘The Mnemosyne number and the rheology of remembrance,’’ Journal of Rheology 66, 1027-1039 (2022).

Keim, N. C., Paulsen, J. D., Zeravcic, Z., Sastry, S., and Nagel, S. R., ‘‘Memory formation in matter,’’ Reviews of Modern Physics 91, 035002 (2019).

Klein, C. O., Spiess, H. W., Calin, A., Balan, C., and Wilhelm, M., ‘‘Separation of the nonlinear oscillatory response into a superposition of linear, strain hardening, strain softening, and wall slip response,’’ Macromolecules 40, 4250-4259 (2007).

Koga, T., Tanaka, F., and Kaneda, I., “Stress growth in transient polymer networks under startup shear flow.” *Gels: Structures, Properties, and Functions* (Springer, 2009).

Kolte, M. I., Rasmussen, H. K., and Hassager, O., ‘‘Transient filament stretching rheometer,’’ Rheologica acta 36, 285-302 (1997).

Koumakis, N., Laurati, M., Jacob, A. R., Mutch, K. J., Abdellali, A., Schofield, A. B., Egelhaaf, S. U., Brady, J. F., and Petekidis, G., ‘‘Start-up shear of concentrated colloidal hard spheres: Stresses, dynamics, and structure,’’ Journal of Rheology 60, 603-623 (2016).

Kundu, P. K., Cohen, I. M., and Dowling, D. R., *Fluid mechanics* (Academic press, 2015).

Larson, R. G., *Constitutive equations for polymer melts and solutions: Butterworths series in chemical engineering* (Butterworth-Heinemann, 2013).

Läuger, J., and Stettin, H., ‘‘Effects of instrument and fluid inertia in oscillatory shear in rotational rheometers,’’ Journal of Rheology 60, 393-406 (2016).

Laun, H., ‘‘Description of the non-linear shear behaviour of a low density polyethylene melt by means of an experimentally determined strain dependent memory function,’’ Rheologica Acta 17, 1-15 (1978).

Lindman, B., and Wennerström, H., ‘‘Micelles: Amphiphile aggregation in aqueous solution,’’ Micelles, 1-83 (2006).

Lionberger, R. A., and Russel, W., ‘‘Microscopic theories of the rheology of stable colloidal dispersions,’’ Advances in Chemical Physics 111, 399-474 (2000).

Mackay, M., and Halley, P., ‘‘Angular compliance error in force rebalance torque transducers,’’ Journal of Rheology 35, 1609-1614 (1991).

Macosko, C. W., *Rheology: principles, measurements, and applications* (Wiley-vch, 1994).

Meissner, J., Garbella, R., and Hostettler, J., ‘‘Measuring normal stress differences in polymer melt shear flow,’’ Journal of Rheology 33, 843-864 (1989).

Mewis, J., ‘‘Thixotropy-a general review,’’ Journal of Non-Newtonian Fluid Mechanics 6, 1-20 (1979).

Mewis, J., and Wagner, N. J., *Colloidal suspension rheology* (Cambridge University Press, 2012).

Moghimi, E., Jacob, A. R., Koumakis, N., and Petekidis, G., ‘‘Colloidal gels tuned by oscillatory shear,’’ Soft Matter 13, 2371-2383 (2017).

Mohan, L., Cloitre, M., and Bonnecaze, R. T., ‘‘Build-up and two-step relaxation of internal stress in jammed suspensions,’’ Journal of Rheology 59, 63-84 (2015).

Møller, P. C., Mewis, J., and Bonn, D., ‘‘Yield stress and thixotropy: on the difficulty of measuring yield stresses in practice,’’ Soft matter 2, 274-283 (2006).

Morrison, F. A., ‘‘Understanding Rheology. 2001,’’ Ox. Un. Press, ISBN, 978-0 (2001).

Nomenclature, A. H. C. o. O., and Symbols, ‘‘Official symbols and nomenclature of The Society of Rheology,’’ Journal of Rheology 57, 1047-1055 (2013).

Oppenheim, A. V., Willsky, A. S., Nawab, S. H., and Ding, J.-J., *Signals and systems Vol. 2* (Prentice hall Upper Saddle River, NJ, 1997).

Parisi, D., Han, A., Seo, J., and Colby, R. H., ‘‘Rheological response of entangled isotactic polypropylene melts in strong shear flows: Edge fracture, flow curves, and normal stresses,’’ Journal of Rheology 65, 605-616 (2021).

Pipkin, A. C., *Lectures on viscoelasticity theory Vol. 7* (Springer Science & Business Media, 2012).

Rubinstein, M., and Colby, R. H., *Polymer physics Vol. 23* (Oxford University Press New York, 2003).

Rubinstein, M., and Obukhov, S., ‘‘Memory effects in entangled polymer melts,’’ Physical review letters 71, 1856 (1993).

Schroyen, B., Hsu, C.-P., Isa, L., Van Puyvelde, P., and Vermant, J., ‘‘Stress Contributions in Colloidal Suspensions: The Smooth, the Rough, and the Hairy,’’ Physical Review Letters 122, 218001 (2019).

Schroyen, B., Swan, J. W., Van Puyvelde, P., and Vermant, J., ‘‘Quantifying the dispersion quality of partially aggregated colloidal dispersions by high frequency rheology,’’ Soft matter 13, 7897-7906 (2017).

Schweizer, T., Hostettler, J., and Mettler, F., ‘‘A shear rheometer for measuring shear stress and both normal stress differences in polymer melts simultaneously: the MTR 25,’’ Rheologica acta 47, 943-957 (2008).

Smith, S., *Digital signal processing: a practical guide for engineers and scientists* (Elsevier, 2013).

Snijkers, F., and Vlassopoulos, D., ‘‘Cone-partitioned-plate geometry for the ARES rheometer with temperature control,’’ Journal of Rheology 55, 1167-1186 (2011).

Sudreau, I., Auxois, M., Servel, M., Lécolier, É., Manneville, S., and Divoux, T., ‘‘Residual stresses and shear-induced overaging in boehmite gels,’’ Physical Review Materials 6, L042601 (2022).

Swan, J. W., Furst, E. M., and Wagner, N. J., ‘‘The medium amplitude oscillatory shear of semi-dilute colloidal dispersions. Part I: Linear response and normal stress differences,’’ Journal of Rheology 58, 307-337 (2014).

Tanford, C., *The hydrophobic effect: formation of micelles and biological membranes 2d ed* (J. Wiley., 1980).

Totten, G. E., *Handbook of residual stress and deformation of steel* (ASM international, 2002).

Tschoegl, N. W., *The phenomenological theory of linear viscoelastic behavior: an introduction* (Springer Science & Business Media, 2012).

Venerus, D., and Kahvand, H., "Normal stress relaxation in reversing double‐step strain flows", Journal of Rheology 38, 1297-1315 (1994).

Wagner, M., ''Analysis of time-dependent non-linear stress-growth data for shear and elongational flow of a low-density branched polyethylene melt,'' Rheologica Acta 15, 136-142 (1976).

Wagner, N. J., ''Rheo-optics,'' Current opinion in colloid & interface science 3, 391-400 (1998).

Yamamoto, J., Nakamura, H., and Okano, K., ''Apparatus for Measurement of Complex Shear Modulus of Liquid Crystals at Low Frequencies,'' Japanese Journal of Applied Physics 26, 29 (1987).

Chapter 2 : Probing particle cage dynamics in concentrated suspensions and glasses of hard spheres particles with high frequency and conventional rheometry

2.1 Introduction: timescales, dynamics and motivation.

Undoubtedly, hard spheres suspension dynamics have been studied rigorously and are nowadays a textbook subject (Mewis and Wagner 2012, Russel *et al.* 1991, Wagner and Mewis 2021). The model of hard spheres, utilized in theoretical studies and simulations, is a simple in terms of constituents system yet with rich structural, thermodynamic and mechanical behavior. The nature of the glass transition in colloidal glasses is still a debated topic while advances are made by comparing the physics of the latter with molecular glass formers (Berthier and Reichman 2023, Biroli and Garrahan 2013, Li *et al.* 2020, Vila-Costa *et al.* 2023). Hard interactions are theoretically defined by an infinite repulsion at contact and no interaction at interparticle distances greater that 2R where R is the particle radius. In a real system such as the sterically stabilized PMMA spheres (Antl *et al.* 1986) the repulsion potential cannot be infinitely steep (Bryant *et al.* 2002) while the softness induced by the steric layer affects the rheological response (Frith *et al.* 1990). In the colloidal regime (length scales) the time scale is governed by the Brownian time τ_0 (= R^2 /$6D_0$), with $D_0 = k_B T/6\pi\eta_s R$ the Stokes-Einstein self-diffusion coefficient at infinite dilution, where k_B is the Boltzmann constant, T the absolute temperature and η_s the solvent viscosity. As the dispersant volume fraction, φ, increases, particles start to interact via solvent-mediated hydrodynamic and excluded volume (entropic) interactions hence the dynamics slowdown. At the onset of supercooled (Ediger and Harrowell 2012) regime $\phi \approx 0.49$ (Figure 2.1) two relaxation process emerge (Van Megen *et al.* 1998) while at the ideal glass transition packing fraction, $\varphi \approx 0.58$, the shear viscosity diverges. Taking the cage model as reference (Pusey 1991, Pusey 2008) the two dominant relaxation mechanisms have different origin: the β-relaxation is linked to in-cage rattling (Donev *et al.* 2005, Gotze and Sjogren 1992) and the structural α-relaxation to thermally activated hopping or cage escape. This mobility reduction is reflected to the mean squared displacement (MSD), $\langle \Delta r^2(t) \rangle = \langle |r(t) - r(0)|^2 \rangle$ where r(t) denotes position coordinate at time t and the brackets averaging over all particle trajectories under consideration. Figure 2.2(a) depicts the MSD determined for colloidal suspensions at various φ via Brownian Dynamics simulations (Koumakis 2011). At φ=0.2 and for all observation times the MSD corresponds to a single diffusion process where the particle exhibits uncorrelated step motion. We note here that at extremely

short times t~10^{-12} the particle moves balistically $\langle \Delta r^2(t) \rangle \propto t^2$ (Dhont 1996, Pusey 2011) but this response is not relevant in our discussion here and is not indicated by the experiments or simulations we present below. At higher φ single particle motion is coupled to the structure and dynamics of neighboring particles, and becomes subdiffusive with a localization plateau predominating at φ>0.58 and intermediate times, separating the dynamics to long time and short time regimes. Hence diffusivity is governed by the long and short time coefficients D_L and D_S (Brady 1993, Dhont 1996, Nägele 2002, van Megan *et al.* 1987). In short time dynamics, $t < \tau_0$, the in-cage rattling (localization) time is $\tau_{loc} = r_{loc}^2 / 6D_s(\varphi)$ where r_{loc} is the localization length related to cage size. As φ approaches the random close packing (RCP), φ_{RCP}, the particle in-cage mobility, hence D_s, are reduced significantly, due to hydrodynamic interactions (Sierou and Brady 2001, Van Megen *et al.* 1998) and attain zero value when free volume around the particle diminishes. Likewise, at long times, $t > t_0$, the hopping time $\tau_{hop} = r_{hop}^2 / 6D_L(\varphi)$ where r_{hop} is (to a reasonable approximation) the particle displacement for cage escape. We note here that this is not a rigorous definition of τ_{hop} and τ_{loc} but rather a generalization of τ_0. Nonetheless, both times are calculated from the NLE theoretical framework discussed below.

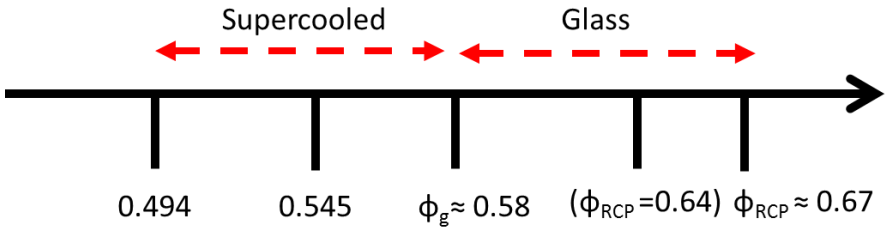

Figure 2.1 Characteristic volume fraction values of the supercooled and glassy regime for non-crystalizing (polydisperse) HS. Glass transition is exhibited at φ≈0.58. Random close packing is considered between 0.64 (monodisperse spheres) and 0.67 for polydisperse spheres with standard deviation from the mean 0.1. Inspired by (Hunter and Weeks 2012).

A similar behavior is exhibited in LVE spectra where long and short time dynamics, low- and high-frequency respectively, are separated by the caging plateau exhibited by the elastic modulus G´ the manifestation of the localization effects, as depicted in Figure 2.2(b). When the probing frequency is decreased sufficiently (sometimes inaccessible by commercial rheometers) the suspension exhibits a liquid like behavior marked by the LF G´- G´´ crossover with time scale $=1/\omega_{c\text{-}LF}$. Similar phenomenology but for completely different reason, is exhibited at elevated frequencies. At these short-time observations the particle is "seen" mobile again as it cannot explore its cage boundaries. This is reflected in the rheological response which exhibits a second solid to liquid transition and a relevant HF G´ - G´´ crossover, this time at $\omega_{c\text{-}HF} > 1/\tau_0 >> \omega_{c\text{-}LF.}$. At these elevated frequencies Brownian motion cannot

randomize the structure and its contribution to G´´ becomes negligible hence only hydrodynamics contribute to the latter that scales linearly with ω as is illustrated in Figure 2.2(b).

On the other hand Brownian motion, unable to restore the perturbation, contributes significantly to elasticity. The weak power law of G´ is sensitive to local interactions (Schroyen *et al.* 2019) hence, is strongly affected by the particle's steric layer that induces deviations from ideal HS interactions (Ikeda *et al.* 2013, Mewis and Haene 1993). The slope of G´ at frequencies above the HF crossover is 0.3 typical for hairy (sterically stabilized) particles (Athanasiou *et al.* 2019, Shikata and Pearson 1994) in agreement with data in Figure 2.2(b).

Below we discuss these microscopic times, and in particular τ_{loc} and how it is related to the macroscopic $1/\omega_{c\text{-}HF}$. The majority of studies focus on the α-relaxation and the caging plateau as the former was in the epicenter of a debate between frozen dynamics predicted by ideal MCT (Reinhardt *et al.* 2010) and finite cage lifetime supported by other theories (Schweizer and Saltzman 2003), scattering experiments (Brambilla *et al.* 2009, Van Megen *et al.* 1998) and direct observations (Weeks and Weitz 2002), while the plateau is the manifestation of the glass transition itself. To the best of our knowledge very few studies link rheological signature of colloidal glasses with theoretical description of β-relaxation. Note however that HF data are rare as most rheometers are limited to frequencies up to 100rad/s. Besides specific instrumental capabilities, these limitations are often imposed by fundamental principles such as tool inertia in the single headed configurations (Ewoldt *et al.* 2015, Läuger and Stettin 2016) and sample inertia. The latter induces errors that are sensitive to the sample modulus and the rheometric gap (Athanasiou *et al.* 2019, Schrag 1977). To this end we utilize HF rheometry by means of an home developed piezo rheometer (PZR) thus extending the accessible frequency range up to 5000 rad/s. Resonant techniques such as (Willenbacher and Oelschlaeger 2007) can also access HF range albeit measurements are made at a small number of discrete frequencies. Merits and limitations of HF techniques are reviewed elsewhere (Schroyen *et al.* 2020). For monodispersed spheres the LF crossover can be mapped to the single element Maxwell fluid. However, this is not the case for the HF crossover where modeling is challenging. On the other hand, it clearly sets a time scale $\tau_{c\text{-}HF} = 1/\omega_{c\text{-}HF}$ and a characteristic modulus $G_{c\text{-}HF}=G'(\omega_{c\text{-}HF})=G''(\omega_{c\text{-}HF})$ that marks the solid to fluid transition, (Figure 2.2(b)) and should reflect the characteristics of the cage.

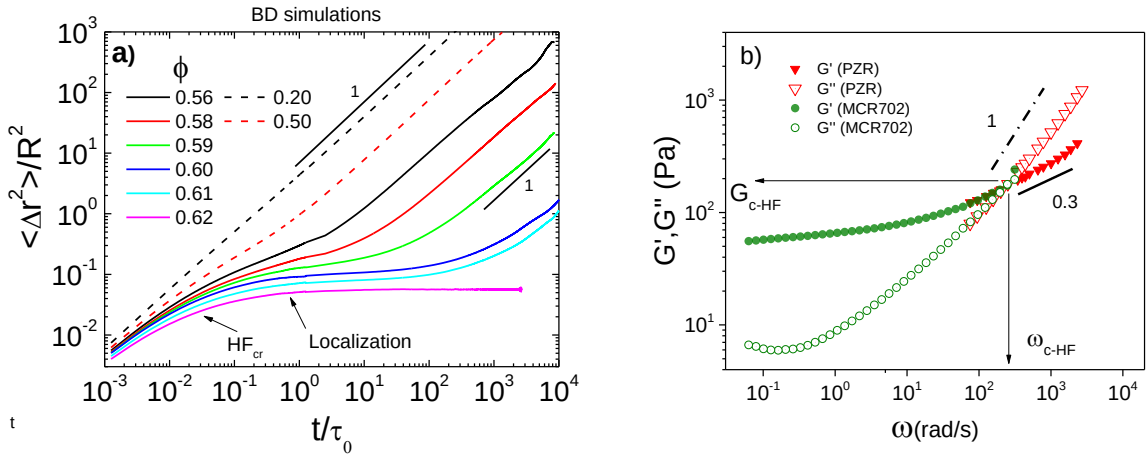

Figure 2.2 a) MSD calculations for varius φ colloidal sunspensions via Brownian Dynamic simulations. Data from N.Koumakis PhD thesis. b) LVE spectum of a typical collodal glass measured with MCR702 (olive spheres) and PZR (red triangles) . Arrows mark the $\omega_{c\text{-}HF}$ and $G_{c\text{-}HF}$ while the LF cossover is not experimetally accesible. Slope 1 in G´´ confirms its pure hydrodynamic origin. G´ weak power law of 0.3 reflects deviation from the lubrication limit.

The classic Stokes-Einstein-Sutherland (SE) equation relates a macroscopic property (solvent viscosity) to a microscopic one (diffusivity) in the dilute limit. By generalizing this equation, Mason related the MSD to the frequency-dependent complex modulus $G^*(\omega)$ given by (Mason 2000):

$$G^*(\omega) = \frac{k_B T}{\pi R i \langle \widetilde{\Delta r^2}(t) \rangle} \tag{2.1}$$

where i is the imaginary and $\langle \widetilde{\Delta r^2}(t) \rangle$ the Fourier transform of the MSD. Hence

$$G'(\omega) = |G^*(\omega)| \cos\left(\frac{\pi\alpha(\omega)}{2}\right) \tag{2.2}$$

$$G''(\omega) = |G^*(\omega)| \sin\left(\frac{\pi\alpha(\omega)}{2}\right) \tag{2.3}$$

where α is the slope of the logarithm of the MSD :

$$\alpha(\omega) = \frac{d \ln\langle \Delta r^2(t) \rangle}{d \ln t} \tag{2.4}$$

Eq. (2.1) is one of the so-called Generalized SE equations, that contrary to SE equation have no rigorous theoretical basis (Cipelletti and Ramos 2005) while require the validity of fluctuation dissipation theorem. The latter implies that the system is at thermodynamic equilibrium, not true for the glassy state. Nevertheless, is has been utilized extensively in microrheology (Squires and Mason 2010) and found to describe data consistently for colloidal glasses (Banchio *et al.* 1999) and other metastable systems where the evolution towards equilibrium is slow.

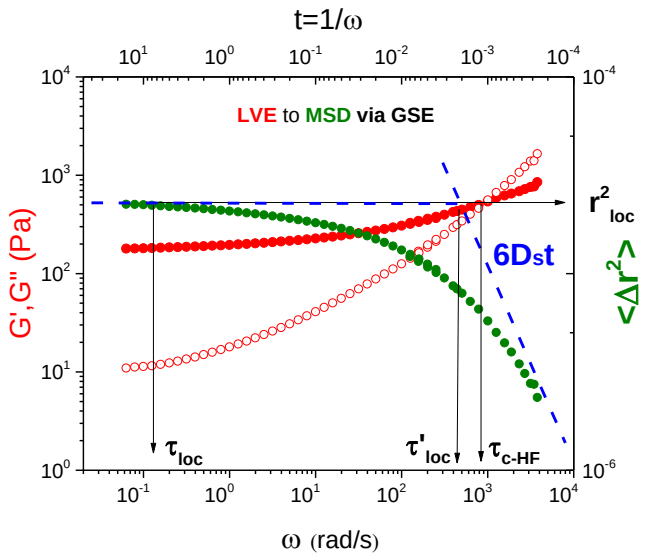

Figure 2.3 LVE of a colloidal glass measured with MCR702 and extended with PZR up to 4000 rad/s. The corresponding MSD (right Y axis) is obtained by rearranging Eq (2.2) and (2.3). Abscissa is either angular frequency or the corresponding observation time t=1/ω (upper x axis). Data conversion A. Papagianopoulos.

we utilize Eq. (2.2), (2.3) to interrelate the measured LVE spectrum of a glass with the corresponding MSD in Figure 2.3 where the abscissa is either angular frequency or the corresponding observation time t=1/ω (upper x axis). At long times (low frequencies) the particle is localized within localization length, r_{loc}, evident by the plateau in MSD and G´. At shorter times the MSD slope approaches 1 (Fickian Diffusion) with a diffusivity equal to D_s. From this simple graphic representation is clear that the microscopic localization time τ'_{loc} and the $\tau_{c\text{-}HF}$ deduced from macroscopic linear viscoelastic measurements are comparable and this motivated us to further explore this analogy. To this end, we measured the volume fraction dependence of $G_{c\text{-}HF}$ and $\omega_{c\text{-}HF}$ and compare data with predictions of the Nonlinear Langevin Eq. (NLE) theory.

2.2 NLE theory

Within the ideal glass transition picture for colloids the short and long time diffusivity, $D_s(\varphi)$ and $D_L(\varphi)$ converge to zero at φ_{RCP} and φ_g respectively. In contrast, NLE predicts non-zero D_L up to RCP as it relates the cage boundaries to entropic barriers that confine the particles for times smaller than hopping ones. Thermally activated hopping, which is introduced by means of a random force, will eventually lead to escape of a few particles from the barrier, within the observation time (Saltzman and Schweizer 2006). Consistent with some experimental observations (Cipelletti and Ramos 2005) the out-of-cage diffusion is predicted to freeze only at RCP i.e. φ_{RCP} =0.64 for monodisperse spheres, avoiding MCT singularities at 0.64> φ >0.515. This entropic barrier is conceived as an effective free energy F_{dyn} calculated for a given

structural input by means of the radial distribution function g(r) or its Fourier image, the structure factor S(q) (Saltzman 2003):

$$\beta F_{dyn}(r) = -3\ln\left(\frac{r}{2R}\right) - \int \frac{d^r q\ \rho C^2(q) S(q)\, e^{[-q^2 r^2 (1+S^{-1}(q))/6]}}{(2\pi)^3} \tag{2.5}$$

where the Boltzmann factor $\beta=1/k_BT$, C(q) is the Fourier image of the direct correlation function, S(q) the dimensionless collective structure factor, and ρ the particle number density. The effective free-energy function based on structural input for φ=0.58 is indicatively depicted in Figure 2.4. It is comprised by a steep, short-range repulsion and a smoothly varying, long-range attraction. The former localizes the particle in a length scale r_{loc} (in cage rattling) while the latter allows the hopping event (out of cage motion) to be attained once the imposed barrier F_B is exceeded by thermal energy. The structural input (S(q) and C(q)) in Eq. (2.5) can be calculated for the hard sphere fluid from the Ornstein-Zernike (OZ) integral equation (Hansen and McDonald 2013):

$$h(r) = c(r) + \rho \int c(|r - r'|) h(r') dr' \tag{2.6}$$

where h(r) ≡ g(r) – 1. In order to calculate g(r) and the direct correlation function, c(r) – one of the various pair functions - some physically based assumption in a form of closure relation is needed. Percus–Yevick (PY) is a classic fairly reasonable approximation at low volume fractions (Hansen and McDonald 2013). However predictions of OZ-PY method are poor at short interparticle distances i.e. r/2R ≈ 1.0 to 1.6 (Henderson and Grundke 1975). Consequently, at low and medium φ predictions are consistent with simulations and scattering experiments but fail at the super cooled and glassy regime. Recent work, focused on NLE, demonstrated more accurate predictions when the modified Verlet (MV) (Verlet 1980, Verlet 1981) closure was utilized (Zhou *et al.* 2020). A fundamental difference is reflected in the direct correlation function where an attractive like tail is introduced for short interparticle distances absent in OZ-PY calculations where c(r)=0. This effective attraction is a result of crowdedness as the neighboring particles force the tagged particles to stay close for longer hence, this effect is increased with φ increase as shown in Figure 2.4(b).

Given that the effective free-energy is known from Eq.(2.5) the time required for the particle to reach a localized state is given by :

$$\frac{\tau_{loc}}{\tau_0} = \frac{2g(\sigma)}{\sigma^2} \int_0^{r_{loc}} dr e^{\beta F_{dyn}(r)} \int_0^r dr' e^{-\beta F_{dyn}(r')} \tag{2.7}$$

where g(σ) is the value of the radial distribution function at contact. The modulus at the localized state can also be calculated by (Schweizer and Yatsenko 2007):

$$G' = \frac{k_B T}{60\pi^2} \int_0^\infty dq \left[q^2 \frac{d}{dq} \ln(S(q))\right]^2 exp\left[\frac{-q^2 r_{loc}^2}{3S(q)}\right] \tag{2.8}$$

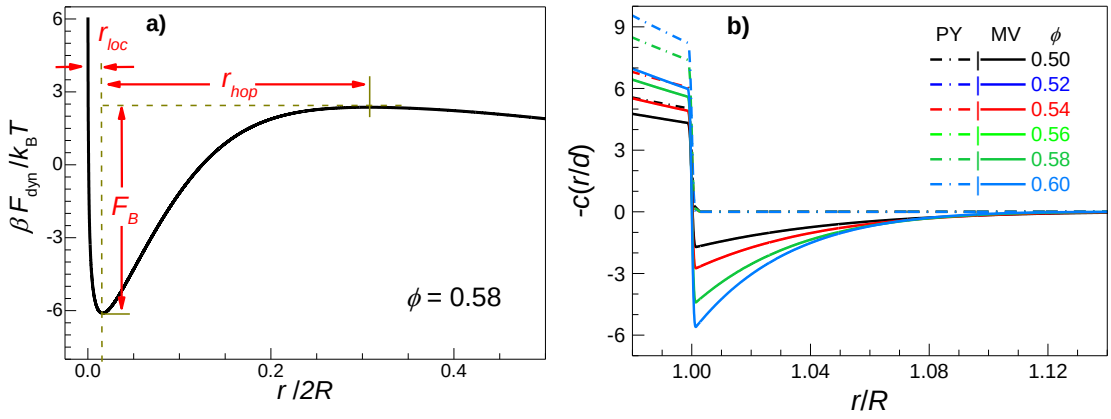

Figure 2.4 a) Effective free-energy function based on PY static input for φ=0.58. Localization and hopping lengths related to in- and out of-cage motion respectively are shown. F_B denotes the barrier while the prefactor β is taken as $1/k_BT$. b) Direct correlation function calculations for φ from 0.5 to 0.6 (bottom to top) based on PY (dash-dotted) and MV (solid) closures. Abscissa is expanded near contact region. From (Zhou, Mei and Schweizer 2020)

2.3 Materials and methods

Repulsive (nearly hard sphere) glasses

Poly-methylmethacrylate (PMMA) particles with hydrodynamic radius R_H=264nm dispersed in squalene where utilized as the primary sample. Squalene (Sigma Aldrich, Germany) was chosen for its high boiling point of 315 $^{\circ}$C and its refractive index proximity to PMMA in order to prevent evaporation and minimize aging effects, respectively. Its relatively high viscosity enhanced torque signal but most importantly slowed down the in-cage dynamics allowing HF crossover to be accessible by conventional rotational rheometers such as MCR501, MCR702 (Anton Paar, Austria) and ARES (TA Instruments, USA) and, our in-lab developed PZR. MCR702 with cone –plate geometry was utilized in separated motor transducer mode when the frequency of interest was greater than 50 rad/s to minimize tool and sample inertia effects (Athanasiou *et al* 2019) (see Appendix (A.2)). The solvent shear viscosity was measured with a DMA 4100M viscometer (Anton Paar, Austria) and found to be η_s = 13.32 mPa s at 23 ^{o}C, where all measurements were performed. Steric stabilization is realized by chemically grafted poly-hydro-stearic acid (PHSA) chains (≈10 nm). The particle hydrodynamic radius was confirmed by dynamic light scattering measurements in the dilute regime. Size polydispersity (standard deviation over the mean) is around 10% suppressing the crystalline phase. The volume fraction was determined by centrifugation to random close packing (RCP) which is assumed to be $\varphi_{RCP} \approx 0.67$. Starting from RCP the sample was successively diluted, varying φ from 0.64 to 0.45, preparing in total 38 discrete samples with

progressive lower volume fractions, (all from the same RCP batch). Aging at these systems affects mainly G´´ at the lower frequency-end as short time in-cage dynamics are age-independent (Athanasiou *et al.* 2019, Ballesta and Petekidis 2016, Jacob *et al.* 2019) hence the system is considered within the measurement timescales as time invariant. The typical large-amplitude rejuvenation is not applicable with the PZR device thus we tried to ensure another method of preparing the sample with similar shear history in all rheometers. Particle swelling can induce significant uncertainties therefore the stock sample was left at rest for two months after solvent exchange and then centrifuged to RCP. After solvent addition the vial was placed on a rolling mixer for sufficiently long period depending on the concentration. Once particle dispersion was completed, followed by a rest time of 12h, the sample was loaded on the rheometer. A reduction of the rest time was required for less concentrated samples ($\varphi<0.58$) to prevent sedimentation. All measurements were completed within 2 hours upon loading with no rejuvenation Small amplitude oscillatory shear measurements were performed at 20 and even more points per decade to capture the HF moduli crossover. Weak moduli evolution was observed in very dense samples ($\varphi > 0.6$) within the first 30 min. At longer times the LVE spectra and particularly the HF crossover were found to be identical. Plate-plate 25mm geometry was utilized in the very dense samples to overcome difficulties related to loading, by squeezing the sample when the gap is lowered. Less concentrated samples were measured with cone –plate 50 mm geometry in the ARES.

Attractive glasses

A series of attractive samples of different attractive strength, namely U= -2, -4, and -6 k_BT were also prepared. The initial stock was a repulsive batch (0 k_BT) and an attractive (-20 k_BT) both at $\varphi=0.60$. The attraction was implemented by depletion i.e. addition of a non-adsorbing linear polymer. A stock solution of polybutadiene (1,4) with M_w = 323 300 g/mol and a radius of gyration, R_g =19 nm (measured by light scattering) was mixed with the colloid. The attraction strength was calculated according to the generalized free volume theory (Fleer and Tuinier 2007). By mixing proper amounts of 0 and -20 k_BT glasses the desired attraction strength was achieved while the volume fraction was kept constant at 0.60. Given the sample polydispersity, φ was calculated based on the assumption that RCP achieved after centrifugation is $\varphi_{RCP}=0.67$ (Schaertl and Sillescu 1994). This among other methods of determining φ induces uncertainties (Poon *et al.* 2012) nevertheless it is in accord with many rigorous studies in the literature.

2.4 Results and discussion

Measurements focused on the Linear Viscoelastic (LVE) spectrum as determined by a dynamic frequency sweep and specifically the $G_{c\text{-}HF}$ and $\omega_{c\text{-}HF}$. Hence MCR702 or ARES data were complemented by PZR when needed, i.e., at very concentrated samples.

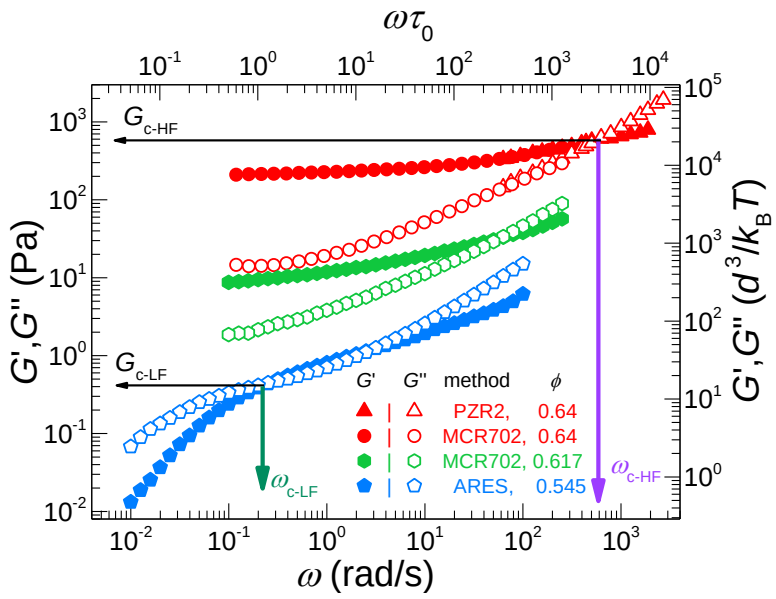

Figure 2.5 Dynamic frequency sweeps of concentrated (φ=0.64, 0.617 and 0.545) hard spheres, R_h=264nm dispersed in squalene at T=23°C. Measurements performed by MCR 702, ARES and PZR as indicated. Vertical and horizontal arrows point to dynamic moduli crossover frequency and magnitude respectively.

The LVE spectra for three samples measured are shown in Figure 2.5. The most concentrated (with φ=0.64) exhibits the HF crossover at 586 rad/s while at lower frequencies the caging plateau predominates. As φ is decreased to 0.617, still in the glassy regime, $\omega_{c\text{-}HF}$ becomes smaller and falls within the experimental range of MCR702. This frequency decrease reflects the cage enlargement and the less frequent exploration of cage boundaries exhibited by the particles as their concentration is reduced. Caging predominates even at low frequencies (0.1 rad/s) with no indication of LF crossover. On the contrary, at φ=0.545 the LF crossover becomes faster and is accessible in the experimental window. In this supercooled regime the cage becomes larger and weaker as the barrier height is decreased resulting in more frequent hopping events.

2.4.1 Short time dynamics

NLE determines the time needed for a particle to reach (feel) its cage boundaries by calculating the time needed to reach r_{loc} from r=0 and t=0 (see Figure 2.4) and (Schweizer and Saltzman 2003). This may be compared with the experimental time (or frequency), of the HF crossover obtained from LVE

measurements. The behavior of $\omega_{c\text{-}HF}$ in the entire φ range probed and the NLE predictions for $\omega_{loc}=1/\tau_{loc}$ from Eq.(2.7) is depicted in Figure 2.6. Theory and experiment reveal two exponential regimes with a stronger exponential increase above $\varphi \approx 0.6$. In particular, the experimental data, for $\varphi > 0.60$ show an exponential increase, $\omega \approx \exp(61\varphi)$, while for lower packing fractions the slope is significantly weaker, as $\omega \sim \exp(31\varphi)$. Data enclosed in the dashed rectangular, corresponding to the lowest volume fraction regime $(0.53< \varphi < 0.55)$ depart from $\omega \approx \exp(31\varphi)$. This regime is also discused in Figure 2.9 below. The NLE predictions for the dimensionless ω_{loc} are in accord with the experimental data as they exhibit two slopes with comparable exponents. Notably, this chage of slope appears only when PY with MV correction is concidered as depicted by the symbols (circles) in Figure 2.6(b). The absolute value of φ of at the transition point is 0.57 and 0.60 for theory and experiment respectively. This discrepancy is expected as NLE considers monodisperse spheres with $\varphi_{RCP}= 0.64$ (Torquato *et al.* 2000) compared to 0.67 for the real, polydisperse PMMA spheres. Remakably, when the distance from RCP is concidered the transition between the two regimes is exhibited at $\varphi_{RCP}-\varphi \sim 0.07$ for both theory and experiment.

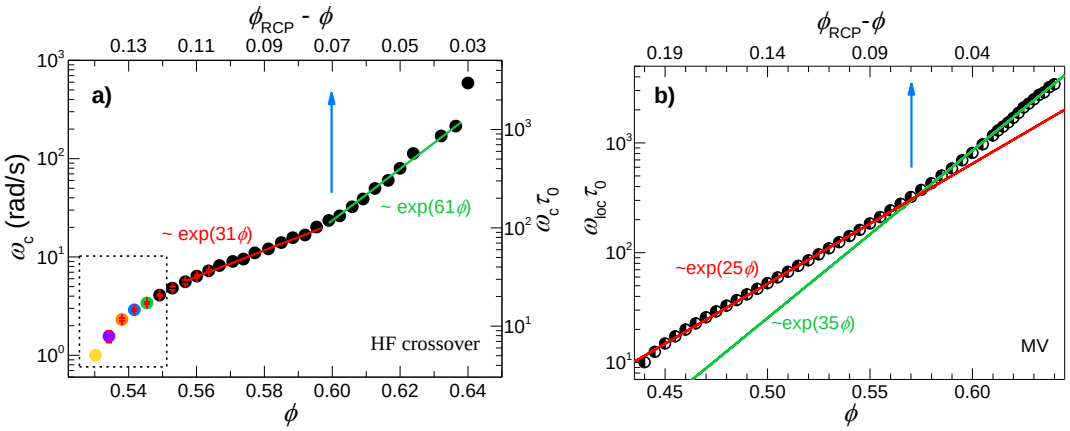

Figure 2.6: Volume fraction dependence of the a) HF crossover frequency obtained from small amplituded oscilatory shear experiments. Data in the area marked by the doted rectangular depart from exp(31φ) and are discussed in Figure 2.9 below. b) Dimensionless localization frequency ($1/\tau_{loc}$) related to in-cage dynamics calculated from NLE theory with MV closure approximation (half-filled symbols). The upper x-axis indicates the distance from RCP while y-axis (ω) is also normalized by the bare Brownian time $\tau_{0=} R^2/6D_0$ as indicated. The lines indicate the two different slopes.

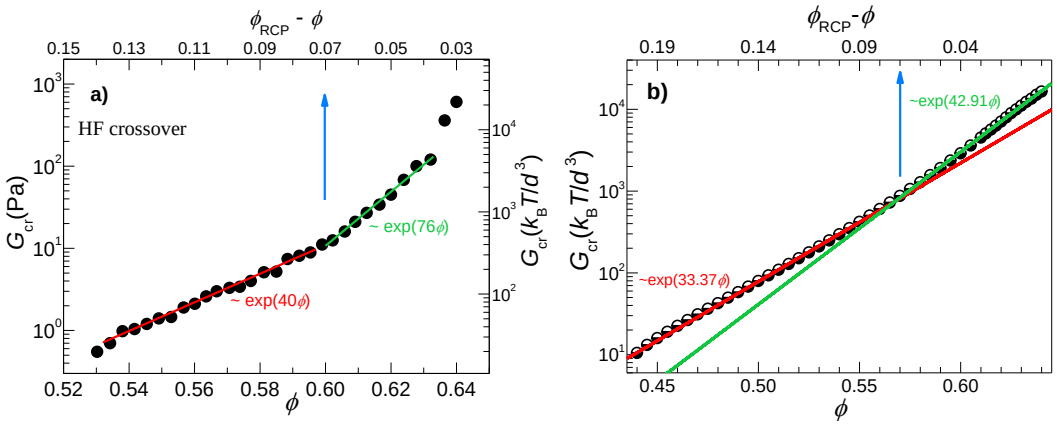

Figure 2.7 Volume fraction dependence of: (a) the HF crossover modulus obtained from experiments. (b) The normalized elastic modulus calculated from NLE theory. The upper x-axis indicates the distance from PCP while y-axis is normalized over thermal energy per volume to allow comparison with theory. The lines indicate the two different slopes.

These two exponential regimes are also evident in $G_{c\text{-}HF}$ experimental measurements and the NLE predictions from Eq. (2.8) as shown in Figure 2.7. The predicted $G_{c\text{-}HF}$ by NLE corresponds to the value of the elastic modules at the particle localized state and exhibits two regimes with a change in slope at φ_{RCP}-$\varphi \approx 0.07$, consistent with the experimental findings. This behavior has been observed in earlier work (Koumakis *et al.* 2012) and attributed to an indication of the glass transition volume fraction that was possibly shifted to values higher than the nominal $\varphi \approx 0.58$ due to particle polydispersity. Most importantly, the NLE model clearly predicts, with no adjustable parameters, the same behavior for monodisperse spheres at a constant distance from close placing, when the effective attraction of MV approximations is utilized. This implies that these many body induced interactions dominate at φ_{RCP}-$\varphi <$ 0.07. This finding fits-in the discussion on the actual volume fraction of the true glass transition hence, could contribute to further understanding of the nature and origin of the cage concept and potentially provide a better picture of the glass transition phenomenon. We will define this fraction as φ_{mb} as it marks the point where many body effective atrractions become important.

2.4.2 Long time dynamics

Contrary to the HF, the LF crossover shifts to shorter times as concentration is decreased due hopping events becoming more frequent and hopping times smaller. Consequently, as φ is decreased the two crossovers approach in the frequency axis until they merge. This is in analogy with molecular glass formers, where the frozen in the glassy state α-modes and the active β-modes timescales, converge as temperature increases over the glass transition temperature (Larson 1999). The merging volume fraction is clearly captured in our LVE experimental data at φ=0.539 as shown in Figure 2.8 where both crossovers are almost coinciding. On the other hand, the sample with φ=0.449 exhibits no crossover and

is liquid-like with G''>G' at all timescales (this is discussed further in appendix A.2). The inverse of the macroscopic crossover times from LVE data of the less concentrated samples, i.e., the $\omega_{c\text{-}HF}$ and $\omega_{c\text{-}LF}$, are plotted as a function of φ in Figure 2.9(a). The lines are guides that indicate how the two crossovers approach in this volume fraction regime and merge at φ≈0.53 (φ_{RCP}-φ=0.14). From the rheological point of view this is the lowest packing fraction where the sample exhibits some solid-like behavior, due to the temporary caging of particles by their neighbors. Since these macroscopic crossover times merge, we can hypothesized that hopping and localization times become comparable. This is confirmed from the microscopic perspective by NLE predictions as shown in Figure 2.9(b). Indeed the microscopic times, τ_{loc} and τ_{hop} seem to increase and decrease respectively with dilution until they become equal at φ≈0.44 (φ_{RCP}-φ=0.2). At this particle concentration the barrier (in the effective free energy) is of the order of k_BT, hence, one could argue that caging has no physical meaning. The particle escapes the cage as soon as it has reached its boundaries. This is a remarkable agreement of experimental observations and NLE predictions considering the uncertainties stemming from aging of low frequency dynamics, φ determination and errors associated to the measurement itself. We argue that this volume fraction defines the caging onset (φ_{ons}). Interestingly, the experimental $\varphi_{ons} \approx 0.53$ (φ_{RCP}-φ=0.14) is comparable with the freezing volume fraction of 0.494 (φ_{RCP}-φ=0.146) (Hunter and Weeks 2012). Freezing and cage formation (onset) volume fraction seem to take place at the similar (if not the same) volume fractions and in this case they can be determined by simple linear viscoelasticity (rheological) measurements.

In summary, we argue that as volume fraction is increased and the two crossover frequencies merge, this point signifies the onset of caging, φ_{ons}. At $\varphi < \varphi_{ons}$ the sample behaves like a liquid at all timescales and caging effects are subtle. By the same token, from theoretical perspective φ_{ons} marks a dynamic crossover that signals the onset of the barrier (larger than k_BT) and, a minimum and a maximum in the dynamic free energy. Hence, this is the minimum packing where short- and long- time dynamics are separated by a caging plateau. This is a very different view from the ideal MCT glass transition where α-relaxation time is infinite and the separation of short- and long- dynamic diverges. Below φ_{ons} (φ_{RCP}-φ > 0.2) experiment and theory agree that at a single relaxation process dominates and Ds and D_L become comparable. Eventually Ds and D_L become equal to D_0 at the dilute limit.

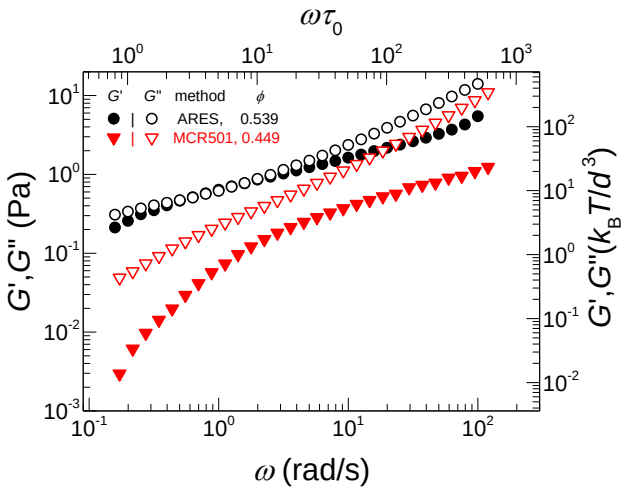

Figure 2.8 Dynamic frequency sweeps of the less concentrated (φ=0.539 and 0.449) Brownian spheres, R=264nm dispersed in squalene at T=23°C. Measurements performed by MCR 501 and ARES rheometers.

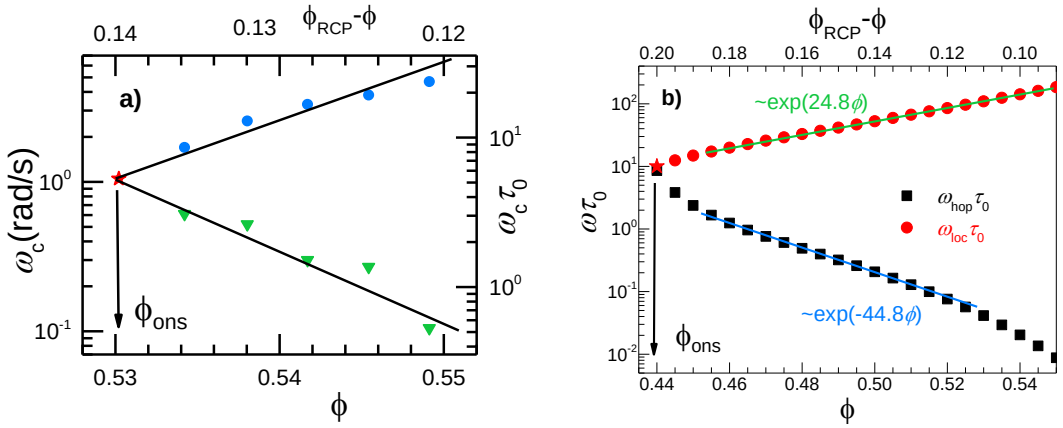

Figure 2.9 Convergence of short- and long-time dynamics as volume fraction is decreased. a) Crossover frequencies from LVE data, i.e., $\omega_{c\text{-}HF}$ (blue symbols) and $\omega_{c\text{-}LF}$ (green symbols). b) The short and long characteristic inverse times, $1/\tau_{loc}$ and $1/\tau_{hop}$ as calculated from NLE. Values are normalized by Brownian time. Red star indicates the merging point where the two crossover frequencies become equal. The merging point volume fraction (φ_{ons}, pointed by the arrow) is found from experiment and theory to be φ ≈0.53 and 0.44, respectively.

2.4.3 Volume fraction consistency

The uncertainties and the various methods of φ determination are well discussed in literature (Poon, Weeks and Royall 2012). Given that all samples derive from the same initial batch by sequential dilution, the uncertainties in the relative φ are reduced considerably. The reduced high frequency viscosity is given by $\eta'_{r,\infty} = \eta'_{\infty}/\eta_s$, where η_s = 13.3 mPa s for squalene at 23^0 C and η'_{∞} is the limiting value of the real part of complex viscosity obtained from oscillatory shear. Once this is known,

the theoretical volume fraction can be calculated (Cheng *et al.* 2002, Sierou and Brady 2001) according to:

$$\eta'_{r,\infty} = 15.78 \ln\left(\frac{1}{1-(\varphi/\varphi_{rcp})^{1/3}}\right) - 42.47 \qquad (2.9)$$

valid for $0.60 \leq \phi < \phi_{RCP} = 0.67$. The denominator portrays the singular behavior (divergence) of the dynamic viscosity at random close packing. Remarkably this empirical equation is limited to φ as low as 0.6 the transition point discussed above as the authors suggest a different equation for less concentrated regime (Cheng *et al.* 2002). The calculated packing fractions from Eq.(2.9) and the experimentally estimated φ for 4 samples are summarized in table Table 4. Predictions are ~ 0.03 higher than the experimentally estimated values and in agreement with findings in our earlier work. This could be attributed to our overestimation of η'_{∞} as the plateau value in Figure 2.10 has not been fully attained or to polydispersity. On the other hand, the relative packing fractions are proven consistent. This indicates a reasonably good agreement of experimental data and theoretical predictions while a shift of volume experimental fractions by 0.03 would not change the main findings of this work.

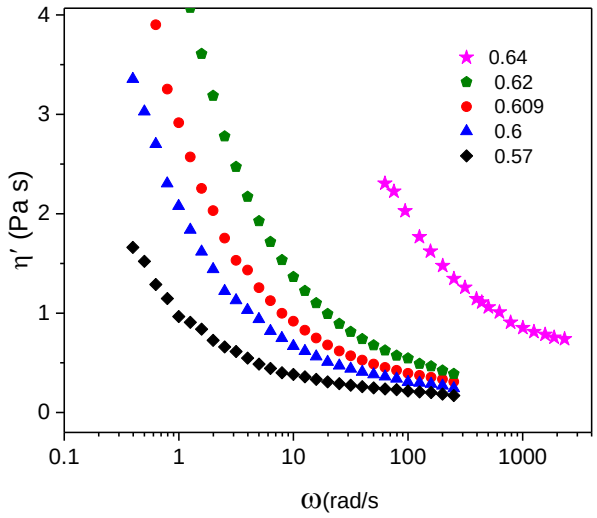

Figure 2.10 The in-phase with strain rate dynamic viscosity limiting behavior. The legend indicates the experimentally estimated volume fraction. Data for φ=0.64 (magenta symbols) are taken with PZR up to 3000 rad/s.

Table 1: Volume fraction of four samples: comparison of the experimental estimation with predictions of Eq (2.6)

Determined from RCP	Prediction of Eq. (2.6)	Deviation
0.64	0.665	0.025
0.62	0.649	0.029
0.609	0.639	0.029
0.6	0.628	0.028

2.4.4 Attractive glasses

Scattering experiments have shown that when a weak short-ranged attraction is induced by depletion effect in a repulsive glass with φ~ 0.6 the latter melts while at higher attraction strengths it becomes non-ergodic again, forming the so-called attractive glass (Pham *et al.* 2004). This reentrant behavior is attributed to an opening of the cage as voids are formed by moderate attractions bringing particles on average closer. The plateau in G´ is only recovered at higher attraction strengths corresponding to higher polymer concentrations (Pham *et al.* 2008) were strong attraction between particles create long-lived bonds and prevent structural rearrangement. To study the effects of the attraction in the HF crossover the LVE of samples with short range attractions of various strengths was measured by MCR702 as shown in Figure 2.11(a). The cage size and rigidity on average are affected by volume fraction and the interparticle potential. In agreement with (Moghimi 2016, Moghimi and Petekidis 2020) we see no distinct repulsive glass melting as U is gradually increased. The modulus and frequency of HF crossover both increase with U (Figure 2.11 (b). Phenomenologically, the effect of U on the HF crossover is very similar to its φ dependence in repulsive glasses, as swohn in Figure 2.6(a) and Figure 2.7(a). As a comparison we note that the $\omega_{c\text{-}HF}$ for φ=0.60 and U=-2k_BT matches the value of φ=0.624 of the repulsive glass. The corresponding $G_{c\text{-}HF}$ values for the former and the latter are similar, i.e., 75.26 and 68 Pa, respectably.

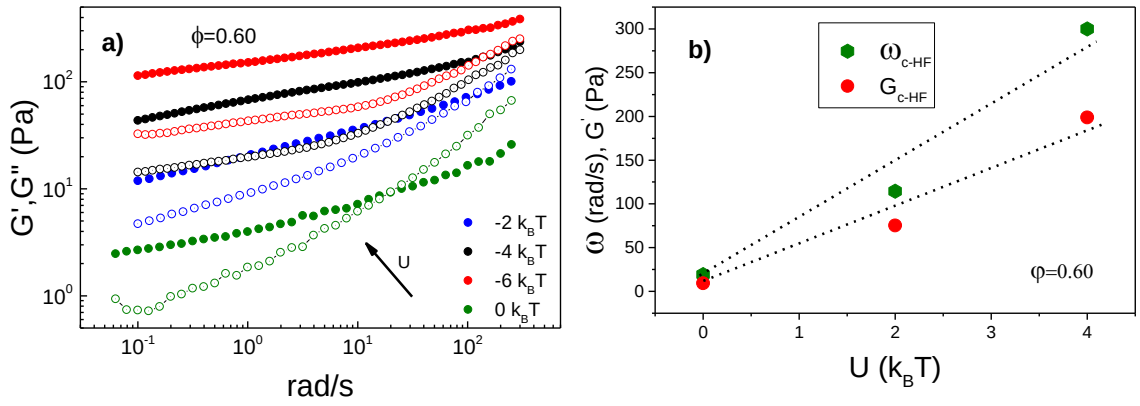

Figure 2.11 LVE data of colloidal glasses with φ=0.60 and depletion induced attraction of various strengths: a) LVE spectra of repulsive glass (U=0k_BT) and attractive glasses with attraction strength U= –2, -4, -6k_BT. b) The dependence of HF crossover frequency and modulus on attraction strength U. Lines are visual guides.

It is tempting though to compare the LVE of these two samples that exhibit the same HF crossover frequency. The HF dynamics are similar as shown in Figure 2.12. The G´ caging plateau and the prominent decrease of G´´ towards a minimum start to emerge as ω is decreased to 1 rad/s for the repulsive glass. In contrast the attractive glass exhibits weaker solid like response in these time scales of observation in agreement with (Pham, Petekidis, Vlassopoulos, Egelhaaf, Poon and Pusey 2008). This is a result of competing interactions, i.e., attractions and repulsive caging. This comparison is intriguing as it relates the LVE of two colloidal glasses with comparable on average caging sizes yet different strengths. This important finding calls for a systematic study which will compare measurements of repulsive and attractive glasses of various φ and U with MSD results from simulations (Moghimi and Petekidis 2020, Zaccarelli and Poon 2009) and scattering experimental results (Eckert and Bartsch 2002, Pham *et al.* 2004).

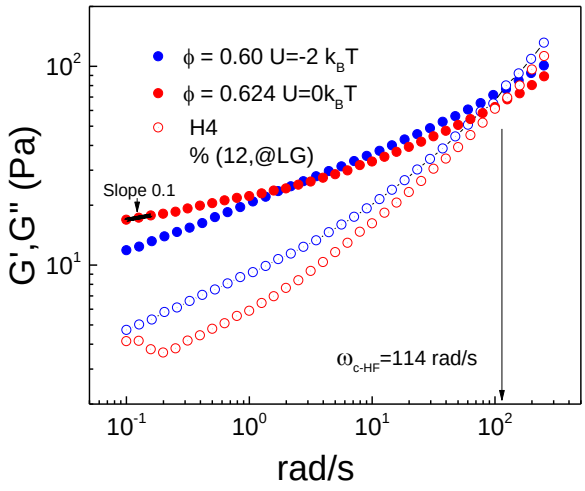

Figure 2.12 Comparison of LVE of repulsive and attractive glasses with same $\omega_{c\text{-}HF.}$ Arrow marks the common HF crossover frequency. Solid line indicates the weak power law of G´ at the lower frequencies signaling the onset of the caging plateau in the repulsive glass.

2.5. Conclusions and future perspectives

The macroscopic times derived from the experimental G´and G´´ dynamic crossovers at high and low frequencies for an extensive range of volume fractions exhibit a remarkable agreement with NLE theory predicted hopping and localization times. Two distinct volume fractions have been identified as the φ_{ons} and the φ_{mb}. The former constitutes the merging point of short- and long-time dynamics and, marks the onset of caging at the volume fraction of about 0.53 and 0.44 as suggested by experiments and NLE theory respectively. The latter is derived from the onset of change of slope in the volume fraction increase of $\omega_{c\text{-}HF}$ and $G_{c\text{-}HF}$ and has been related within the NLE model as the onset of significant many-body effects manifested as effective attractions in c(r). Both the NLE theory and experiments agree that φ_{RCP}-φ_{mb} = 0.07. Based on experimental findings and NLE-OZ-MV predictions the Figure 2.1 is revised to Figure 2.13 where we summarize our understanding on the mechanism of cage formation and the effect of many body interactions.

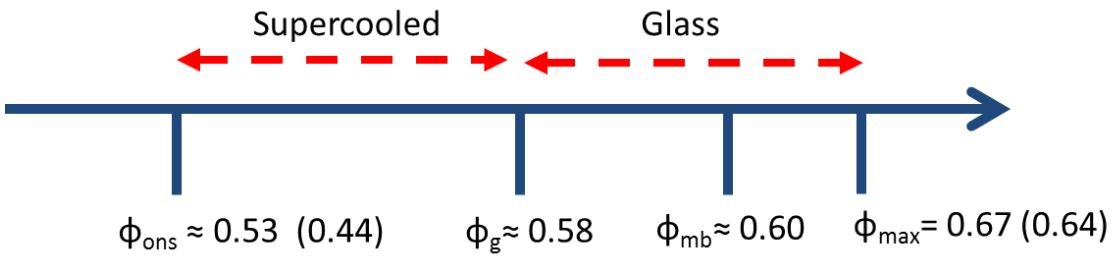

Figure 2.13 Reconstruction of Fig 2.1 with characteristic volume fractions derived from this work. Values in brackets are related to NLE. The ideal glass transition packing fraction (φ_g) is also shown for reference.

Depletion induced attraction leads to a HF crossover phenomenology qualitatively similar to the φ increase in repulsive glasses. Future work could correlate φ_{ons} and φ_{mb} with other characteristic volume fractions discussed in theoretical and experimental work such as (Li *et al.* 2020). A systematic study of HF data of attractive glasses will also provide insights on the cage formation when short ranged attractions are present.

Appendix A.2

A.2.1 LVE data at volume fractions with no dynamic crossover ($\varphi < \varphi_{ons}$)

At packing fractions below 0.53 dynamic moduli do not exhibit a crossover yet they approach at a certain frequency (Figure 2.8) and this is clearly seen in the minimum of tanδ as shown in Figure A.1(a). We can assume that this frequency marks a time scale $\tau_{tan\delta\text{-}min} = 1/\omega_{tan\delta\text{-}min}$. At this time the effect of crowding is maximized while at shorter or longer times particle mobility seems to increase. Remarkably, $\omega_{tan\delta\text{-}min}$ exhibits the opposite trend from $\omega_{c\text{-}LF}$ as shown in Figure A.1(b).

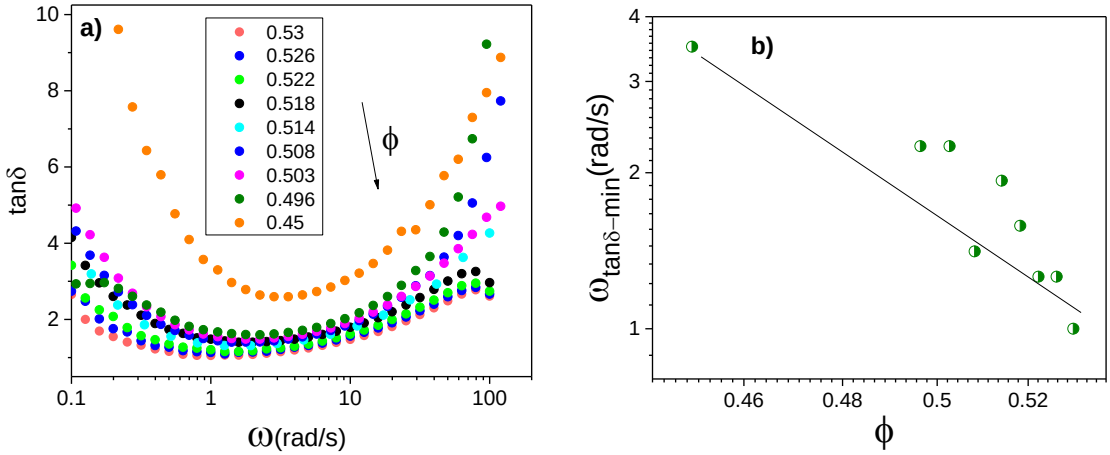

Figure A.1 LVE data for samples with $\varphi < \varphi_{ons} = 0.54$ where no G′,G′′ crossover is exhibited a) Loss angle tangent dependence on angular frequency b)The frequency of the minimum in tanδ plotted as a function of φ. Line is a guide.

A.2.2 Sample inertia limit

The sample inertia limit was exploited experimentally by utilizing large Brownian spheres (R_H=625nm) that exhibit HF crossover at approximately 0.1 rad/s consequently, HF dynamics where fully accessible by the MCR 702 rheometer as shown in Figure A.2(a). The G′′ unphysical increase at elevated frequencies clearly deviates from the typical power law behavior of Figure A.2(b) and this is a result of

the gap dependent sample inertia. The relevant gap loading limit can be calculated by (Athanasiou *et al.* 2019, Schrag 1977) :

$$G_d = 100\, f^2 cos^2\left(\frac{\delta}{2}\right)\, \rho\, d^2 \qquad (2.10)$$

where G_d is the magnitude of the complex modulus, ρ the sample's density, d the rheometric gap, f=2πω and $cos^2\left(\frac{\delta}{2}\right) = 1$. Results in Figure A.2(b) clearly indicate a phase angle underestimation in accord with Schrag's calculations (Schrag 1977) for the separated motor transducers arrangement. The onset of the effect of sample inertia of G′ in Figure A.2(a) is in good agreement with the calculated limits from Eq.(2.10) . The inertia limits indicated by the dashed line correspond to liquid-like samples (worst case) and varius gaps while the solid line indicates the limit for a solid–like sample and a gap of 0.2 mm (best case).

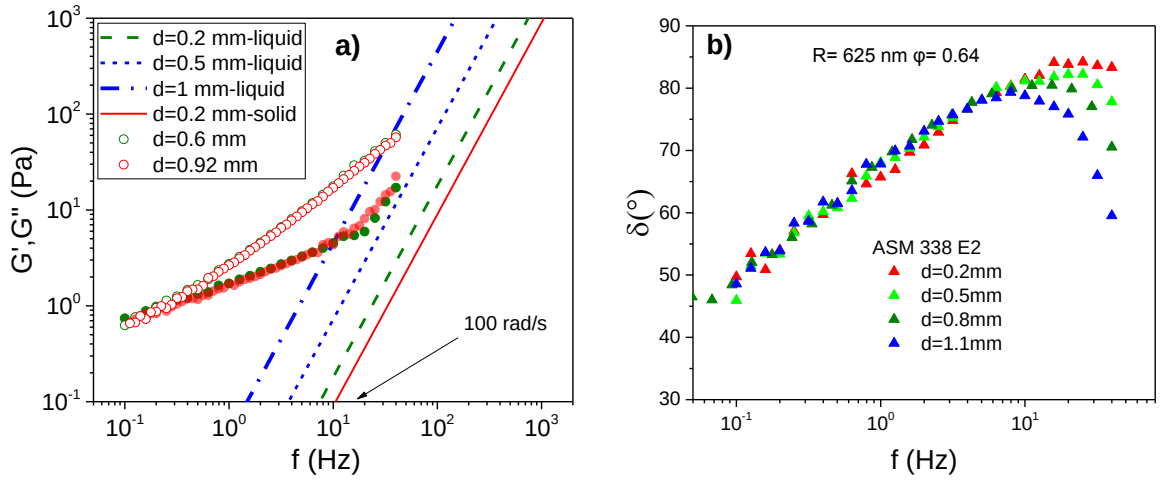

Figure A.2 LVE of large Brownian spheres dispersed in squalene R=625nm and φ=0.64. a) Symbols denote measurement with PP25mm at two different gaps of 0.6 and 0.92mm. Dashed and dotted lines indicate G inertia limit (minimum value) calculated from Eq. (2.10) for various gaps and a liquid-like sample. Solid line indicates the solid like sample inertia limit at the minimum gap of 0.2mm. b) Phase angle measurements at various gaps. All measurements were taken with MCR702 in separated motor transducer configuration. Note the frequency scale is at Hz.

References

Antl, L., Goodwin, J., Hill, R., Ottewill, R. H., Owens, S., Papworth, S., and Waters, J., ‘‘The preparation of poly (methyl methacrylate) latices in non-aqueous media,’’ Colloids and Surfaces 17, 67-78 (1986).

Athanasiou, T., Auernhammer, G. K., Vlassopoulos, D., and Petekidis, G., ‘‘A high-frequency piezoelectric rheometer with validation of the loss angle measuring loop: application to polymer melts and colloidal glasses,’’ Rheologica Acta 58, 619-637 (2019).

Ballesta, P., and Petekidis, G., ‘‘Creep and aging of hard-sphere glasses under constant stress,’’ Phys Rev E 93, 042613 (2016).

Banchio, A. J., Nägele, G., and Bergenholtz, J., ‘‘Viscoelasticity and generalized Stokes–Einstein relations of colloidal dispersions,’’ The Journal of chemical physics 111, 8721-8740 (1999).

Berthier, L., and Reichman, D. R., ‘‘Modern computational studies of the glass transition,’’ Nature Reviews Physics, 1-15 (2023).

Biroli, G., and Garrahan, J. P., ‘‘Perspective: The glass transition,’’ The Journal of chemical physics 138, 12A301 (2013).

Brady, J. F., ‘‘The rheological behavior of concentrated colloidal dispersions,’’ The Journal of Chemical Physics 99, 567-581 (1993).

Brambilla, G., El Masri, D., Pierno, M., Berthier, L., Cipelletti, L., Petekidis, G., and Schofield, A. B., ‘‘Probing the equilibrium dynamics of colloidal hard spheres above the mode-coupling glass transition,’’ Physical review letters 102, 085703 (2009).

Bryant, G., Williams, S. R., Qian, L., Snook, I. K., Perez, E., and Pincet, F., ‘‘How hard is a colloidal "hard-sphere" interaction?,’’ Phys Rev E Stat Nonlin Soft Matter Phys 66, 060501 (2002).

Cheng, Z., Zhu, J., Chaikin, P. M., Phan, S. E., and Russel, W. B., ‘‘Nature of the divergence in low shear viscosity of colloidal hard-sphere dispersions,’’ Phys Rev E Stat Nonlin Soft Matter Phys 65, 041405 (2002).

Cipelletti, L., and Ramos, L., ‘‘Slow dynamics in glassy soft matter,’’ Journal of Physics: Condensed Matter 17, R253 (2005).

Dhont, J. K., *An introduction to dynamics of colloids Vol. 2* (Elsevier, 1996).

Donev, A., Torquato, S., and Stillinger, F. H., ‘‘Pair correlation function characteristics of nearly jammed disordered and ordered hard-sphere packings,’’ Physical Review E 71, 011105 (2005).

Eckert, T., and Bartsch, E., ‘‘Re-entrant glass transition in a colloid-polymer mixture with depletion attractions,’’ Physical review letters 89, 125701 (2002).

Ediger, M., and Harrowell, P., ‘‘Perspective: Supercooled liquids and glasses,’’ The Journal of chemical physics 137, 080901 (2012).

Ewoldt, R. H., Johnston, M. T., and Caretta, L. M., “Experimental challenges of shear rheology: how to avoid bad data.” *Complex fluids in biological systems* (Springer, 2015).

Fleer, G. J., and Tuinier, R., ‘‘Analytical phase diagram for colloid-polymer mixtures,’’ Physical Review E 76, 041802 (2007).

Frith, W. J., Strivens, T. A., and Mewis, J., ‘‘Dynamic mechanical properties of polymerically stabilized dispersions,’’ Journal of colloid and interface science 139, 55-62 (1990).

Gotze, W., and Sjogren, L., ‘‘Relaxation processes in supercooled liquids,’’ Reports on progress in Physics 55, 241 (1992).

Hansen, J.-P., and McDonald, I. R., *Theory of simple liquids: with applications to soft matter* (Academic press, 2013).

Henderson, D., and Grundke, E., ‘‘Direct correlation function: Hard sphere fluid,’’ The Journal of Chemical Physics 63, 601-607 (1975).

Hunter, G. L., and Weeks, E. R., ‘‘The physics of the colloidal glass transition,’’ Reports on Progress in Physics 75, 066501 (2012).

Ikeda, A., Berthier, L., and Sollich, P., ‘‘Disentangling glass and jamming physics in the rheology of soft materials,’’ Soft Matter 9, 7669 (2013).

Jacob, A. R., Moghimi, E., and Petekidis, G., ‘‘Rheological signatures of aging in hard sphere colloidal glasses,’’ Physics of Fluids 31, 087103 (2019).

Koumakis, N., “Mechanisms of Yielding and Flow in Colloidal Glasses, Crystals and Gels,” Phd Thesis, UOC, (2011).

Koumakis, N., Pamvouxoglou, A., Poulos, A., and Petekidis, G., ‘‘Direct comparison of the rheology of model hard and soft particle glasses,’’ Soft Matter 8, 4271-4284 (2012).

Larson, R. G., *The structure and rheology of complex fluids Vol. 150* (Oxford university press New York, 1999).

Läuger, J., and Stettin, H., ‘‘Effects of instrument and fluid inertia in oscillatory shear in rotational rheometers,’’ Journal of Rheology 60, 393-406 (2016).

Li, B., Lou, K., Kob, W., and Granick, S., ‘‘Anatomy of cage formation in a two-dimensional glass-forming liquid,’’ Nature 587, 225-229 (2020).

Mason, T. G., ‘‘Estimating the viscoelastic moduli of complex fluids using the generalized Stokes–Einstein equation,’’ Rheologica Acta 39, 371-378 (2000).

Mewis, J., and Haene, P., “Prediction of rheological properties in polymer colloids,” 1993.

Mewis, J., and Wagner, N. J., *Colloidal suspension rheology* (Cambridge University Press, 2012).

Moghimi, E., “Microscopic dynamics and rheology of colloidal gels,” Πανεπιστήμιο Κρήτης. Σχολή Θετικών και Τεχνολογικών Επιστημών. Τμήμα …, (2016).

Moghimi, E., and Petekidis, G., ‘‘Mechanisms of two-step yielding in attractive colloidal glasses,’’ Journal of Rheology 64, 1209-1225 (2020).

Nägele, G., ‘‘Viscoelasticity and diffusional properties of colloidal model dispersions,’’ Journal of Physics: Condensed Matter 15, S407 (2002).

Pham, K., Egelhaaf, S., Pusey, P., and Poon, W. C., ‘‘Glasses in hard spheres with short-range attraction,’’ Physical Review E 69, 011503 (2004).

Pham, K., Petekidis, G., Vlassopoulos, D., Egelhaaf, S., Poon, W., and Pusey, P., ‘‘Yielding behavior of repulsion-and attraction-dominated colloidal glasses,’’ Journal of Rheology 52, 649-676 (2008).

Poon, W. C., Weeks, E. R., and Royall, C. P., ‘‘On measuring colloidal volume fractions,’’ Soft Matter 8, 21-30 (2012).

Pusey, P., ‘‘Colloidal Suspensions in Liquids, Freezing, and the Glass Transition: Les Houches,’’ (1991).

Pusey, P., ‘‘Colloidal glasses,’’ Journal of Physics: Condensed Matter 20, 494202 (2008).

Pusey, P. N., ‘‘Brownian motion goes ballistic,’’ Science 332, 802-803 (2011).

Reinhardt, J., Weysser, F., and Fuchs, M., ‘‘Comment on “Probing the equilibrium dynamics of colloidal hard spheres above the mode-coupling glass transition”,’’ Physical review letters 105, 199604 (2010).

Russel, W. B., Russel, W., Saville, D. A., and Schowalter, W. R., *Colloidal dispersions* (Cambridge university press, 1991).

Saltzman, E. J., and Schweizer, K. S., ‘‘Activated hopping and dynamical fluctuation effects in hard sphere suspensions and fluids,’’ J Chem Phys 125, 44509 (2006).

Schaertl, W., and Sillescu, H., ‘‘Brownian dynamics of polydisperse colloidal hard spheres: Equilibrium structures and random close packings,’’ Journal of Statistical Physics 77, 1007-1025 (1994).

Schrag, J. L., ‘‘Deviation of velocity gradient profiles from the “gap loading” and “surface loading” limits in dynamic simple shear experiments,’’ Transactions of the Society of Rheology 21, 399-413 (1977).

Schroyen, B., Hsu, C.-P., Isa, L., Van Puyvelde, P., and Vermant, J., ‘‘Stress Contributions in Colloidal Suspensions: The Smooth, the Rough, and the Hairy,’’ Physical Review Letters 122, 218001 (2019).

Schroyen, B., Vlassopoulos, D., Van Puyvelde, P., and Vermant, J., ‘‘Bulk rheometry at high frequencies: A review of experimental approaches,’’ Rheologica Acta 59, 1-22 (2020).

Schweizer, K. S., and Saltzman, E. J., ‘‘Entropic barriers, activated hopping, and the glass transition in colloidal suspensions,’’ The Journal of chemical physics 119, 1181-1196 (2003).

Schweizer, K. S., and Yatsenko, G., ‘‘Collisions, caging, thermodynamics, and jamming in the barrier hopping theory of glassy hard sphere fluids,’’ The Journal of chemical physics 127, 164505 (2007).

Shikata, T., and Pearson, D. S., ‘‘Viscoelastic behavior of concentrated spherical suspensions,’’ Journal of Rheology 38, 601-616 (1994).

Sierou, A., and Brady, J. F., ‘‘Accelerated Stokesian Dynamics simulations,’’ Journal of Fluid Mechanics 448 (2001).

Squires, T. M., and Mason, T. G., ‘‘Fluid mechanics of microrheology,’’ Annual review of fluid mechanics 42, 413-438 (2010).

Torquato, S., Truskett, T. M., and Debenedetti, P. G., ‘‘Is random close packing of spheres well defined?,’’ Physical review letters 84, 2064 (2000).

van Megan, W., Underwood, S. M., Ottewill, R. H., Williams, N. S. J., and Pusey, P. N., ‘‘Particle diffusion in concentrated dispersions,’’ Faraday Discussions of the Chemical Society 83, 47-57 (1987).

Van Megen, W., Mortensen, T., Williams, S., and Müller, J., ‘‘Measurement of the self-intermediate scattering function of suspensions of hard spherical particles near the glass transition,’’ Physical Review E 58, 6073 (1998).

Verlet, L., ‘‘Integral equations for classical fluids: I. The hard sphere case,’’ Molecular Physics 41, 183-190 (1980).

Verlet, L., ‘‘Integral equations for classical fluids: II. Hard spheres again,’’ Molecular Physics 42, 1291-1302 (1981).

Vila-Costa, A., Gonzalez-Silveira, M., Rodríguez-Tinoco, C., Rodríguez-López, M., and Rodriguez-Viejo, J., ‘‘Emergence of equilibrated liquid regions within the glass,’’ Nature Physics 19, 114-119 (2023).

Wagner, N. J., and Mewis, J., *Theory and applications of colloidal suspension rheology* (Cambridge University Press, 2021).

Weeks, E. R., and Weitz, D., ‘‘Properties of cage rearrangements observed near the colloidal glass transition,’’ Physical review letters 89, 095704 (2002).

Willenbacher, N., and Oelschlaeger, C., ‘‘Dynamics and structure of complex fluids from high frequency mechanical and optical rheometry,’’ Current Opinion in Colloid & Interface Science 12, 43-49 (2007).

Zaccarelli, E., and Poon, W. C., ‘‘Colloidal glasses and gels: The interplay of bonding and caging,’’ Proceedings of the National Academy of Sciences 106, 15203-15208 (2009).

Zhou, Y., Mei, B., and Schweizer, K. S., ‘‘Integral equation theory of thermodynamics, pair structure, and growing static length scale in metastable hard sphere and Weeks-Chandler-Andersen fluids,’’ Physical Review E 101, 042121 (2020).

Chapter 3 : Linear viscoelasticity, yielding and structural recovery of hydrogels formed by amphiphilic pentablock copolymers

3.1 Introduction: Peptide hydrogels for drug delivery

Hydrogels are space-filing networks (Rubinstein and Colby 2003) consisting of a small filling percentage of polymer swollen in the most abundant solvent on earth, water. The water absorption is due to hydrophilic groups and the presence of ions. Polymer dissolution is prevented by the bonds of the networking chains, which may be covalent (permanent) or non-covalent (transient, as in the present case with amphiphilic polypeptides). Mechanical strength reflects the number density of junctions. The latter translates into mesh size, the average distance between neighboring junctions, and in the present case depends, among other factors, on the peptide concentration and the exact nature of junctions. Hydrogels can therefore be considered as interconnected, albeit not concentrated materials, as the polymer concentration is typically low. Polymeric content does matter though when it relates to the density of elastically active chains. As concentration increases the proximity of the macromolecules eventually will affect molecular conformation especially when amphiphilic interactions are present (Charbonneau *et al.* 2013) forming micellar self-assemblies. Amphiphilic polypeptide assemblies are known to form responsive hydrogels suitable for therapeutic applications (Das and Das 2021, Mart *et al.* 2006, Wang *et al.* 2019) such as drug delivery (Sis and Webber 2019, Webber and Pashuck 2021) as their morphology can be tailored to exhibit the desired properties. For instance, the mesh size determines how drugs penetrate into the network, to be later released to the targeted area due to pH or temperature stimulus (Mahinroosta *et al.* 2018). These hydrogels are also biocompatible, degradable and exhibit low immunogenicity. They also exhibit a secondary structure due to the synergy of steric interactions, hydrophobic interactions, hydrogen bonds, and other local forces which is therefore sensitive to the environment. Secondary structure offers a major advantage for two reasons: a) the strands between hydrogen bonds are semiflexible and result in stronger gels with elastic moduli on the order of 10^3 Pa even at low concentrations, and b) the mechanical properties can be tailored for a given application, by changing both this structure and hydrogen bonding interactions (pH, T).

The task of a targeted delivery of a therapeutic agent, inside the body is far from trivial as the hydrogel must meet the following requirements:

a) exhibit mechanical strength to facilitate drug entrapment (Rodriguez *et al.* 2016)
b) be injectable, i.e., exhibit shear-thinning when injected (Guvendiren *et al.* 2012), thus allowing it to pass through the thin needle.
c) have the shortest possible self-healing time, i.e., reconstruct quickly within the body (Guvendiren, Lu and Burdick 2012)
d) respond to the lower extracellular pH values of the cancer (malignant) tissue and adjust conformation to deliver the drug.
e) remain intact when in contact with the healthy tissue, minimizing the loss of the drug.
f) exhibit slow degradation rates and achieve slow and controlled drug release.

This chapter aims at understanding the interplay of structure, yielding and self-healing mechanism of biocompatible hydrogels used in medical applications such as chemotherapy. To this end, we study the rheology of an amphiphilic pentablock hydrogel which was designed and synthesized to serve as drug carrier for anticancer treatment, targeting pancreatic malignant cells (Bilalis *et al.* 2018). This well-characterized hydrogel (Kasimatis, PhD thesis 2023) will be tested with or without the added anticancer drug, in this case Paclitaxel. We address the above challenge for a pentablock of given composition, total polymer concentration, pH, temperature and added drug concentration. LVE will be probed by dynamic frequency sweeps (DFS) to quantify the gel strength while dynamic strain sweeps (DSS) and dynamic time sweeps (DTS) will capture the effective shear thinning and structural recovery -time evolution of LVE after flow cessation-, respectively. This structural recovery is very much connected to the so-called self-healing behavior (Wang and Urban 2020).

The amphiphilic pentablock forms a supramolecular percolated network primarily due to solvophobic associations and other interactions such as ionic and hydrogen bonding. Each block can be seen as a linear random heteropolymer with potentially charged segments with a propensity to attain unique structures sensitive on environmental conditions. The resultant gel exhibits weak junctions with respective energies of 2–250 kJ mol^{-1} compared to ones of permanent covalent bonds 100–600 kJ mol^{-1} (Benson 1965, Israelachvili 2011). In rubber-like polymeric networks the linear elasticity stems from the entropic penalty paid upon strand deformation due to the reduction of the available number of conformations (microstates). Based on theory of rubber elasticity (Green and Tobolsky 1946, Treloar 1975) the elastic plateau modulus G_o can be approximated by:

$$G_o = \nu RT \tag{3.1}$$

where ν is the number density of elastically active chains, R is the ideal gas constant, and T is the absolute temperature of the material. Equation (3.1) assumes purely elastic behavior, chain flexibility and junction affine motion, i.e., proportional to the macroscopic deformation. The latter is not always true given the swollen-network nature of the hydrogel (Onck *et al.* 2005, Richbourg and Peppas 2020). Deducing the

modulus from Eq.(3.1) would be an oversimplification given the semiflexible character of the strands, self-assembly motifs and the plethora of interactions. Nevertheless, from Eq.(3.1) we can extract an effective junction density. Modeling the linear rheological response is challenging as it cannot be easily decomposed, on a molecular scale, to its various contributions such as block secondary structure, bridges, loops, free chains and dangling-ends (Tripathi *et al.* 2006) while multiple relaxation modes are exhibited (Wang and Larson 2018). Also gel microstructure may not be self-similar (Dinsmore and Weitz 2002), and in this regard the recently emerged modeling strategy based on the concept of hierarchy of fractal elements seems promising (Bantawa *et al.* 2022). On the other hand, there are similarities in rheological response and self-assembly with simpler systems. On a first coarse grained approach, LVE of peptide based hydrogels can be predicted by theories constituted for semiflexible polymeric networks (MacKintosh *et al.* 1995). The modulus is linked to the bridging density, based on theory of elasticity modified for semiflexible chains. We utilize this approach in an attempt to understand the origin of elasticity.

From a coarsed grained point of view, the molecule is a pentablock with amphiphilic interactions. Triblock BAB copolymers with middle solvophilic blocks (Balsara *et al.* 1991, Castelletto *et al.* 2005, Karayianni and Pispas 2021) and telechelic polymers (Van Ruymbeke *et al.* 2010, Winnik and Yekta 1997), a subgroup of associative polymers, exhibit similarities in structural motifs with peptide based amphiphiles. Above a critical concentration they do self-assemble in flower like micelles when the middle block is sufficiently large and flexible (Khalatur *et al.* 1999) to form loops. By altering the length of the middle solvophobic block different micellar architectures are formed leading to diversity in rheological response with analogies ranging from hard to soft spheres (Buitenhuis and Förster 1997). This is consistent with earlier studies where micellar aggregates were treated, to a very good approximation, as topologically interacting spherical objects (Kinning and Thomas 1984, Mortensen *et al.* 1992). Micelle formation in triblocks is an endothermic process and fundamentally the same with aqueous diblock solutions (Watanabe *et al.* 2001), however the latter do not form bridges (Zhulina and Borisov 2012). In BAB solutions with polymeric concentration of 20% micelle crystallization was evidenced by SANS a behavior in analogy to hard spheres dispersions and volume fraction of 0.53 (Mortensen 1992). In all cases the formation of micelles is governed by balancing hydrophobic interactions forming the micelle core and the opposing repulsion between hydrophilic loops that limit the size of the micelle (Tanford 1974). The micellar stability is sensitive to the molecular architecture (De Silva *et al.* 2017). In aqueous solutions the core of the micelles consisting of B groups is regarded free of water, while the A groups are swollen in water. As a consequence, the effective volume fraction of the micelles is generally about a factor of 2-3 larger than the actual one (Wanka *et al.* 1994). Telechelic polymers are also reasonably well understood thanks to many structural (SANS) studies (Soledad Lencina *et al.* 2021), rheological (Annable

et al. 1993) and theoretical studies (Semenov *et al.* 1995). Their simple architecture consists of a long solvophilic mid-block terminated by a solvophobic short chain at both ends. Above a certain polymer concentration c*, close packed flower like micellar structures are formed (Winnik and Yekta 1997). At this concentration micelles can also aggregate to a pearl necklaces morphology, when the solvophilic corona pertains attractions for instance due to hydrogen bonding (Yang *et al.* 2010). On the contrary, when corona repulsion dominates, as in the case of our HG, bridging is the only way of networking. Bridging increases with concentration, as cores exchange hydrophobic blocks belonging to a different copolymer, leading to gelation in a similar way to linear triblocks (Hugouvieux *et al.* 2011). Given this inter-micellar association, two dominant interactions emerge, an effective attraction due to bridging, and a repulsion due to excluded volume interactions of the solvophilic corona (Semenov *et al.* 1995, Witten and Pincus 1986). Within this context the dominant relaxation modes considered are the bridge destruction due to the motion of a micelle in the network (Clement *et al.* 2000) and micelle creeping rearrangement that depends on the concentration. We limit the discussion to these two modes although the actual relaxation picture is certainly more complicated as more modes are exhibited (Wang and Larson 2018).

Micelle formation and bridging is sketched in Figure 3.1. In dense systems bridging length of close neighbors decreases and even distant ones may be bridged (Annable *et al* 1993) resulting in very long relaxation times, a feature of our pH6.5 and 7.4 HG LVE response. Phase separation cannot be excluded under certain conditions (Semenov *et al* 1995) however strong excluded volume repulsion can suppress it (Semenov and Rubinstein 1998). We have not observed such a rheological response or syneresis (Boral *et al.* 2010) for the pH and T range tested. Rheological properties stem from the colloidal nature of micelles and the reversible bridging. We note a difference between telechelic and triblock copolymers that the solvophobic ends are relatively short in the former but this will not change the big picture. Triblock and telechelic copolymers are the closest and simpler “relatives” to our pentablock amphiphiles and these will provide structural insight and augment the study of their nonlinear response.

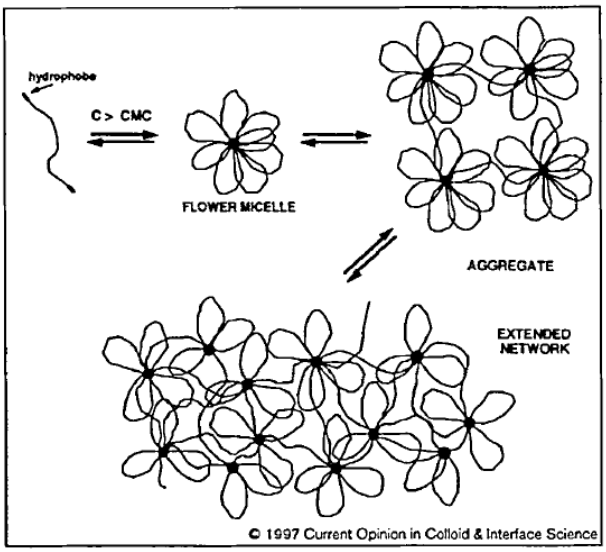

Figure 3.1Visual representation of transition from isolated chains to packed bridged micelles in telechelic polymers. As concentration c exceeds the critical micellar concentration (CMC). From (Winnik and Yekta 1997)

3.2 Materials and sample preparation

The basic hydrogel under study, HG batch 1, 2, 3 and 5, consists of an amphiphilic pentablock (ABABA) polypeptide moiety, where A is poly(L-lysine) (PLL) and B is a random copolymer poly(L-histidine)-co-poly(γ-benzyl-L-glutamate) (Phis-PBLG) with block composition 50%. The two outer A blocks consist of 60 PLL residues while the middle one is significantly longer with 500 ones. The B block consists of 30 repeat units of Phis-PBLG. In a simplified visualization the molecule is coarsely seen as a pentablock block copolymer, Figure 3.2. Secondary structure here is ignored. Due to the long middle block the molecule has the propensity to form loops at low concentrations. Above a critical value CMC, micellar formation is favorable, while at even higher concentrations bridges are formed when the B blocks of the same chain belong to different micellar cores. This is discussed in the next section. The pentablock synthesized by Maria Kasimatis, was initially stored in dry powder form.

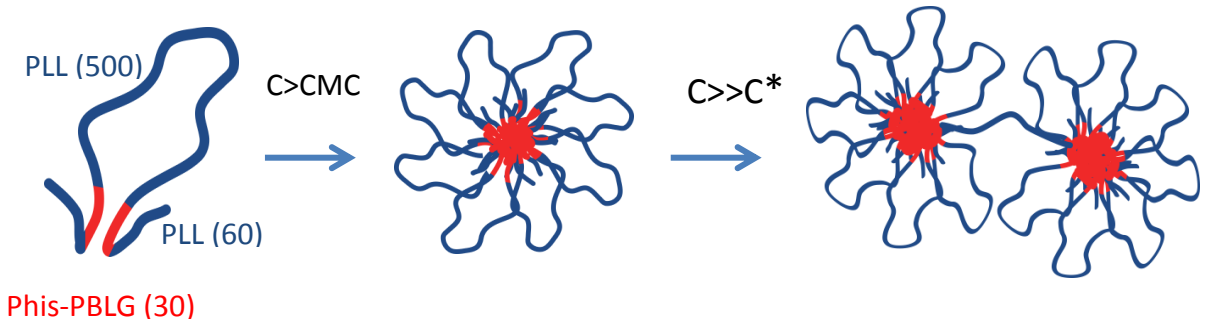

Figure 3.2 A simplified visualization of micelle formation with concentration increase. From left to right: Below a critical concentration (CMC) loops are formed while at increased concentration loops aggregate to micelles. Eventually bridges are formed. The secondary structure is not visualized. Numbers indicate the number of repeat

units in the blocks. Red indicates hydrophobic **B** blocks and blue hydrophilic **A** ones. Inspired by (Annable *et al.* 1993)

During preparation of each batch, the dried polymer was dissolved in nano-purred water and pH was decreased to 6.5 and 5 by adding hydrochloric acid. Mixing was completed by cycles of mild centrifugation (670g for 20s) by inverting the vial after each cycle. All samples were left to equilibrate for more than two weeks at 7°C before loading on the rheometer. This equilibration time proved vital as initial measurements with freshly prepared samples showed significant time evolution even after 2 days. LVE, yielding and structural recovery were studied with oscillatory shear rheometry as described in the Chapter1. Measurements were conducted with a single-headed MCR 501 (Anton Paar, Austria) rheometer using a stainless steel cone-and-plate (CP) geometry with cone angle of 2° , diameter of 25mm and truncation of 100 μm, while the temperature was controlled by a Peltier heating/cooling element. Water evaporation was prevented by sealing the sample periphery with low viscosity (10cp) silicon (PDMS) oil. The contribution of the oil to the measured torque was negligible, as verified experimentally. Only when the sample was exposed to strong flows, edge instabilities caused oil ingress in the measuring gap. This was avoided by keeping shear rate below $10s^{-1}$. As a precaution, a reference DFS test was performed before commencing nonlinear tests. Sample loading condition was verified by comparison of the reference with LVE spectra taken after nonlinear tests. The main study focuses on temperatures of 37, 40°C and pH 6.5, 7.4. These are the conditions usually met in the human body. Temperature of 25°C and pH5 was also studied for reference, the latter mainly to understand pH responsiveness and structural changes. Samples are labeled as per Table 1. Most of the studies concern hydrogels HG1, HG2, HG3 which are of the same chemistry and concentration but have been prepared in different times with the same protocol. To identify possible differences, we kept the distinction between batches 1, 2, 3. Batch 5 (HG5) differs only in polymer concentration while batch 4 (HG4S) in chemistry where the B block was modified by substitution of histidine with sarcosine aminoacid residues.

Table 1: Sample details and labeling. Hydrogels HG1, HG2 and HG3 are of the same concentration and chemistry but prepared in different times. In hydrogel HG4S histidine was substituted by poly- sarcosine. PAC refers to Paclitaxel concentration.

Polymer concentration	HG1,2,3	PLL- **Phis**-PBLG C= 33.3 mg/ml
	HG4**S**	PLL- P**Sar**-PBLG C= 33.3 mg/ml
	HG5	PLL- **Phis**-PBLG C= 25 mg/ml
pH	a	7.4
	b	6.5
	c	5
Paclitaxel concentration	PAC1	1.28 mg/ml
	PAC2	2.24 mg/ml

PAC3	3. 03mg/ml

3.3 Structural characterization

The supramolecular character of this pentablock alone is a sufficient factor for the chain statistics to deviate from ideal Gaussian chains. Complete structural characterization requires extensive experiments, given the variety of intermolecular forces (Stendahl *et al.* 2006), chain folding of polypeptide blocks (Ghélis 2012) and self-assembly motifs exhibited (Löwik and van Hest 2004), and is beyond the scope of the present study which focuses on the rheological responsiveness. First complexity arises from the pentablock architecture ABABA with the B blocks being the hydrophobic ones leading to micellar or flower like primary structures with bridging chains (Annable *et al.* 1993, Huysecom *et al.* 2023, Koga *et al.* 2009, Maibaum *et al.* 2004). Hydrophobic polypeptides tend to minimize the exposed surface area of their non-polar side chains to water molecules, because the latter are relatively small and with extremely strong hydrogen bonds due to oxygen. Disruption of this cohesive network is energetically unfavorable (Tanford 1980). Due to the hydrophobic nature of the two B blocks, the ABABA pentablock has the propensity for intra-chain folding, a process sensitive to the length of the middle block (Li and Deming 2010). Shorter middle block lead to small micellar aggregates while long ones promote the formation of extended fibrils. Therefore with proper molecular tuning pentablocks also self-assembly in micellar hierarchical ordered structures (Skoulas *et al.* 2021). To this end the middle A block in HG is significantly larger as visualized in Figure 3.2. Hydrophobicity of the B block induces intra- and inter-chain associations with a finite lifetime, i.e., junctions can break and reform due to thermal fluctuations. Since this is the dominant network formation mechanism, the hydrogel's mechanical response depends on the bridges and loopy micelles with a given bond life time. Temperature increase will decrease bond lifetime and modulus as in "pure" transient networks.

Complexity also arises from the secondary structure motifs of the individual polypeptide blocks in different environments namely, temperature and pH. This can be used as an advantage as their conformational structure can be modified depending on the environment, enhancing pH and T responsiveness. Polylysine, a model polypeptide, has a propensity to form random coils at pH range of interest. On the other hand polyhistidine with a dissociation constant pK_a= 6 forms β-turn at pH=6.5, 7.4 while its protonation at pH=5 results into random coil secondary structure and reduced hydrophobicity. Circular dichroic spectra have shown PBLG to form α-helices enhancing gel strength (Bilalis *et al.* 2018) and this structure is expected for all pH values, since the monomer is not pH responsive. More details on the dominant secondary structure at the quiescent state can be found in these publications. The secondary structure is affected by many parameters such as temperature (Davidson and Fasman 1967), concentration

(Aggeli *et al.* 2001) and shear flow (Bekard *et al.* 2011, Courty *et al.* 2006). The secondary structure may unfold under shear when the hydrodynamic forces exceed the stabilizing intra-chain hydrogen bonds as illustrated in Figure 3.3. Aggregates may also break-down and reform in different sizes or motifs (Sharma and Pattanayek 2018). This is reflected in the nonlinear shear response of the hydrogel.

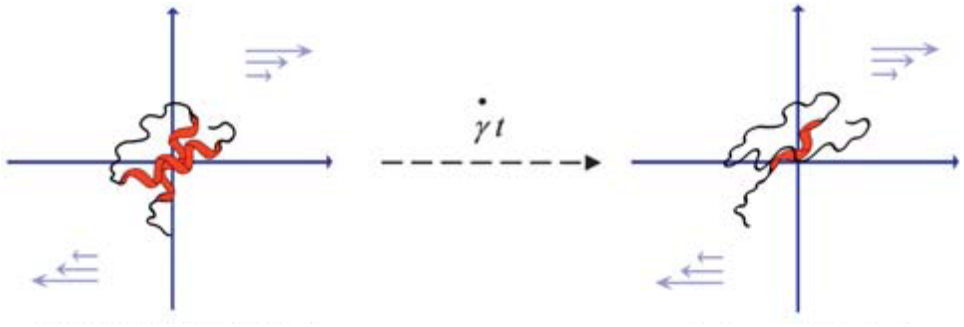

Figure 3.3 Cartoon of PLL gradually unfolding under shear due to hydrodynamic forces. The red color depicts residues that have retained their ordinary secondary structure, i.e., α-helix. From (Bekard, Barnham, White and Dunstan 2011)

An extensive chemical and structural characterization was performed by Maria Kasimatis and coworkers, including transmission and scanning electron microscopy (TEM, SEM), NMR and circular dichroism (CD) the latter to determine the secondary structure (Kasimatis, PhD thesis 2023). To further investigate the structure in the gel state, scattering experiments were performed. Neutrons were selected as a scattering medium for various reasons. Their wavelength of a few Angstroms is comparable to the interatomic spacing while contrast is due to the substantial difference between the scattering lengths of hydrogen and deuterium, b_H = -3.739 *10^{-13} cm and b_D = 6.671 *10^{-13} cm, respectively. This renders the d-solvent "invisible". Neutrons are also less absorbed by most elements, an advantage for probing the average structure in gels. A limitation is the poor mono-chromaticity that results to insensitivity to secondary structure. The small-angle neutron scattering (SANS) experiments were performed in collaboration with Dr. Joachimin Kohlbrecher at the Laboratory for Neutron Scattering and Imaging (LNS) at Paul Scherrer Institute (PSI) in Switzerland. The SINQ spallation source was used at different sample-to-detector distances from 18m down to 2m with the use of a focusing neutron guide (Kohlbrecher and Wagner 2000), corresponding to a wide scattering vector (q) range. HG1a,b,c samples where measured at their nominal concentration to probe the structure in the gel state. Samples where deuterated by diluting the stock dry polymer to D_2O (labeling) to the gel concentration 33.3 mg/ml. Deuteration may admit minor changes such as enhancement of hydrophobicity (Price *et al.* 2013) but is not expected to affect the structure of the HG. A set of more diluted samples was also tested however the signal was weak close to the noise floor, a Neutron sources disadvantage. Chain aggregation was also considered possible hence dilute regime and form factor is not discussed.

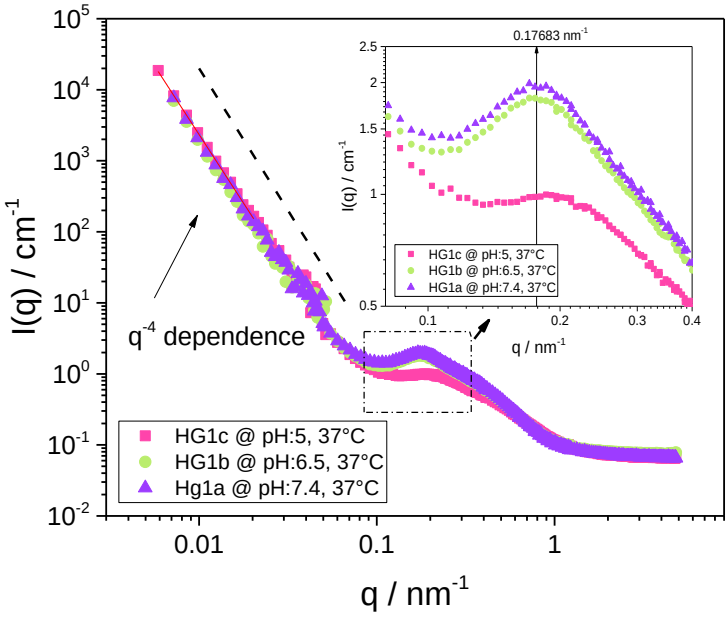

Figure 3.4 Scattering intensity I versus wavevector q for the HG1 at all pH conditions. Inset shows a magnification of the area enclosed by the dashed rectangular. The corelation peak coresponds to the micellar distance. The dashed line indicates the -4 slope.

The scattering intensity (I) for an extensive range of q, is plotted in Figure 3.4. The prominent correlation peak at q=0.177 nm^{-1} corresponds to a length scale of 35nm and is indicative of a micellar structure or micellar aggregates due to the hydrophobic interactions. Interestingly, this length scale is very similar to the nearest neighbor distances measured by SANS in telechelic polymers of similar concentration, i.e., 30nm and 4% respectively (Serero *et al.* 2000). We can't exclude that this similarity may be coincidental; nevertheless it supports the analogies of these two systems. The same scattering signature has been observed in a very similar hydrogel where the middle block is substituted with hydrophilic PEO (Skoulas *et al.* 2021). The peak starts to decrease weakly with pH form 7.4 to 6.5 while the curve it almost flattens at pH5. It is attributed to the protonation of histidine residues at lower pH values, leading to B blocks becoming more hydrophilic hence network density decreases dramatically. This supports the argument that the dominant networking mechanism is due to hydrophobic molecular associations. The Porod intensity increase with q^{-4} dependence for q< 0.05nm^{-1} suggests smooth interfaces (Bale and Schmidt 1984) and spatial concentration heterogeneities at length scales of ~500nm. This relates to the rheological finding that the material stores large residual stresses and may exhibit local fracture. The plateau at high q cannot be trivially analyzed as it contains the contribution from incoherent neutron scattering.

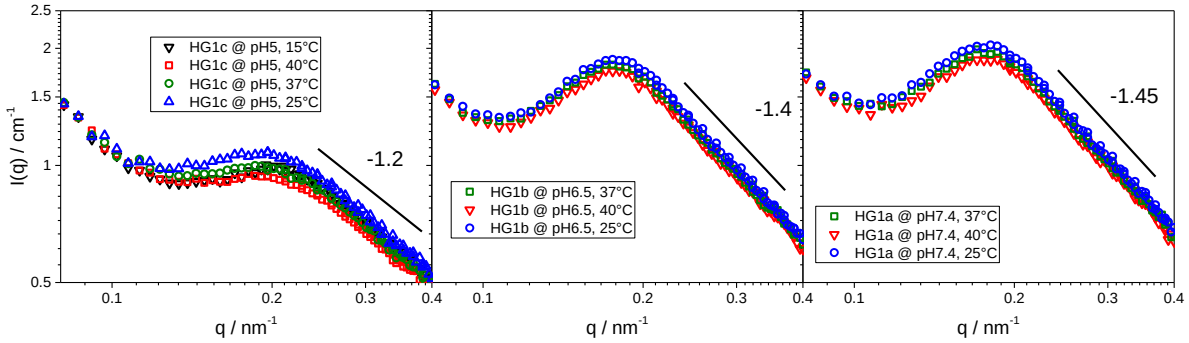

Figure 3.5 Temperature dependence of the correlation peak in scattering intensity for HG1 at all pH conditions. Lines indicate the slope of the best fit to data.

Scattering intensity was also performed for various temperatures of interest, as shown in Figure 3.5. Sample with pH 5 seems to be more temperature responsive that pH 6.5 and 7.4. Nevertheless, intensity decreases when heating from 25 to 40°C, for all samples. This monotonicity is violated at 15°C for pH=5. This temperature was tested out of curiosity as rheological data indicate some kind of structural change but pH 5 and T=15°C are not directly related to the application. The discussion is limited to the features of the I(q) curve. A more detailed work would consist of modeling I(q) under the conjecture of hierarchical structure with micelle to be the primary element. With this method (Hammouda 2010) length scales can be calculated by the model in detail. In a simpler approach the micellar contribution to the scattering profile can be modeled as spheres (Kinning and Thomas 1984) of various softness (Hamley *et al.* 2000).

3.4 Linear viscoelasticity

The pH dependence of LVE was investigated for the pristine samples (without drug) at the healthy body temperature of 37 °C. Sample with pH5 was tested only for reference as pH 6.4 (malignant tissue) and 7 (healthy tissue) conditions are only relevant to human body.

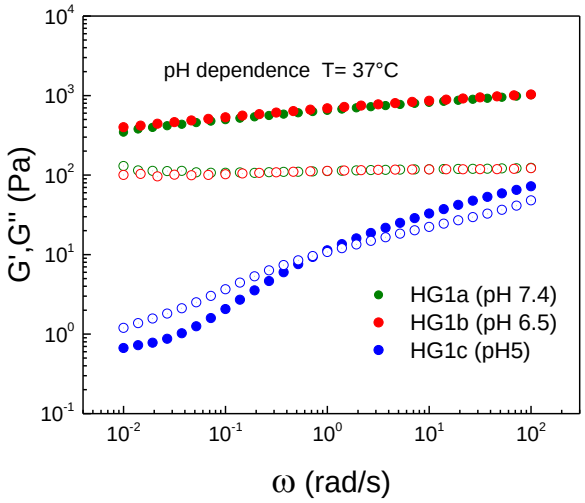

Figure 3.6 pH dependence of LVE for pristine HG at 37°C. HG1a and HG1b are very similar while HG1c exhibits terminal flow regime. The upturn in G´ at low frequencies is discussed in the text.

The hydrogel exhibited a strong solid-like response within the experiment frequency window for pH 7.4 and 6.5 and temperature of 37°C as shown in Figure 3.6. The pH dependence of LVE is weak between pH 6.5 (malignant tissue) and 7.4 (healthy tissue) while at pH 5 there is a substantial decrease in both moduli and a liquid-like response at low frequencies. The upturn in G´ at low frequencies can be attributed to a slow relaxation process of the fibrilar network. It could also originate from a systematic phase angle error at low torque signals (see also Fig. 3.7(b) below). Apparently, the dominant relaxation modes for pH=7.4 and 6.5 are too slow to be captured in the experimental frequency window.

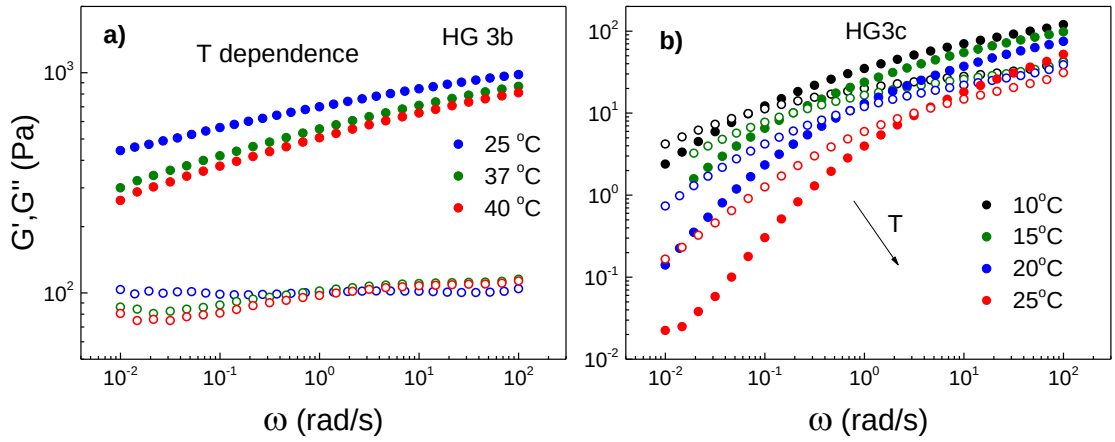

Figure 3.7. Temperature dependence of LVE a) for the stronger gel HG3b and b) the weaker HG3c. G´ upturn for T=25°C at low frequency is an articact due to low torque and sensitivity of G´ to phase angle error.

Suspensions of diblock copolymer micelles in selective solvents have been shown to exhibit terminal regime (Watanabe and Kotaka 1983). In HG1a and HG1b the high packing of micelles and possibly

micellar bridging contributes to slow modes and yield stress discussed in the next chapter. In pH=5 micellar population decreases considerably along with bridging hence faster modes dominate. The temperature dependence is also weak, yet monotonic, as G´ decreases with temperature increase as shown for pH=6.5 Figure 3.7(a). Although weak, this trend supports the T-responsiveness of the hydrogel which weakens when encountering the environment of the malignant cell. The weaker pH=5 exhibits a terminal regime and stronger T dependence Figure 3.7(b). The structural relaxation time defined by the inverse of G´, G´´ crossover decreases with T increase in agreement with findings in associative polymers (Ng *et al.* 2000) where the authors reported two relaxation modes. The longer one (structural) was attributed to the relaxation time of the network, decreasing with T increase. The shorter however, was attributed to the bond lifetime and exhibited the opposite trend. When data of Figure 3.7(b) are shifted horizontally to T_{ref}=25°C a reasonable master curve is obtained (Figure 3.8). The minor disagreement in higher frequencies hence, smaller length scales could be attributed to a short-time mode with different time dependence, in analogy with (Ng *et al.* 2000). On the other hand the moderate agreement suggests that solvency conditions are not affected in this T range and excluded volume interactions are not present in HG1c.

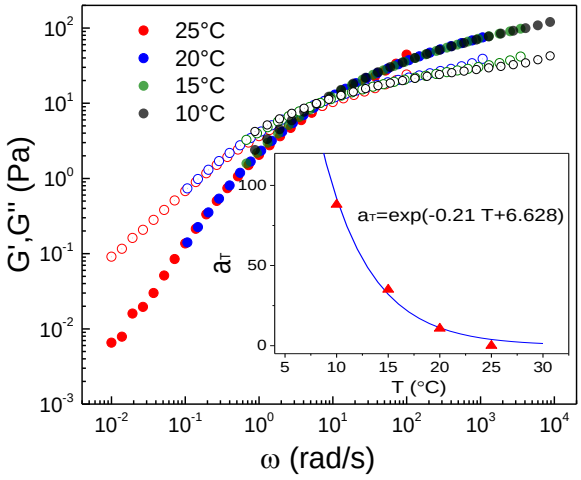

Figure 3.8 Master curve obtained by shifting LVE data of HG3c horizontally to T_{ref}= 25°C. Inset shows the values of shifting factor a_T as a function of temperature. Solid blue line is a fit to data .

Given the potential application of the HG as a drug carrier, its sensitivity to strain history and its stability were evaluated. Shear history does not affect LVE, suggesting that the microstructure recovers quickly after yielding. LVE spectra are identical for the recently pre-sheared at $1s^{-1}$ for 100s HG3b and the case where it has been at rest for 12h Figure 3.9(a). The same picture emerges for HG1a with Paclitaxel 3.03mg/ml before and after LAOS cycles of 200% strain amplitude Figure 3.9(b). However, the nonlinear response is sensitive to shear history, as discussed in the next chapter. The HG displayed excellent

stability. The LVE response did not change even after 12h on the rheometer nor after heating to 40°C and then cooling back to 25°C Figure 3.10(a). This confirmed also the effectiveness of the oil sealing against evaporation. Following the measurements with pristine HG, the question arises weather the addition of the drug changes the rheological behavior of the hydrogel. The "entrapment" of the anticancer drug Paclitaxel marginally altered G'' and only at high frequencies, still changes are comparable with the experimental error Figure 3.10(b).

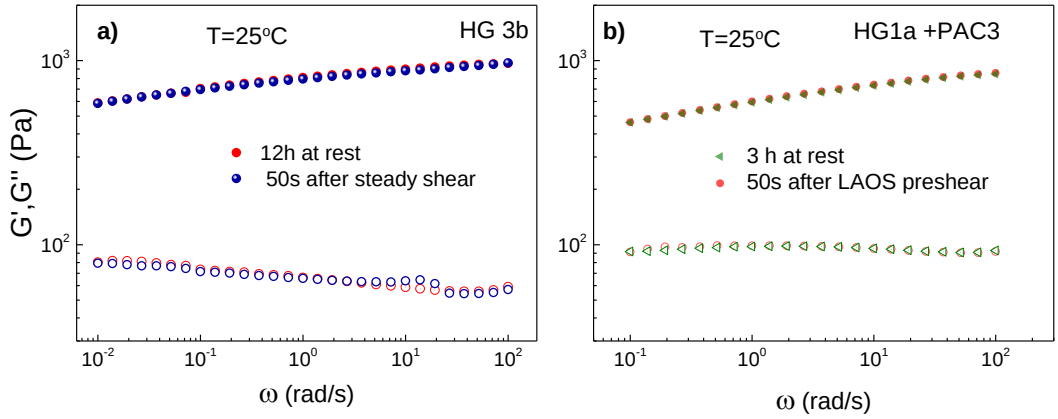

Figure 3.9 LVE response with and without pre-shear a) Steady preshear at $1s^{-1}$ for 100s. b) Oscillatory preshear at 1 rad/s and 100% strain amplitude.

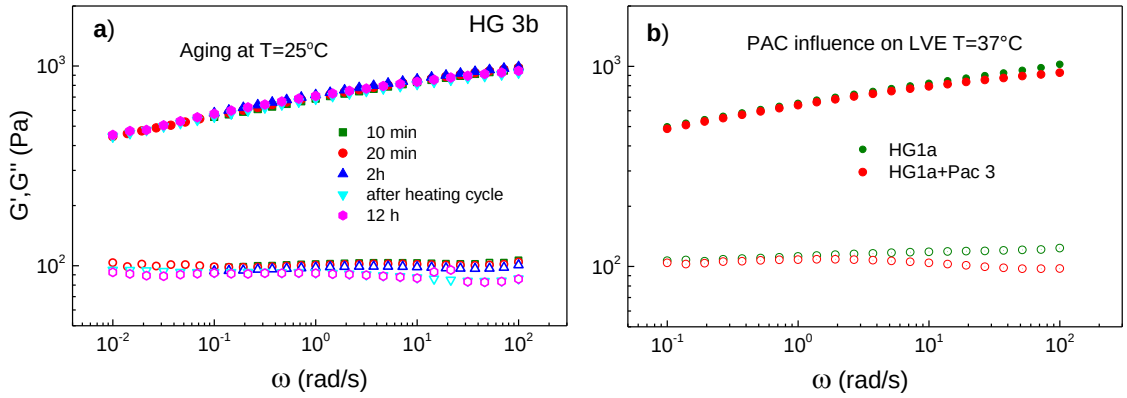

Figure 3.10 a) Aging behavior of the HG batch 3 and pH 6.5.at 25°C. Legend indicates time from loading. Cyan and magenta curves are measurements after heating the sample to 40°C and then cool it to 25°C. b) Influence of the addition of Paclitaxel to a concentration of 3.03 mg/ml to the hydrogel. Weak decrease of moduli at higher frequencies.

The overall sensitivity of LVE in pH, T and drug concentration is summarized in Figure 3.11 for all samples tested.

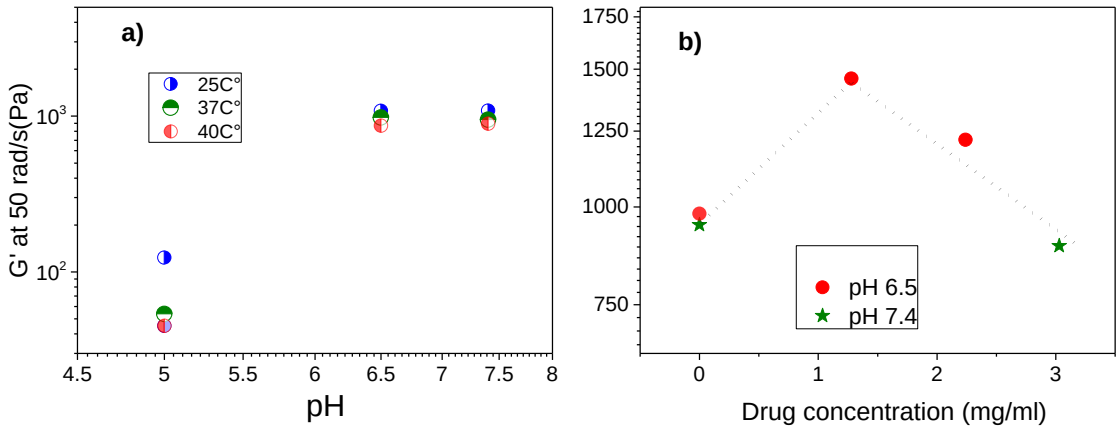

Figure 3.11 Summary of the apparent plateau modulus (G´ at 50 rad/s) for a) pristine HG at all pH and temperatures tested b) temperature of 37°C and various pH and drug (Paclitaxel) concentrations. Lines are guides to the eye.

An apparent plateau modulus was identified as the G´ value which was selected arbitrarily albeit consistently at a high frequency of 50 rad/s. Heating facilitates break-reformation process. Data clearly confirm this at pH 6.5 and 7.4 where the modulus increased by 200 Pa approximately with cooling from 40 to 25°C as bond lifetime increases. The pH=5 hydrogel (HG1c) is more thermo-responsive with a twofold G´ increase of 45 Pa. A decrease of pH leads to weaker gel structure with a more sensitive to bond lifetime modulus. The addition of Paclitaxel leads to a non-monotonic dependence of modulus on concentration, but seems not to affect gel strength in general. The interaction of Paclitaxel with the HG is not known even at qualitative level. Modulus comparison would be fair if performed at the same Deborah number, however the terminal time was not accessed. For the case of flexible segments we can deduce from Eq. (3.1) a gross estimate for an effective junction density v_{ef} = 20.7x10^{16} cm^{-3} for G_0=900 Pa. On the other hand, from SANS data we can assume a micellar radius of 17.5nm. A 1cm^3 volume filled at random closed packing with monodisperse hard spheres (0.64) of 17.5nm radius, can accommodate 25.5x10^{15} micelles. If all are bridged with one neighbor then this estimation is a decade lower than the effective junction points calculated from (3.1). This rough estimation suggests that either packing is denser (they are soft objects after all) or distant neighbors are also bridged (super-bridges) (Annable *et al.* 1993), or even that strands are more rigid.

On another note, rheology can provide a gross estimate of the bending rigidity of the network strands, quantified as persistence length (L_p), the typical length scale for the decay of tangent–tangent correlations. This is the maximum length over which the chain segment remains effectively rigid and straight, despite thermal fluctuations. LVE response of synthetic and natural peptide hydrogels has been found to agree well with predictions for semiflexible polymeric networks (Ozbas *et al.* 2004, Rodriguez *et*

al. 2016). Building-up on the theory of rubber elasticity, a model was developed to predict the elasticity of semiflexible actin filament network (MacKintosh *et al.* 1995) where Lp is given by:

$$L_p = \sqrt{\frac{G_p\, \xi^5}{k_B\, T}} \tag{3.2}$$

and ξ is the correlation length or mesh size of the network, k_B the Bolzman constant and G_p the plateau modulus. For model polymeric systems G_p is taken at the minimum of G¨, here we will arbitrarily use the value at 50 rad/s where all samples behave like solids Figure 3.6.

The parameter ξ is taken from SANS data to be 35nm, i.e., the length corresponding to peak position in Figure 3.4 . This is for pH 7.4 and 6.5 as the peak for pH5 seems to shift to larger length scales but the position is not clearly resolved. The calculated L_p values are listed in Table 2.

Table 2: Persistence length (L_p) [nm] for all pH and T values, calculated from Eq.(3.2)

Sample	$25°C$	$37°C$	$40°C$
HG1a-pH7.4	117.7	107.9	104.2
HG1b-pH 6.5	117.6	109.7	102.7
HG1c-pH 5	39.6	25.7	23.4

In principle Eq.(3.2) is incorrectly used for HG1a, 1b with micellar structure as it describes a network (in our case, formed by bridging rather than excluded volume interactions). This explains why the calculated persistence length is larger compared to HG1c and to the micellar length scale. Interestingly, L_p =23.4 nm for HG1c is comparable with the SANS correlation length of 35nm.

The effect of concentration was studied for two values. Linear viscoelasticity seemed unaffected by the reduction in polymeric concentration from 33.3 mg/ml to 25mg/ml Figure 3.12(a) suggesting that the number of elastically active strands are the same. Only at higher frequencies there is a larger difference probably due to changes in smaller length scales. But this is not conclusive as differences are within experimental error and it should be noted that these samples have been prepared independently (different batches). Temperature responsiveness of the less concentrated HG10a is stronger as depicted in Figure 3.12(b). This hydrogel proved also easier to be injected in practice. We can summarize that the less

concentrated HG10 with concentration of 25 mg/ml is better suited for the application. Lower concentrations also should be studied in the future as they may prove more T responsive. Lastly on LVE the effect of nanoparticle addition was studied as they are also potential drug carriers. Contrary to typical reinforcement the addition of 25mg/ml mPEG-PCL particles reduced the strength of the hydrogel (Figure 3.13) possibly due to osmotic effects or configurational changes (Mackay *et al.* 2003) but did not affect severely the network, i.e., its solid-like character. We conclude that similar and lower particle loadings will have minimal effect on the hydrogel strength which is important for drug delivery applications.

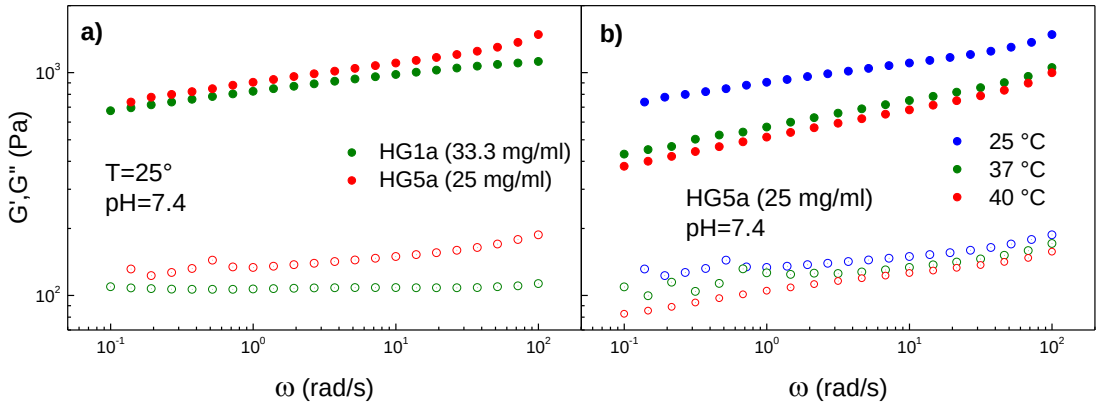

Figure 3.12 LVE dependence on a) polymeric concentration for HG1a (33.3 mg/ml) and HG5a (25mg/ml) b) temperature for the less concentrated sample HG5a.

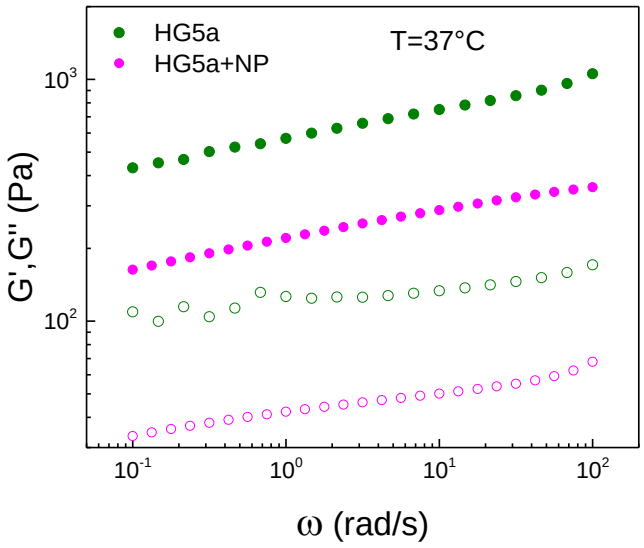

Figure 3.13 Effect of the addition of nanoparticles on LVE. Both moduli of pure hydrogel at pH7.4 decrease with the addition of 25 mg/ml nanoparticles.

3.5 Yielding behavior

Up to now, we have confirmed that our pentablock forms a stable and strong gel. T and pH responsiveness is low for HG1a and HG1b yet detectable. Now we turn our attention to the yielding behavior and structural recovery. It is of utmost importance for medical applications that the gel thins under flow so can be injected into the blood stream. Once injected the fluidized gel should rapidly restructure to carry its payload to the malignant tissue. To test this, dynamic strain sweeps were performed. The angular frequency was chosen to be 10 and 1 rad/s to allow comparison of the yielding response of the same sample at different deformation rate amplitudes. Nevertheless, 10 rad/s will be considered as the reference as torque signal is stronger and the period of the oscillation hence the data acquisition time is shorter than 1rad/s. The latter is an advantage in the structural recovery test below.

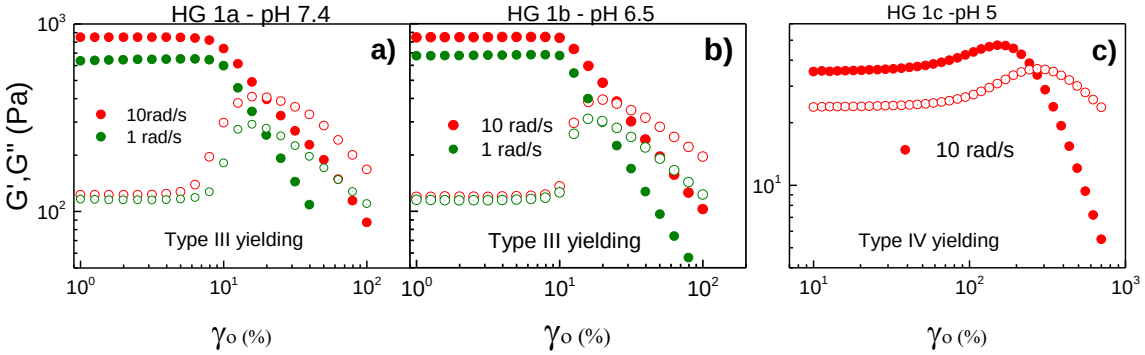

Figure 3.14 Yielding behavior under oscillatory shear of increasing strain amplitude for all pH at 10 and 1 rad/s and T=25°C. The weaker HG1c was measured only at 10 rad/s, note different y axis scale. Torque signal at 1 rad/s was below the resolving limit of MCR 501. All samples have the same concentration. Yielding is categorized according to (Hyun *et al.* 2002) to type III and IV where only G´´ and both G´, G´´ exhibit overshoot, respectively.

Firstly, we discuss qualitatively, the yielding behavior of HG1a and 1b. They both exhibit, similar behavior (Figure 3.14) with an overshoot in G´´ at the yielding point resembling type III yielding (Hyun *et al.* 2002, Hyun *et al.* 2011). For comparison, type III yielding is common in PEO/PBO diblock copolymer solution with FCC crystalline structure. Type III yielding is also typical in fumed silica solutions. The latter forms colloidal gels (Raghavan and Khan 1995) where microstructural entities can be seen as percolated clusters with mutual attractions an analogue to micelles with bridges respectively. Type III yielding supports but does not prove by itself micellar primary structure as other systems such as jammed spheres exhibit similar behavior (Pellet and Cloitre 2016). On the other hand if bridged micelles are considered (HG1a,b) then the stress response is a result of excluded volume interactions and effective attractions due to bridging consistent with type III yielding. As another reference to type III yielding we note that entangled networks exhibit mostly strain-softening behavior due to chain orientation and convective constraint release (Ianniruberto and Marrucci 2014) that results in the loss of constraints

(entanglements) well before chains are considerably stretched. Likewise, many yield stress fluids show strain softening as plastic rearrangements also release internal stress before any primary structure stretches considerably. For HG1a and HG1b we can assume that bridges break (detach) well before chains are stretched as in the opposite case strain stiffening would be present. Secondly, the weaker HG1c in a very different behavior exhibits strain-stiffening. Specifically, as strain increases the material strain-stiffens first (overshoot in G´ which precedes G´´) and then yields, resembling a type IV yielding (Figure 3.14). This is a common behavior observed in telechelic associative polymers (Pellens *et al.* 2004) and in biopolymers with fibrilar structure such as collagen I (Motte and Kaufman 2013). These authors concluded that the initial stiffening observed in DSS was attributed to the stretching of individual fibrils while there was a contribution from nonaffine (potentially reversible) fibril rearrangements. In a similar vein, we may attribute strain stiffening to the strong associative junctions that break well after molecular bridges are stretched beyond their linearity limit. But this will unlikely happen as HG1c with pH 5 has weaker hydrophobic association. Following insights from the dumbbell model, strain hardening was explained (Ianniruberto and Marrucci 2015) by accounting for the repulsive interaction between the micellar coronas being brought to interpenetrate by the shear flow at low concentrations. This could be a possible scenario for HG1c: low concentration micelles interpenetrate due to shear flow resulting in repulsive interactions and strain hardening. But this is not supported by the Master curve of Figure 3.8 and SANS data. Alternatively, hardening may be due to fibrilar structure (Janmey *et al.* 2009). This supports the argument that the significant change in network structure from pH=6.5 to 5 that is evident in rheological and scattering signatures, results from a microstructural transition from a micellar to fibril primary structural element. Fibrils and bundles of them are ubiquitous in many similar systems. Stiffening for pH5 occurs at >100% strain indicative of flexible fibrils (Storm *et al.* 2005). HG1c with pH5 has persistence length comparable to the SANS derived correlation length. Fibril-based bio-polymeric networks with relative low rigidity may exhibit nonaffine deformation (rearrangements). Simulations in 2d space, for networks with nonaffine motion revealed the existence of a transition from bending-dominated at low strains to a stretching-dominated response at large strains (Onck *et al.* 2005). When flexible or semi-flexible filaments stretch, they respond elastically due to entropy: stretching reduces the accessible number of microstates accessed via thermal transverse fluctuations (entropic spring) in an analogy to flexible polymers. On the contrary when rigid (bundled or cross-linked) fibrils stretch the elasticity origin is also enthalpic due to actual bending. Whatever the origin of stiffening the individual contributions cannot be decoupled. We note here we consider filament to be the primary linear aggregate that may lead to larger assemblies defined as fibrils. Fibrils are morphologies with diameters typically on the order of 10nm however for our study the boundaries between fibrils and filaments are not sharp. The

interest reader can find more on this kinetic process of these assemblies and definitions in these review works (Gillam and MacPhee 2013, Murphy 2007).

We summarize now the discussion on yielding behavior and structural insights. For pH=5 strain hardening is due to chain or fibril stretching beyond their linear elastic limit. Increased bundling enhances rigidity and strain hardening due to bending, consistent with the argument of fibrilar primary structure. Hydrophobic associations become weaker in pH 5 as histidine protonates hence micelles collapse as SANS data revealed. Nevertheless, the scenario of small micellar population cannot be totally excluded. In this case, strain hardening could be a consequence of the interpenetration of micellar coronas (Ianniruberto and Marrucci 2015). On the other hand interpenetration of the dense micelles of HG1a,b, is dominant at the quiescent state leading to the absence of strain hardening (Ianniruberto and Marrucci 2015). This behavior suggests dominant excluded volume interactions of soft sphere nature (micelles) with effective attractions due to bridging. Further insights on structural changes under flow can be provided from the few cases where shear thickening has been exhibited at low rates and low micellar concentrations attributed either to increased shear-induced associations (Tripathi *et al.* 2006) or the nonlinear stretching of the finite extensibility network strands i.e. the polymeric backbone (Serero *et al.* 2000). In the latter work the authors argued that shear induced associations cannot be the cause of shear thickening as they are governed by timescales longer that those observed in rheological data. Shear thickening concerns the viscous response nevertheless, it can complement the understanding of the flow-structure coupling mechanism.

The yielding behavior for all pH values is summarized in Figure 3.15, where the yielding point is identified by the horizontal line at a phase angle of 45°. All curves have similar shape while the decrease of pH results in less brittle, yet weaker hydrogel. This trend is weak between pH=7.4 and 6.5 but dramatically increases at pH 5.

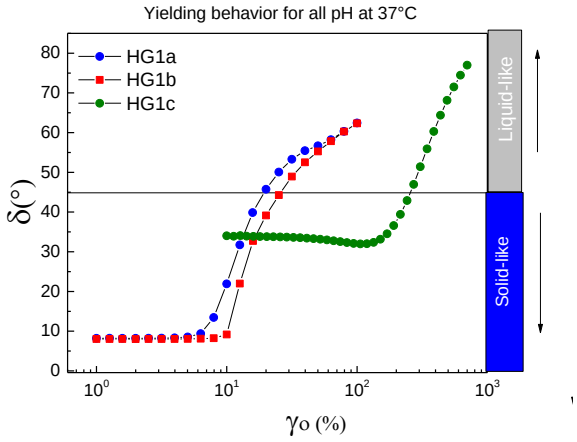

Figure 3.15 Phase (loss) angle as a function of strain amplitude for all pH conditions of pristine HG. The DSS experiments were performed at 10rad/s. At the corresponding (observation) time scale of 0.1s HG1c (pH 5) forms the weaker, yet the less brittle gel. Line indicates the boundary between solid and liquid limit (45°)

Before we comment on brittleness and wrap-up the discussion on the yielding mechanism, the stress relaxation mechanism in bridged dense micellar structure is discussed as suggested by (Semenov *et al.* 1995) . The latter is based on telechelic polymers where the core is formed by the hydrophobic end groups Figure 3.1 in a similar way to triblock BAB amphiphiles with long middle hydrophilic block. The corona consists of the hydrophilic loops (middle blocks) while in our pentablock it will also include the hydrophilic end-blocks as dangling ends. The interactions between micelles are both repulsive, when micelles approach due to hydrophilic blocks interpenetration - the latter envisaged as polymer brushes with excluded volume interactions-, and effectively attractive due to bridging, when micelles move apart. The pentablock versus triblock architecture results in enhanced by the outer blocks "shielding" of the cores (larger grafting density) and promote repulsion and, consequently, micellar stability. At concentrations larger than the overlapping one, micelles are osmotically compressed, for example, forming polyhedron cells such as those of Figure 3.16, and relaxation is slowed down due to the creeping motion consistent with HGa, HGb LVE data.

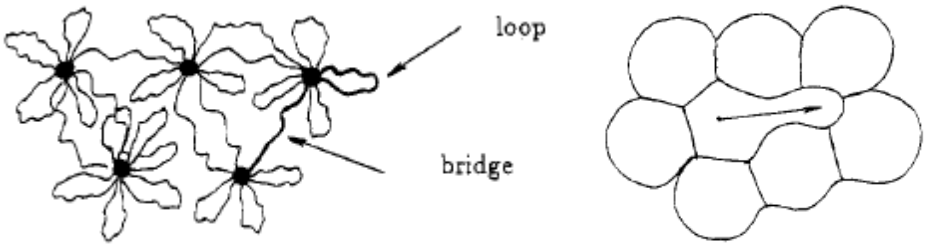

Figure 3.16 Left: Flower like micelles connected with bridging chains. The "flowers" form a transient network with hydrophobic aggregates as junction points. The cartoon refers to telechelic polymers an analogue to triblock BAB (B hydrophobic). Right: Creeping relaxation of a densely packed micelle. From (Semenov *et al.* 1995)

Now, the yielding mechanism can be envisaged as follows: at pH=7.4 and 6.5, the network is dominated by packed bridged micelles. Reduced bridging does not contribute to strain hardening (Creton *et al.* 2009). Hydrophilic blocks establish a soft intermicellar repulsive potential that does not show strain hardening. As strain is increased bridges break-down, hence plastic events release the stress before any stretching takes place at a microscopic level on average. Micelles rearrange by a slow "creeping motion" (Semenov *et al.* 1995). At higher strain or rates larger length-scale plastic events occur. These processes entrap stresses that persist over time, see Chapter 4. On the other hand at pH=5 bridging is already collapsed and the micellar primary structure has turned into filaments or even fibrils. The network becomes weaker though more deformable in other words less brittle as observed in Figure 3.15. Stresses first accumulate due to stretching (Motte and Kaufman 2013) driving elasticity to a local maximum while at larger strains junctions break and plastic rearrangements dominate increasing dissipation, as shown in Figure 3.14(c).

3.6 Structural recovery

Structural recovery was explored by means of a sequence of two tests. DSS was performed initially imposing amplitudes beyond the yielding point, until the gel was fluidized. Then, Dynamic Time Sweeps (DTS) at the same frequency probed the recovery of the mechanical properties, i.e., the time needed to revert back to gel-like LVE response in the spirit of (Mewis and De Bleyser 1972). From the olive curve in Figure 3.17(b) it is evident that the gel recovers almost 90% of its mechanical strength in 8 seconds. Surprisingly, the less concentrated HG5a exhibited the same modulus and recovery time with HG1a. This could be attributed to a saturation of the number of elastically active chains, in other words the addition of more chains does not form more micelles or bridges. It is consistent with studies of associative polymers where relaxation time and viscosity increase weakly with concentration above >> c* (Rubinstein and Semenov 1998) and observations in scattering experiments where the micellar size and

aggregation number did not vary significantly upon increasing the concentration (Huysecom *et al.* 2023) and reached a saturation level (Mortensen and Pedersen 1993). This does not explain the decrease of the yielding point of HG5a by almost on order of magnitude. Although interesting, this point won't be discussed further in this work. This "saturation" of micellar population supports the argument that micelles are packed.

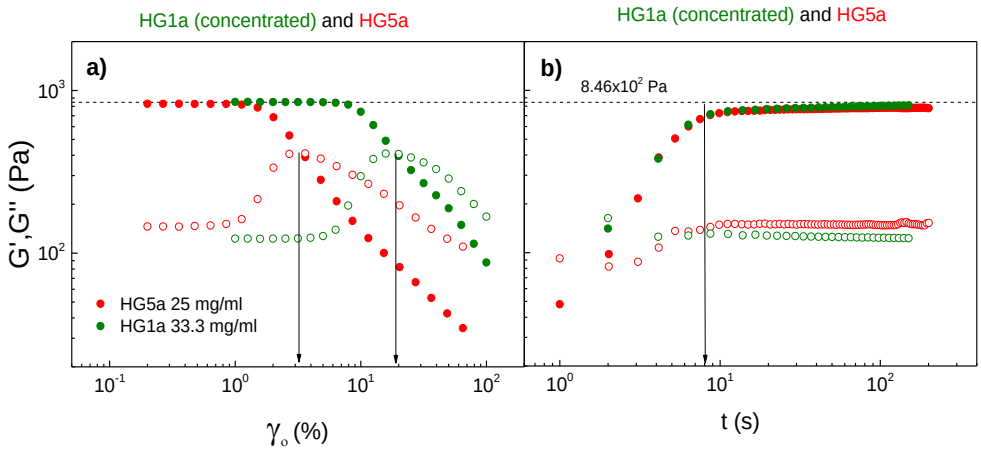

Figure 3.17 Data from a) DSS at 10rad/s and b) DTS, performed in series to yield and probe the structural recovery of the HG, respectively. Sample is HG1a and HG5a with pH 7.4 and concentration of **33.3 mg/ml** and 25 mg/ml (less concentrated), respectively. In panel (b) the abscissa denotes the elapsed time from the beginning of the interval, i.e., immediately after the last DSS oscillation at the highest strain amplitude.

HG4S was also synthesized for drug delivery where histidine is substituted with the neutrally charged sarcosine. We tested its self-healing properties as depicted in Figure 3.18 for two pH conditions 6.5 and 7.4. Gel properties are partially recovered in 10s, however it takes 400s for G´ to recover almost to its original value. Yielding is more gradual in HG4S compared to HG1a, b, see also Figure A. in the Appendix. This of course does not render the HGS unsuitable for drug delivery.

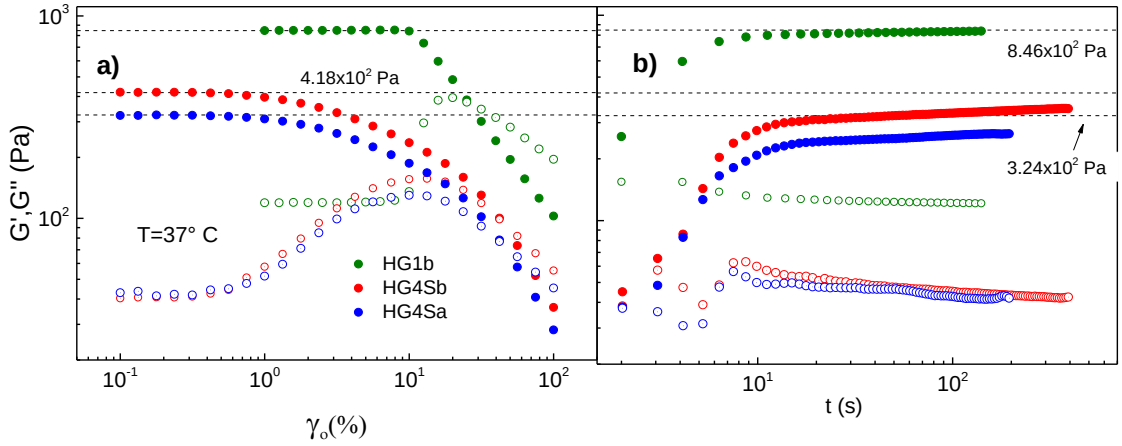

Figure 3.18 Comparison of yielding and structural recovery of HG1b (pH 6.5) with HG4Sa and HG4Sb. In both HG4Sa, b histidine is substituted with Sarcosine. a) DSS at strain amplitude of 10 rad/s b) DTS performed immediately after yielding captures the recovery of the mechanical properties. Full structural recovery seems to take more time in HG4S (sarcosine) for both pH. In panel (b) the abscissa denotes the elapsed time from the beginning of the interval, i.e., immediately after the last DSS oscillation at the highest strain amplitude.

3.7 Conclusions and perspectives

SANS and rheological data support the existence of bridged micellar structure in hydrogels with pH 6.5 and 7. This is consistent with previous work (Skoulas *et al.* 2021) in a very similar hydrogel. We showed the suitability of HG for drug delivery applications from the rheological perspective. The HG exhibits high-plateau modulus to ensure coherence, as well as fast recovery time after yielding. It shear thins to be injectable. Temperature responsiveness is weak between 37 and 40°C for the concentrated case, but improves dramatically for the less concentrated HG5 of 25 mg/ml. Lower polymer concentration resulted in a less fragile gel with the same modulus. To this end, we suggest that 25 mg/ml and lower concentrations should be utilized in drug delivery. Mechanical properties do not seem to change dramatically for variations of pH between 6.5 and 7.4. The entrapment of Paclitaxel (1.28 -2.24 mg/ml) does not alter the mechanical response or the gel structure. On the contrary pH=5 weakens the gel significantly due to weaker hydrophobic associations as a consequence of histidine protonation.

Based on the micellar structure, nonlinear rheology provided insights into the yielding mechanism and the origin of strain softening and strain hardening for pH 6.5 and 5 respectively. To better understand structural changes under flow more work is required. Rheo-SANS and particle image velocimetry will provide solid evidence of the microstructural changes (interplay of inter- and intra-chain associations) and flow conditions respectively, in the rheometric gap during steady shear as well as in the transient part. A systematic study of different concentrations will capture the onset of bridging and other

possible intermediate self-assembly motifs. The effect of ionic interactions can also be studied by the gradual addition of salt to achieve various degree of screening. Finally, the proper modeling of SANS I(q) profile will rationalize microstructural parameters while the comparison of LVE predictions based on hierarchy of fractal elements model (Bantawa *et al.* 2022) with rheological data will provide further insights into the origin of elasticity and its individual contributions .

Appendix A.3

Deformation profile

All linear and nonlinear rheological experiments performed require the existence of homogeneous deformation in the gap. This is violated in case of shear banding, wall slip and other instabilities. To ensure homogeneous deformation we performed digital Fourier microscopy (Giavazzi and Cerbino 2014) in a series of oscillatory tests at various strain amplitudes in an MCR 302 rheometer (Anton Paar, Austria) coupled with a confocal microscope setup. The setup consists of an inverted microscope TE Eclipse 300 (Nikon, Japan) with a confocal scan head VTEYE (Visitech, UK). More detail on the setup can be found (Mohandas, PhD thesis 2021). Measurements were performed at strain amplitudes of 0.8 and 20% corresponding to the linear regime and yielding point, respectively, and larger ones of 50, 100% at the fluidized state. Point by point scan was performed at the pre-adjusted z coordinate (plane normal to velocity gradient direction), corresponding to a specific gap height. For every plane a series of frames were constructed while the displacement at each plane was calculated by correlating the images in the Fourier space (Edera *et al.* 2021) and then fitted to a sinusoidal function for the duration of four periods. With this method the displacement amplitude at different planes (z-coordinates) was extracted. From Figure , it is evident that the displacement amplitude increases almost linearly in the z-coordinate (gap) for rate amplitudes of $0.5s^{-1}$ and starts to deviate at rates > $1.2s^{-1}$. The deformation corresponds to a complete oscillation and it is derived by 200 individual frames during each cycle therefore sampling rate is two decades larger that Nyquist limit of 2 Hz. Hence, we can safely assume that the velocity field is also proportional to deformation for the whole period of oscillation. Reproducibility is satisfactory except for strain amplitude of 100%. This supports the consistency of DSS measurements up to the yielding point and the steady shear ones with rates up to $1s^{-1}$ discussed in the next chapter. At even higher rate amplitudes Figure the deformation profile indicates a stationary band at the lower plate of the geometry up to 120μm in height. Notably these are preliminary results and more work is needed in order to quantify the deviation from the ideal linear flow profile as well as define relevant criteria.

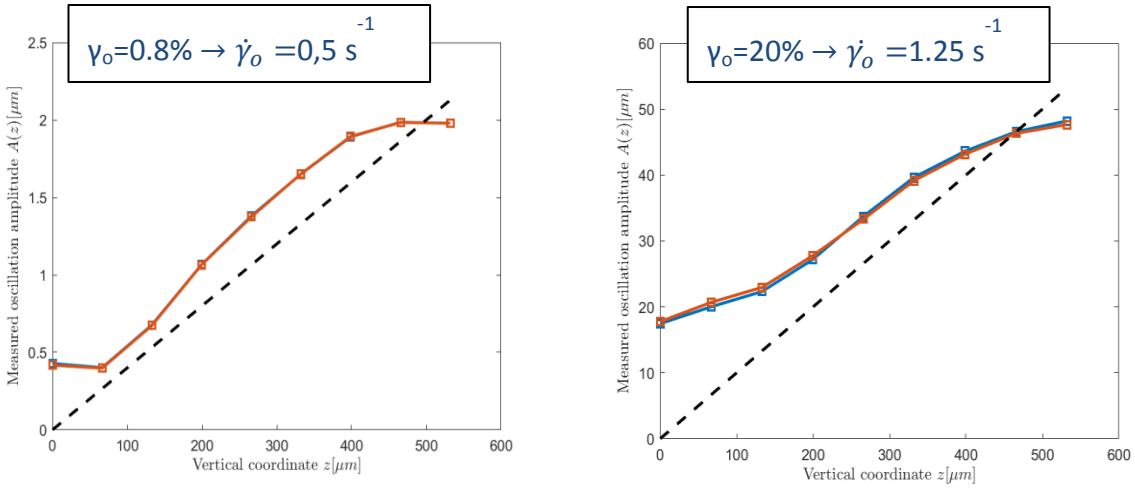

Figure A.1 Deformation amplitude profile during oscillatory shear of 1Hz (6.28 rad/s). The strain amplitude was set to 0.8% and 20% corresponding to shear rate amplitudes of 0.5 and 1.25s^{-1} respectively, as indicated in the legend. Different colors correspond to separate iterations and dashed line to the ideal homogenous flow. Data processed by Paolo Edera.

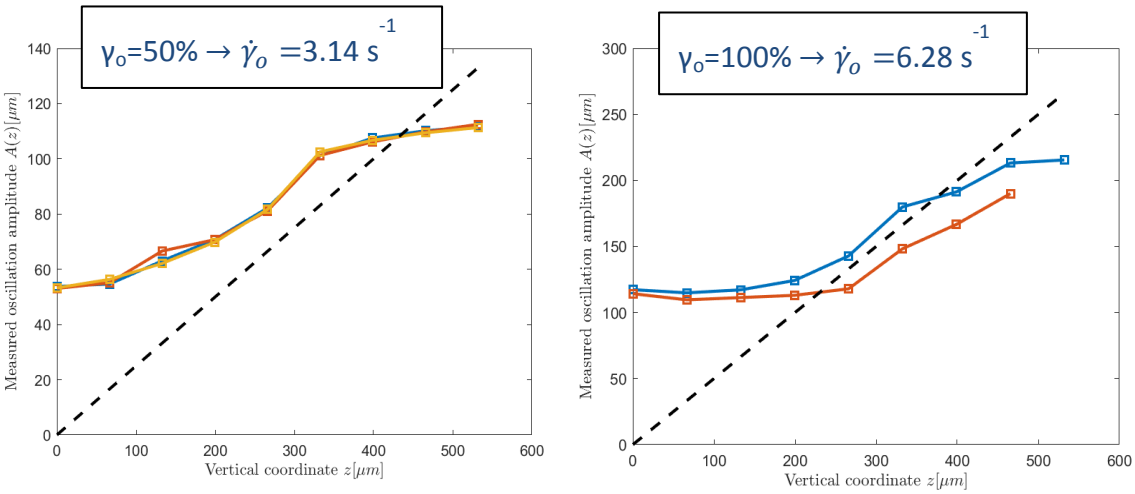

Figure A.2 Deformation amplitude profile during oscillatory shear of 1Hz (6.28 rad/s). The strain amplitude was set to 50% and 100% corresponding to shear rate amplitudes of 3.14 and 6.28 s^{-1} respectively, as indicated in the legend. Different colors correspond to separate iterations and dashed line to the ideal homogenous flow. Data processed by Paolo Edera.

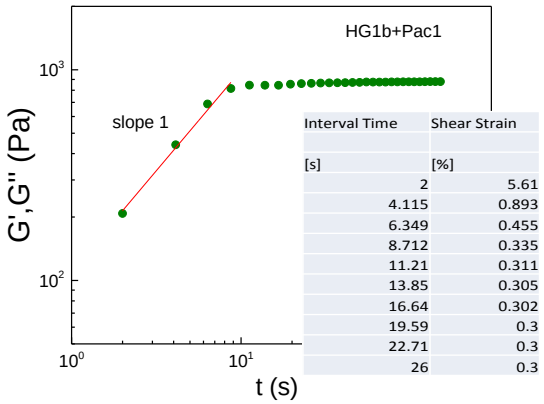

Figure A.3 G´recovery after yielding (DSS). Table indicates strain amplitude values. Commanded strain amplitude is achieved after 6.4s. This suggests that possibly G´ recover faster than 8 s and the instrument is not able to impose the proper sinusoidal strain waveform at earlier times.

All experiments discussed are strain controlled. It would be interesting to repeat the experiment of Figure A.3 with oscillatory stress as excitation (stress controlled mode) and monitor the time it takes for the instrument to reach the commanded values. This method may shorten the 6.4s observed in Figure A.3.

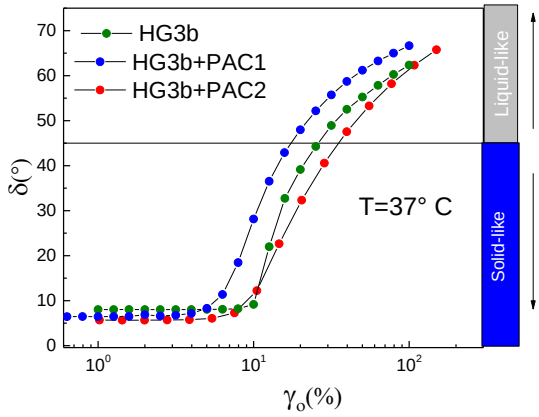

Figure A.4 Yielding behavior for HG pH 6.5 with and without Paclitaxel. Response is marginally affected. DSS performed at 10 rad/s

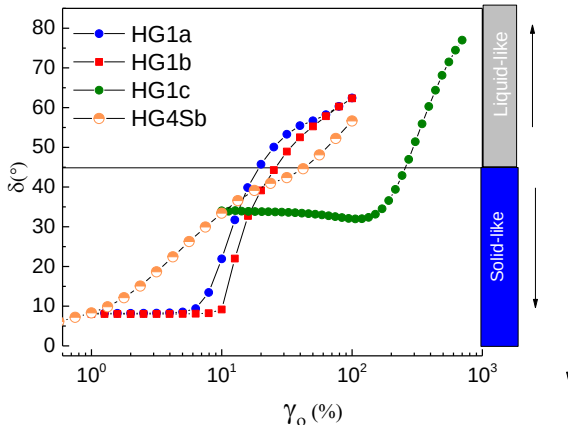

Figure A. 5 Yielding behavior for HG1 all pH compared to HG4Sb (Sarcosine). In the latter yielding is more gradual. DSS performed at 10 rad/s

References

Aggeli, A., Fytas, G., Vlassopoulos, D., McLeish, T. C., Mawer, P. J., and Boden, N., ‘‘Structure and dynamics of self-assembling β-sheet peptide tapes by dynamic light scattering,’’ Biomacromolecules 2, 378-388 (2001).

Annable, T., Buscall, R., Ettelaie, R., and Whittlestone, D., ‘‘The rheology of solutions of associating polymers: Comparison of experimental behavior with transient network theory,’’ Journal of Rheology 37, 695-726 (1993).

Bale, H. D., and Schmidt, P. W., ‘‘Small-angle X-ray-scattering investigation of submicroscopic porosity with fractal properties,’’ Physical Review Letters 53, 596 (1984).

Balsara, N., Tirrell, M., and Lodge, T., ‘‘Micelle formation of BAB triblock copolymers in solvents that preferentially dissolve the A block,’’ Macromolecules 24, 1975-1986 (1991).

Bantawa, M., Keshavarz, B., Geri, M., Bouzid, M., Divoux, T., McKinley, G. H., and Del Gado, E., ‘‘The hidden hierarchical nature of soft particulate gels,’’ arXiv preprint arXiv:2211.03693 (2022).

Bekard, I. B., Barnham, K. J., White, L. R., and Dunstan, D. E., ‘‘α-Helix unfolding in simple shear flow,’’ Soft Matter 7, 203-210 (2011).

Benson, S. W., ‘‘III-Bond energies,’’ Journal of Chemical Education 42, 502 (1965).

Bilalis, P., Skoulas, D., Karatzas, A., Marakis, J., Stamogiannos, A., Tsimblouli, C., Sereti, E., Stratikos, E., Dimas, K., and Vlassopoulos, D., ‘‘Self-healing pH-and enzyme stimuli-responsive hydrogels for targeted delivery of gemcitabine to treat pancreatic cancer,’’ Biomacromolecules 19, 3840-3852 (2018).

Boral, S., Saxena, A., and Bohidar, H., ‘‘Syneresis in agar hydrogels,’’ International journal of biological macromolecules 46, 232-236 (2010).

Buitenhuis, J., and Förster, S., ‘‘Block copolymer micelles: Viscoelasticity and interaction potential of soft spheres,’’ The Journal of chemical physics 107, 262-272 (1997).

Castelletto, V., Hamley, I., Yuan, X.-F., Kelarakis, A., and Booth, C., ‘‘Structure and rheology of aqueous micellar solutions and gels formed from an associative poly (oxybutylene)–poly (oxyethylene)–poly (oxybutylene) triblock copolymer,’’ Soft Matter 1, 138-145 (2005).

Charbonneau, C., Lima, M. M. D. S., Chassenieux, C., Colombani, O., and Nicolai, T., ‘‘Structure of pH sensitive self-assembled amphiphilic di-and triblock copolyelectrolytes: micelles, aggregates and transient networks,’’ Physical Chemistry Chemical Physics 15, 3955-3964 (2013).

Clement, F., Johner, A., Joanny, J.-F., and Semenov, A., ‘‘Stress relaxation in telechelic gels. 1. Sticker extraction,’’ Macromolecules 33, 6148-6158 (2000).

Courty, S., Gornall, J. L., and Terentjev, E. M., ‘‘Mechanically induced helix-coil transition in biopolymer networks,’’ Biophysical journal 90, 1019-1027 (2006).

Creton, C., Hu, G., Deplace, F., Morgret, L., and Shull, K. R., ‘‘Large-strain mechanical behavior of model block copolymer adhesives,’’ Macromolecules 42, 7605-7615 (2009).

Das, S., and Das, D., ‘‘Rational design of peptide-based smart hydrogels for therapeutic applications,’’ Frontiers in Chemistry 9 (2021).

Davidson, B., and Fasman, G. D., ‘‘The conformational transitions of uncharged poly-L-lysine. α helix-random coil-β structure,’’ Biochemistry 6, 1616-1629 (1967).

De Silva, C. C., Leophairatana, P., Ohkuma, T., Koberstein, J. T., Kremer, K., and Mukherji, D., ‘‘Sequence transferable coarse-grained model of amphiphilic copolymers,’’ The Journal of Chemical Physics 147, 064904 (2017).

Dinsmore, A., and Weitz, D., ‘‘Direct imaging of three-dimensional structure and topology of colloidal gels,’’ Journal of Physics: Condensed Matter 14, 7581 (2002).

Edera, P., Brizioli, M., Zanchetta, G., Petekidis, G., Giavazzi, F., and Cerbino, R., ‘‘Deformation profiles and microscopic dynamics of complex fluids during oscillatory shear experiments,’’ Soft Matter 17, 8553-8566 (2021).

Ghélis, C., *Protein folding* (Academic Press, 2012).

Giavazzi, F., and Cerbino, R., ‘‘Digital Fourier microscopy for soft matter dynamics,’’ Journal of Optics 16, 083001 (2014).

Gillam, J., and MacPhee, C., ‘‘Modelling amyloid fibril formation kinetics: mechanisms of nucleation and growth,’’ Journal of Physics: Condensed Matter 25, 373101 (2013).

Green, M. S., and Tobolsky, A. V., ‘‘A new approach to the theory of relaxing polymeric media,’’ The Journal of chemical physics 14, 80-92 (1946).

Guvendiren, M., Lu, H. D., and Burdick, J. A., ‘‘Shear-thinning hydrogels for biomedical applications,’’ Soft matter 8, 260-272 (2012).

Hamley, I. W., Daniel, C., Mingvanish, W., Mai, S.-M., Booth, C., Messe, L., and Ryan, A. J., ‘‘From hard spheres to soft spheres: the effect of copolymer composition on the structure of micellar cubic phases formed by diblock copolymers in aqueous solution,’’ Langmuir 16, 2508-2514 (2000).

Hammouda, B., ‘‘Analysis of the Beaucage model,’’ Journal of Applied Crystallography 43, 1474-1478 (2010).

Hugouvieux, V., Axelos, M. A., and Kolb, M., ‘‘Micelle formation, gelation and phase separation of amphiphilic multiblock copolymers,’’ Soft Matter 7, 2580-2591 (2011).

Huysecom, A.-S., Thielemans, W., Moldenaers, P., and Cardinaels, R., ‘‘A generalized mechano-statistical transient network model for unravelling the network topology and elasticity of hydrophobically associating multiblock copolymers in aqueous solutions,’’ Macromolecules (2023).

Hyun, K., Kim, S. H., Ahn, K. H., and Lee, S. J., ‘‘Large amplitude oscillatory shear as a way to classify the complex fluids,’’ Journal of Non-Newtonian Fluid Mechanics 107, 51-65 (2002).

Hyun, K., Wilhelm, M., Klein, C. O., Cho, K. S., Nam, J. G., Ahn, K. H., Lee, S. J., Ewoldt, R. H., and McKinley, G. H., ‘‘A review of nonlinear oscillatory shear tests: Analysis and application of large amplitude oscillatory shear (LAOS),’’ Progress in Polymer Science 36, 1697-1753 (2011).

Ianniruberto, G., and Marrucci, G., ‘‘Convective constraint release (CCR) revisited,’’ Journal of Rheology 58, 89-102 (2014).

Ianniruberto, G., and Marrucci, G., ‘‘New interpretation of shear thickening in telechelic associating polymers,’’ Macromolecules 48, 5439-5449 (2015).

Israelachvili, J. N., *Intermolecular and surface forces* (Academic press, 2011).

Janmey, P. A., Winer, J. P., and Weisel, J. W., ‘‘Fibrin gels and their clinical and bioengineering applications,’’ Journal of the Royal Society Interface 6, 1-10 (2009).

Karayianni, M., and Pispas, S., ‘ ‘Block copolymer solution self‐assembly: Recent advances, emerging trends, and applications,’’ Journal of Polymer Science 59, 1874-1898 (2021).

Khalatur, P. G., Khokhlov, A. R., Kovalenko, J. N., and Mologin, D. A., ‘‘Molecular dynamics study of the solution of semiflexible telechelic polymer chains with strongly associating end-groups,’’ The Journal of chemical physics 110, 6039-6049 (1999).

Kinning, D. J., and Thomas, E. L., ‘‘Hard-sphere interactions between spherical domains in diblock copolymers,’’ Macromolecules 17, 1712-1718 (1984).

Koga, T., Tanaka, F., and Kaneda, I., “Stress growth in transient polymer networks under startup shear flow.” *Gels: Structures, Properties, and Functions* (Springer, 2009).

Kohlbrecher, J., and Wagner, W., ‘‘The new SANS instrument at the Swiss spallation source SINQ,’’ Journal of applied crystallography 33, 804-806 (2000).

Li, Z., and Deming, T. J., ‘‘Tunable hydrogel morphology via self-assembly of amphiphilic pentablock copolypeptides,’’ Soft Matter 6, 2546-2551 (2010).

Löwik, D. W., and van Hest, J. C., ‘‘Peptide based amphiphiles,’’ Chemical Society Reviews 33, 234-245 (2004).

Mackay, M. E., Dao, T. T., Tuteja, A., Ho, D. L., Van Horn, B., Kim, H.-C., and Hawker, C. J., ‘‘Nanoscale effects leading to non-Einstein-like decrease in viscosity,’’ Nature materials 2, 762-766 (2003).

MacKintosh, F., Käs, J., and Janmey, P., ‘‘Elasticity of semiflexible biopolymer networks,’’ Physical review letters 75, 4425 (1995).

Mahinroosta, M., Farsangi, Z. J., Allahverdi, A., and Shakoori, Z., ‘‘Hydrogels as intelligent materials: A brief review of synthesis, properties and applications,’’ Materials Today Chemistry 8, 42-55 (2018).

Maibaum, L., Dinner, A. R., and Chandler, D., ‘‘Micelle formation and the hydrophobic effect,’’ The Journal of Physical Chemistry B 108, 6778-6781 (2004).

Mart, R. J., Osborne, R. D., Stevens, M. M., and Ulijn, R. V., ‘‘Peptide-based stimuli-responsive biomaterials,’’ Soft Matter 2, 822-835 (2006).

Mewis, J., and De Bleyser, R., ‘‘Dynamic behavior of thixotropic systems,’’ Journal of Colloid and Interface Science 40, 360-369 (1972).

Mortensen, K., ‘‘Phase behaviour of poly (ethylene oxide)-poly (propylene oxide)-poly (ethylene oxide) triblock-copolymer dissolved in water,’’ EPL (Europhysics Letters) 19, 599 (1992).

Mortensen, K., Brown, W., and Nordén, B., ‘‘Inverse melting transition and evidence of three-dimensional cubatic structure in a block-copolymer micellar system,’’ Physical review letters 68, 2340 (1992).

Mortensen, K., and Pedersen, J. S., ‘‘Structural study on the micelle formation of poly (ethylene oxide)-poly (propylene oxide)-poly (ethylene oxide) triblock copolymer in aqueous solution,’’ Macromolecules 26, 805-812 (1993).

Motte, S., and Kaufman, L. J., ‘‘Strain stiffening in collagen I networks,’’ Biopolymers 99, 35-46 (2013).

Murphy, R. M., ‘‘Kinetics of amyloid formation and membrane interaction with amyloidogenic proteins,’’ Biochimica et Biophysica Acta (BBA)-Biomembranes 1768, 1923-1934 (2007).

Ng, W., Tam, K., and Jenkins, R., ‘‘Lifetime and network relaxation time of a HEUR-C20 associative polymer system,’’ Journal of Rheology 44, 137-147 (2000).

Onck, P., Koeman, T., Van Dillen, T., and van der Giessen, E., ‘‘Alternative explanation of stiffening in cross-linked semiflexible networks,’’ Physical review letters 95, 178102 (2005).

Ozbas, B., Rajagopal, K., Schneider, J. P., and Pochan, D. J., ‘‘Semiflexible chain networks formed via self-assembly of β-hairpin molecules,’’ Physical review letters 93, 268106 (2004).

Pellens, L., Gamez Corrales, R., and Mewis, J., ‘‘General nonlinear rheological behavior of associative polymers,’’ Journal of rheology 48, 379-393 (2004).

Pellet, C., and Cloitre, M., ‘‘The glass and jamming transitions of soft polyelectrolyte microgel suspensions,’’ Soft matter 12, 3710-3720 (2016).

Price, D. L., Fu, L., Bermejo, F. J., Fernandez-Alonso, F., and Saboungi, M.-L., ‘‘Hydrogen/deuterium isotope effects in water and aqueous solutions of organic molecules and proteins,’’ Chemical Physics 424, 62-69 (2013).

Raghavan, S. R., and Khan, S. A., ‘‘Shear‐induced microstructural changes in flocculated suspensions of fumed silica,’’ Journal of rheology 39, 1311-1325 (1995).

Richbourg, N. R., and Peppas, N. A., ‘‘The swollen polymer network hypothesis: Quantitative models of hydrogel swelling, stiffness, and solute transport,’’ Progress in Polymer Science 105, 101243 (2020).

Rodriguez, L. M. D. L., Hemar, Y., Cornish, J., and Brimble, M. A., ‘‘Structure–mechanical property correlations of hydrogel forming β-sheet peptides,’’ Chemical society reviews 45, 4797-4824 (2016).

Rubinstein, M., and Colby, R. H., *Polymer physics Vol. 23* (Oxford University Press New York, 2003).

Rubinstein, M., and Semenov, A. N., ‘‘Thermoreversible gelation in solutions of associating polymers. 2. Linear dynamics,’’ Macromolecules 31, 1386-1397 (1998).

Semenov, A., Joanny, J.-F., and Khokhlov, A., ‘‘Associating polymers: equilibrium and linear viscoelasticity,’’ Macromolecules 28, 1066-1075 (1995).

Semenov, A. N., and Rubinstein, M., ‘‘Thermoreversible gelation in solutions of associative polymers. 1. Statics,’’ Macromolecules 31, 1373-1385 (1998).

Serero, Y., Jacobsen, V., Berret, J.-F., and May, R., ‘‘Evidence of nonlinear chain stretching in the rheology of transient networks,’’ Macromolecules 33, 1841-1847 (2000).

Sharma, I., and Pattanayek, S. K., ‘‘Effect of characteristics of shear force on secondary structures and viscosity of bovine serum albumin solution,’’ Rheologica Acta 57, 801-812 (2018).

Sis, M. J., and Webber, M. J., ‘‘Drug delivery with designed peptide assemblies,’’ Trends in Pharmacological Sciences 40, 747-762 (2019).

Skoulas, D., Mangiapia, G., Parisi, D., Kasimatis, M., Glynos, E., Stratikos, E., Vlassopoulos, D., Frielinghaus, H., and Iatrou, H., ‘‘Tunable Hydrogels with Improved Viscoelastic Properties from Hybrid Polypeptides,’’ Macromolecules 54, 10786-10800 (2021).

Soledad Lencina, M. M., Ko, C.-H., Jung, F. A., Schweins, R., Rikkou-Kalourkoti, M., Patrickios, C. S., Papadakis, C. M., and Tsitsilianis, C., ‘‘Effect of pH on the Dynamics and Structure of Thermoresponsive Telechelic Polyelectrolyte Networks: Impact on Hydrogel Injectability,’’ ACS Applied Polymer Materials 3, 819-829 (2021).

Stendahl, J. C., Rao, M. S., Guler, M. O., and Stupp, S. I., ‘‘Intermolecular forces in the self‐assembly of peptide amphiphile nanofibers,’’ Advanced Functional Materials 16, 499-508 (2006).

Storm, C., Pastore, J. J., MacKintosh, F. C., Lubensky, T. C., and Janmey, P. A., ‘‘Nonlinear elasticity in biological gels,’’ Nature 435, 191-194 (2005).

Tanford, C., ‘‘Thermodynamics of micelle formation: prediction of micelle size and size distribution,’’ Proceedings of the National Academy of Sciences 71, 1811-1815 (1974).

Tanford, C., *The hydrophobic effect: formation of micelles and biological membranes 2d ed* (J. Wiley., 1980).

Treloar, L. G., ‘‘The physics of rubber elasticity,’’ (1975).

Tripathi, A., Tam, K. C., and McKinley, G. H., ‘‘Rheology and dynamics of associative polymers in shear and extension: Theory and experiments,’’ Macromolecules 39, 1981-1999 (2006).

Van Ruymbeke, E., Vlassopoulos, D., Mierzwa, M., Pakula, T., Charalabidis, D., Pitsikalis, M., and Hadjichristidis, N., ‘‘Rheology and structure of entangled telechelic linear and star polyisoprene melts,’’ Macromolecules 43, 4401-4411 (2010).

Wang, H., Feng, Z., and Xu, B., ‘‘Assemblies of peptides in a complex environment and their applications,’’ Angewandte Chemie 131, 10532-10541 (2019).

Wang, S., and Larson, R. G., ‘‘Multiple relaxation modes in suspensions of colloidal particles bridged by telechelic polymers,’’ Journal of Rheology 62, 477-490 (2018).

Wang, S., and Urban, M. W., ‘‘Self-healing polymers,’’ Nature Reviews Materials 5, 562-583 (2020).

Wanka, G., Hoffmann, H., and Ulbricht, W., ‘‘Phase diagrams and aggregation behavior of poly (oxyethylene)-poly (oxypropylene)-poly (oxyethylene) triblock copolymers in aqueous solutions,’’ Macromolecules 27, 4145-4159 (1994).

Watanabe, H., Kanaya, T., and Takahashi, Y., ‘‘Equilibrium elasticity of diblock copolymer micellar lattice,’’ Macromolecules 34, 662-665 (2001).

Watanabe, H., and Kotaka, T., ‘‘Rheology of ternary mixtures of styrene‐butadiene diblock copolymer, homopolybutadiene, and n‐tetradecane,’’ Journal of Rheology 27, 223-240 (1983).

Webber, M. J., and Pashuck, E. T., ‘‘(Macro) molecular self-assembly for hydrogel drug delivery,’’ Advanced Drug Delivery Reviews 172, 275-295 (2021).

Winnik, M. A., and Yekta, A., ‘‘Associative polymers in aqueous solution,’’ Current opinion in colloid & interface science 2, 424-436 (1997).

Witten, T., and Pincus, P., ‘‘Colloid stabilization by long grafted polymers,’’ Macromolecules 19, 2509-2513 (1986).

Yang, S., Yu, X., Wang, L., Tu, Y., Zheng, J. X., Xu, J., Van Horn, R. M., and Cheng, S. Z., ‘‘Hydrogen-Bonding-Driven Complexation of Polystyrene-block-poly (ethylene oxide) Micelles with Poly (acrylic acid),’’ Macromolecules 43, 3018-3026 (2010).

Zhulina, E., and Borisov, O., ‘‘Theory of block polymer micelles: recent advances and current challenges,’’ Macromolecules 45, 4429-4440 (2012).

Chapter 4 : Rheological signatures of structural memories in bridged micellar hydrogels.

4.1 Basic Concepts and Motivation

It is established that "memory effects" correspond to a very broad type of behaviors (Keim *et al.* 2019) of soft materials. From a rheological perspective, specific rheometric protocols are utilized to "train" the sample by imposing a well-controlled deformation history. The aim is to imprint as well as, read or erase memories and this has been well accomplished in sheared suspensions (Corte *et al.* 2008, Schwen *et al.* 2020). Structural memory is the material's recollection of these past-time plastic deformations. Shear-strain profile (rate and direction) may encode in the constituent's relative position and shape, for instance in materials with deformable constituents such as soft spheres and micelles. Structural memory decays with time and it is completely erased when the equilibrium structure is attained via Brownian motion. Nevertheless, in glassy materials equilibration requires superficially long times (Hunter and Weeks 2012) whereas it is unattainable in jammed soft systems. In the previous chapter we addressed the role of the peptide based hydrogel (HG) as a drug carrier by examining its viscoelastic response to different environments. Here, we extend this study by focusing on macroscopic stress decay as a rheological signature of structural memory of a past-time nonlinear deformation. The work is motivated by the HG3b distinct idiosyncrasy: followed a nonlinear strain deformation, the resultant structural changes persist over long periods and this is reflected in the considerable time required for the macroscopic stresses to decay once flow is stopped. We refer to these macroscopic stresses, probed in rheometry, as residual stresses. The gel exhibits also thixotropic behavior that is related to structural memories, referred also as kinematic memories (Jamali and McKinley 2022). However how thixotropy and these residual stresses are connected remains unclear, and to the best of our knowledge this topic is not extensively discussed in the literature.

Once the gel is shear-melted and shear is stopped, there are two competing processes with relevant timescales, the structural recovery (τ_{rec}) and the stress decay time (τ_{dec}). The former depends on the ability of the material to reform its equilibrium network while the latter on the mobility of the microstructural entities at the shear-melted state. At the latter state the material is mechanically incoherent and the stress decay time is shorter than the quiescent state, structural relaxation time (Rathinaraj *et al.* 2022). It has been shown that in star-like micelles the stress decays as $\tau_{dec}(\dot{\gamma}) \propto \dot{\gamma}^{-0.8}$ (Jacob *et al.* 2019). Hence, on flow cessation and when the structural recovery is long enough ($\tau_{rec} >> \tau_{dec}$), flow

induced microscopic will relax quickly to negligible values. On the contrary, when (τ_{rec}<<τ_{dec}) microscopic stresses will be entrapped in the recovered solid-like microstructure thus the former relax slowly, as governed by the equilibrium structural relaxation time. In this case the entrapped stresses decay slowly or not at all (Mohan *et al.* 2015), a clear case of strong structural memory. These memories are "expressed" by the material's mechanical response (Di Dio *et al.* 2022), while when ignored they render the interpretation of rheological results ambiguous . This implication is crucial in protocols aiming to decouple recoverable and unrecoverable strain, such as the iteratively punctuated oscillatory tests (Donley *et al.* 2020). At the microscopic level, stress entrapment may take place in a rheometric experiment, where strain is rigorously controlled. In this case a study can relate the well-known history to the measurement. In a more complicated scenario, stress entrapment can be a consequence of uncontrolled strain history such as compression during loading on the rheometer, mixing, rapid temperature changes and even instabilities and secondary flows when sheared at elevated rates. Hence the annealing of the sample before any measurement commences, is essential.

The entrapping entities can be of various length scales (Withers 2007) such as molecular, cluster or fractured domain, and their distribution may change dramatically when stress localization events take place (Dhont *et al.* 2017, Larson 1992). When flow is stopped, constituents of sub-micron length scales will rearrange locally, augmented by thermal fluctuations. On the other hand, larger entities will rearrange, driven solely by these locally entrapped stresses. This predominantly dissipative process will release stresses locally but not uniformly. Following a local rearrangement (plastic) event and given sufficient elasticity, a shear wave will propagate in the material over long distances possibly triggering other localized rearrangements resulting in avalanche-like behavior. Likewise, relaxation at smaller scales triggers motion at larger scales (Speck 2019). In a fundamentally different but phenomenological similar process, the short-time dynamics of supercooled liquids becomes strongly heterogeneous, with large regions of the material being immobile while small pockets maintain local mobility hence the avalanche may result from the cooperative motion of small domains overtime. In this dynamic facilitation scenario, relaxation of different domains is not a parallel process (Palmer *et al.* 1984). In general, depending on the material, many regions may remain in a highly strained configuration for long times (Withers 2007), affecting its mechanical properties such as relaxation and fracture. Consequently, both processes depend on the sample history. The importance of understanding and quantifying internal stresses is now evident. Motivated by the non-vanishing residual stresses observed in the polypeptide hydrogel, we will deploy a series of nonlinear experiments to study the effect of strain history to the shear start-up response. We will also present a novel protocol to eliminate the directional biasing effects, i.e., the material's memory of the direction of the previous deformation. The results and analysis that will follow may be applied to further

understand the interplay of residual stresses and the mechanism of relaxation, and tailor the rheological response of similar structured materials.

Shear start-up is a common test to probe nonlinear response. The sample is suddenly subjected to a step-rate, a constant shear rate of certain duration, and the transient stress response, the so-called stress growth function, is monitored. A typical response of a yield stress fluid (Møller *et al.* 2006) is depicted in Fig. 4.1. It consists of the initial linear elastic region, the peak-stress (σ_p) which is the maximum value of the shear stress growth function (σ^+), and the stress at the plateau (σ_{st}) corresponding to the phenomenological steady state. The latter is a state where the macroscopic stress is steady over time, however this does not ensure steady or homogenous flow conditions in the rheometric gap. Very often stress localization will occur and this may or may not be detectable in the stress while steady-state is attained. Static yield stress is defined by the peak of stress growth function (peak-stress) while the peak-time (τ_p) corresponds to the peak- (yield) strain $\gamma_p = \tau_p \cdot \dot{\gamma}$.

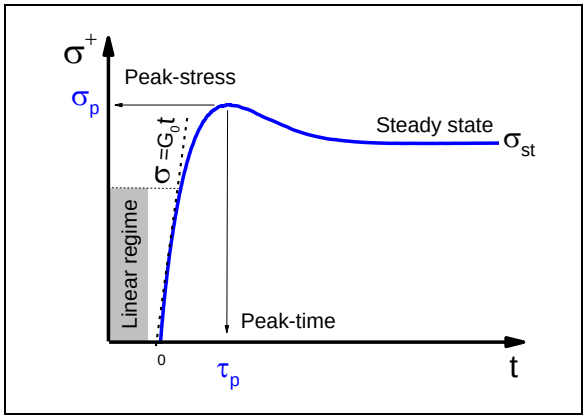

Fig. 4.1 Typical stress growth function of a yield stress fluid during a step-rate interval. Dashed line indicates the slope corresponding to elastic modulus G_0. Peak-stress and peak-time are shown.

We will refer to both stress growth function (σ^+) and stress decay function (σ^-) as stress and stress decay, respectively. Step-rate is a simple test with significant importance since it emulates flow conditions in many industrial applications. On the other hand, a step-rate interval may induce structural changes due to flow-structure coupling (Fielding and Olmsted 2004, Olmsted 2008, Vermant and Solomon 2005) that will affect the response of subsequent step-rate tests. The significance of flow-structure coupling in materials future response is evident in stress-controlled experiments where yield stress fluids exhibited viscosity bifurcation (Coussot *et al.* 2002). The resultant long- or short-lived structural memories of previous flows are attributed to structural anisotropy as reported in studies of dynamically arrested colloidal hard spheres with repulsive (Koumakis *et al.* 2016) and attractive interactions (Masschaele *et al.* 2009, Moghimi *et al.* 2017), as well as soft deformable microgel pastes (Khabaz *et al.* 2021), and are evidenced by scattering experiments under flow (Aime *et al.* 2018, Gordon

et al. 2021). Structural anisotropy is captured by the stress signal in shear step-rate or flow reversal experiments. When flow is resumed or reversed after a waiting time t_w, the directional memory is probed. Capturing and analyzing such signatures is challenging. The former requires that the structural changes due to flow take place at long enough times or more precisely, large enough strains that can be resolved in the stress response by the rheometer at the given probe shear-rate. The latter requires that deformation history is well controlled. It is not uncommon for transient shear-banded regions to form in the rheometric gap, followed by phenomenologically steady and homogeneous flow. The stress plateau that follows the overshoot does not guarantee the absence of steady-state shear bands observed in thixotropic materials (Coussot *et al.* 2002), and this hydrogel is thixotropic. Linking rheological data to structural information is challenging (Møller, Mewis and Bonn 2006), calling for system-tailored rheometric protocols and caution on the data analysis.

Data reproducibility requires at least all experiments to start with the sample at a state of the same structural memory while for other studies it is essential to start with all memories erased, i.e., from the equilibrium structure. This is trivially achieved in polymeric glasses or associating polymers by thermally annealing the sample before each test. In such a case all entrapped microscopic stresses are relaxed and very often equilibration is attained in reasonable times. On the contrary, equilibration is a major challenge for samples where temperature melting is not possible. Shear melting is a mechanical alternative way to erase strain history in particulate glasses or polymeric gels such as the present hydrogels. It is accomplished by the application of steady shear at an elevated rate, compared to the inverse structural relaxation time, rates (Divoux *et al.* 2011). A 2nd alternative is the application of large amplitude oscillations of time decaying strain amplitude. The assumption is that shear will break-down all entities such as clusters or, in general, completely fluidize the material, allowing all entrapped stresses to quickly relax. This approach was shown to be effective in cases where LAOS of constant amplitude failed (Keim and Medina 2022), however it is not universal. Concerns regarding the initial state and how it compares to that after the sample has aged for considerable time (Gordon *et al.* 2021) arise. Elevated shear rates may lead to stress localization causing typical shear banding or fracture in domains. Strain history is not well-controlled along with it the entrapment of microscopic stresses and the imprintement of structural memories. These shear-induced heterogeneities do not conform to the targeted mechanically annealed microstructure, therefore the pre-shear protocol should be tested thoroughly and adjusted (tailored) to the sample under investigation.

Given the structural complexity of the present hydrogel simpler analogues will need to be examined for comparison. Firstly, block copolymers and telechelic polymers in aqueous solution, that form bridged flowerlike micelles in the spirit of the previous chapter should be considered. Secondly, soft colloidal suspension may provide insight. Indeed, the rheological properties of bridged micellar solutions

reflect both the colloidal nature of micelles and the dynamics of transient networks (Pham *et al.* 1999). On the other hand, the phenomenology of the jammed microgel suspensions exhibits a few vital similarities with our HGs (Khabaz, Di Dio, Cloitre and Bonnecaze 2021). The latter reach a shear thinning exponent of -0.85 as seen in Fig. 4.2(a) for the microgel with the highest concentration of 55mg/g. This is similar with the shear thinning exponent of the strong hydrogels HGa, b that exhibits larger viscosity by about two decades for the same shear rate. Another similarity is the long structural relaxation time (outside the experimental window) and the persistent residual stresses that decay only after long times of $\approx 10^4$ s upon flow cessation. This behavior has been observed also in hard spheres glasses (Ballauff *et al.* 2013), but in this case the yielding phenomenology is very different from the soft microgels. As the concentration of microgel suspensions increase, an increase in stress overshoot is observed during shear start-up, whereas for hard spheres glasses the overshoot disappears at large φ due to decreased free volume.(Koumakis *et al.* 2016).

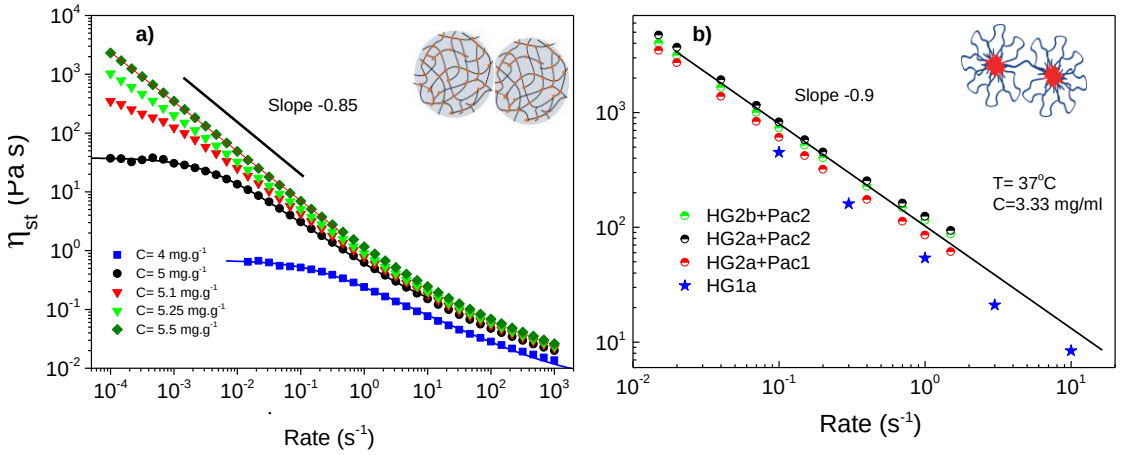

Fig. 4.2 Comparison of shear thinning behavior for a) dense microgel suspension. Data taken from (Di Dio *et al.* 2022) b) HGa and HGb with and without drug (Paclitaxel). Blue stars denote measurement performed with MCR502 in ESPCI Paris with roughened cone- plate geometry.

4.2 Signatures of entrapped stresses in small amplitude oscillatory shear and relaxation experiments.

In Chapter 3, we reported HG3b and HG3c yielding behavior based on oscillatory shear experiments, the DSS test. When the strain amplitude is increased during the test, the material response becomes nonlinear and strain history becomes quite complex. A rigorous data interpretation requires specific methodologies by considering higher order even harmonics (Ewoldt *et al.* 2008), in addition to the base frequency considered in conventional DFS. During these nonlinear amplitude oscillations,

stresses are entrapped and this can be tested. After a long period at rest, MCR 702 was commanded by tabulated data to impose 5 strain oscillations of 0.8 amplitude, acting as a nonlinear pre-shear, followed by a 7 cycles of linear strain amplitude 0.03. The former is as LAOS and the latter a SAOS (DTS) test, both at the frequency of 1Hz. The commanded strain waveform (blue) and the logged by the instrument's optical encoder (black) are identical Fig. 4.3(a). The abscissa corresponds to the digitized sample index equivalent to 1/60 s time step, given the sampling frequency F_s=60Hz. The sinusoidal stress response was logged only for the linear oscillations depicted by the red curve in Fig. 4.3(b), i.e., sample index Nr ≥ 300, the point where the linear probing started. Clearly, the mean value of the stress response is nonzero an analogue to the presence of a decaying "DC component" term borrowed from electrical engineering. The decaying stress in Fig. 4.3(b), referred as residual stress in experiments, is on the order of 70 Pa. This quantity reflects the global average of the entrapped microscopic stresses in 1,2 direction (see definition in Chapter1) of the whole sample. Whether the origin is the strain history of LAOS cycles or previous deformations, the message remains the same: LAOS cycles with a strain amplitude 4 times larger than the yield strain (see Chapter 3) did not manage to erase the mechanical memory of the system in agreement with (Keim and Medina 2022).

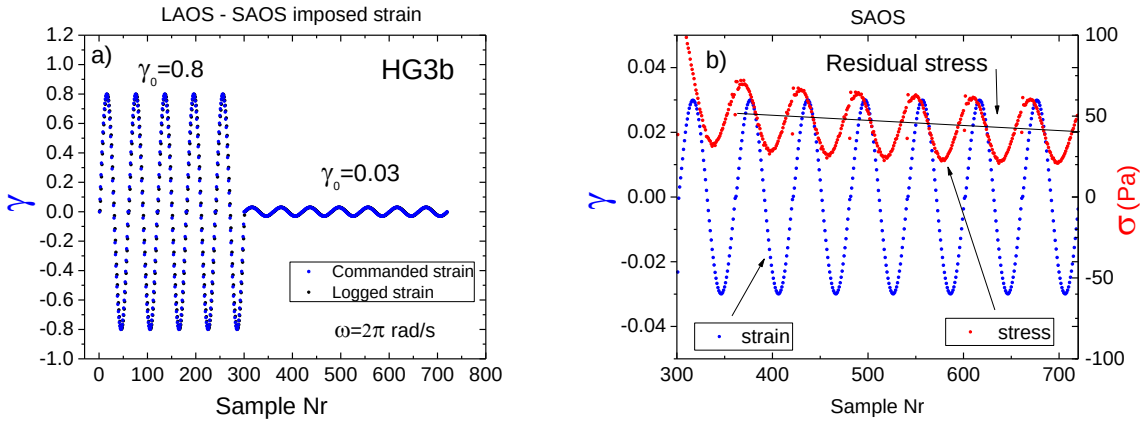

Fig. 4.3 DTS experiment after LAOS preshear for HG3b at T=25°C; a) the imposed excitation (strain) waveform plotted as a function of digital sample number: 5 LAOS and 7 SAOS cycles at 1Hz b) stress response (red) for SAOS cycles. The coresponding strain from (a) is also shown (blue) for reference. Stress signal phase angle advances over strain as expected for a viscoelastic material.

We note another important aspect. The DC offset will not affect LVE measurements as the rheometer evaluates only the phase and amplitude of the oscillation of the base frequency via Fast Fourier Transformation (see Chapters 1 and 5), while any low-frequency component is completely rejected by the high pass filtering. This explains why the measurement of LVE is insensitive to the presence of residual stresses, consistent with findings in Chapter 3.

The decay of residual stress followed a step-rate is commonly monitored by setting shear-rate to $0s^{-1}$. As evidenced in Fig. 4.4(a) by the green curve corresponding to pre-shear rate of 1 s^{-1} , the stress decay is long, sustaining values of 11Pa even after 30ks (green star). There is an indication of two-step relaxation similar to an observed in dense microgel suspensions (Mohan *et al.* 2015). For preshear rates of 1, 3 and 6 s^{-1}, the stress fluctuates in a similar pattern at long times. We hypothesize three possible origins; i) first, cascading plastic rearrangements triggered and sustained by entrapped stresses, in analogy to avalanche-like behavior (Denisov *et al.* 2016) observed in yield stress fluids in stress-controlled experiments (Coussot *et al.* 2002) and modeling (Kamani *et al.* 2021). This mechanism implies that the material rearranges locally at weak regions, which are elastically coupled to each other, resulting in highly correlated slip avalanches. Similar kinks in stress curve have been observed in high volume fraction (φ=0.63) hard sphere glasses (Jacob *et al.* 2019), supporting the universality of this behavior to highly packed systems. Interestingly, avalanches mediate crystallization in a hard-sphere glasses (Sanz *et al.* 2014). MD simulations revealed that particles that exhibit in-cage rattling at early times, exhibit large-scale rearrangements before they crystalize. In analogy, micelles can also crystalize under certain conditions (Mortensen 1992); ii) slippage between fractured domains; iii) coupling of stress with instrument's inertia. The latter is less likely to occur at long times. Pre-shear rates of 15 and $30s^{-1}$ were also applied, and a decrease of entrapped stresses with increasing rate was observed, similarly to the behavior of microgels (Fig. 4.4(b)). However, we should interpret these data with caution, since during the pre-shear step the stress did not attend steady-state possibly due to instabilities, hence the flow field was not well-controlled.

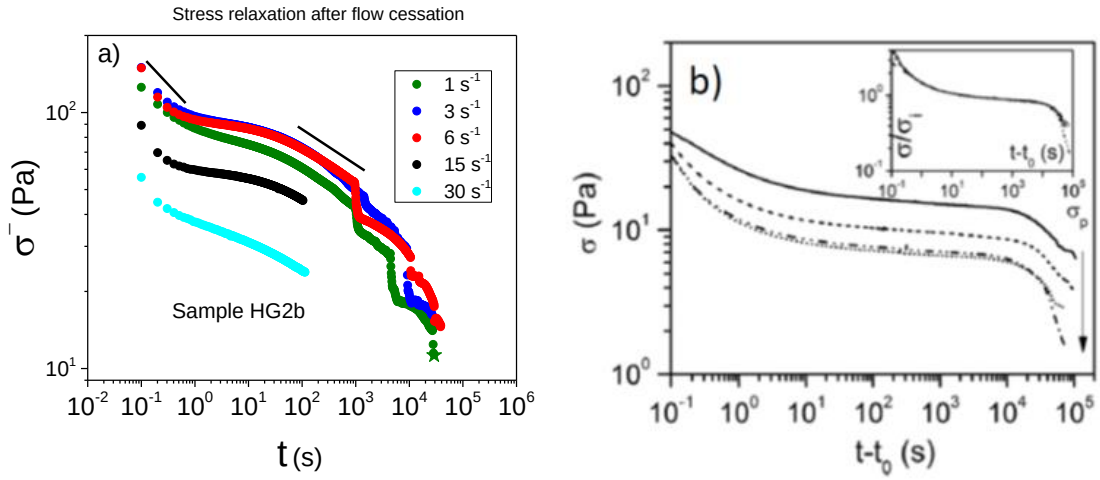

Fig. 4.4 a) Stress decay after cessation of flow at three shear rates. Sample is HG2b with concentration 33.3 mg/ml and pH6.5 at 25°C. Black lines indicate two distinct slopes (regimes) at short and intermediate times. b) Effect of preshear on the two-step relaxation for a microgel suspension. Preshear stresses increase from top to bottom: 62 (solid line), 148 ,250 and 350 Pa from (Mohan, Cloitre and Bonnecaze 2015) . Microgel has particle volume fraction φ=0.8 and comparable to hydrogel concentration of 20 mg/g.

4.3 Thixotropic behavior

Thixotropy is defined as the "continuous decrease of apparent viscosity with time under shear and the subsequent recovery of viscosity when the flow is discontinued" (Mewis 1979). The underlying physical mechanism is the shear-induced break-up of microstructure or bonds. Indeed, thixotropic behavior is expected in yield stress fluids where microstructure is sensitive to strain history, and its networking breaks-down with shear and builds-up upon flow cessation due to attractions, in our case physical crosslinks and Brownian motion. This is described by structural-kinetic models where a scalar parameter λ varies from 0 to 1 corresponding to a completely broken-down (mechanical incoherent) or re-covered microstructure (Larson and Wei 2019), respectively. This is in-line with the notion of rate dependent stress decay time (τ_{dec}) discussed above. Thixotropic behavior is mainly related to viscous processes and is often characterized in steady shear experiments. Given the rheometer's finite time resolution, the time scales of structural break-down and recover are really critical as they define the feasibility of capturing the thixotropic response. Thixotropic materials may also be viscoelastic (Sharma *et al.* 2023), like HGb, therefore the two behaviors need to be decoupled and this can be done mainly by two set of experiments, rate-loops and rate step–down (Mewis and Wagner 2009). In the former experiment, known as thixotropic loop, shear rate is ramped-up to a maximum value and then ramped-down in discrete steps. Two time scales govern this experiment the inverse of each rate applied and the time step Δt that the instrument "spends" at each rate before logging the stress value. As these two parameters are coupled, quantitative predictions are tricky, yet feasible when the area formed by the hysteresis loop is evaluated (Divoux *et al.* 2013). Hence we will discuss the results only qualitatively. The stress path in Fig. 4.5(a) is different when the strain history refers to lower rates (ramp-up) and higher rates (ramp-down). This is the so-called stress hysteresis which is typical signature of the thixotropic behavior. Hysteresis is a memory effect (Jamali and McKinley 2022) as the different histories (lower and higher rate than the tested) lead to different response at the given Δt. At this point it will suffice to conclude that the strong HG3b is clearly a thixotropic material. To quantify the structural rebuild time a rate step-down experiment is utilized. Steady shear is applied at a moderate rate ($1.2s^{-1}$) until steady-state is reached. This may be considered as a strain "history-making" interval. Despite the steady-state response we can't claim that all memories are erased. A probing interval follows where the rate is reduced abruptly. The response to rate reduction exhibits an undershoot as shown in Fig. 4.5(b) relating to the transition of microstructure from the previous quasi-equilibrium steady state at $1.2s^{-1}$ to the current at $0.05s^{-1}$. These two states reflect the competition between structural break-down and recovery at the two rates of 1.2 and $0.05s^{-1}$. The duration of the undershoot suggests structural recovery time, $\tau_{rec\_max} \approx 8s$.

This is in agreement with the recovery time probed by oscillatory shear (DTS) in Chapter 3. A link to structural insights from chapter 3 is now warranted.

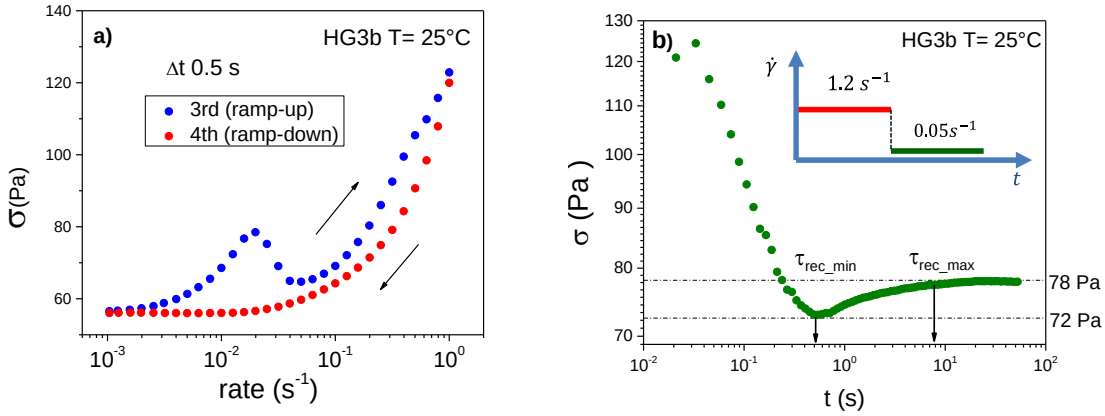

Fig. 4.5 a) Thixotropic loop for HG3b with Δt=0.5s. Legend indicates the sequence of intervals. b) Stress response to rate down-step rate from 1.2 to 0.05s^{-1}. The inset shows the complete shear history. Green indicates the second interval where stress is monitored. Arrows point to restructuring times (onset and complete recover). The sample was left at rest for 12h before the experiment.

Concluding remark 1: Entrapped stress are relaxed mainly by two major processes in analogy, but not identical to jammed microgel suspensions (Mohan *et al* 2015): i) break-down of bridges that start to rebuild upon cessation of flow. It seems that the elastically active segments reach their equilibrium density in 8 s. This restores the elasticity of the network quite fast ii) the slower creeping relaxation of dislocated micelles. This should persist until all entrapped stresses are relaxed via cooperative local rearrangements. Bridging restricts this relaxation hence the entrapped stress decay is long. These two contributions are convoluted to the decaying stress which is history-dependent, in analogy to aging.

4.4 Structural memory rheological signatures in start-up shear

Motivated by these findings we performed a series of tests based on step-rate experiment and stress relaxation upon flow secession for the strong HG3b with pH 6.5 comprising the main study in this chapter. We also compare with the weaker and less brittle (see Chapter 3) HG3c with pH5 for reference. HG3b was tested at T= 25 and 37°C, where subtle differences exist in the amplitude of the response, hence temperature dependence will not be discussed. HG3c was tested at T= 15 and 25°C where significant changes occur in LVE response. The stress response to a sequence of 11 step-rates intervals of increasing rates is plotted as a function of the accumulated strain in Fig. 4.6. Each step-rate was preceded by 2h waiting time (t_w) where shear rate was set to 0s^{-1}. There are two unusual observations regarding the first two step intervals at the lowest rates of 0.015 and 0.02 s^{-1}: i) their response in the linear regime

(shaded area), seem to deviate from the response exhibited by the higher rates. The slope of σ(t) indicates a modulus of 500 Pa equal to the linear value at 10 rad/s; ii) in step-rate 2 the rate is increased by 33% compared to step-rate 1, but the peak-stress (overshoot) is very similar. This is the opposite trend exhibited by the step-rate intervals at higher rates that followed and in agreement to similar experiments with microgels (Di Dio *et al.* 2022). iii) the peak-strain dependence on accumulated strain is not monotonic. A major reason for these discrepancies is the internal stresses and microstructural changes that have not fully relax and recover respectively, in the inadequately long, 2h waiting time between step intervals. Apart from the first step at $0.015s^{-1}$ stress response does not extrapolate to the origin of the axis. As we shall see this behavior renders the measurement inconsistent and this must be addressed.

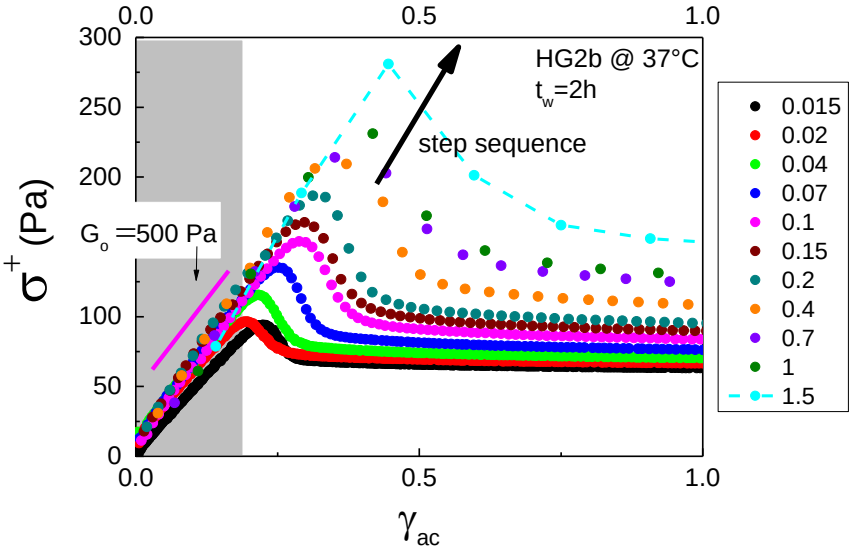

Fig. 4.6 Shear stress response for a series of step-rates of increasing rate plotted as a function of accumulated strain in linear scale. Shaded area marks the linear regime. Magenta line indicates the slope of the linear part of magenta curve of rate $0.1s^{-}$. Black arrow indicates the time sequence of step-rate intervals.

A difficulty to interpret results arises as the response of a step-rate interval is affected by the previous intervals even after 2h waiting time. Modeling suggests that in amorphous materials, when shear is stopped after steady state stress is reached and resumed after a waiting time t_w, the peak-stress becomes smaller in the second step-rate interval while the peak-time (see Fig. 4.1) advances, i.e., shifts to earlier times (Barlow *et al.* 2020). Stress overshoot is known to be sensitive to preshear history in experiments of repeated step-rate intervals in many microstructured materials such as colloidal attractive glasses (Moghimi *et al.* 2017), jammed suspensions of microgels (Di Dio *et al.* 2022), but also entangled solutions of linear polymers (Ianniruberto and Marrucci 2014, Robertson *et al.* 2004, Stratton and Butcher 1973) when the waiting time between intervals is not sufficiently long to facilitate complete structural recovery. Let us compare now with linear entangled polymers, which are relative simple in the sense that the physical network is due to entanglement. Pioneered by Butcher and Stratton a series of start-up and

stop shear flows experiment was introduced for entangled linear polymeric solutions (Stratton and Butcher 1973). The observed peak-stress reduction with decreasing t_w is controlled by the competition of the degree of chain orientation and partial annihilation of entanglements due to convection - the latter process being affected by the former - (Baig *et al.* 2010, Ianniruberto and Marrucci 2014) with, the microstructural recovery rate upon flow cessation. This peak-stress reduction is evident, in experiments with linear entangled melts, for t_w significantly longer than the terminal relaxation time and even longer than the time needed for G(t) to almost completely relax (Roy and Roland 2013). This suggests that chains need more time to attain their equilibrium state than the time it takes for stresses to relax after linear perturbations from equilibrated samples. In other words nonlinear strain history fades away slower than the time it takes for macroscopic stresses to relax. The underlying mechanism of this fading structural memory (Rubinstein and Obukhov 1993) is an active topic even for well-studied and well-modeled systems such as linear polymers (Galvani Cunha *et al.* 2022). The important message is: structural anisotropy imposed by the preceding step-rate interval results in reduction of peak-stress of the following intervals. Ironically, nonlinear deformation imprints these structural memories and on the same time nonlinear rheometry provides a sensitive tool to measure them. Interestingly, a strain history sensitive overshot was also observed in unentangled melts at rates promoting chain stretching (Santangelo and Roland 2001), however, in this case the reference overshoot, i.e., when starting from equilibrium structure, was recovered for t_w on the order of the Rouse time, the characteristic time of chain stretching. The nonlinear response of entangled chains is currently under intensive investigation (Ianniello and Costanzo 2022, Watanabe *et al.* 2021).

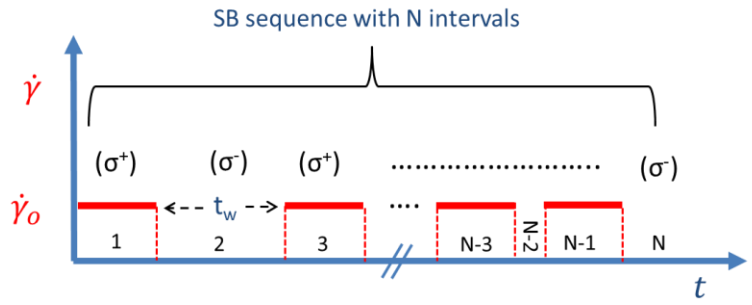

Figure 4.7 The applied shear-rate profile at SB protocol with N intervals. Red line indicates the imposed shear rate (γ_0) at constant duration. Step-rate intervals are odd-numbered while stress decay intervals are even-numbered. The duration of latter is the waiting time t_w. Brackets indicate the parameter that is monitored.

Here we adopt the Stratton –Butcher (SB) protocol for our hydrogel. The sequence of the applied shear-rates profile is depicted in Figure 4.7. We utilize a sequence of 12 step-rate intervals (1, 3, 5,…11), each followed by a relaxation interval (2, 4, 6,…N=24). After each step-rate interval, the flow was stopped by commanding the rheometer (MCR501) to set $\dot{\gamma} = 0\ s^{-1}$ for decreasing values of t_w, as

indicated in the legend of each figure. We initially discuss generic observations with a reference to Fig. 4.8 where only step-rate intervals, 1, 7, 9, 11 and the corresponding relaxation intervals, 2, 8, 10, 12 are depicted for clarity and simplicity. For each interval the stress growth function (σ^+) or the stress decay (σ^-) is depicted in Fig. 4.8(a) or Fig. 4.8(b), respectively. The red curve (1st interval) that corresponds to step-rate after a rest time of 6h exhibits a peak at τ_p=0.5s. At the 7th interval the peak-stress is smaller (the HG is weakened) and peak-time shifted to earlier times hence, implying that shear history facilitates yielding at smaller strain (γ_p). We argue that the γ_p reduction and the narrowing of the overshoot imply increased brittleness. We can also extend the argument that repetitive step-rates impose phenomenology similar to fatigue in metals however with the fundamental difference that the HG has the ability to self-recover the fatigue (Bai *et al.* 2018) when given enough time. Linear response (regime I) exhibits the same slope in all steps-rate intervals of 850 Pa consistent with the G´=808 Pa obtained from small amplitude oscillatory shear at 1 rad/s in Chapter 3. This validates the homogeneous flow at this rate for the region I and most importantly proves the insensitivity of LVE spectra to strain history, as discussed in Chapter 3. On the other hand, the linear elastic limit of 50% strain ($\tau_p\dot{\gamma} = 0.5$ strain units) of the 1st interval decreases with decreasing t_w resulting in a decrease of the modulus of resilience (Beer *et al.* 2015). In DSS the departure from linearity is exhibited at only around 10% strain.

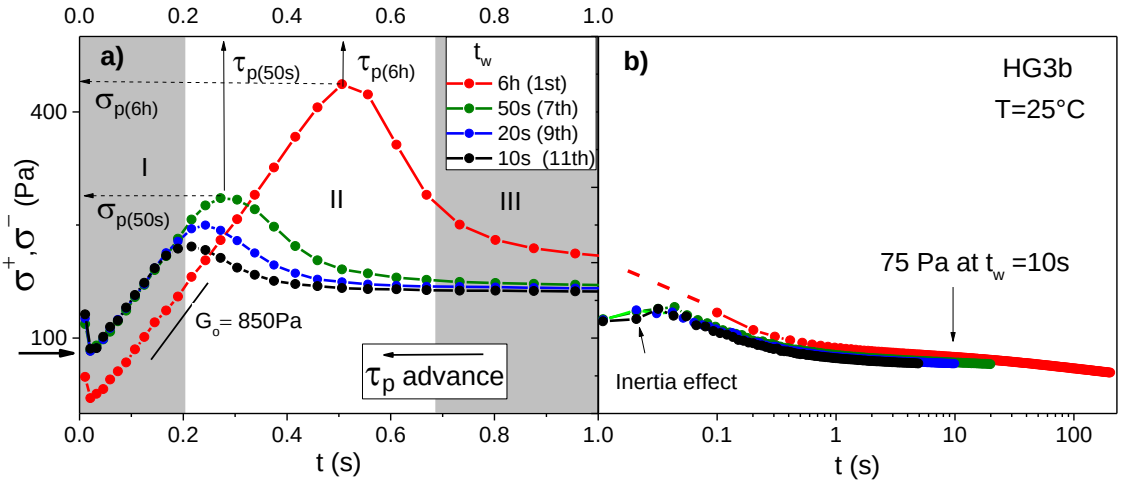

Fig. 4.8 The SB protocol consisting of a sequence of alternating step-rates and relaxation intervals a) stress grown function during 4 out of 12 shear start-up intervals. Areas I, II and III correspond to the linear, yielding and steady state regime. b) stress decay (σ^-) upon flow cessation. Dashed red line is a guide. Only 4 out of 12 step-rate intervals (1, 7, 9, 11) and their corresponding relaxation intervals are shown for clarity. Waiting times are indicated in the legend. Arrow indicates residual stresses from previews intervals. Note lin-log scale.

Although these values are not fairly comparable, we can ascribe the 5 times lower elastic limit in DSS to the cycling deformation history (fatigue) in line with the argument of increased brittleness. This show the fundamental difference between the yield strain obtained by DSS and step-rate experiments as

the memories of the material at the onset of yielding are different. In contrast to the red curve that extrapolates to the origin of the axes (coordinates 0,0) the linear responses of all other curves are shifted vertically by a value of ~70Pa indicated by the arrow. This is comparable to the residual stress of 75 Pa probed 10s after flow cessation, indicated by the arrow Fig. 4.8(b). Clearly, the measurements of internal stresses are consistent. If we consider the peak-stress as the static yield stress, then we remark that the ability of the material to store energy, known as toughness in mechanics of solids, is greatly reduced by this shear history.

Concluding remark 2: the overshoot in SB step-rate intervals is very sensitive to previous deformations. Peak-time is considerably shifted to earlier times (advanced) and peak-stress to lower values as t_w is decreased. In contrast, LVE is not sensitive to deformation history but the elastic limit, the strain required to depart from linear regime, is greatly reduced with t_w decrease. This resembles the phenomenology of fatigue. The yield strain extracted from DSS and step-rate (static) experiments refer to different histories therefore should be compared with caution in materials with long-lived structural memories.

To further analyze this behavior, a full sequence of start-up and stop shear runs, in the context of the SB protocol is depicted in Fig. 4.9 at two different shear rates. There is a σ_p and τ_p decrease with decreasing t_w for both imposed shear rates. Remarkably, the peak is eliminated for t_w,< 0.5s. This suggests the possibility to identify the onset of structural reform. At shorter waiting times, the material remains macroscopically in a "mechanically incoherent" state. Internal stresses are completely unrelaxed as suggested by the nearly flat response for $t_w \leq 0.5$s marking the maximum waiting time before the stress overshoot appears. From hydrogels HG3b thixotropic behavior in Fig. 4.5(b) we deduced the onset of structural recovery to be $\tau_{rec_min} \sim 0.5$s. This is in agreement with the maximum waiting time before the stress overshoot appears in Fig. 4.9. By considering these findings and the structural recovery studied by DTS in Chapter 3, it becomes clear that the network starts to reform at $\tau_{rec_min} \sim 0.5$s and acquires its nominal junction density at $\tau_{rec_max} \sim 8$s. However, the nonlinear mechanical response, hence quiescent state microstructure, is restored only after many hours. This is in analogy with linear entangled polymers where stress overshoot is restored at times longer than the G(t) relaxation (Roy and Roland 2013). Hence long lived structural memories are only probed by nonlinear rheometry in both systems. Concluding remark 3: Network density starts to reform at 0.5s and reach its saturation value at 8s. This is why elasticity (G´) acquires its nominal values at 8s in the DTS test performed immediately after yielding (see Chapter 3). Most importantly, the structural memories persist considerably longer for times (up to 12h) and this signature is only present in step-rate experiment. This long-lived memory decays via the process (ii) in Concluding remark 1.

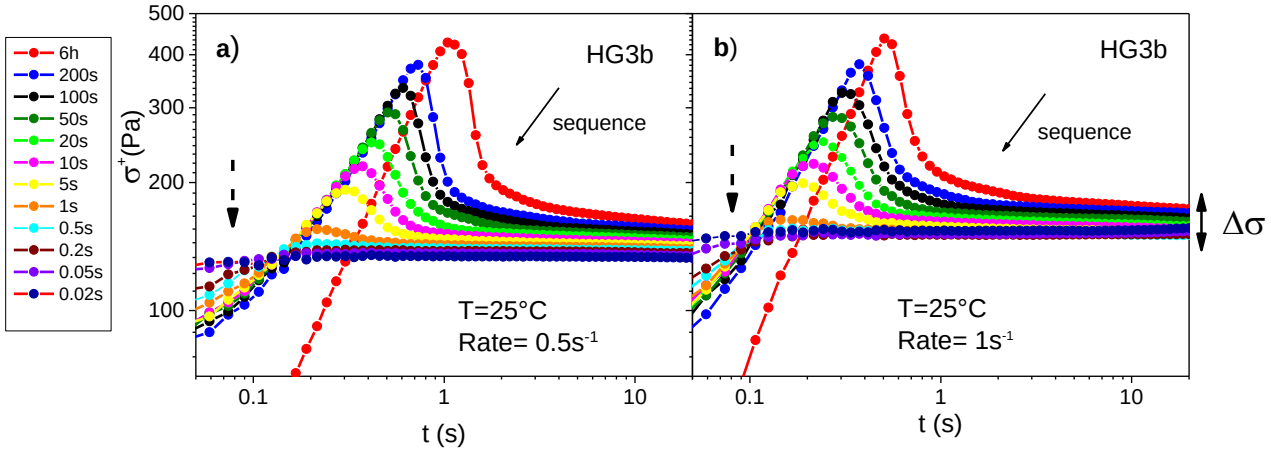

Fig. 4.9 Stress response of HG3b to step-rate intervals (SB protocol) with shear rates of a) 0.5 and b) 1 s^{-1}. The first interval (red curve) started after 6h at rest. The presence of internal stresses is evident on the initial value of each curve indicated by dashed arrow. The solid line arrow marks the sequence of intervals. Legend indicates the variation of waiting time.

The respective relaxation patterns in Fig. 4.10 (a) provide insights on structural memory. Stress decay in the 2nd interval (followed the 1st step-rate) depicted in red, starts from the same residual stress value but follows different paths when the protocol is executed at different shear rates. The shear stress decay followed the rate of $1s^{-1}$ relaxes faster as expected, given the simple notion of the more fluidized sample at higher rates. Same picture emerges from the comparison of the 8th interval. More importantly, the 2nd and the 8th interval differ even when compared to the same rate preceding step-rate. There are two distinct exponential decays indicated by the dashed lines in the 1st interval. The long-times decay is absent at the 8th (green curve). This trend is clear in Fig. 4.10(b) where 2nd to 8th intervals for the rate of $1s^{-1}$ are shifted vertically for clarity. There are two weak power law decays with approximate exponents of -0.24 and -0.12 in the 2nd, as indicated by the dashed lines, while the second decay is not seen in the subsequent runs. This implies that the preceding step at rate of $1s^{-1}$, corresponding to Wi >>1, did not eliminate all previous structural memories. Every step-rate interval imprints a new memory and does not eliminate the previous ones completely. Consequently stress relaxation follows different path in analogy with aging in metastable systems (Fielding *et al.* 2000) The attained steady state stress is slightly lower each time, in contrast with the linear part that remains unaffected Fig. 4.9(b)). The same experiment was performed at 37°C. The arrows in Fig. 4.11 point to the time it takes for stresses to decay at 60 Pa for HG3b at two different temperatures. Clearly, structural memories relax faster by a factor of 10 at the higher T=37°C due to thermal motion.

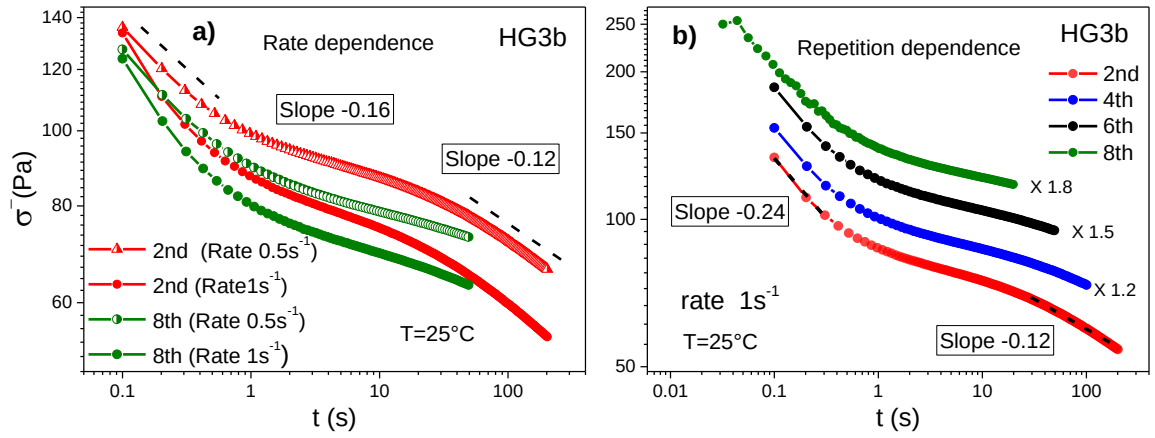

Fig. 4.10 Stress decay for a) 2nd and 8th runs for two preceding shear rates of 0.5 and 1 s^{-1} b) 2nd through 8th run and preceding rate of $1s^{-1}$.Curves are shifted vertically as indicated. Dashed lines are best fits to data. Stress decay intervals are even numbered.

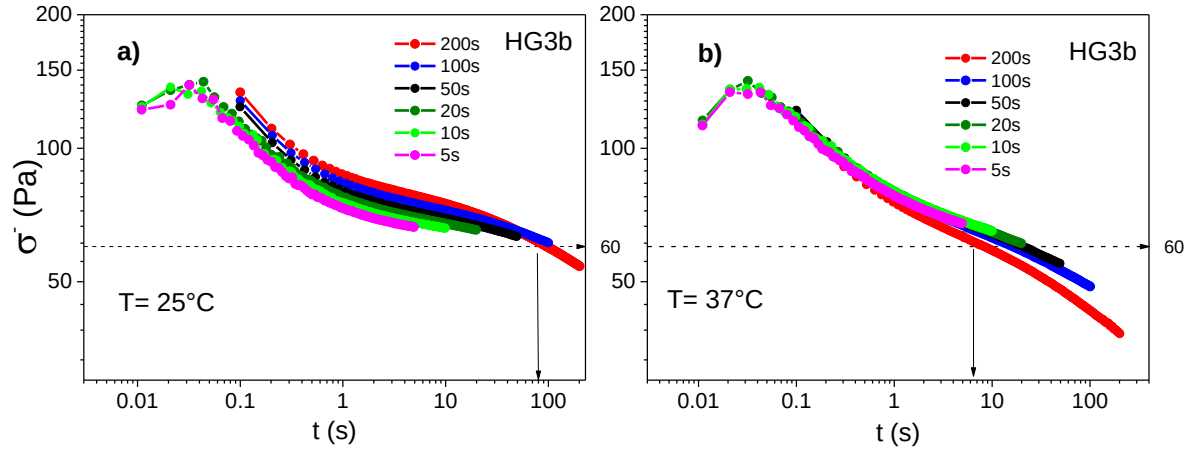

Fig. 4.11 First 6 stress decay intervals (2, 4, 6, 8, 10, 12) at a) T=25° and b) T=37°C. The preceding shear rate is $1s^{-1}$. Memories are erased faster due to thermal motion. Solid arrows indicate the time it takes for the stress to decay at 60Pa for interval 2.

Concluding remark 4: A step at rate of $1s^{-1}$, corresponding to Wi >>1, is not sufficient to eliminate all previous structural memories. Every step-rate interval imprints a new memory and does not eliminate the previous memories completely. Once flow is stopped and for $t < \tau_{rec\_min} \approx 0.5s$ the network is still incoherent, hence stresses relax at a fast pace as $\sigma \propto t^{-0.24}$. Junctions start to reform after 0.5s where at time scales of $\tau_{rec\_max} \approx 8s$ the network has attained its full density. The entrapped stresses now relax slower as $\sigma \propto t^{-0.12}$, as dislocated micelles rearrange via creeping motion (Semenov *et al.* 1995) at longer times order on the order of a few hours. Regarding shear start-up the σ_p decrease for $t_w < \tau_{r\_max}$ =

8s is attributed to unrecovered network microstructure (number density) and structural anisotropy whereas at $t_w > \tau_{r\_max}$ = 8s only the latter contribution dominates. On the other hand τ_p decrease (σ^+ peak advance) results solely from this frozen anisotropy and is reflected in the residual stresses. The already distorted microstructural constituents, i.e., the dislocated micelles, yield at smaller strains, as the strain is additive to the already stored strain. The latter is the recoverable strain monitored in recoil experiment. To test the above hypothesis we utilize flow reversal and recoil experiments discussed in the next section. The weak HG3c differs from the micellar structured HG3b and is discussed for comparison. The former exhibits terminal regime in DFS and strain hardening in DSS, is less brittle, and more responsive to temperature. Nevertheless, the SB protocol shows differences and similarities as well. Peak-stress decreases with t_w decrease in both HG3b and HGc step-rate intervals.

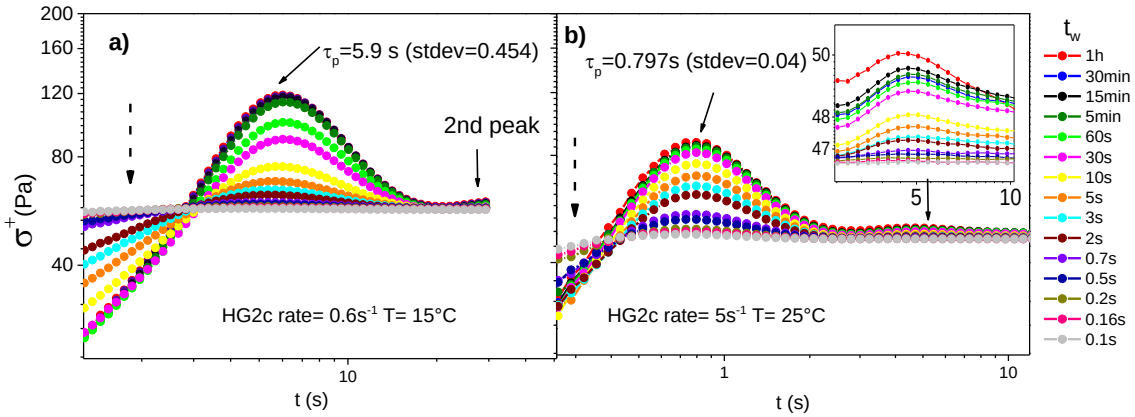

Fig. 4.12 Stress response of HG3c to step-rate intervals (SB protocol) with shear rates of a) 0.6 s^{-1} and T=15°C, b) 5 s^{-1} and T=25°C. The first interval (red curve) started after 1h at rest. The presence of internal stresses is evident on the initial value of each curve indicated by dashed arrow. Legend indicates the variation of waiting time. Inset on b) is an expanded view of a second peak evident in both temperatures.

However, the peak-time (τ_p) reduces with t_w in HG3b whereas in in HG3c is history independent (see Fig. 4.12 in comparison to Fig. 4.9). Peak-time was calculated by peak analyzer (Origin Lab) and found 6.014s and 0.797s for T=15 and 25 °C respectively. The standard deviation of the mean (see legend) is small. Remarkably for T=25 °C and 1h $\leq t_w \leq$ 0.7s all peak times where found 0.797 ±0.001. This peak-time insensitivity is similar to the behavior of entangled polymeric melts and solutions (Roy and Roland 2013). We can attribute this in HG3c to the fast decay of residual stress on the order of 30s (see Figure A.2). The onset of structural reform requires 0.7 s while the peak-stress is recovered after only 300 s. The stress decay path of different intervals is identical especially at early times as shown in Figure A.3.

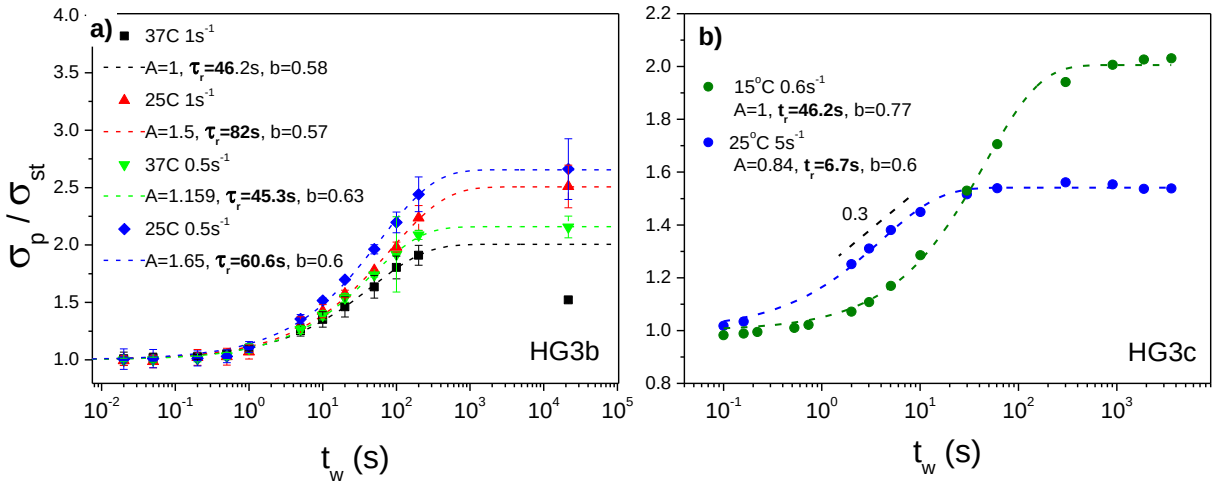

Fig. 4.13 Summary of the fractional stress overshoot magnitude, normalized by the steady state value, as afunction of waiting time for the a) strong HGb b) weak HGc. Legend indicates the fitting and experimental parameters. Dashed lines are fits to Eq. (1).

Until now we have extracted the elastic network recovery time τ_{rec_max}. The peak-stress dependence on waiting time reflects the structural memories. The normalized peak-stress over steady state stress dependence on waiting time is summarized in Fig. 4.13 for HG3b and HG3c. At early waiting times the plateau indicates that the network recovery is subtle, almost undetectable. As t_w increases the overshoot is gradually recovering, while after a certain t_w, the peak-stress saturates to its maximum value, implying that the microstructural recovery is completed and most importantly, memory is lost. To quantify this memory time, and in accord with (Stratton and Butcher 1973) the data were fitted to:

$$\sigma_{max}/\sigma_{steady} = A(1 - \exp\left[-\left(\frac{t}{\tau_{mem}}\right)^{\beta}\right]) \quad (1)$$

where A is a constant and τ_{mem} is a characteristic memory decay time. We argue the latter reflects the transition time from anisotropic to isotropic microstructure (Di Dio, Khabaz, Bonnecaze and Cloitre 2022). The exponent β varies between 0.57 and 0.77 with most of the cases exhibiting β~0.6 , a value utilized commonly in literature for linear chains (Roy and Roland 2013). The recovery time calculated with this method for HG3b at 25°C is 82 and 60.6 s for the rates of 1 and 0.5s^{-1} respectively. The higher rate seems to induce more structural anisotropy hence recovery is slower. On the other hand the microstructure of HG3c needs only 6.7s to erase structural memories.

The peak-time exhibits a weak power law ($\tau_p \propto \tau_w^{0.2}$) for the HG3b (Fig. 4.14). Given that shear rate is the same for all intervals, the material becomes more brittle and less tough when t_w is decreased. In solids toughness is defined as the mechanical energy per volume that a material can absorb before

rupturing. Rupture is not relevant to our HG although it can be argued it corresponds to static or dynamic yield stress/strain (Møller *et al.* 2006). On the other hand, the modulus of resilience is the energy per volume absorbed by a material at the onset of plastic regime (Beer *et al.* 2015), i.e., where stress departures from linear dependence on strain. It is represented by the area under the stress-strain curve corresponding to strain up to the elastic limit. The modulus of resilience (U) for the step-rate intervals (SB protocol) of Fig. 4.9(a) is shown in Figure 4.15.

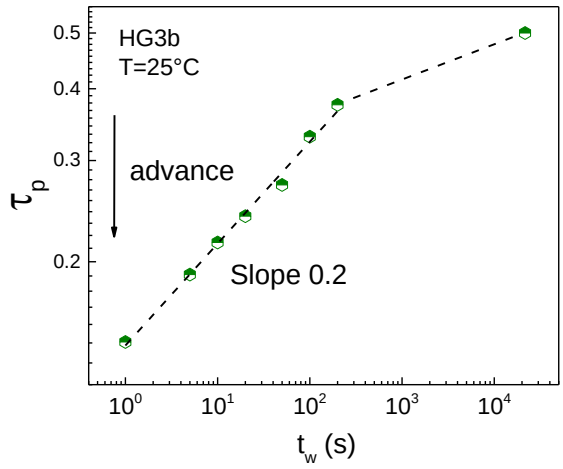

Fig. 4.14 Peak-time reduction (advance) as a function of waiting time, for HG3b. Line indicates slope of 0.2 ($\tau_p \propto \tau_w^{0.2}$). Data corespond to step-rate intervals at the rate of $1s^{-1}$ (Fig. 4.9).

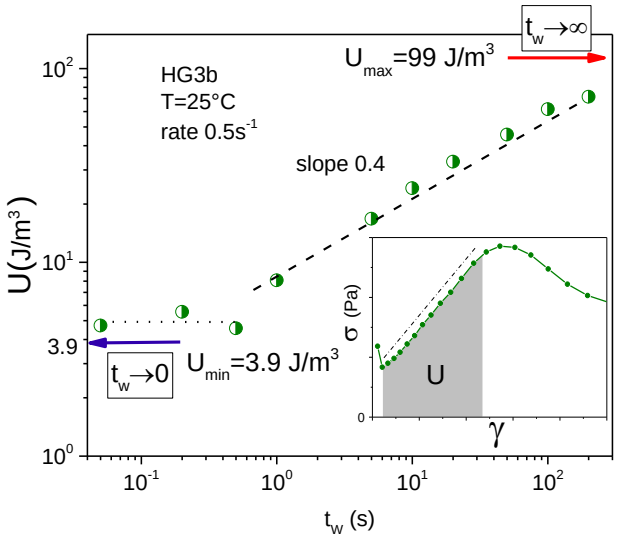

Figure 4.15 The modulus of resilience (U) as a function of waiting time in SB protocol. It is derived from calculation of the area under the stress-strain curve of Fig. 4.9(a). An example is shown in the inset. The red arrow indicates U_{max} the saturation value at long t_w (interval 1). The blue arrow indicates U_{min} at the fluidized state obtained from flow reversal experiments (Figure 4.23).

Apparently, the modulus of resilience quantifies both features of step-rate response that reflect the structural memory: the peak-stress (hence elastic limit) reduction and the peak-time retardation with decreasing waiting time. Both quantities $\tau_p(t_w)$ and $\sigma_p(t_w)$ affect the modulus of resilience. When the sample is sheared after long time at rest t_w>6h (t_w =>∞) the energy needed to deform the sample beyond the elastic limit and initiate plastic rearrangement is U_{max} =99J/m^3. On the opposite case when $t_w < t_{rec\_min}$ = 0.5s (t_w =>0) the already fluidized sample needs only U_{min}=3.9J/m^3 to be inelasticaly deformed. This behavior of U reflects the memory decay in hydrogel HG3b.

Concluding remark 5: structural memories affect the ability of the material to store energy elastically in steady shear. This is quantified by the modulus of resilience. LVE by no means can capture these memory effects.

4.5 Mechanical annealing by flow reversal

Given the sensitivity of stress overshoot to strain history, the comparison of start-up shear responses at sequential intervals is not possible unless one waits for 12h before each measurement, while at the same time the question on the role of residual stresses remains. To test the hypothesis that residual stresses are the only cause of this behavior the 3-intervals Mechanical Annealing Sequence (3MAS) is proposed: The excitation and response, i.e., applied shear rate, the resultant transient strain and stress response, are illustrated in Figure 4.16, Fig. 4.17(a) and (b) respectively.

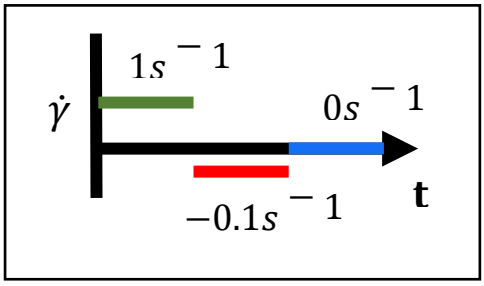

Figure 4.16 Sequence of applied shear rates in the 3 intervals of 3MAS.

A rate of 1s^{-1} is applied for 20s (green curve) resulting in a stress overshoot followed by a steady state. In the 2nd interval (red curve), the flow is immediately reversed at the slower rate of -0.1s^{-1} to fine tune the amount of recovered strain. At the last interval the rate is set to 0s^{-1} and stress relaxation is monitored.

The accumulated and recovered strain during the 3 intervals of 3MAS is depicted in Fig. 4.17(a). The response plotted in Fig. 4.17(b) indicates that transient stress jumps to negative values when reverse shearing commences (2nd interval) and then relaxes upon cessation of flow. By properly adjusting the amount of reverse strain (γ_{rev}) (or time (τ_{rev})) the residual stresses can be relaxed faster to almost 0 Pa.

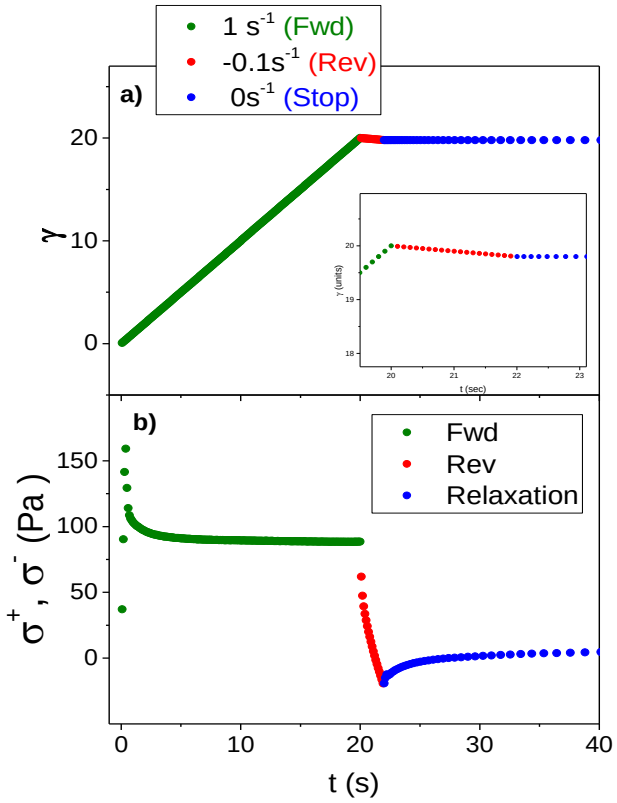

Fig. 4.17 The associated with the imposed forward, reverse and zero (Stop) shear rate a) accumulated strain b) stress, during the three intervals comprising the 3MAS. Inset is an expanded view of the reverse interval. Data are shown as an example. Sample is HG3b at T=25°C.

This is actually illustrated in Fig. 4.18(a) with four different 3MAS runs where the reversed interval was varied in duration from 2 to 4 s and. Hence, the resulting $\gamma_{rev} = \tau_{rev} \cdot 0.1s^{-1}$ ranged from 0.2 τo 0.4 strain units. From the stress relaxation of Fig. 4.18(b) it is clear that a reverse strain $\gamma_{rev} = 0.3$ reduces the internal stress below 10 Pa in a few seconds (note the linear scale), while the equivalent time for the stresses to relax without the reverse interval would be on the order of 10^4 s (Fig. 4.4). Any test performed after the 3MAS ensures zero residual stresses on a macroscopic scale. Indeed, the rheometer senses only an average of microstructural internal stresses as components of opposite directions are canceled out while any tensorial aspects of the stresses are integrated. To test whether the 3MAS erases strain biasing effects, three step-rate ($1s^{-1}$) responses with different strain histories are compared in Fig. 4.19(a). Two experimental sequences were performed; i) in the first sequence a 3MAS was performed after the sample being at rest for 6h. The stress response to the 1st 3MAS interval (step-rate of $1s^{-1}$) depicted in black, is considered the reference one. A 2nd step-rate was performed immediately after the 3MAS was completed (reverse strain is applied) and its response is depicted in red.

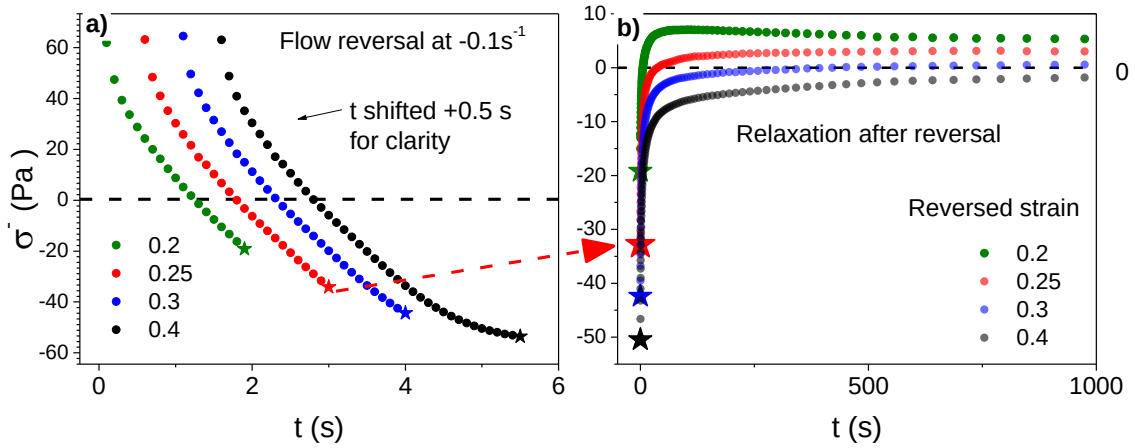

Fig. 4.18 Reverse and relaxation intervals of four 3MAS runs a) transient stress reduction during the reverse interval. Legend indicates the reversed strain at the end of the interval. Curves are shifted horizontally by 0.5s for clarity b) Stress decay after each reversal interval. Star denotes the first stress value upon cessation of flow. Red arrow indicates the time sequence of data acquisition for the 0.25 strain reverse-relaxation interval. Blue curve (0.3) is closer to zero stress limit denoted by the dashed black line.

Both responses are in satisfactory agreement. The memory of the 1st interval was completely erased; ii) in the 2nd sequence, a probing step-rate was performed with 50s waiting time after a "history" making step-rate interval. The peak-time typically shifts to earlier times (advance) and peak-stress decreases, consistently with the behavior in SB protocol in Fig. 4.9. The effectiveness of the 3MAS to erase the directional memory was further assessed. Probing the sample in both directions can verify whether there is a directional memory in the microstructure. Two different experimental sequences where performed. Before each one the sample was subjected to 3MAS as a rejuvenation protocol to erase the strain history. Followed this rejuvenation a probing step-rate interval was performed in forward ($1s^{-1}$) and reversed ($-1s^{-1}$) for the 1st and 2nd experimental sequence, respectively. The resulting stress overshoots of Fig. 4.19(b) are in good agreement .This confirms the ability of 3MAS to restore structural anisotropies imposed in the past or more generally erase kinetic memories. This supports that memory and structural anisotropy are closely related at least in this case (HG3b). Nonlinear rheology is indeed sensitive to this anisotropy as indicated by the measurement of the macroscopic residual stresses. The amount of reverse strain needed for anisotropy restoration in the present case is 0.3, consistent with the recovered strain after flow is stopped by setting stress (rather than strain) to 0 Pa, as shown in Fig. 4.20. The latter is a very different experiment from the creep and recovery test which is utilized to establish an optimum preshear protocol (Choi and Rogers 2020). The recoverable strain of Fig. 4.20 corresponds to the saturation value of the elastic deformation when steady state is reached (Kamani, Donley and Rogers 2021). This implies that by utilizing 3MAS with reverse strain equal to the recoverable strain (after steady shear), we can eliminate

the structural anisotropy at least to such degree that nonlinear rheometry cannot sense. A systematic work with diverse materials is needed to prove the universality of this statement.

The recoverable strain after flow cessation is not affected by strain history in HG3b. Its value for a preceding step rate of $1s^{-1}$ is approximately 0.23 units. There is some uncertainty stemming from the typical ringing (Baravian *et al.* 2007) at early times and the long time needed to approach a proper plateau. This value is remarkably close to the γ_{rev} extracted from the 3MAS. This supports the argument that by reversing we facilitate the structure to recoil in few seconds compared to 1000 s and more when the sample is left at rest.

Concluding remark 6: The reverse strain imposed by 3MAS at values equal to recoverable strain erase the macroscopic residual stresses and structural memories. We suggest it can be used in two ways; i) as a preshear protocol in samples that entrap stresses. The reverse strain should be set equal to the recovered strain in recoil experiment (σ set to 0) ii) as an alternative way to estimate the recoverable strain. This is a more complicated method than recoil but avoids the ringing artifact.

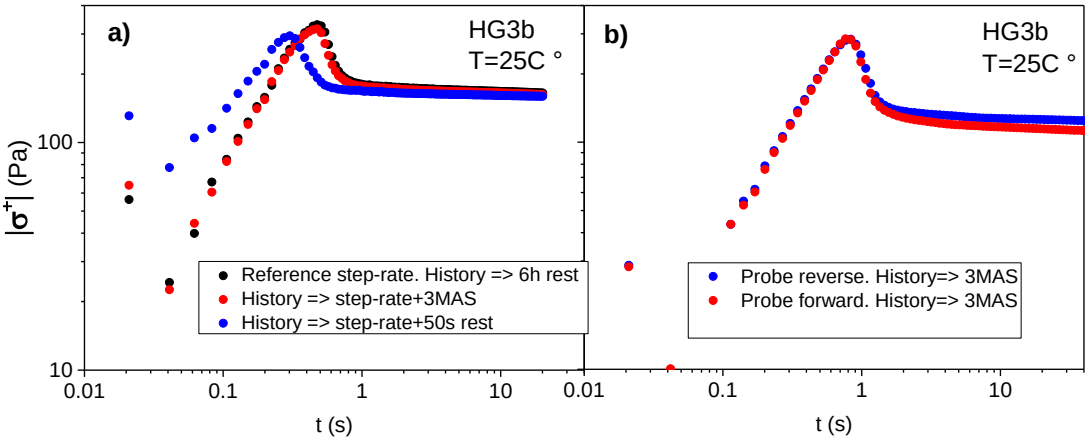

Fig. 4.19 Stress response to step-rate intervals with different strain histories as indicated in the legend a) black: reference step-rate interval performed after 6h rest time; red: step-rate interval performed after a step-rate and 3MAS; blue: step-rate interval performed after step-rate and 50s rest time. b) Two probing steps-rates, forward ($1s^{-1}$) and reverse ($-1s^{-1}$). Both performed after utilizing 3MAS as a preshear protocol. All step-rates applied at the rate of $1s^{-1}$ or $-1s^{-1}$ (reverse). Note the ordinate is the absolute value of stress.

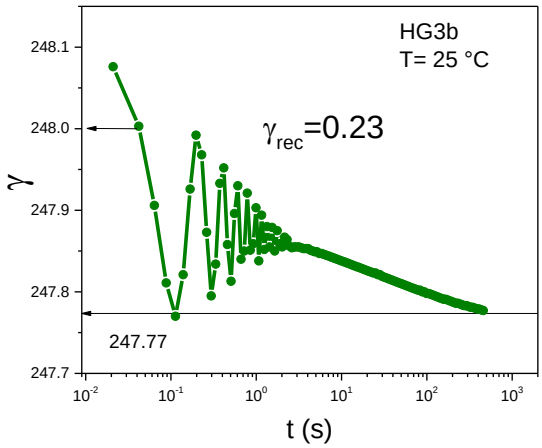

Fig. 4.20 Recoil experiment after step-rate interval at the shear rate of $1s^{-1}$. Ordinate shows the accumulated strain. The recovered strain is calculated from subtraction of the values pointed by the arrows.

4.6 Alternative probing protocols

4.6.1 Interrupted start-up shear and relaxation

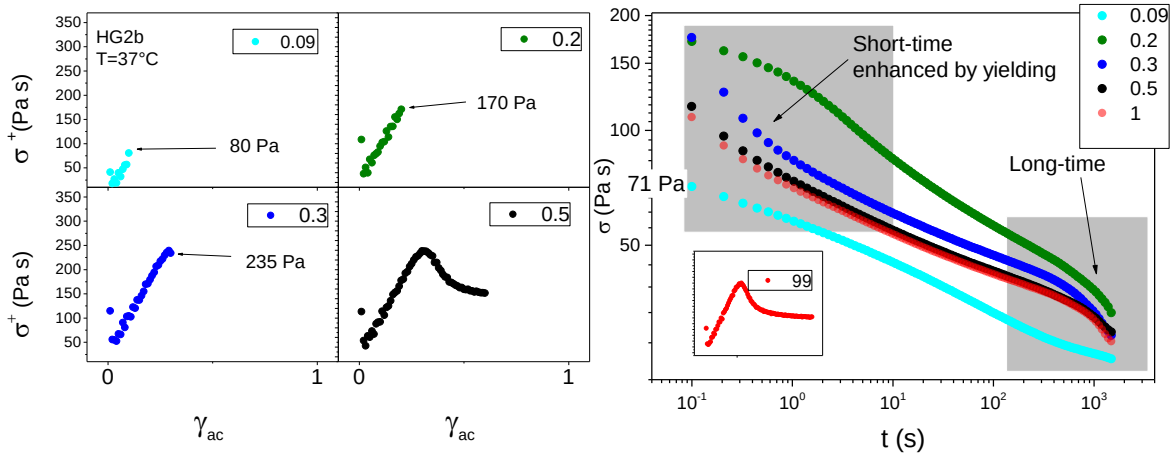

Fig. 4.21 The interrupted start-up shear protocol: Stress response and relaxation after "incomplete" step-rate runs of 0.09, 0.2, 0.3, 0.5 and 1 strain. All experiments were performed at $1s^{-1}$.

Further insights on the signature of residual stresses can be obtained by the interrupted start-up shear protocol, where flow time hence accumulated strain is gradually increased. After 6 h at rest, start-up shear was performed at the rate of $1s^{-1}$ (Fig. 4.21). The procedure was repeated 5 times, while at each run the flow time hence the accumulated strain (γ_{ac}) was gradually increased. At the shortest strain tested, 0.09, the material responded with 80 Pa that gradually decayed on flow was stopped within 10^3s. The stress response increased monotonically with γ_{ac} (cyan and green curve) as long as the preceding strain

was within the "linear regime before overshoot (stress accumulation). By the time the static yield stress was reached (blue) the stress decreased and then remained almost unchanged for 50 and 100% strain. By focusing on the 4 larger strains we deduce that relaxation at short times (t < 10s) is accelerated considerably by yielding. The 10s are comparable with the maximum time for network recovery of 8s. On the contrary long time stress decay is not sensitive to the degree of yielding. This supports the argument of two distinct stress relaxation processes in accord with jammed suspensions of soft spheres (Mohan *et al.* 2015)

4.6.2 Alternating forward and reverse

Flow reversal has been widely used to decouple viscous hydrodynamic from elastic contribution in microstructured materials such as fumed silica (Dullaert and Mewis 2005) and nearly hard sphere suspensions (Lin *et al.* 2015). It has been also utilized to study, the kinetics of fiber orientation in fiber suspensions via experiments (Eberle *et al.* 2009) and modeling (Sepehr *et al.* 2004), (Wang *et al.* 2008). After sufficient rest time the sample was sheared at alternating directions at the same rate. The stress response of the first three intervals is shown in Fig. 4.22(a) as subsequent intervals exhibit identical or symmetrical response. The almost instantaneous flow reversal does not allow sufficient time for this thixotropic material to recover its microstructure. Therefore, the first interval fluidizes the material and the following intervals probe it in opposite directions while at a mechanically incoherent state. Nevertheless, at the fluidized state (2nd and 3rd interval) and at low enough rate a weak overshoot appears at almost the same peak-time with the 1st interval (black curve) as shown in Fig. 4.22(a).

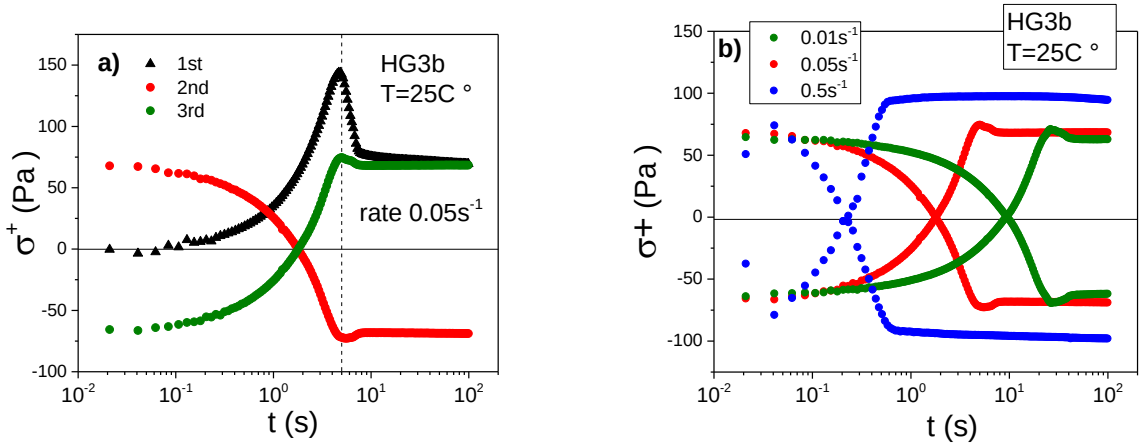

Fig. 4.22 Alternating forward and reverse experiment for HG3b. The 2nd and 3rd intervals produce symmetrical response with respect to the horizontal line at σ=0 Pa. a) The first three intervals at rate 0.05s^{-1} b) The 2nd and 3rd interval of different sequences performed at various rates. The overshoot is not present at the rate of 0.5s^{-1}.

It seems that at the rate of 0.05s^{-1} the partial rebuild of the structure is possible while at 0.5s^{-1} the overshoot is absent as shown in Fig. 4.22(b). This is in agreement with the 8s restructuring time as the

rates of $0.05s^{-1}$ and $0.5s^{-1}$ correspond to probe times of 20 and 2s, respectively. Transient stress response was found to be symmetrical for all intervals except the first. However, peak-strain does not depend on rate as shown in Figure 4.23. Three regimes can be defined. In regime I the reverse strain eliminates quickly the residual stresses, reaching 0 Pa at 0.1 strain units. The linear regime II commences with residual stress of 0 Pa. The slope of the dashed line indicates the elastic modulus of G_0~600 Pa which is 20% lower that the 750Pa extracted from data of Fig. 4.8. A possible explanation is that the stored from previous interval residual stresses act in a synergic manner with the motor in regime II as they do in regime I hence, stress is underestimated. On the other hand, the overshoot that follows in the yielding regime III is not biased by opposite residual stresses, and this explains why the peak-time advance seen in SB experiments of HG3b (Fig. 4.8) is nonexistent. Given that flow reversal eliminates internal stresses, we can deduce that the stress overshoot advance observed in previous experiments is solely due to residual stresses.

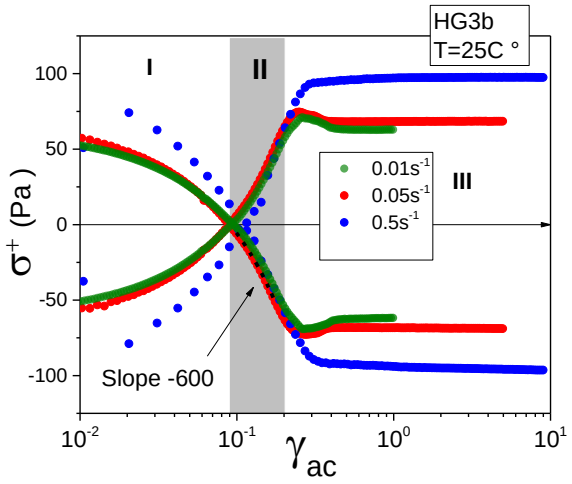

Figure 4.23 Alternating forward/reverse experimental runs of HG3b performed at rates of 0.01, 0.05 and 0.5 s^{-1}. Only the 2nd and 3rd intervals that produce symmetrical response with respect to the horizontal line at σ=0 Pa are shown. Stress overshot (static yield) strain is identical for the two lower rates. Three regimes are defined: I) internal stress elimination, II) linear and III) yielding. Dashed curve is a linear fit of red symbols (depicted as curve due to lin-log scale) with a slope=G = -600 Pa.

4.7 General conclusions and perspectives

The structural memories of the strong, micellar-structured and thixotropic HG3b where studied. These structural memories, imprinted by previous plastic deformations, reduce the modulus of resilience, i.e., the ability of the material to store energy elastically. The typical SAOS LVE measurements are not sensitive to these memory effects. Start-up shear is the experiment of choice to probe, as well as, to encode these memories. Every step-rate interval imprints a new memory and does not necessarily eliminate the previous memories. Peak-time is considerably shifted to earlier times (advanced) and peak-

stress to lower values as t_w is decreased Since memory encoding and read is achieved by the same experiment, specific protocols where developed. The utility of a mechanical annealing protocol was also demonstrated. We believe this will prove useful as a preshear in brittle materials that exhibit residual stresses.

On the microscopic level the entrapped stress are relaxed mainly by two major processes in analogy, but not identical to jammed microgel suspensions (Mohan *et al.* 2015): i) break-down of bridges that start to rebuild upon cessation of flow. It seems that the elastically active segments reach their equilibrium density in 8 s. This restores the elasticity of the network quite fast ii) the slower creeping relaxation of dislocated micelles. This should persist until all entrapped stresses are relaxed via cooperative local rearrangements. Bridging restricts this relaxation hence the entrapped stress decay is long. These two contributions are convoluted to the decaying stress which is history-dependent, in analogy to aging. The yield strain extracted from DSS and step-rate (static) experiments refer to different histories therefore should be compared with caution in materials with long-lived structural memories.

Results were compared with the weaker HG3c for reference. As a next step modeling of the micellar creeping relaxation will provide insights on the long-lived structural memories of the HG3b. Structural probe techniques at different memory states will confirm our rheological findings. Even then, the universality of our findings will need to be rigorously tested and compared with results from similar rheological protocols but with simpler and well-modeled systems.

Appendix A.4

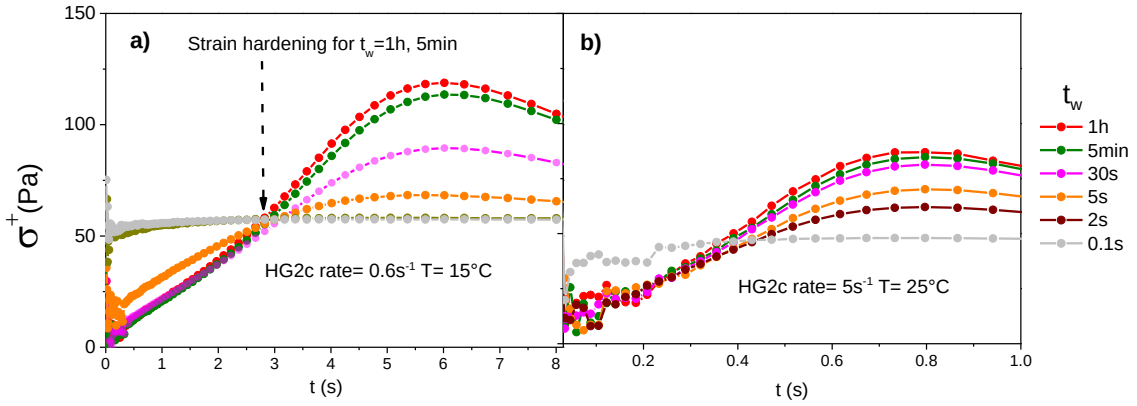

Figure A.1 Expanded view of stress response of HG3c to step-rate intervals (SB protocol) with shear rates of a) 0.6 s^{-1} and T=15°C, b) 5 s^{-1} and T=25°C. Only the few intervals are shown for clarity. Strain hardening is captured for long t_w at (b).

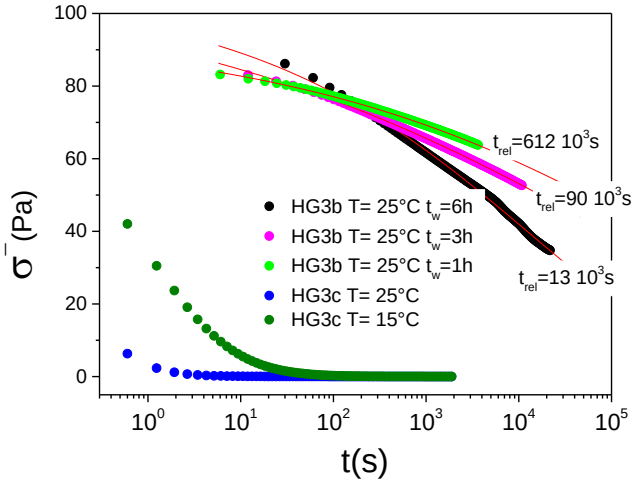

Figure A.2 Stress decay comparison for HG3b and HG3c for different conditions as indicated. Relaxation times extracted from single exponential decay are shown for HG3c at different waiting times. Stress decay is independent of waiting time in HG3c. Data fit K. Peponaki

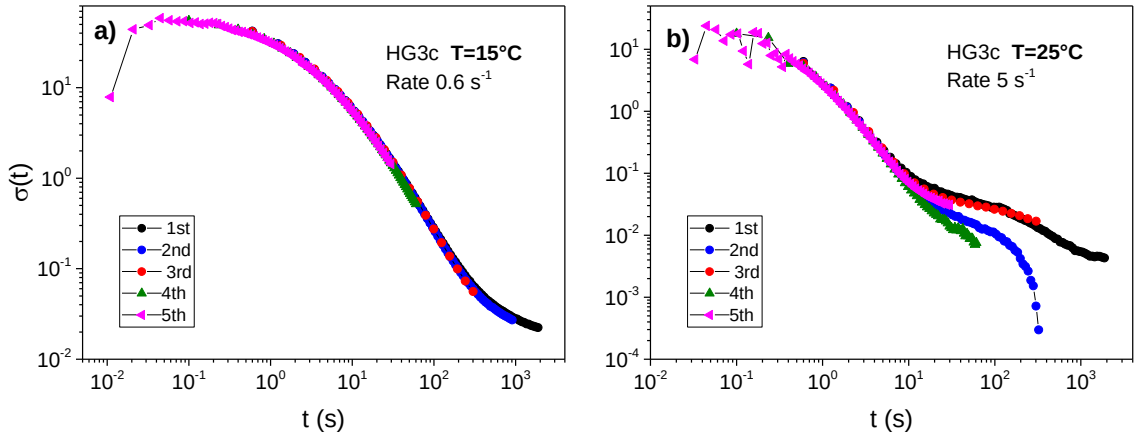

Figure A.3 Relaxation paths in SB protocol for the first 5 intervals for HG3c with preceding rates as indicated. Nevertheless path is similar at 15°C while differentiates at 25 °C among intervals. The first part of the curves is similar while a second plateau emerges at curves of 25 °C and this is the point where differentiation starts

.

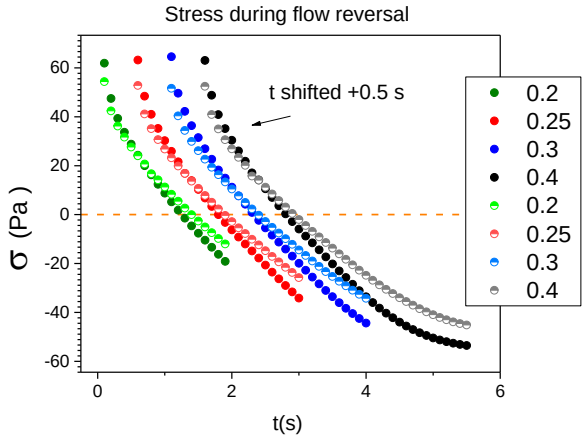

Figure A.4 Comparison of stress response during the reverse step of 3MAS for HG3a (pH=7.4) and HG3b (pH=6.5). Legend indicates the total amount of reverse strain. Half-filled symbols correspond to pH 7.4

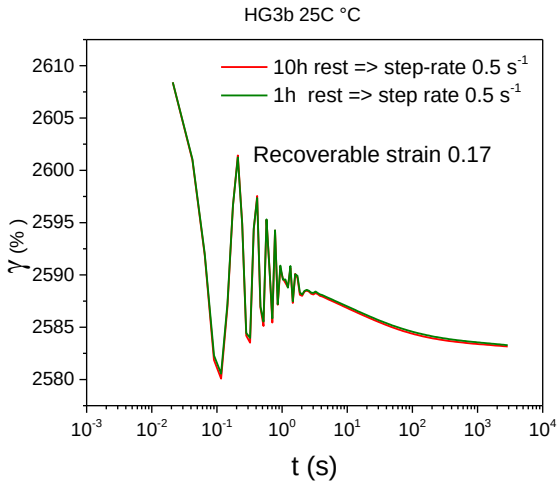

Figure A.5 Recovered strain (recoil) followed step-rate of $0.5s^{-1}$ for HG3b at T=25°C. The before the preceded step-rate the sample was at rest for 1 and 10h as indicated in the legend. Strain approaches a plateau at 1000 s and is not affected by the rest time that preceded the step-rate.

References

Aime, S., Ramos, L., and Cipelletti, L., ‘‘Microscopic dynamics and failure precursors of a gel under mechanical load,’’ Proceedings of the National Academy of Sciences 115, 3587-3592 (2018).

Bai, R., Yang, J., Morelle, X. P., Yang, C., and Suo, Z., ‘‘Fatigue Fracture of Self-Recovery Hydrogels,’’ ACS Macro Letters 7, 312-317 (2018).

Baig, C., Mavrantzas, V. G., and Kroger, M., ‘‘Flow effects on melt structure and entanglement network of linear polymers: Results from a nonequilibrium molecular dynamics simulation study of a polyethylene melt in steady shear,’’ Macromolecules 43, 6886-6902 (2010).

Ballauff, M., Brader, J. M., Egelhaaf, S. U., Fuchs, M., Horbach, J., Koumakis, N., Kruger, M., Laurati, M., Mutch, K. J., Petekidis, G., Siebenburger, M., Voigtmann, T., and Zausch, J., ‘‘Residual stresses in glasses,’’ Phys Rev Lett 110, 215701 (2013).

Baravian, C., Benbelkacem, G., and Caton, F., ‘‘Unsteady rheometry: Can we characterize weak gels with a controlled stress rheometer?,’’ Rheologica acta 46, 577-581 (2007).

Barlow, H. J., Cochran, J. O., and Fielding, S. M., ‘‘Ductile and brittle yielding in thermal and athermal amorphous materials,’’ Physical Review Letters 125, 168003 (2020).

Beer, F., Johnston, E., DeWolf, J., and Mazurek, D., ‘‘Mechanics of Materials. 7th_Edition,’’ New York. MeGraw-Hill Education Ltd (2015).

Choi, J., and Rogers, S. A., ‘‘Optimal conditions for pre-shearing thixotropic or aging soft materials,’’ Rheologica Acta 59, 921-934 (2020).

Corte, L., Chaikin, P. M., Gollub, J. P., and Pine, D. J., ‘‘Random organization in periodically driven systems,’’ Nature Physics 4, 420-424 (2008).

Coussot, P., Nguyen, Q. D., Huynh, H., and Bonn, D., ‘‘Avalanche behavior in yield stress fluids,’’ Physical review letters 88, 175501 (2002).

Coussot, P., Nguyen, Q. D., Huynh, H., and Bonn, D., ‘‘Viscosity bifurcation in thixotropic, yielding fluids,’’ Journal of rheology 46, 573-589 (2002).

Coussot, P., Raynaud, J., Bertrand, F., Moucheront, P., Guilbaud, J., Huynh, H., Jarny, S., and Lesueur, D., ‘‘Coexistence of liquid and solid phases in flowing soft-glassy materials,’’ Physical review letters 88, 218301 (2002).

Denisov, D., Lörincz, K., Uhl, J., Dahmen, K. A., and Schall, P., ‘‘Universality of slip avalanches in flowing granular matter,’’ Nature communications 7, 1-6 (2016).

Dhont, J. K., Kang, K., Kriegs, H., Danko, O., Marakis, J., and Vlassopoulos, D., ‘‘Nonuniform flow in soft glasses of colloidal rods,’’ Physical review fluids 2, 043301 (2017).

Di Dio, B. F., Khabaz, F., Bonnecaze, R. T., and Cloitre, M., ‘‘Transient dynamics of soft particle glasses in startup shear flow. Part II: Memory and aging,’’ Journal of Rheology 66, 717-730 (2022).

Divoux, T., Barentin, C., and Manneville, S., ‘‘Stress overshoot in a simple yield stress fluid: An extensive study combining rheology and velocimetry,’’ Soft Matter 7, 9335-9349 (2011).

Divoux, T., Grenard, V., and Manneville, S., ‘‘Rheological hysteresis in soft glassy materials,’’ Physical review letters 110, 018304 (2013).

Donley, G. J., Singh, P. K., Shetty, A., and Rogers, S. A., ‘‘Elucidating the G″ overshoot in soft materials with a yield transition via a time-resolved experimental strain decomposition,’’ Proceedings of the National Academy of Sciences 117, 21945-21952 (2020).

Dullaert, K., and Mewis, J., ‘‘Stress jumps on weakly flocculated dispersions: Steady state and transient results,’’ Journal of colloid and interface science 287, 542-551 (2005).

Eberle, A. P., Baird, D. G., Wapperom, P., and Vélez-García, G. M., ‘‘Using transient shear rheology to determine material parameters in fiber suspension theory,’’ Journal of Rheology 53, 685-705 (2009).

Ewoldt, R. H., Hosoi, A., and McKinley, G. H., ‘‘New measures for characterizing nonlinear viscoelasticity in large amplitude oscillatory shear,’’ Journal of Rheology 52, 1427-1458 (2008).

Fielding, S. M., and Olmsted, P. D., ‘‘Spatiotemporal oscillations and rheochaos in a simple model of shear banding,’’ Physical review letters 92, 084502 (2004).

Fielding, S. M., Sollich, P., and Cates, M. E., ‘‘Aging and rheology in soft materials,’’ Journal of Rheology 44, 323-369 (2000).

Galvani Cunha, M. A., Olmsted, P. D., and Robbins, M. O., ‘‘Probing the nonequilibrium dynamics of stress, orientation, and entanglements in polymer melts with orthogonal interrupted shear simulations,’’ Journal of Rheology 66, 619-637 (2022).

Gordon, M. B., Kloxin, C. J., and Wagner, N. J., ‘‘Structural and rheological aging in model attraction-driven glasses by Rheo-SANS,’’ Soft Matter 17, 924-935 (2021).

Hunter, G. L., and Weeks, E. R., ‘‘The physics of the colloidal glass transition,’’ Reports on Progress in Physics 75, 066501 (2012).

Ianniello, V., and Costanzo, S., ‘‘Linear and nonlinear shear rheology of nearly unentangled H-polymer melts and solutions,’’ Rheologica Acta 61, 667-679 (2022).

Ianniruberto, G., and Marrucci, G., ‘‘Convective constraint release (CCR) revisited,’’ Journal of Rheology 58, 89-102 (2014).

Jacob, A. R., Moghimi, E., and Petekidis, G., ‘‘Rheological signatures of aging in hard sphere colloidal glasses,’’ Physics of Fluids 31, 087103 (2019).

Jacob, A. R., Poulos, A. S., Semenov, A. N., Vermant, J., and Petekidis, G., ‘‘Flow dynamics of concentrated starlike micelles: A superposition rheometry investigation into relaxation mechanisms,’’ Journal of Rheology 63, 641-653 (2019).

Jamali, S., and McKinley, G. H., ‘‘The Mnemosyne number and the rheology of remembrance,’’ Journal of Rheology 66, 1027-1039 (2022).

Kamani, K., Donley, G. J., and Rogers, S. A., ‘‘Unification of the rheological physics of yield stress fluids,’’ Physical review letters 126, 218002 (2021).

Keim, N. C., and Medina, D., ‘‘Mechanical annealing and memories in a disordered solid,’’ Science Advances 8, eabo1614 (2022).

Keim, N. C., Paulsen, J. D., Zeravcic, Z., Sastry, S., and Nagel, S. R., ‘‘Memory formation in matter,’’ Reviews of Modern Physics 91, 035002 (2019).

Khabaz, F., Di Dio, B. F., Cloitre, M., and Bonnecaze, R. T., ‘‘Transient dynamics of soft particle glasses in startup shear flow. Part I: Microstructure and time scales,’’ Journal of Rheology 65, 241-255 (2021).

Koumakis, N., Laurati, M., Jacob, A. R., Mutch, K. J., Abdellali, A., Schofield, A. B., Egelhaaf, S. U., Brady, J. F., and Petekidis, G., ‘‘Start-up shear of concentrated colloidal hard spheres: Stresses, dynamics, and structure,’’ Journal of Rheology 60, 603-623 (2016).

Larson, R. G., ‘‘Instabilities in viscoelastic flows,’’ Rheologica Acta 31, 213-263 (1992).

Larson, R. G., and Wei, Y., ‘‘A review of thixotropy and its rheological modeling,’’ Journal of Rheology 63, 477-501 (2019).

Lin, N. Y., Guy, B. M., Hermes, M., Ness, C., Sun, J., Poon, W. C., and Cohen, I., ‘‘Hydrodynamic and contact contributions to continuous shear thickening in colloidal suspensions,’’ Physical review letters 115, 228304 (2015).

Masschaele, K., Fransaer, J., and Vermant, J., ‘‘Direct visualization of yielding in model two-dimensional colloidal gels subjected to shear flow,’’ Journal of rheology 53, 1437-1460 (2009).

Mewis, J., ‘‘Thixotropy-a general review,’’ Journal of Non-Newtonian Fluid Mechanics 6, 1-20 (1979).

Mewis, J., and Wagner, N. J., ‘‘Thixotropy,’’ Advances in colloid and interface science 147, 214-227 (2009).

Moghimi, E., Jacob, A. R., Koumakis, N., and Petekidis, G., ‘‘Colloidal gels tuned by oscillatory shear,’’ Soft Matter 13, 2371-2383 (2017).

Mohan, L., Cloitre, M., and Bonnecaze, R. T., ‘‘Build-up and two-step relaxation of internal stress in jammed suspensions,’’ Journal of Rheology 59, 63-84 (2015).

Møller, P. C., Mewis, J., and Bonn, D., ‘‘Yield stress and thixotropy: on the difficulty of measuring yield stresses in practice,’’ Soft matter 2, 274-283 (2006).

Mortensen, K., ‘‘Phase behaviour of poly (ethylene oxide)-poly (propylene oxide)-poly (ethylene oxide) triblock-copolymer dissolved in water,’’ EPL (Europhysics Letters) 19, 599 (1992).

Olmsted, P. D., ‘‘Perspectives on shear banding in complex fluids,’’ Rheologica Acta 47, 283-300 (2008).

Palmer, R. G., Stein, D. L., Abrahams, E., and Anderson, P. W., ‘‘Models of hierarchically constrained dynamics for glassy relaxation,’’ Physical Review Letters 53, 958 (1984).

Pham, Q., Russel, W., Thibeault, J., and Lau, W., ‘‘Micellar solutions of associative triblock copolymers: The relationship between structure and rheology,’’ Macromolecules 32, 5139-5146 (1999).

Rathinaraj, J. D. J., Hendricks, J., McKinley, G. H., and Clasen, C., ‘‘Orthochirp: A fast spectro-mechanical probe for monitoring transient microstructural evolution of complex fluids during shear,’’ Journal of Non-Newtonian Fluid Mechanics 301, 104744 (2022).

Robertson, C., Warren, S., Plazek, D., and Roland, C., ‘‘Reentanglement kinetics in sheared polybutadiene solutions,’’ Macromolecules 37, 10018-10022 (2004).

Roy, D., and Roland, C., ‘‘Reentanglement kinetics in polyisobutylene,’’ Macromolecules 46, 9403-9408 (2013).

Rubinstein, M., and Obukhov, S., ‘‘Memory effects in entangled polymer melts,’’ Physical review letters 71, 1856 (1993).

Santangelo, P., and Roland, C., ‘‘Interrupted shear flow of unentangled polystyrene melts,’’ Journal of Rheology 45, 583-594 (2001).

Sanz, E., Valeriani, C., Zaccarelli, E., Poon, W. C., Cates, M. E., and Pusey, P. N., ‘‘Avalanches mediate crystallization in a hard-sphere glass,’’ Proceedings of the National Academy of Sciences 111, 75-80 (2014).

Schwen, E. M., Ramaswamy, M., Cheng, C.-M., Jan, L., and Cohen, I., ‘‘Embedding orthogonal memories in a colloidal gel through oscillatory shear,’’ Soft matter 16, 3746-3752 (2020).

Semenov, A., Joanny, J.-F., and Khokhlov, A., ‘‘Associating polymers: equilibrium and linear viscoelasticity,’’ Macromolecules 28, 1066-1075 (1995).

Sepehr, M., Carreau, P. J., Grmela, M., Ausias, G., and Lafleur, P., ‘‘Comparison of rheological properties of fiber suspensions with model predictions,’’ Journal of polymer engineering 24, 579-610 (2004).

Sharma, S., Shankar, V., and Joshi, Y. M., ‘‘Viscoelasticity and rheological hysteresis,’’ Journal of Rheology 67, 139-155 (2023).

Speck, T., ‘‘Dynamic facilitation theory: A statistical mechanics approach to dynamic arrest,’’ Journal of Statistical Mechanics: Theory and Experiment 2019, 084015 (2019).

Stratton, R. A., and Butcher, A. F., ‘‘Stress relaxation upon cessation of steady flow and the overshoot effect of polymer solutions,’’ Journal of Polymer Science: Polymer Physics Edition 11, 1747-1758 (1973).

Vermant, J., and Solomon, M. J., ‘‘Flow-induced structure in colloidal suspensions,’’ Journal of Physics: Condensed Matter 17, R187 (2005).

Wang, J., O’Gara, J. F., and Tucker III, C. L., ‘‘An objective model for slow orientation kinetics in concentrated fiber suspensions: Theory and rheological evidence,’’ Journal of Rheology 52, 1179-1200 (2008).

Watanabe, H., Matsumiya, Y., and Sato, T., ‘‘Revisiting nonlinear flow behavior of rouse chain: Roles of FENE, friction-reduction, and Brownian force intensity variation,’’ Macromolecules 54, 3700-3715 (2021).

Withers, P., ‘‘Residual stress and its role in failure,’’ Reports on progress in physics 70, 2211 (2007).

Chapter 5 : High-frequency Optimally Windowed Chirp rheometry: Application in fast evolving thermosets.

5.1 Introduction

Capturing the linear viscoelasticity (LVE) of a fast time-evolving material is an analogue of high-speed photography of a moving object, where exposure times should be kept short. Likewise, rheometry requires that material's response measurement is completed in a short duration T compared to its LVE evolution rate (Mours & Winter, 1994) which is rationalized by the mutation time:

$$\tau_{Mu_{|G*|}}(\omega,t) = |G^*(\omega,t)|/\ \frac{\partial|G^*(\omega,t)|}{\partial t} \quad (1)$$

Here the complex modulus magnitude $|G^*|$ is the parameter of interest. Notably τ_{Mu} may be frequency (ω) and aging time dependent. Despite the significant progress in technology, current commercial rotational rheometers still interrogate material LVE with "conventional" dynamic frequency sweeps (DFS) within the small amplitude oscillation (SAOS) framework. The sample is excited by a series of stress or strain-sinewaves of fixed amplitude. The response is acquired sequentially in time as the frequency of oscillation is varied in steps, yielding corresponding data points, a discrete LVE spectrum. There are two timescales related to this experiment. On the one hand the period of oscillation $T_{osc}=2\pi/\omega$ sets the observation timescale for each data point. When the former is long compared to τ_{Mu} the assumption of translational time invariance collapses invalidating the measurement. In this case the requirement that strain history response is additive, the so called Boltzman superposition principle (Markovitz, 1977), is not guaranteed (Fielding, Sollich, & Cates, 2000). Hence the evolution of the material under test should be slower compared to T_{osc} for each data point to be valid. On the other hand, the total duration of the DFS sets a longer timescale T, which governs the coherence of the LVE spectrum. When measuring for instance a metastable system each data point corresponds to a different frequency and age hence, to a material with a potentially different relaxation time (Kawasaki & Tanaka, 2014; Negi & Osuji, 2010). The duration of the whole experiment can last from a few minutes up to a few hours. To this end, a stricter requirement is imposed for the whole LVE spectrum to be meaningful: the evolution of the material under test at all frequencies and times tested, expressed by $\tau_{Mu}(\omega,t)$ to be large compared to the duration of the experiment, T. The rate of time-evolution for a given experiment can be quantified by the Mutation number $N_{Mu} = T/\tau_{Mu}$ where values smaller than 0.15 have been found sufficient to follow the time evolution of the material (Curtis et al., 2015).

Contradictory to this requirement, the stress response of many soft materials, including industrial products and model systems, exhibit strong time dependence due to: flow history (Larson & Wei, 2019), physic-chemical evolution or number of active bonds (Macosko, 1985; Snijkers, Pasquino, & Maffezzoli, 2017), crystallization during cooling (Reiter & Strobl, 2007), micro-phase separation (Bates & Fredrickson, 1990), evaporation (Lehéricey et al., 2021), shear induced transition (Parisi et al., 2020) and other microstructural changes. In particular, the LVE properties of crosslinking materials evolve nearly exponentially when the percolation limit is reached, due to the densification of junction points in a 3D space spanning cluster (Flory, 1953). The so-called thermosets, such as epoxies, polyesters, cyanoacrylics and polyurethanes are ubiquitous in myriads of construction and repair or renovation projects in areas spanning from buildings, vehicles, wind turbines, to marine and aviation parts (Biron, 2013). Such polymeric resins constitute the matrix for glass, carbon or other fiber and filler composites that can be shaped to any form, by casting or laminating process (Weatherhead, 2012). Vinylester resins, a subset of thermosets, are gaining popularity nowadays in industrial applications and marine construction and repair. They stand between epoxy and polyester based resins as they combine the superior mechanical strength, adhesiveness, substantial resistance to chemicals and minimal water permeability of the former with the easiness of use of the latter. The final product can be a vinylester-fiber reinforced composite or a vinylester-fumed silica putty with tunable fracture toughness (Adachi et al., 2008). The superior resistant of such composites to water permeation makes them the material of choice for boat hulls almost "immune" to water degradation (Du Plessis, 2010), known as "osmosis" in the technical community.

In general, the evolution of shear modulus of the curing matrix is very important as it provides: a) insights of the network density and the curing kinetics b) information on its processability c) indications on the presence of entrapped stresses as a result of volume changes during curing (Crasto & Kim, 1993; O'Brien, Mather, & White, 2001) and d) data to calculate fracture energy and stress travel distance in fiber reinforced networks (Lin et al., 2014) of various degrees of cure. The LVE evolution can be quite fast in these systems. In order to address this, many techniques involving alternatives to pure sinusoidal excitation have been developed. In the multiwave excitation (Holly et al., 1988) a superposition of sinusoids is utilized; therefore the sample is interrogated simultaneously at a number of frequencies. While this decreases T substantially, it may easily violate the linearity assumption as the total excitation (strain) amplitude increases considerably, due to the constructive superposition of the different sine-waveforms combined. This practically limits the number of superimposed frequencies. On the other hand, a frequency-modulated excitation waveform, known as chirp, corresponds to a range of frequencies with a lower and an upper limit, ω_{Min} and ω_{Max}, respectively, while the amplitude remains constant. These type of signals, are abundant in nature (Wijers, 2018) given that any pulse may "chirp" as it propagates in a dispersive medium i.e. it will gradually transform to a chirp waveform. Chirps are widely used nowadays

in many applications such as sonars and radars (Klauder et al., 1960). Fourier transformed rheometry (Wilhelm, 2002) evolved naturally to chirp rheometry, validated and applied to many soft materials (Curtis et al., 2015; Ghiringhelli et al., 2012) and advanced considerably by the optimal amplitude modulation (Geri et al., 2018). The nowadays mature chirp has been applied orthogonally to steady shearing (Rathinaraj et al., 2022) to interrogate material properties under flow.

In modern commercial rotational rheometers the advanced motors-transducers aided by smart electronics, have significantly improved the data quality and extended the operability range of conventional DFS (Läuger et al., 2002). The commanded oscillatory and transient strain profiles, are consistently imposed as long as settings remain within the design parametric envelope. Recently the applicability of an amplitude-frequency modulated chirp was tested in a conventional rotational rheometer, ARES G2, by using the arbitrary function option, (Geri *et al*., 2018). Nevertheless, the utilization of these complex strain waveforms in commercial rheometers possesses technical challenges. The ability of these firmware-controlled motors, to impose chirps requires instrument specific protocols. This can be tricky given the complexity of modern instruments and their sample-biased response when operated at the limits of their operational envelope. Our homemade high-frequency piezo-rheometer (PZR) offers a more flexible alternative. Its simplicity and fast response (Athanasiou *et al*., 2019) renders this instrument an ideal test-bed for any arbitrary excitation function and therefore also for the chirp. Its upper high frequency limit of 6 krad/s extends significantly the accessed frequency range and most importantly allows the use of very short-time interrogating chirps of the order of 1 s.

The aim of this work from the technical perspective is twofold: firstly to explore the merits and limitations of chirp in a sophisticated commercial rotational rheometer, here an Anton Paar MCR702; secondly, to validate high frequency chirp on PZR. As a next step we utilize chirps to study the fast evolving LVE of our test system, a commercial vinylester resin under cure. This technique has been applied successfully to a commercial rheometer before (Geri *et al*., 2018) as well as in simulations (Bouzid *et al*., 2018) however, to the best of our knowledge this is the first trial in an Anton Paar MCR 702 and most importantly in a parallel plate high frequency piezo-based setup such as our PZR.

5.2. Linear Fourier transform rheometry: from DFS to Optimally Windowed Chirp (OWCh)

In a conventional strain control DFS test, the frequency dependence of the complex modulus (G*(ω)) is derived by correlating the stress response waveform σ(t) of the material under test to the harmonic strain excitation $\gamma(t) = \gamma_0 \sin(\omega_i t)$ for each angular frequency measured at a given strain amplitude γ_0. Index i =1,2,3,..N where N is the number of the frequency points tested. The derivation of the discrete spectrum from the time-domain signals is expressed mathematically:

$$G^*(\omega_i) = \frac{\hat{\sigma}(\omega_i)}{\hat{\gamma}(\omega_i)} \tag{2}$$

where the accent denotes the Fourier Transform of the relevant signal. In this single-wave (harmonic) excitation (Figure 5.1(a)) and within the linear limit, the material will respond with a "pure" sinusoidal stress waveform $\sigma(t) = \sigma_0 \sin(\omega_i t + \delta)$, i.e., respond on the same frequency with a phase advance δ related to its viscoelasticity. A continuous signal obeying the Dirichlet conditions related to convergence (Lanczos & Boyd, 2016), can be decomposed into a superposition integral of exponentials of infinite duration by the Continuous Fourier Transform (CFT) (Bachman, Narici, & Beckenstein, 2000). In real measurements the excitation and response signals are discrete functions (i.e. sequences of numeric values, indexed on integer variables). Sampling time which is the reciprocal of sampling frequency (F_s) and duration T are finite hence, the Discrete Fourier Transform (DFT) is relevant. DFT maps $N=F_s T$, equally acquired in time data to N equally spaced discrete frequencies (bins) in the Fourier space. In this framework DFT will represent a discrete time signal, stress for instance, with a Fourier series by calculating its similarity with an orthogonal base such as complex exponentials or the more intuitive sine (δ=0°) and cosine (δ=90°) waveforms of frequencies ω_i:

$$\sigma[t_n] = \sum_{i=0}^{N-1} a_i \cos[\omega_i\, t_n] + b_i \sin[\omega_i\, t_n] \tag{3}$$

where sample index n= 0,1,2..N, time flows in discrete steps $t_n = n/F_s$, and frequency of the analyzing Fourier series $\omega_i = i \cdot 2\pi F_s/N$ i.e. integer multiples of the frequency spacing. Equation 3 describes the synthesis of the time series from its analyzing Fourier series and shown in the most intuitive, in relation to the discussion below, form, with the brackets indicating its discrete nature. Notably ω_0 is zero resembling a DC component, not directly related to LVE of the material and always rejected by the rheometric software. In our data this is also ignored. Nonetheless its value could reflect residual stresses from strain history. When the two Fourier coefficients a_i and b_i are normalized by the applied strain amplitude in the spirit of Eq.2 they yield the in-phase with strain $G'(\omega_i)$ and the 90° shifted $G''(\omega_i)$ respectively. In most application the DFT is computed via Fast Fourier Transform (FFT) which is actually a class of algorithms

capable of reducing computational effort from being proportional to N^2, to N $\log_2$N. FFT cleverly assumes a number of calculations as redundant exploiting symmetry. For detailed DFT definition and calculation FFT algorithms see (Oppenheim et al., 2001). The most prominent limitation of DFT stems from the relation $\Delta\omega = \frac{2\pi F_S}{N} = 1/T$ i.e. the measurement duration trades-off frequency resolution. Consequently an optimum combination of F_s and N is needed for a given application. A spectral component between two bins inevitably is smeared over them inducing errors, the so-called spectral leakage. Another characteristic of DFT is inherited from the CFT of continuous signals where it is assumed that the waveform is infinite in time or at least integer number of periods long. Likewise, the DFT considers discrete signals as periodic (Harris, 1978) while input and output can be both represented in a periodic form (Oppenheim et al., 2001). A chirp is one period of a signal consisting of a repetition of clones of the base signal.

Multiwave can also reduce T as excitation acquires simultaneously multiple frequency data points minimizing T (Holly et al., 1988). Eq. 2 does hold for the superposition of any number of sine waves as well as for any arbitrary excitation signal as long as the total strain amplitude remains within the LVE limit. The latter restricts the number of exciting sine waves (frequencies) applied, as the different components superimpose constructively. This is clearly indicated in Figure 5.1b where four waves with ω_1=1, ω_2=4, ω_3=14 and ω_4=53 rad/s are superimposed. The strain amplitude of this waveform with a period of 2π is 4% compared to 1% of each component. An ideal multiwave signal would contain all frequencies of interest in a single waveform keeping on the same time the amplitude envelope constant. A frequency modulated signal known as chirp fulfills these requirements. Is has been utilized in rheometry as an excitation signal (Ghiringhelli et al., 2012) with the method been referred as Optimal Fourier rheometry. Chirps, named after the sound that birds make, are ubiquitous in nature. A pulse propagating in a dispersive medium will eventually "chirp". Light pulses in a transparent medium will also chirp due to effects of chromatic dispersion and other nonlinearities. Chirp can be conceived as a sine wave with an instantaneous frequency that grows in time (up-chirp), as

$$\omega(t) = \frac{d\varphi(t)}{dt} = \omega_{Min}\left(\frac{\omega_{Max}}{\omega_{Min}}\right)^{\frac{t}{T}} \quad (4)$$

where the instantaneous frequency $\omega(t)$ is deduced from the time-derivative of the phase angle $\varphi(t)$ and T is the total duration of the chirp.

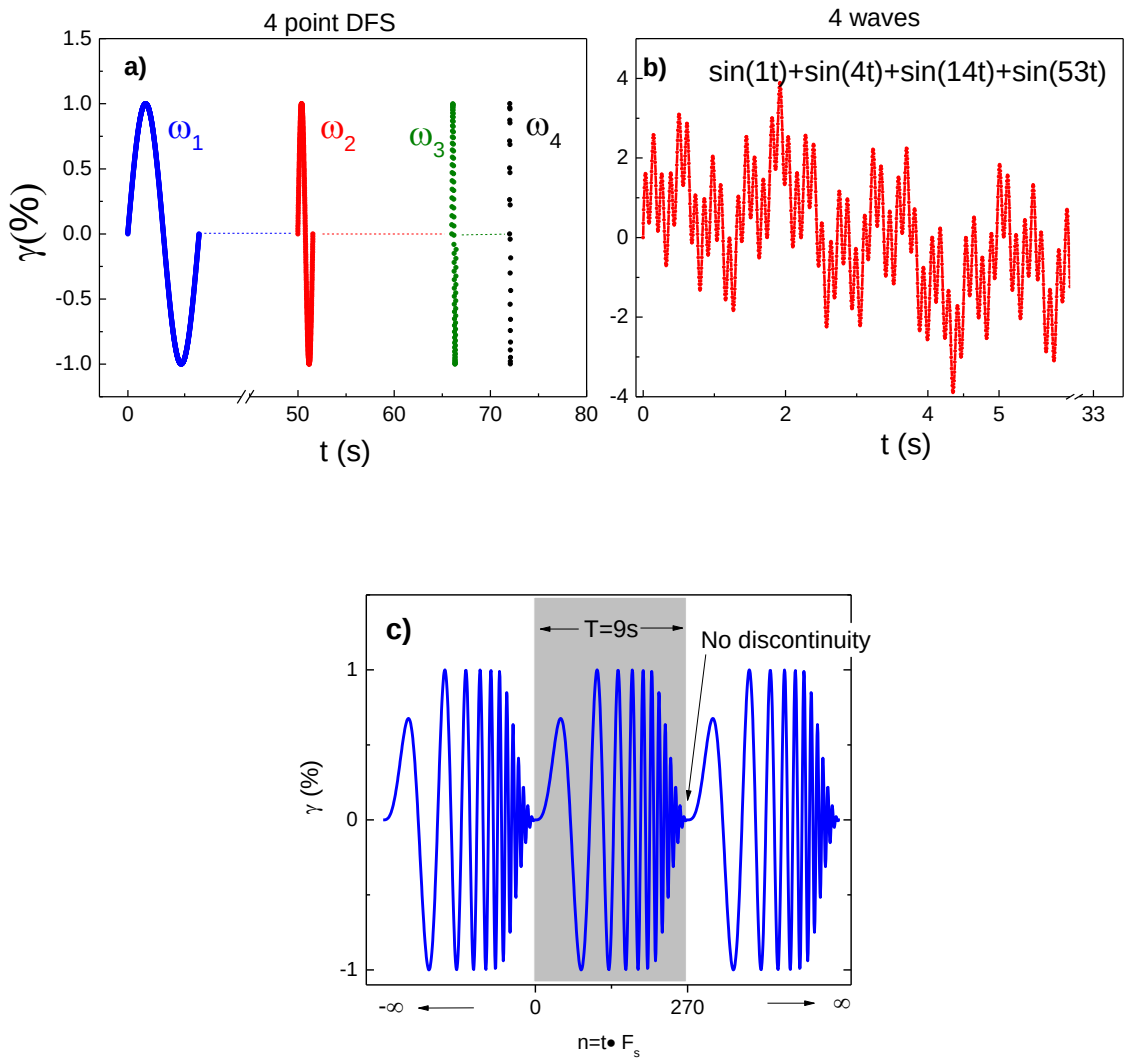

Figure 5.1 : Strain waveforms utilized in three popular rheometric tecniques in linear Fourier rheometry: a) DFS at four frequencies: ω_1=1, ω_2=4, ω_3=14 and ω_4=53 rad/s. Only 1 period is shown for clarity. Typical time for the MCR702 in default settings is 70s. b) Multiwave with a superposition of the same frequencies each with γ_0=1%. The resulting wave has the period of 1 rad/s (2π) but the strain amplitude is 4%. A time of 5 periods is assumed. The x axis is broken for clarity. c) OWCh ranging from 1 to 30 rad/s (grey shaded area). The signal is considered periodic by infinite repetition of the sequence to past and future times. Tapering is increased to 50% for illustrating the absence of discontinuities as the chirp front and end reduce to zero. T=9s. Abscissa is the sample index with N=270 and F_s=30Hz.

In conventional DFS, frequency is varied by applying a sequence of sine-waveforms, few periods long, with frequencies ranging from ω_1 το ω_N. This is illustrated in Figure 5.1(a) for a case of N=4 (with ω_1=1, ω_2=4, ω_3=14 and ω_4=53 rad/s) where only one period of this four point DFS is shown for clarity. The typical duration of this test is on the order of 70 s as multiple periods are needed. The DFT input is a sinewave (stress and strain) in discrete form, reducing the transform to a multiplication of the discrete signal with a sine and cosine reference time series of the same frequency. Here there is only one and

known output frequency (bin), thus with proper frequency spacing spectral leakage becomes non-existent. As DFT acts like a combination of band-pass filters (Prabhu, 2014), in this case a single one, all noise and harmonics are rejected and only the base frequency is considered. On the other hand, in a chirp signal the DFT is computed once for the whole spectrum hence, only frequencies smaller than ω_{Min} and larger than ω_{Max} can be ruled out. The chirp in the grey shaded area of Figure 5.1(c) is 9s or 270 samples long. The inherent periodicity of DFT extends this sequence, with infinite repetitions, in the past and in the future an analogue to FT integral evaluation range. The amplitude tapering induces a similarity on the chirp front and end removing thus discontinuities. Discontinuities induce harmonics that eventually spoil the whole spectrum by leakage.

By reducing the observation time T we reduce the information acquired and most importantly we increase the effect of spectral leakage known also as Fresnel ripples (Kowatsch & Stocker, 1982; Oppenheim et al., 2001). Spectrum leakage is thus the smearing of a frequency component or relaxation mode in rheological terms, to adjacent frequencies. The vulnerability of the resultant LVE spectrum to this, intrinsic to the DFT artifact, can be quantified by the dimensionless time bandwidth product (Levanon & Mozeson, 2004)

$$TB = T(\omega_{Max} - \omega_{Min})/2\pi \tag{5}$$

Equation (4) is easily conceived from the fact that both T and frequency range affect the frequency resolution. Leakage is considerably mitigated by increasing TB and by tapering the amplitude at the beginning and end of the chirp by a suitable windowing function such as the widely used Hann, Hamming, Tukey or others (Harris, 1978; Nuttall, 1981). The choice of the windowing function affects the competing requirement to resolve similar or dissimilar in strength adjacent frequency components (Prabhu, 2014). An optimally windowing chirp is a frequency-amplitude modulated waveform with proper tapering to avoid unnecessary loss of power at the edges of the spectrum. A tapering ratio of 6-15 % was found to be optimum by Geri et al hence the name Optimally Windowed Chirp (OWCh) (Geri et al., 2018). Based on this study we will utilize tapering of 10% by Tukey function throughout our experiments.

5.3. Experimental setup

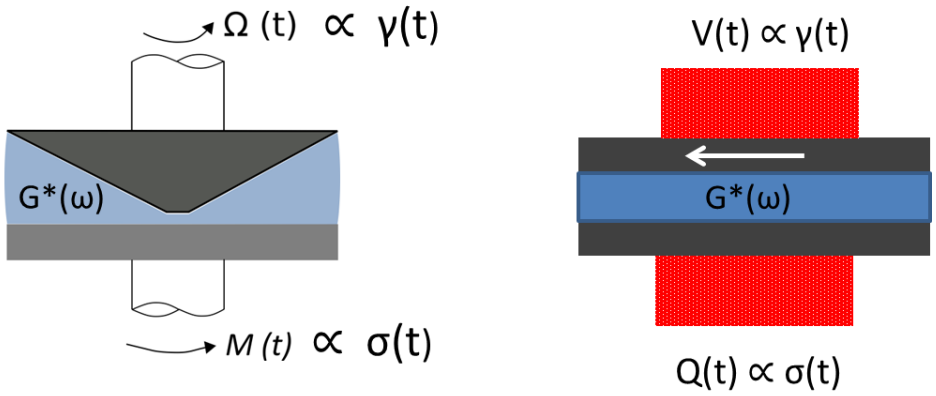

Figure 5.2 Cone-plate and sliding-plate geometries in seperated motor transducer arangement and strain controled mode.The upper plate is the actuator and the lower the sensor: a) Cone and plate in a rotational rheometer. Angular deflection $\Omega(t) \propto \gamma(t)$ is the controlled parameter (excitation) while torque response $M(t) \propto \sigma(t)$ is the measured quantity (response) b) Parallel or sliding plates geometry driven by piezoelectric ceramics depicted in red. The voltage $V(t) \propto \gamma(t)$ is the controlled parameter while the total charge generated $Q(t) \propto \sigma(\tau)$ is the measuring quantity .

Whatever the excitation signal may be, the sample's transfer function G*(ω), is interrogated by means of a strain actuator and a stress sensor, referred in commercially rotational rheometers language as motor and transducer respectively. A typical strain control setup is visualized in Figure 5.2 for two of the most popular geometries: a) the cone and disk (cone-plate) found in commercial rotational rheometers. For small cone angles the strain excitation γ(t) can be approximated as being proportional to the angular deflection Ω(t) of the upper tool connected to the motor. The stress response is followed by the lower tool connected to the transducer being proportional to the torque signal M(t) (Macosko, 1994). In the Anton Paar MCR 702, motor and transducer consist of identical components. b) the elementary sliding plates utilized in our homemade high frequency piezo-rheometer (PZR). Here rectilinear deformation is given by design (no curved streamlines). A voltage waveform V(t) excites the piezo actuator to induce a proportional strain, γ(t), while the stress is followed by the lower piezo acting as a stress sensor via the proportional generated charge, Q(t).

Both setups comprise separated motor transducer arrangement (Läuger & Stettin, 2016) where tool inertia effects are minimal (Athanasiou et al., 2019) . While the operational principles are the same, there are differences mainly as the user has neither the knowledge of the working principle nor any control on the sophisticated MCR 702 firmware. The latter controls the motor and the stress acquisition loop. Sliding plates are not found in commercial rheometers as they cannot impose steady shear. They suffer less though from edge effects and trim errors, as the sample at the interface, does not contribute in the stress as much as the one at the rim of a rotational geometry (Cardinaels, Reddy, & Clasen, 2019).

In this work all the experiments are strain controlled. The OWCh discrete strain signal was initially generated in tabulated form, by means of modified MIT OWCh Matlab code (Geri et al., 2018) and then applied to the instrument. Both MCR702 and PZR, were commanded to apply a series of n strain steps $\gamma[t_n]$, with $t_n = n\Delta t$ in sufficiently small time steps $\Delta t = 1/F_s$. The stress response, $\sigma(t_n)$, was followed with the same F_s. For the strain signal to be approximated as continuous and avoid parasitic harmonics we required $F_s >> 2\omega_{max}$=Nyquist sampling rate (Nyquist, 1928) referred as oversampling. This is vital to prevent aliasing (higher frequencies components are observed at a lower i.e. *aliased* frequency) and reduce high order harmonics due to quantization. The technical limitations of each instrument impose restriction on the maximum F_s and N. In the Anton Paar MCR702, the data points for both strain and stress are limited to N_{max}=2000 per interval, as more data points cannot be handled efficiently by the instrument's digital circuitry resulting is loss of data. The maximum acquisition rate is F_{s_max} = 200 Hz. By maximizing F_s and N digitization error is reduced and, the corresponding chirp duration $T=N/F_s$=10 s. This optimum combination of N, F_s and T is summarized in Table 1. To eliminate the possibility of data loss we safely performed most measurements in the MCR702 with T=9 s resulting is N=1800 samples.

Table 1: Limitations related to data aquisition for MCR702 and PZR. Measurement is optimized at their maximum value. Oversampling is the ratio of sampling frequency over $4\pi\omega_N$ where ω_{Max} is the maximum frequency tested denoted in brackets. Amplitude resolution is not known in MCR 702.

	N_{max}	**F_{s_max}**	**Oversampling**	**Amplitude resolution**
MCR702	2000 samples	0.2 kHz	6 (100 rad/s)	-
PZR1	>200 ksamples	800 kHz	66 (6000 rad/s)	65536 steps

The PZR strain actuator and stress sensors are piezoelectric ceramics allowing measurements at frequencies up to 6000 rad/s. We modified the original setup (Athanasiou et al., 2019) by adding a multichannel digital to analogue (D/A) and analogue to digital (A/D) converter, MicroDAQ 2000 (Embedded solutions, Poland). Contrary to the MCR702 rheometer, here circuitry is fast enough to process data in real time while N is restricted only by the computer's memory capacity. The stress response is digitized after conditioning of the signal by means of a charge amplifier (essentially a current integrator) (Horowitz, Hill, & Robinson, 1989; Starecki, 2014). The output of the charge amplifier, V(t), is proportional to the generated charge Q(t) and the parameter of interest i.e. the stress, $\sigma(t)$. Since the dependence is linear the conversion, from volt to Pa is accomplished via calibration. Both D/A and A/D converters are set to a minimum of 12 bit corresponding to a quantization in 2^{12} steps, to enhance amplitude resolution and minimize induced harmonics. Sampling frequency can be as high as 800 kHz,

66 times the Nyquist rate an order of magnitude higher than in the MCR702. To perfectly synchronize $\sigma[t_n]$ and $\gamma[t_n]$the latter was re-measured by an additional A/D channel. This provided an accurate reference strain signal to be fed in Eq. (2). Failure to perform such synchronization would result in a few ms delay of the actual excitation compared to the commanded one and therefore induce a considerable δ error at higher frequencies. This error was initially detected by our calibration method described below.

The OWCh signal can be as short as the period of the lower frequency component contained i.e $2\pi/\omega_{Min}$. On the other hand, as T is increased TB increases and the deviation from FFT assumption of the infinitely long signal is mitigated resulting in decreased spectrum leakage. Although the limit is not rigorous a value of TB above 100 is preferred (Kowatsch & Stocker, 1982). Fig 2 summarizes the operability window given all the operating parameters and limiting factors discussed. TB is calculated for PZR and MCR (red and olive dashed line respectively) based on their operational frequencies and by requiring N_{Mu} = 0.1 to 0.2. Due to restrictions in F_s and N (see table 1) the MCR 702 signal is optimized at 10s indicated with the olive arrow. Larger T will improve TB at the expense of F_s. PZR1 has been operated mainly at T=1 s indicated by the red arrow, nevertheless T has sufficient margin to be increased (red shaded area) for the benefit of TB, when τ_{Mu} is large. The grey shaded area marks the preferably non-operating area where TB<100 for both instruments.

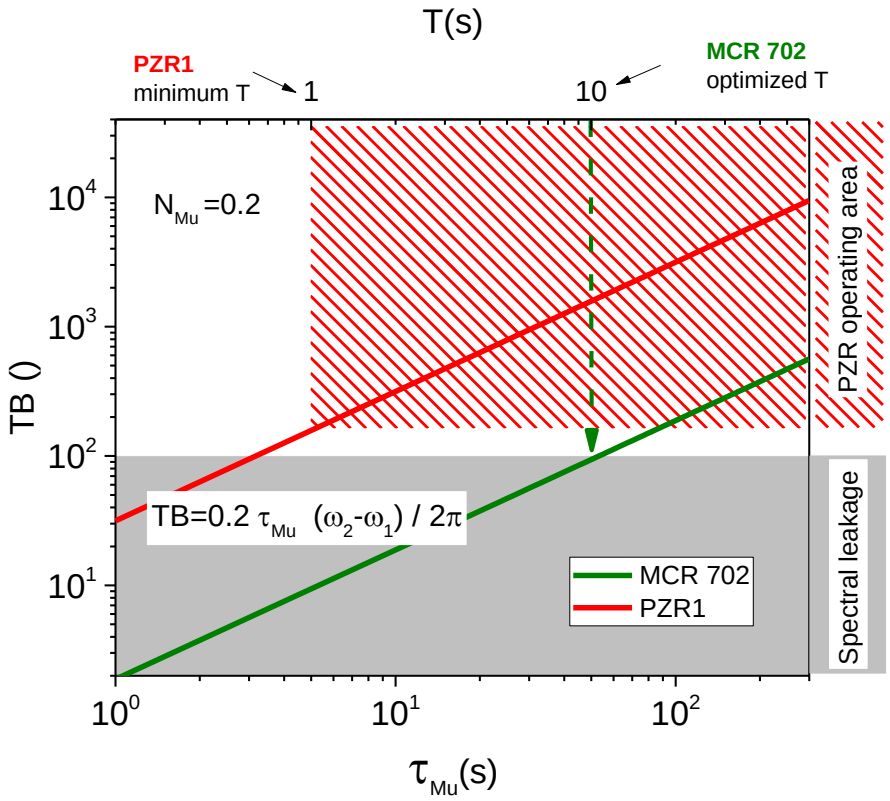

Figure 5.3 Operability window for MCR 702 and PZR under the requiremet that $T=\tau_{Mu}$ / 5. Grey shaded area indicates regime with increased spetrum leakage. Dashed green and red solid line depict TB values for given τ_{Mu} for MCR702 and PZR1 respectively as indicated in the text box. Green arrow indicates the optimized T for MCR702. PZR1 can operate in the red shaded area with minimum T=1s

5.4 Validation in MCR702

Modern rotational rheometers excel in conventional tests such as DFS. MCR702 performs well even at frequencies as high as 300 rad/s (Athanasiou et al., 2019) as its firmware can compensate for motor and transducer inertia in the separated motor transducer mode. However, when commanded to impose a non-conventional excitation such as the OWCh, the actual strain deviates from the commanded (nominal) value mainly at the last cycles of the chirp corresponding to higher instantaneous frequencies. This deviation was significantly increased when the instrument was commanded to perform a 5s OWCh with ω_{Max}=100rad/s (see Figure **S1**). In this "dummy" mode it seems that the build-in EC motor is not augmented much by the smart electronics and algorithms compared to classic oscillatory deformations (Läuger et al., 2002). The F_{s_max} of 200 Hz is 6 times above Nyquist limit (Table 1). This 6 fold oversampling is sufficient to prevent aliasing yet remains a limiting factor to minimize spurious frequency components when the signal is D/A converted. The number of acquired points per measurement is also limited, N_{max} = 2000. Given these factors a chirp duration of 9 to 10 s is optimum as it exploits the

sampling rate of 200Hz and mitigates mismatch of commanded and actual strain such as in Fig S1. Nevertheless, small distortions of strain can be taken into account by normalizing the stress response in (1) with the actual strain logged by the instrument. On the other hand large distortion of the strain waveform will eventually alter significantly the power spectrum of the signal resulting in unwanted harmonics. Noise will impair the measured spectrum as the signal to ratio decreases. Contrary to a conventional DFS, these harmonics may spread along the whole VE spectrum introducing additional relaxation modes, not related to material properties. The whole LVE spectrum may be affected in this case and not just few frequency points as in DFS. We therefore limited the chirp experiment to frequencies up to 60rad/s and N=1800 samples to improve the overall data quality and avoid overloading MCR702 data buffer. As we want to explore the limits of the method no data averaging nor smoothing was performed.

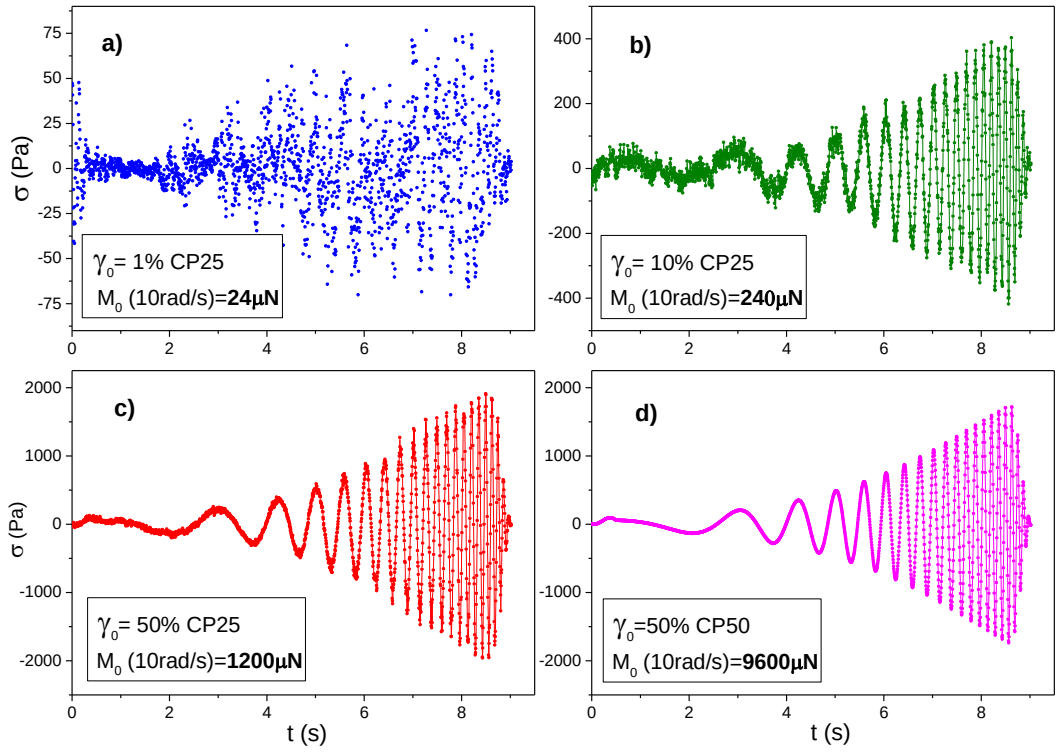

Figure 5.4: Discrete stress response signals of PDMS 100 Pa s to chirp excitation with ω_{Min}=1rad/s, ω_{Max}=60 rad/s, taper=10%, T_w=0.2 s and T=9 s in the MCR702, Anton-Paar rheometer. The legends indicate the strain amplitude, the geometry used and the equivalent torque amplitude at 10 rad/s. T_w is a delay time introduced in the excitation signal, in accord with previous work.

To experimentally demonstrate the effect of the response signal (stress) strength i.e. transducer torque amplitude M_0, we performed a series of tests with a PDMS oil of zero shear rate viscosity of 100 Pa s (Brookfield, USA). The excitation chirp parameters ω_{Min}=1 rad/s, ω_{Max}=60 rad/s taper=10%, T_w=0.2 s and T=9 s were kept constant while γ_0 and the tool geometry were varied to increase systematically the torque

amplitude, i.e.to gradually increase the response signal strength (all in the linear regime). To indicate this we report in Figure 5.4 the equivalent torque value, $M_{0,}$ corresponding to a 10 rad/s oscillation, at each strain amplitude and geometry. At the weaker torque signal (with CP25 mm and γ_o =1%), the stress response to OWCh is quite noisy. The signal improves as γ_0 is increased, with the M_0 indicated in the legend. As expected this noise affects the whole LVE spectrum (Figure 5.5(a))and the more sensitive to phase angle scattering G´ (Figure 5.5 (b)). Satisfactory agreement of OWCh with the conventional DFS derived spectra was achieved only when γ_0 was increased to 50% while scatter in G´ was eliminated at even stronger torque signal when the geometry was doubled in radius (CP50mm). A nominal torque amplitude of M_0(10rad/s)=1200 μNm was thus required for an acceptable measurement. In contrast when the MCR702 executes a conventional DFS with CP25mm a torque amplitude of $M_{10rad/s}$ = 24 μNm, two decades larger that the nominal sensitivity limits of the instrument, is sufficient for the measurement.

The effect of noise is also evident in the spectral energy distribution (Figure 5.6) where the whole spectrum is compromised for the γ_0=1%. Tapering reduces power at the higher frequencies in the excitation (black curve) while the response signal retains high values at higher frequencies due to increase of |G*| with ω. In conventional DFS this results in the improvement of data quality in moderate to higher frequencies for samples where |G*| increases with ω. Application-wise, the torque strength should be at least 10 times higher in a chirp based than in a conventional DFS. The difficulty to impose accurate criteria stems from the fact that the error is sample dependent. For instance a weak dependence of |G*| on frequency or the phase angle, δ, approaching the limits of 0 and 90° where tan(δ) is sensitive, will increase the error. A spectral leakage effect prediction is also non-trivial. The presence of noise in the response signal at any time of the experiment (within T) can affect the whole spectrum. This cannot be filtered out with conventional signal processing, as time information is lost in the frequency domain (John Rathinaraj & McKinley, 2023). The limits and optimal settings discussed in this section refer only to MCR 702 and can serve only as a general guidance.

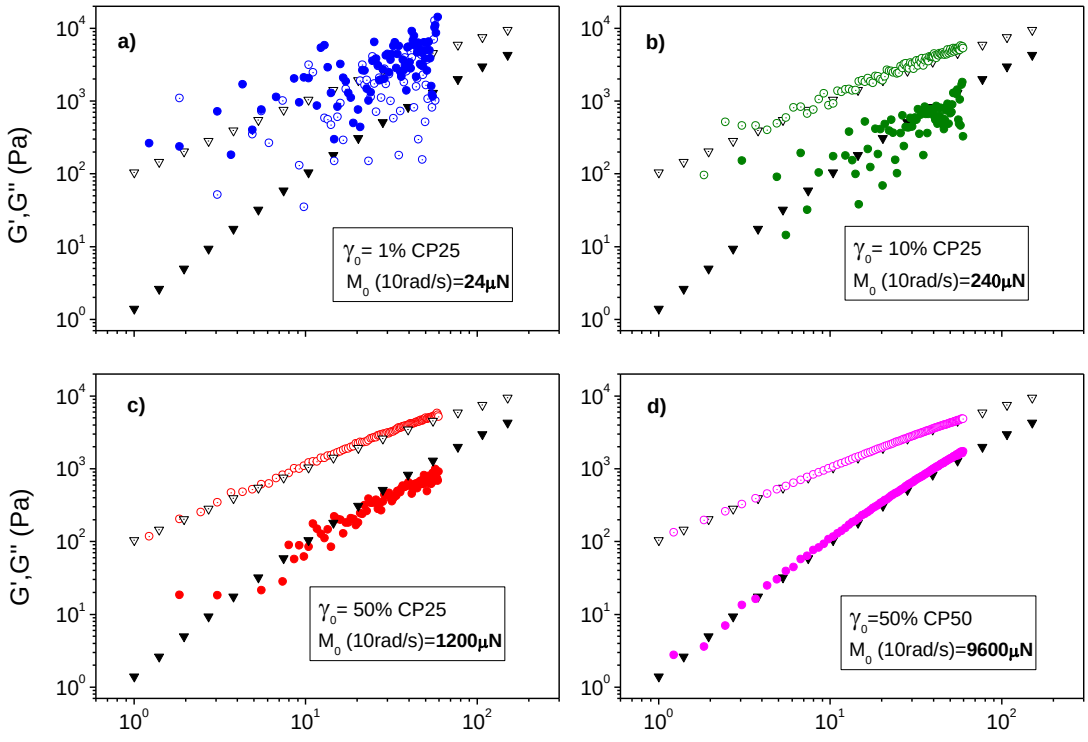

Figure 5.5: LVE spectra of PDMS 100 Pa s obtained by OWCh excitation in MCR702 at 23 °C. Torque signal strength is gradually increased from a) to d) as indicated in the legend. Black triangles are reference data from conventional DFS from the same instrument. Filled and unfilled sysmols denote G' and G" respectively.

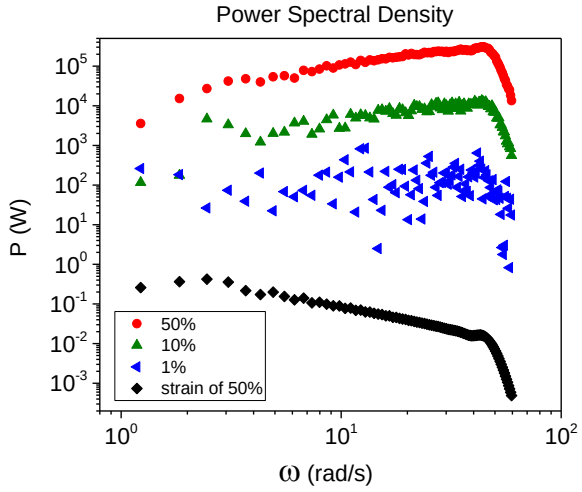

Figure 5.6: From the top: the spectral energy distribution per unit time (s) of stress response for 50, 10 and 1 % strain amplitude. The black curve is the PSD of actual strain at 50% amplitude.

5.5. Validation in PZR

The applicability of PZR-OWCh was validated in a frequency range of 10 to 1000 rad/s. High frequency chirp signals can have short duration without compromising the data integrity by keeping TB>100. Even T as short as 0.7 s is possible with reduced spectrum leakage effect (Figure 5.3). To validate chirp measurements in the PZR, a pDMS and a linear polybutadiene solution were measured. The former is a viscosity standard ((Brookfield, USA) with nominal zero shear viscosity of 1000Pa s at 25 °C. LVE reference data were provided by means of conventional DFS-MCR702 up to 300 rad/s. The latter sample is a thermo-rheological simple material hence its LVE spectrum can be time-temperature shifted. This allows the conventional rotational rheometers to extend their frequency range to higher frequencies by cooling and shifting the data. Polybutadiene of 44.5 kg/mol, was diluted in squalene at a concentration of 75% wt/wt. Cyclohexane was used as co-solvent with squalene and subsequently removed with vacuum while 2,6 di-tert-butyl-p-cress was added to prevent oxidation. The sample prepared is a well entangled solution with 19 entanglements per chain (Rubinstein & Colby, 2003). Dynamic frequency sweeps were performed at various temperatures from 23 to – 60 °C with an ARES rheometer (2 k FRTN1) at 3% strain amplitude. All data were shifted to 23 °C. The reference LVE data were obtained with this method extending the high frequency limit to 10^5 rad/s. The same sample was also measured in PZR with the OWCh method. The chirp frequency varied exponentially in time from 10 to 1000 rad/s as shown in Figure 5.7a, according to eq. 3. The whole frequency scan lasted only 0.7 s including a 0.2 s of waiting time for the setup initiation. The excitation and the response, raw signals are illustrated in Figure 5.7(b), (c) as voltage waveforms.

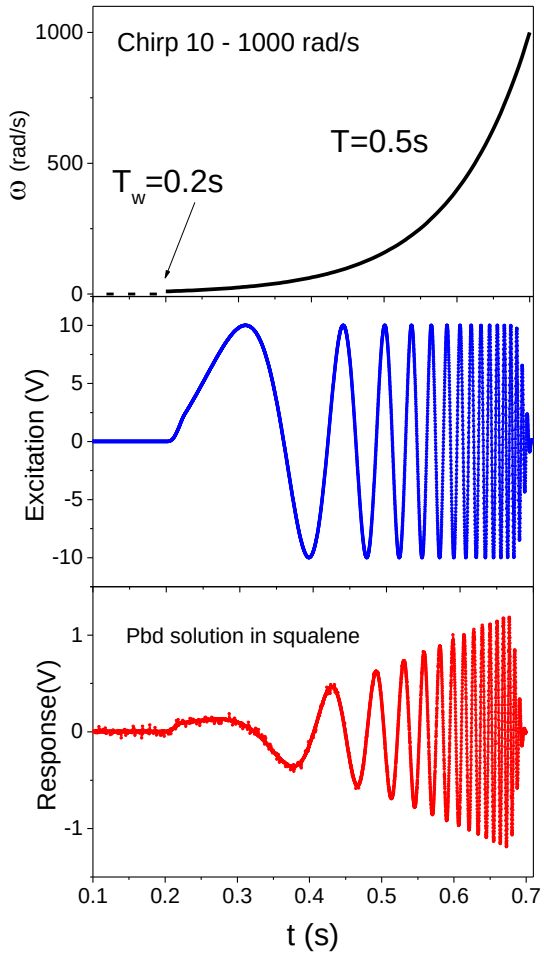

Figure 5.7: High-frequency excitation chirp (OWCh) and response of polybutadiene solution in PZR2. From top to bottom : the exponential variation of instantaneus frequency ω(t) calculated from Eq.3 varying 10 to 1000 rad/s , the excitation and the response raw signal in volts. T=5 s, T_w =0.2 s, taper 10% and TB=78. Tw is a delay time introduced in the excitation signal, in accord with previous work.

After normalization of the response signal based on the initial PZR calibration (Athanasiou et al., 2019) and by means of Eq. (1) data were converted in the frequency domain. Figure 5.8(a) depicts the medium frequency validation. Data obtained by the OWCh –PZR method superimpose nicely with that from DFS-PZR and the reference DFS measurement by MCR702 albeit the latter are limited in frequency range. The high frequency OWCh-PZR method is validated in Figure 5.8(b) where data are now compared with time-temperature shifted reference data of linear polybutadiene solution. Notably, the PZR-OWCh data were validated at the shorter allowable measurement time, T=0.5 s, corresponding to a marginal TB=78. Nonetheless, below we will utilize for all our applications a safer value of T=1 s resulting in a twofold increase of TB that prohibits further the effect of spectrum leakage.

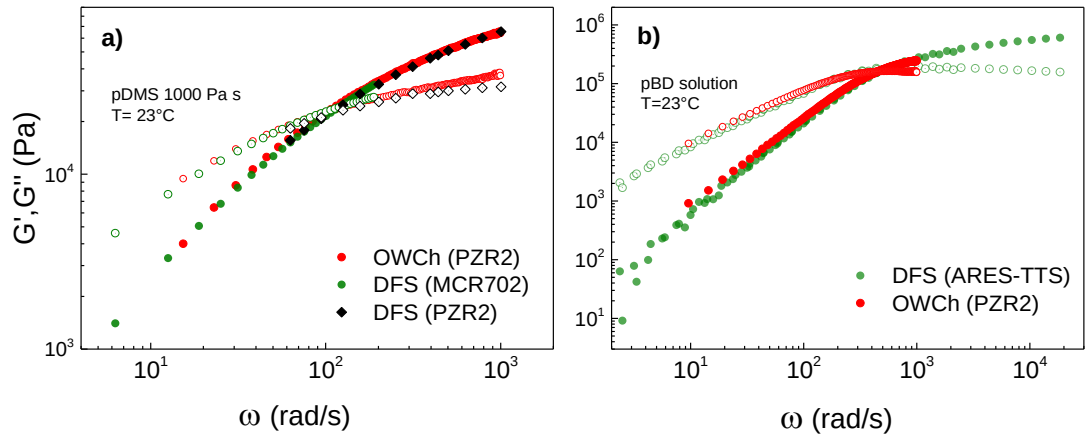

Figure 5.8: Validation of PZR-OWCh method. a) comparison of LVE spectra of pDMS obtained by MCR702-DFS (reference), PZR2 (DFS) and PZR2-OWCh. b) comparison of LVE spectra of pBD solution in squalene obtained by time temperature shifted ARES-DFS data (reference), and PZR2-OWCh .

5.6. Curing of a vinylester (VER) resin

VERs consist of a blend of an epoxy resin and methacrylic acid. Many commercial vinylester resins can "cold" cure i.e. under room temperature through a free-radical polymerization. An accelerator, usually cobalt hexanoate (HxCo) is pre-added, in order to boost the free radical process. Methyl ethyl ketone peroxide (MEKP) serves as an initiator thus pot-life counts from the moment of mixing. Styrene monomer serves as solvent of the uncured resin while it participates in the reaction leaving no by-products. Our test sample is a commercial resin, HQ800 A45 (Sirca s.p.a., Italy), with a styrene content of 32% w/w the latter measured via gas chromatography-flame ionization detection. It is a slow curing resin suitable to produce fiber reinforced composites with vacuum infusion method (Abdurohman, Satrio, & Muzayadah, 2018). Usually posturing at elevated temperatures is required for these resins to acquire their optimum mechanical strength. Its slow curing facilitated the experiment. Followed the addition of MEKP, mixing was completed in a roller mixer for 3 min. The cure kinetics are temperature and MEKP concentration dependent (Martin, Laza, Morras, Rodrıguez, & Leon, 2000) and for most of our experiments were kept constant i.e., T=23°C and 1.8% wt/wt respectively unless noted. All times reported were counted from the moment of MEKP addition. After another 3 min of rest the sample was loaded to the instrument where the moduli evolution was followed.

Macroscopically, during isothermal curing, resins exhibit gelation and vitrification. In the ideal case when the network initially densifies the gel point is defined when G´´/G´=tan(δ) is frequency independent (Chambon & Winter, 1987) while past this point the sample behaves as a rubbery solid. As

the degree of crosslinking further increases, glass transition temperature increases and vitrification occurs when the latter is greater than the curing temperature (Harran & Laudouard, 1986; Langeet al., 2000). Free volume is reduced and chain mobility slows down significantly. As a result, in this glassy state curing rate drops significantly and the modulus approaches a plateau over time. Capturing the gel point is not in the scope of this study. There are cases where the percolating network deviates from the ideal self-similarity (Aoki et al., 2019; Lieleg & Bausch, 2007; Bantawa et al., 2022) hence gelation can be attributed to the transition point from liquid to solid-like behavior yet this is frequency dependent. We will focus on the post-gel state where the high signal to noise ratio prevents spurious bands to emerge as artifacts in the measured spectrum. Only SAOS data taken with MCR702 are shown for the pre-gel state.

5.6.1 Mechanical response during curing

Below we first discuss results with conventional DFS and specifically a short duration DFS. This 5-point DFS from 200 down to 1 rad/s lasts only 84s. Nevertheless, G´ data are inconsistent as suggested by the negative slope in Figure 5.9(a). On the other hand, only when |G*| for each frequency point is plotted against the actual measuring time, the data become meaningful. Indeed Figure 5.9(b) shows the time evolution of |G*| for 4 different frequencies. They all refer to the same loading hence same crosslinking path (with MEKP content 2% wt/wt). The data exhibit two exponential regimes at early and late times typically seen in many evolving, crosslinking systems (Martin et al., 2000). From these different slopes in figure 9 it is clear that τ_{Mu} is frequency and time dependent. We will focus on the faster |G*| evolution that is detected for ω=1rad/s for t >1500 s. The dashed line indicates the best data fit with a fit function indicated in the inset of figure 9b. Following eq. 1 we get a τ_{Mu} =101 s constant within this time range corresponding to a N_{mu}= 0.83, a value larger than the criterion of N_{mu}<0.2. This clearly suggests that T must be reduced further, below 20 s, values that are however not feasible in conventional DFS even with a frequency step of a few points per decade.

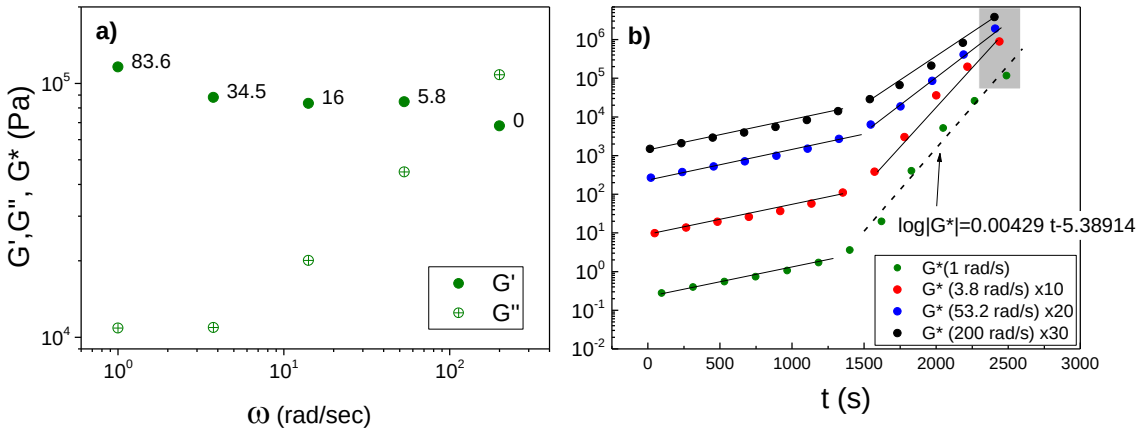

Figure 5.9: LVE of crosslinking VER measured with MCR 702 a) 5 point conventional DFS inconsistency : a negative slope in G´ . Numbers indicate test time. b) |G*| data from a sequence of 5 point DFS intervals ploted against actual time of measurement of each frequency point. Only 4 out of 5 different frequencies are shown, shifted vertically for clarity as indicated. Solid lines are guides whereas the dashed one is data best fit. Data included in the grey shaded area corespond to DFS interval depicted in (a).

Here the benefit of OWCh rheometry becomes evident. Contrary to a conventional DFS, a T=10 s OWCh-MCR702 measurement is sufficiently short for the proper determination of the LVE of the sample with a N_{Mu} ~ 0.1. Likewise, the 1 s OWCh-PZR measurement corresponds to N_{mu} ~0.01 providing nearly isotemporal data at each frequency scan.

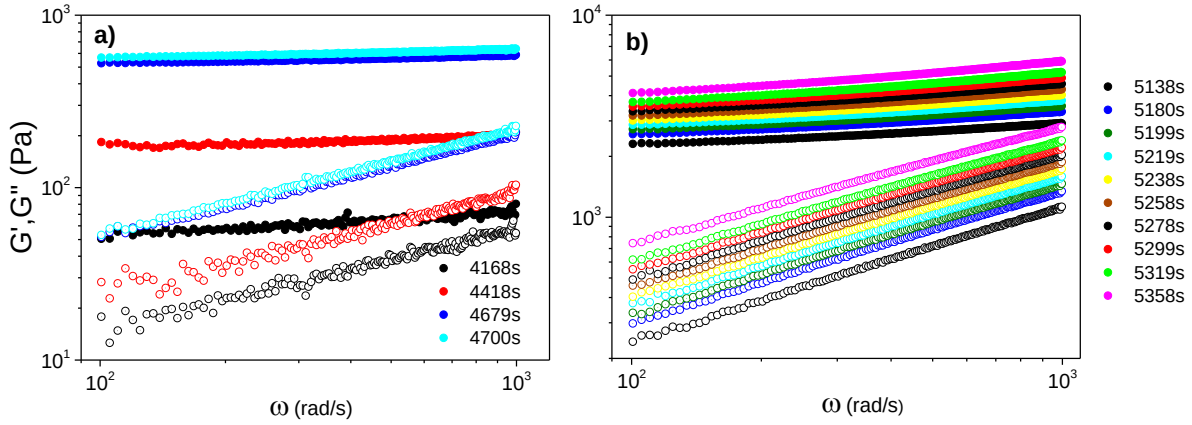

Figure 5.10 LVE spectra of curing vinylester resin measured with the OWCh-PZR tecnique. Few out of the 56 measurements are shown for clarity at: a)early and b)long times. Legend indicates the elapsed time from MEKP addition and mixing.

Catalyzed vinylester resin (with MEKP 1.8% wt/wt) was loaded in the PZR. A series of 56 OWCh measurements were performed with a repetition period of approximately 20 s and T=1 s at the post gel

regime. The obtained spectrum of four of these, namely the 1st, 12th, 25th and 26th chirp, at early times, is shown in Figure 5.10(a). The 1st OWCh-PZR measurement at 4168 s (70 min) indicates a high frequency G′, G′′crossover slightly above 1000 rad/s, attributed to local interactions. In these, shorter than millisecond, time scales there is still some freedom for local motion therefore G′′ approaches G′ in analogy with dynamics related to the in-cage rattling of colloidal glasses (Athanasiou et al., 2019) although in the latter, the physics are fundamentally different. As the network densifies this crossover shifts to higher frequencies and further out of the experimental window (red curve at 4418 s), while both moduli increase one order of magnitude within 500 s (blue curve at 4679 s). Cyan curve corresponds to times only 21 s later capturing the finite moduli evolution in this short period. The evolution at long times represented by the last 10 chirps is followed in Figure 5.10(b) where both moduli continue to increase with G′ observed to increase faster at high frequencies consistently with the data of Figure 5.9. On the other hand, the phase angle exhibits a non-monotonic behavior as seen in Figure 5.11(a). At early times it constantly decreases as the sample becomes more solid-like whereas at long times it increases again. This increase, indicative of an increased dissipation in the system during curing is counter intuitive for a crosslinking network with a constantly increasing junction density.

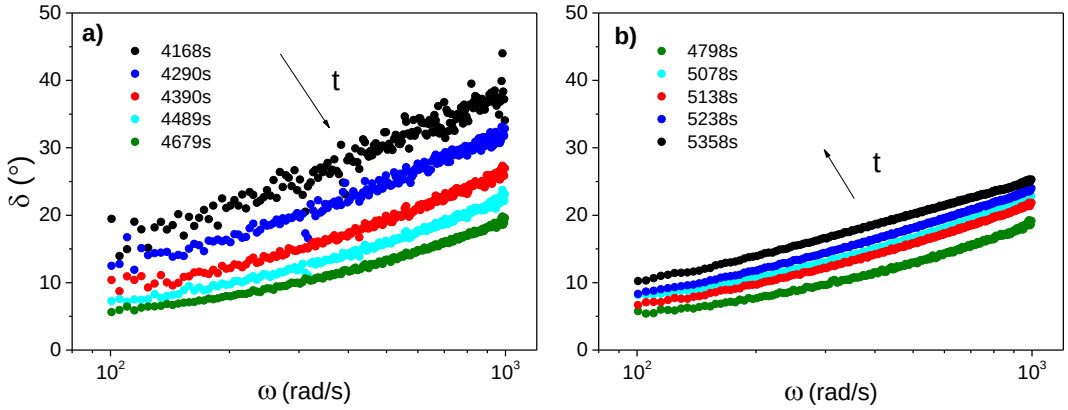

Figure 5.11 Phase angle dependence on curing time of vinylester resin measured with the OWCh-PZR tecnique. Few out of the 56 measurements are shown for clarity at a)early and b)long times. Arrows indicate time order.

However LVE properties are also affected by the glass transition temperature that constantly evolves with curing times. The distance from this temperature differs significantly at each moment and apparently is related to the curing temperature (Aoki et al., 2019; Harran & Laudouard, 1986; Lange et al., 1999).

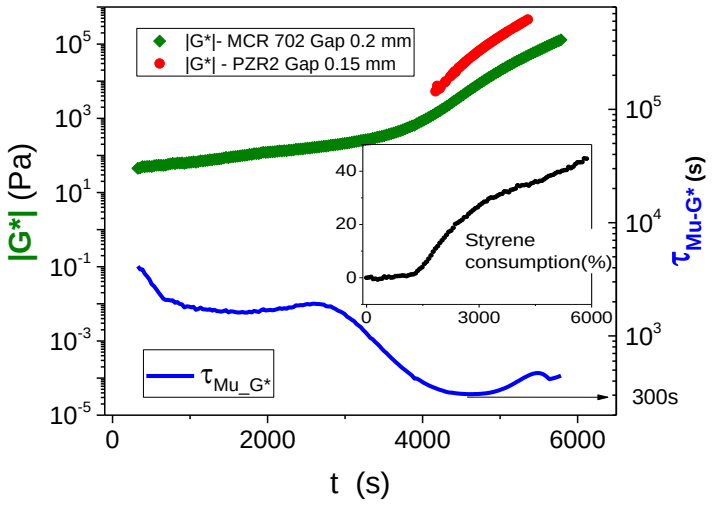

Figure 5.12: The evolution of |G*| at 200 rad/s. Data correspond to DTS with MCR702 (olive curve) and a sequence of 56 OWCh (chirps) with PZR. Blue curve denotes the mutation time variation as curing evolves. Black arrow points the shortest value of τ_{Mu_G*}. Inset show the styrene consumption for the same period from FTIR measurement.

It is tempting to compare |G*| derived from OWCh-PZR and DTS-MCR702 at the frequency of 200rad/s that is accessible by both instruments. The moderate discrepancy between the olive and red curve in Figure 5.12 can be attributed to minor differences in temperature history during and after mixing. The uncertainty of time cannot be entirely eliminated due to different loading procedure between MCR702 and PZR. Two additional reasons, potentially important are the following: Firstly, the crosslinking path is not identical when the experiment is repeated. This differentiation is enhanced when the sample dimensions and the dissipation rate of the generated heat is different. Secondly, the confinement effect becomes important in the smaller gap of PZR or similarly in small gap plate-plate geometries in conventional rheometers or near the center in cone-plate geometry. Therefore, we used parallel plate (25 mm) geometry with a gap of 0.2 mm in the MCR 702, which is close to the gap of 0.15 mm used in the PZR. Still however this does not ensure data direct quantitative comparison between the two instruments even though the gap is comparable due to the inhomogeneous microstructure and different history. The dependence of mutation time on curing time can be calculated from Eq. (1) based on MCR702-DTS data as depicted in Figure 5.12 (blue curve). The shortest time is 300 s corresponding to Mu< 0.03 and 0.003 for OWCh-MCR702 and OWCh-PZR measurements respectively. Notably, this estimation is only related to G* at a frequency of 200 rad/s. Given that this information is not *apriori* known in experiments, working at small Mu values is important to ensure proper measurement of the LVE of a time evolving material. Here, this is important considering that most general purpose resins cure considerably faster, usually within 15-30 minutes while fast-curing epoxies require only 5 min.

5.6.2 Microscopic changes during curing

The degree of crosslinking during curing was quantified by FTIR spectroscopy (Chung & Greener, 1988) where changes in the chemical composition, such as the styrene consumption, can be monitored. Although several peaks can be attributed to styrene in the FTIR absorbance spectrum other substances may also interfere with these peaks. To identify a reference peak the styrene content at the initial state was removed via evaporation and the IR absorbance spectra was compared before and after styrene removal (see Fig S2). The peak at 910 cm^{-1} was then confirmed to reflect styrene content with its strength decreasing as curing advanced. Results are plotted in the inset of Figure 5.12 indicating similar trend with |G*| (Fig S3).

Our LVE measurements were limited at long times by the build-up of strong normal forces that exceeds eventually the limits of the rheometer transducer. This point is now determined at ~ 40% degree of crosslinking. For a more accurate estimation the bisphenol-A diglycerol ether metacrylate consumption must also be measured however the corresponding peak at 815 cm^{-1} overlaps with one attributed likely to an aromatic origin. Differential scanning calorimetry is an alternative way to determine the crosslinking evolution (Guo et al., 2009). However, the reaction path changes substantially at these small sample dimensions and mapping the exothermic rate to the rate of conversion is not trivial (Roose, Vermoesen, & Van Vlierberghe, 2020) and outside the scope of this.

5.6.3 Curing of Vinyl-ester resin with inorganic fillers

The addition of inorganic fillers is a common practice to strengthen the mechanical properties of resin based composites. Reinforcement increases the modulus and response signal strength therefore measurements via an OWCh are possible even at the very early stages of crosslinking. A sequence of 16 OWCh-MCR702 with T=9 s was applied to vinylester resin reinforced with 8% wt/wt fumed silica R200 (Degussa, Germany). At this concentration and once the mixing is completed the sample exhibits solid like response (gel). The LVE evolution during cure is shown in Figure 5.13 where the modulus at 2500 s is almost one order of magnitude higher than pristine vinylester resin of Figure 5.12. At early times, t<4000 s, colloidal interactions are predominant. The space-filling network of flocks is formed due to interparticle attractions (Barthel, 1995) and the modulus evolution is weakly affected by the slow increase of the matrix viscosity. The crosslinking rate is significantly reduced due to reinforcement (Nikzamir, Mortezaei, & Jahani, 2019). At longer times the matrix crosslinking leads to a dramatic increase of the elastic modulus. The mechanical properties of the cured, as well the uncured sample, are greatly affected by the dispersion quality of the filler. Strain history is important and this cannot be fully controlled during loading and mixing affecting data reproducibility (Dullaert & Mewis, 2005; Raghavan & Khan, 1995).

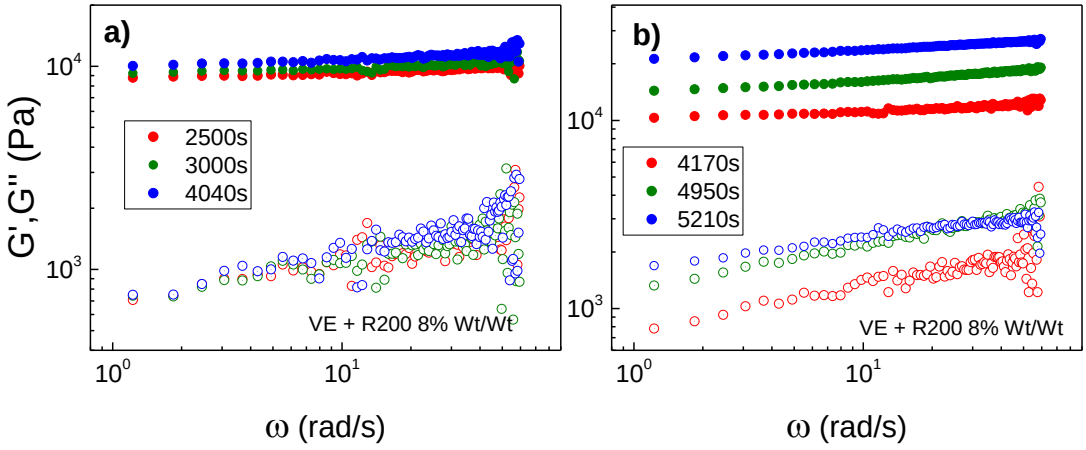

Figure 5.13 LVE spectra of curing vinilester resin and fumed silica measured with the OWCh-MCR702 tecnique. Few out of the 16 measurements are shown for clarity at early (a) and long (b) times. Legend indicates the elapsed time from MEKP addition and mixing.

5.7 Sensitivity to gap dimension

When the gap decreases at values comparable to the characteristic length scale of the microstructure the continuum assumption brakes down and the measurement becomes sensitive to microstructural details, the so called confinement effect. The PZR operates at gaps of 150μm to mitigate sample inertia while a typical gap for plate-plate measurement in a rheometer ranges between 0.5 and 1.5 mm. Large gaps are limited by the distortion of the air-sample interface when hydrostatic pressure overcomes surface tension and, sample inertia (Schrag, 1977). On the other hand, small gaps promote paralelicity errors and enhance confinement effect as the crosslinking sample may not be micro-structurally homogeneous (Clasen & McKinley, 2004). In Carbopol gels the confinement effect has been found to dominate at gaps smaller than ~150 μm (Liu et al., 2018; Yan et al.,Adams, 2010) yet these studies concern nonlinear deformations. The effect of gap dimension on the measured LVE of a crosslinking system stems from two major reasons the sensitivity of the followed crosslinking path to sample dimension (thickness) and confinement effect. To verify this we performed different runs of DTS in MCR702 with parallel plate of 25mm radius. The gap was varied from 1.2 to 0.15 mm. To rule out the possibility of an alignment error or the finite optical encoder angular deflection resolution becoming important in small gaps, we performed a test run with pDMS oil with the same gap values. No gap dependence was observed.

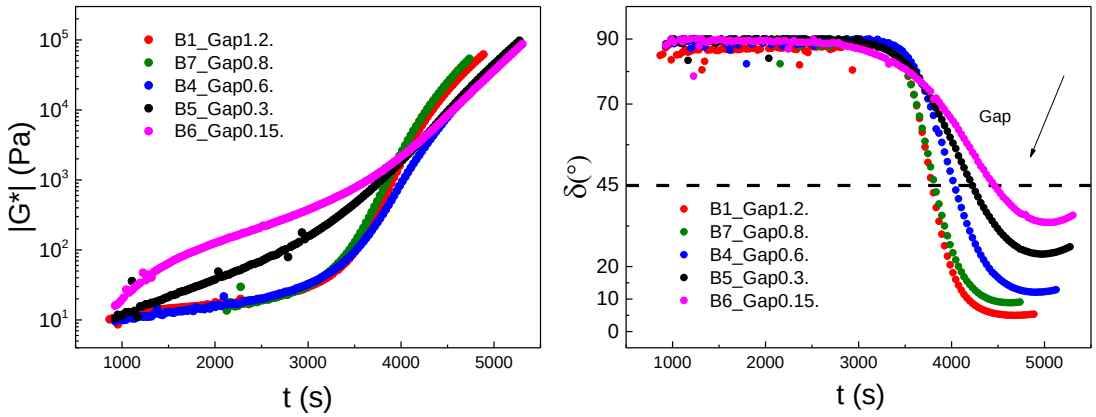

Figure 5.14 Gap dependence of G*(a) and phase angle (b) . DTS was performed with MCR702 with PP25 geometry at 53.2 rad/s and T=23 °C. Dashed line indicates the liquid to solid-like transition.

To the contrary, results from the crosslinking VER (see Figure 5.14) confirm a G* gap dependence. At early times (up to 3500 s) the reduction of gap from 1.2 to 0.6 mm has no effect in |G*| evolution. Minor differences can be attributed to variations in crosslinking path. When the gap was further reduced to 0.3 and 0.15mm, |G*| exhibited faster increase at early times, presumably due to the confinement effect. Once the network is fully established |G*| evolution is similar (t > 4000s) for all gaps. Phase angle dependence seems weak at early times while there is a strong increase with gap decrease at post gel regime. This can be both due to confinement and slower crosslinking as supported by the lower values of |G*| for smaller gaps. This gap dependence could in principle be due to wall slip (Yoshimura & Prud'homme, 1988) however this can be ruled out as during this curing stage the sample is literally glued to the tools. Instrument compliance could also affect data as gap is reduced. A purely elastic instrument compliance results in phase angle underestimation (Sternstein 1983) and introduces a gap dependent error in both |G*| and phase angle (Liu *et al.*, 2011). This is clearly not the case here as verified by the LVE measurements of a homogeneous reference sample (PDMS) at similar gap range (see Fig.A.8 in Appendix A.5). On the other hand gap clearly affects measurements of non-homogenous samples and this should be accounted for when comparing data from different instruments and geometries. Small gaps promote apparent solid-like response as stresses are transmitted via shorter paths. Under constant gap the time evolution of δ exhibits a non-monotonic behavior. For all gaps at early times, δ decreases initially towards the liquid to solid transition (δ=45^{o}) however, exhibits an upturn at long times suggestive of an increased dissipation in the system, confirming the trend observed in OWCh-PZR measurements (see Figure 5.11). This inflection point has been attributed to the onset of vitrification process (Aoki et al., 2019; Harran & Laudouard, 1986; Jakob Lange et al., 1999). Chemical cross-linking promotes denser packing thus volume shrinkage

leads to normal forces from the sample held at constant gap during cure. To this end a zero normal force protocol is utilized by many authors (Lehéricey et al., 2021). In PZR such a protocol is not feasible. In an effort to keep similar experimental conditions in both instruments zero normal force was not used in MCR702 where experiments were run up to a normal force of 5N FigA6. Small gaps mitigate normal forces as the total normal deformation is reduced.

5.8 Conclusions

Undoubtedly, amplitude-frequency modulated chirp rheometry reduces the test time considerably compared to conventional DFS hence, it is the method of choice for the LVE interrogation of fast evolving systems. The application in commercial rotational rheometers is straight forward though requires protocols tailored to the specific instrument. Limitations are mainly imposed by the data acquisition system of the rheometer and the motor-controller ability to impose the commanded strain waveform. These limits were exploited for the Anton Paar MCR702 and the simpler PZR with the operability window and the optimum parameters was discussed. The torque strength should be increased at least 10 times more than in a conventional DFS for the MCR702. The PZR is less affected by data acquisition limitations and is capable of producing short interrogating chirps on the order of 1 s, keeping N_{mu} sufficiently low, even for fast evolving systems. The technique was validated for both instruments and exploited to follow a fast curing vinylester resin. The LVE evolution was measured in conjunction with styrene consumption. The G´ evolution seems faster in higher frequencies The mutation time varies considerably with curing time hence a safe margin should be adopted. Confinement effects were found to be critical in gaps smaller than 0.3mm and should be considered when data are evaluated and modeled. Given the proof of concept is established, a systematic study with industrial resins reinforced with various fillers such as fumed silica will provide valuable information on the curing process of many commercial products. The developed toolbox can be utilized for studying a plethora of curing and fast evolving materials in the context of fundamental and application-driven research.

Appendix A.5

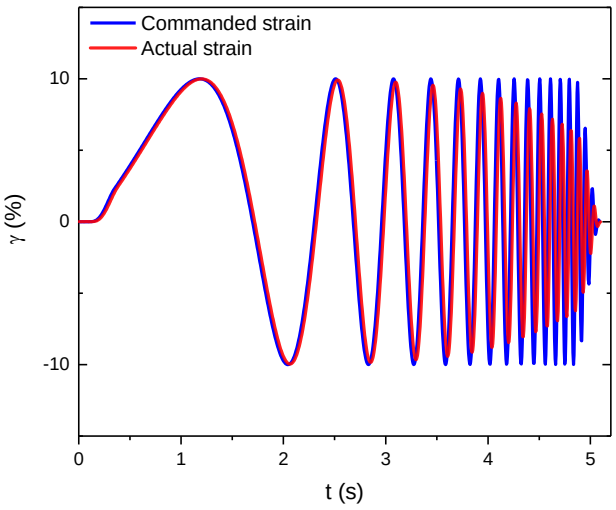

Figure A.1 Chirp strain waveform performed by MCR 702. Blue curve denotes the commanded strain as calculated by Matlab and fed to the instrument's software. The red is the actual starin logged by the instruments angular deflection encoder. Chirp parameters are ω_{Min}=0.83 rad/s, ω_{Max}= 100 rad/s, γ_o = 10%, taper 10% **and T=5 s.** Data N Kalafatakis

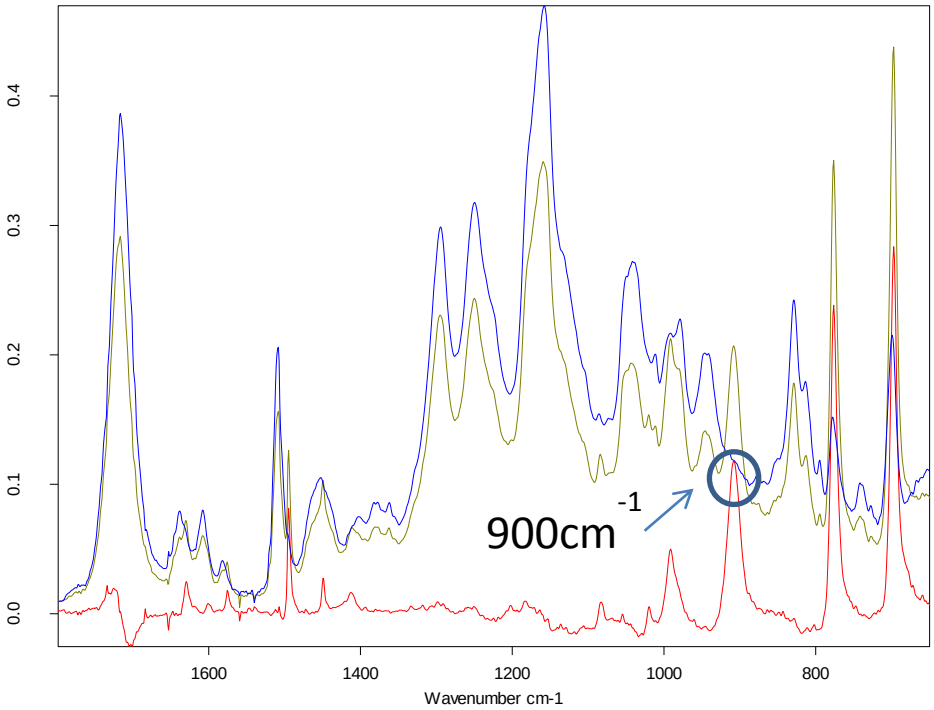

Figure A.2: FTIR spectra of uncured pristine resin (green curve) , uncured resin after styrene evaporation (blue curve) and the sunbtraction of the above (red curve) that coresponds to styrene. Peak at 900cm^{-1} is absent from the blue spectrum hence can be utilized to quantify sturene consumtion. Data Patrice Rose

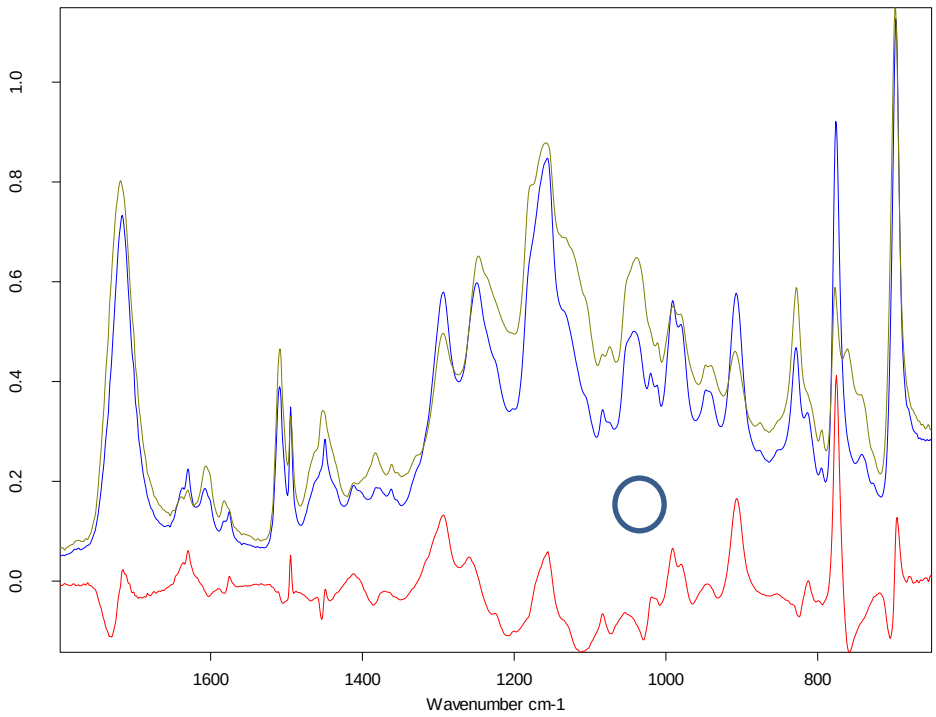

Figure A.3 FTIR spectra of partially cured resin (green curve) , uncured resin after styrene evaporation (blue curve) and the sunbtraction of the above (red curve) that coresponds to styrene content at the present state of cure. Peak heigt at 910cm^{-1} is significantly reduced. Data Patrice Rose

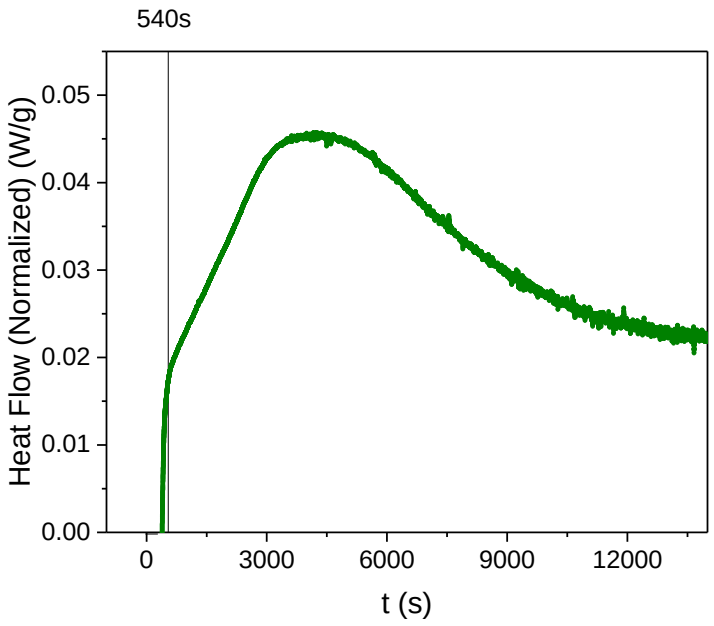

Figure A.4 Differential scanning calorimetry of isothermally curing vinylester resin at 23 °C.

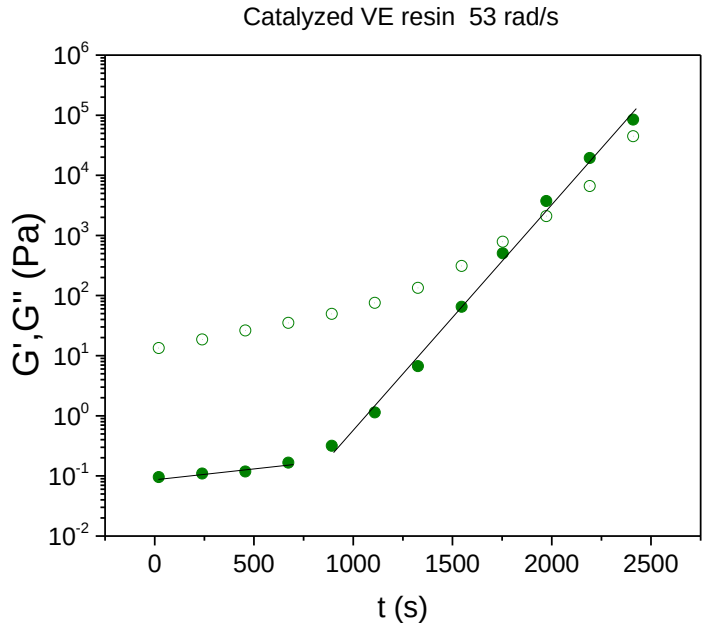

Figure A.5 Evolution of G´,G´´ of catalyzed vinylester at 53 rad/s . Data obtained by the 5Point DFS protocole with MCR702.

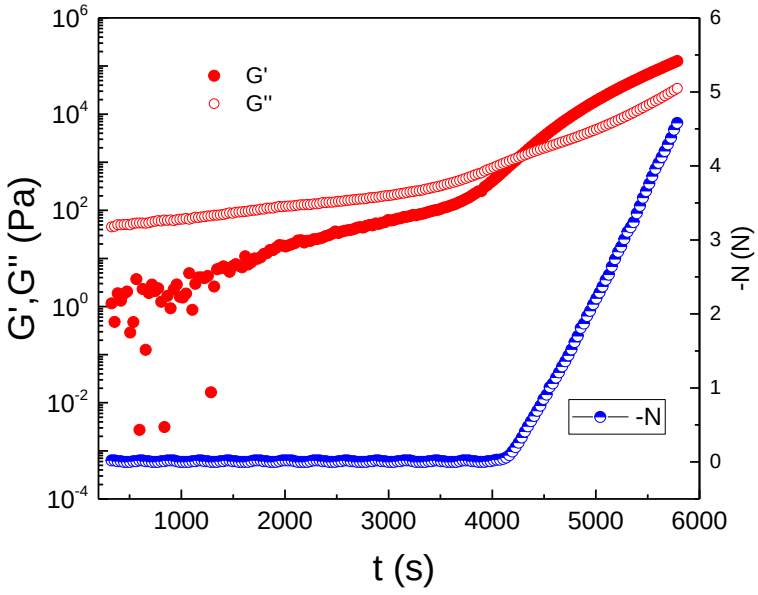

Figure A.6 Evolution of G´,G´´ of pristine vinylester at 200 rad/s . Data obtained by DTS protocole, with PP25 geometry and gap 0.2mm in MCR702. Blue curve shows the evolution of normal forces due to shringage.

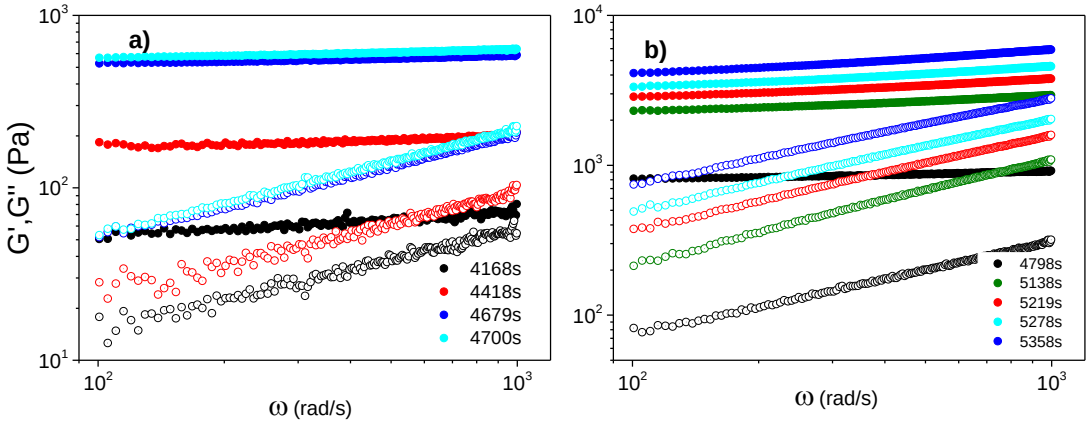

Figure A.7 LVE spectra of curing vinilester resin measured with the OWCh-PZR tecnique. Few out of the 56 measurements are shown for clarity at early (a) and long (b) times. Legend indicates the elapsed time from MEKP addition and mixing.

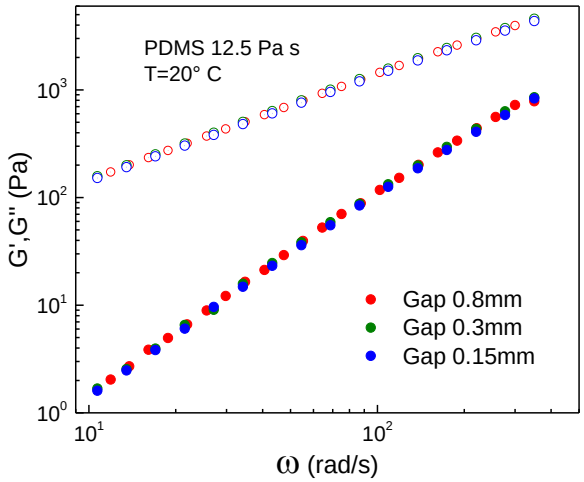

Figure A.8 LVE spectra of a homogeneous reference sample (PDMS standard) measured with PP25mm geometry in MCR702 at different rheometric gaps. Data agreement supports the absence of compliance effects.

References:

Abdurohman, K., Satrio, T., & Muzayadah, N. (2018). *A comparison process between hand lay-up, vacuum infusion and vacuum bagging method toward e-glass EW 185/lycal composites.* Paper presented at the Journal of Physics: Conference Series.

Adachi, T., Osaki, M., Araki, W., & Kwon, S.-C. (2008). Fracture toughness of nano-and micro-spherical silica-particle-filled epoxy composites. *Acta Materialia, 56*(9), 2101-2109.

Aoki, M., Shundo, A., Kuwahara, R., Yamamoto, S., & Tanaka, K. (2019). Mesoscopic heterogeneity in the curing process of an epoxy–amine system. *Macromolecules, 52*(5), 2075-2082.

Athanasiou, T., Auernhammer, G. K., Vlassopoulos, D., & Petekidis, G. (2019). A high-frequency piezoelectric rheometer with validation of the loss angle measuring loop: application to polymer melts and colloidal glasses. *Rheologica Acta, 58*(9), 619-637.

Bachman, G., Narici, L., & Beckenstein, E. (2000). *Fourier and wavelet analysis* (Vol. 586): Springer.

Bantawa, M., Keshavarz, B., Geri, M., Bouzid, M., Divoux, T., McKinley, G. H., & Del Gado, E. (2022). The hidden hierarchical nature of soft particulate gels. *arXiv preprint arXiv:2211.03693*.

Barthel, H. (1995). Surface interactions of dimethylsiloxy group-modified fumed silica. *Colloids and Surfaces A: Physicochemical and Engineering Aspects, 101*(2-3), 217-226.

Bates, F. S., & Fredrickson, G. H. (1990). Block copolymer thermodynamics: theory and experiment. *Annual review of physical chemistry, 41*(1), 525-557.

Biron, M. (2013). *Thermosets and composites: material selection, applications, manufacturing and cost analysis*: Elsevier.

Bouzid, M., Keshavarz, B., Geri, M., Divoux, T., Del Gado, E., & McKinley, G. H. (2018). Computing the linear viscoelastic properties of soft gels using an optimally windowed chirp protocol. *Journal of Rheology, 62*(4), 1037-1050.

Cardinaels, R., Reddy, N. K., & Clasen, C. (2019). Quantifying the errors due to overfilling for Newtonian fluids in rotational rheometry. *Rheologica Acta, 58*(8), 525-538.

Chambon, F., & Winter, H. H. (1987). Linear viscoelasticity at the gel point of a crosslinking PDMS with imbalanced stoichiometry. *Journal of Rheology, 31*(8), 683-697.

Chung, K., & Greener, E. (1988). Degree of conversion of seven visible light-cured posterior composites. *Journal of Oral Rehabilitation, 15*(6), 555-560.

Clasen, C., & McKinley, G. H. (2004). Gap-dependent microrheometry of complex liquids. *Journal of Non-Newtonian Fluid Mechanics, 124*(1-3), 1-10.

Crasto, A., & Kim, R. (1993). On the determination of residual stresses in fiber-reinforced thermoset composites. *Journal of Reinforced Plastics and Composites, 12*(5), 545-558.

Curtis, D., Holder, A., Badiei, N., Claypole, J., Walters, M., Thomas, B., . . . Williams, P. (2015). Validation of optimal Fourier rheometry for rapidly gelling materials and its application in the study of collagen gelation. *Journal of Non-Newtonian Fluid Mechanics, 222*, 253-259.

Du Plessis, H. (2010). *Fibreglass boats: Construction, gel coat, stressing, blistering, repair, maintenance*: A&C Black.

Dullaert, K., & Mewis, J. (2005). A model system for thixotropy studies. *Rheologica Acta, 45*(1), 23-32.

Fielding, S. M., Sollich, P., & Cates, M. E. (2000). Aging and rheology in soft materials. *Journal of Rheology, 44*(2), 323-369.

Flory, P. J. (1953). *Principles of polymer chemistry*: Cornell university press.

Geri, M., Keshavarz, B., Divoux, T., Clasen, C., Curtis, D. J., & McKinley, G. H. (2018). Time-resolved mechanical spectroscopy of soft materials via optimally windowed chirps. *Physical Review X, 8*(4), 041042.

Ghiringhelli, E., Roux, D., Bleses, D., Galliard, H., & Caton, F. (2012). Optimal fourier rheometry. *Rheologica Acta, 51*(5), 413-420.

Guo, Z., Ng, H. W., Yee, G. L., & Hahn, H. T. (2009). Differential scanning calorimetry investigation on vinyl ester resin curing process for polymer nanocomposite fabrication. *Journal of Nanoscience and Nanotechnology, 9*(5), 3278-3285.

Harran, D., & Laudouard, A. (1986). Rheological study of the isothermal reticulation of an epoxy resin. *Journal of Applied Polymer Science, 32*(7), 6043-6062.

Harris, F. J. (1978). On the use of windows for harmonic analysis with the discrete Fourier transform. *Proceedings of the IEEE, 66*(1), 51-83.

Holly, E. E., Venkataraman, S. K., Chambon, F., & Winter, H. H. (1988). Fourier transform mechanical spectroscopy of viscoelastic materials with transient structure. *Journal of Non-Newtonian Fluid Mechanics, 27*(1), 17-26.

Horowitz, P., Hill, W., & Robinson, I. (1989). *The art of electronics* (Vol. 2): Cambridge university press Cambridge.

John Rathinaraj, J. D., & McKinley, G. H. (2023). Gaborheometry: Applications of the discrete Gabor transform for time resolved oscillatory rheometry. *Journal of Rheology, 67*(2), 479-497.

Kawasaki, T., & Tanaka, H. (2014). Structural evolution in the aging process of supercooled colloidal liquids. *Physical Review E, 89*(6), 062315.

Klauder, J. R., Price, A., Darlington, S., & Albersheim, W. J. (1960). The theory and design of chirp radars. *Bell System Technical Journal, 39*(4), 745-808.

Kowatsch, M., & Stocker, H. (1982). *Effect of Fresnel ripples on sidelobe suppression in low time-bandwidth product linear FM pulse compression.* Paper presented at the IEE Proceedings F (Communications, Radar and Signal Processing).

Lanczos, C., & Boyd, J. (2016). *Discourse on Fourier series*: SIAM.

Lange, J., Altmann, N., Kelly, C., & Halley, P. (2000). Understanding vitrification during cure of epoxy resins using dynamic scanning calorimetry and rheological techniques. *Polymer, 41*(15), 5949-5955.

Lange, J., Ekelöf, R., & George, G. A. (1999). Charge-recombination luminescence as a monitor of network formation during cure of epoxy resins. *Polymer, 40*(1), 149-155.

Larson, R. G., & Wei, Y. (2019). A review of thixotropy and its rheological modeling. *Journal of Rheology, 63*(3), 477-501.

Läuger, J., & Stettin, H. (2016). Effects of instrument and fluid inertia in oscillatory shear in rotational rheometers. *Journal of Rheology, 60*(3), 393-406. doi: 10.1122/1.4944512

Läuger, J., Wollny, K., & Huck, S. (2002). Direct strain oscillation: a new oscillatory method enabling measurements at very small shear stresses and strains. *Rheologica Acta, 41*(4), 356-361.

Lehéricey, P., Snabre, P., Delots, A., Holten-Andersen, N., & Divoux, T. (2021). Time-resolved rheometry of drying liquids and suspensions. *Journal of Rheology, 65*(3), 427-436.

Levanon, N., & Mozeson, E. (2004). *Radar signals*: John Wiley & Sons.

Lieleg, O., & Bausch, A. R. (2007). Cross-linker unbinding and self-similarity in bundled cytoskeletal networks. *Physical Review Letters, 99*(15), 158105.

Lin, S., Cao, C., Wang, Q., Gonzalez, M., Dolbow, J. E., & Zhao, X. (2014). Design of stiff, tough and stretchy hydrogel composites via nanoscale hybrid crosslinking and macroscale fiber reinforcement. *Soft Matter, 10*(38), 7519-7527.

Liu, Y., Lorusso, D., Holdsworth, D. W., Poepping, T. L., & de Bruyn, J. R. (2018). Effect of confinement on the rheology of a yield-stress fluid. *Journal of Non-Newtonian Fluid Mechanics, 261*, 25-32.

Liu, C. Y., Yao, M., Garritano, R. G., Franck, A. J., & Bailly, C. (2011). Instrument compliance effects revisited: linear viscoelastic measurements. Rheologica acta, 50(5-6), 537

Macosko, C. W. (1985). Rheological changes during crosslinking. *British polymer journal, 17*(2), 239-245.

Macosko, C. W. (1994). *Rheology: principles, measurements, and applications*: Wiley-vch.

Markovitz, H. (1977). Boltzmann and the beginnings of linear viscoelasticity. *Transactions of the Society of Rheology, 21*(3), 381-398.

Martin, J., Laza, J., Morras, M., Rodrıguez, M., & Leon, L. (2000). Study of the curing process of a vinyl ester resin by means of TSR and DMTA. *Polymer, 41*(11), 4203-4211.

Mours, M., & Winter, H. (1994). Time-resolved rheometry. *Rheologica Acta, 33*(5), 385-397.

Negi, A. S., & Osuji, C. O. (2010). Time-resolved viscoelastic properties during structural arrest and aging of a colloidal glass. *Phys Rev E Stat Nonlin Soft Matter Phys, 82*(3 Pt 1), 031404. doi: 10.1103/PhysRevE.82.031404

Nikzamir, M., Mortezaei, M., & Jahani, M. (2019). Effect of surface area of nanosilica particles on the cure kinetics parameters of an epoxy resin system. *Journal of Applied Polymer Science, 136*(37), 47958.

Nuttall, A. (1981). Some windows with very good sidelobe behavior. *IEEE Transactions on Acoustics, Speech, and Signal Processing, 29*(1), 84-91.

Nyquist, H. (1928). Certain topics in telegraph transmission theory. *Transactions of the American Institute of Electrical Engineers, 47*(2), 617-644.

O'Brien, D. J., Mather, P. T., & White, S. R. (2001). Viscoelastic Properties of an Epoxy Resin during Cure. *Journal of Composite Materials, 35*(10), 883-904. doi: 10.1106/hlym-5cm7-bp9n-l1y1

Oppenheim, A. V., Buck, J. R., & Schafer, R. W. (2001). *Discrete-time signal processing. Vol. 2*: Upper Saddle River, NJ: Prentice Hall.

Parisi, D., Seo, J., Nazari, B., Schaake, R. P., Rhoades, A. M., & Colby, R. H. (2020). Shear-induced isotropic–nematic transition in poly (ether ether ketone) melts. *ACS Macro Letters, 9*(7), 950-956.

Prabhu, K. M. (2014). *Window functions and their applications in signal processing*: Taylor & Francis.

Raghavan, S. R., & Khan, S. A. (1995). Shear-induced microstructural changes in flocculated suspensions of fumed silica. *Journal of Rheology, 39*(6), 1311-1325.

Rathinaraj, J. D. J., Hendricks, J., McKinley, G. H., & Clasen, C. (2022). Orthochirp: A fast spectro-mechanical probe for monitoring transient microstructural evolution of complex fluids during shear. *Journal of Non-Newtonian Fluid Mechanics, 301*, 104744.

Reiter, G., & Strobl, G. R. (2007). *Progress in understanding of polymer crystallization* (Vol. 714): Springer.

Roose, P., Vermoesen, E., & Van Vlierberghe, S. (2020). Non-steady scaling model for the kinetics of the photo-induced free radical polymerization of crosslinking networks. *Polymer Chemistry, 11*(14), 2475-2484.

Rubinstein, M., & Colby, R. H. (2003). *Polymer physics* (Vol. 23): Oxford University Press New York.

Schrag, J. L. (1977). Deviation of velocity gradient profiles from the “gap loading” and “surface loading” limits in dynamic simple shear experiments. *Transactions of the Society of Rheology, 21*(3), 399-413.

Snijkers, F., Pasquino, R., & Maffezzoli, A. (2017). Curing and viscoelasticity of vitrimers. *Soft Matter, 13*(1), 258-268.
Starecki, T. (2014). Analog front-end circuitry in piezoelectric and microphone detection of photoacoustic signals. *International Journal of Thermophysics, 35*(11), 2124-2139.
Sternstein, S. S. (1983). Transient and dynamic characterization of viscoelastic solids.
Weatherhead, R. (2012). *FRP technology: fibre reinforced resin systems*: Springer Science & Business Media.
Wijers, R. (2018). A chirp, a roar and a whisper: Nature Publishing Group.
Wilhelm, M. (2002). Fourier-transform rheology. *Macromolecular Materials and Engineering, 287*(2), 83-105.
Yan, Y., Zhang, Z., Cheneler, D., Stokes, J., & Adams, M. (2010). The influence of flow confinement on the rheological properties of complex fluids. *Rheologica Acta, 49*(3), 255-266.
Yoshimura, A. S., & Prud'homme, R. K. (1988). Wall Slip Effects on Dynamic Oscillatory Measurements. *Journal of Rheology, 32*(6), 575-584. doi: 10.1122/1.549982

Chapter 6 : Measuring normal stress differences in cone-plate rheometry with a single loading.

6.1 Basic Concepts and Motivation

When solids are deformed plastically by shear, the normal stresses (diagonal elements of the extra stress tensor, defined in Chapter 1) become nonzero, resembling the so-called Poynting effect (Poynting 1909). Likewise, when polymeric soft materials are sheared these normal stresses $\sigma_{11,}$ $\sigma_{22,}$ σ_{33} and their differences, N_1 and N_2, attain nonzero values as soon as chains are deformed away from their equilibrium conformation. The study of this behavior is quite challenging due to the lack of complete molecular understanding (Larson and Desai 2015) and the technically demanding measurements needed. Following the analysis in the introduction, it is clear that the nonlinear shear response can be described by three material viscometric functions i.e. shear stress $\sigma(\dot{\gamma})$ and the first and second normal stress differences, $N_1(\dot{\gamma})$, $N_2(\dot{\gamma})$. Here, we focus on their steady state values and especially on the $N_2(\dot{\gamma})$, a cumbersome to measure (Macosko 1994) and model (Larson 2013) material function. The knowledge of normal stresses is undoubtedly vital for polymer processing, for instance in extrudate swell (Huang and White 1979), as well as in rheometry itself. In a cone-plate geometry N_1 and N_2 originate from the tension along flow and vorticity lines respectively, due to the distortion of the material's microstructure. Despite their different origin, they both result additively on the same effect i.e. thrusting the geometry apart. Since this thrust F_N is the sole measurable quantity, there is an intrinsic difficulty in separating the smaller N_2 from the almost one decade larger (for polymeric systems) N_1. Making matters worse, the tension along vorticity direction leads to edge fracture. When a critical value of N_{2C} is exceeded edge fracture is expected to commence, as implied by:

$$N_{2c} = 2\Gamma/3a \tag{6.1}$$

where Γ is the sample's surface tension (Tanner and Keentok 1983). This criterion is derived by considering the balance of the "elastic" energy of the sample and its surface energy. Parameter α refers to the radius of the elastically-driven meniscus distortion i.e. a semicircular indentation, typically observed in polymeric samples, ranged between h/2 and h/10 where h denotes the rheometric gap (Keentok and Xue 1999). Consequently, the ability to measure N_2 in a cone-plate geometry, even at moderate shear rates, depends on the edge fracture itself. If the sample's edge is distorted, shear rate can no longer be considered as constant in the rheometric gap, thus shear and normal stress data are invalidated. Earlier theoretical work (Hutton 1969) showed that fracture is not a secondary flow type instability. Inertial

driven instabilities and secondary flow may indeed take place anywhere in the sample and impair the measurement, but only at Re > 800 which typically corresponds, for similar geometries to shear rates of the order of 600 s^{-1} (Larson 1992). This limit is way above our range tested here. Controlling, the onset and propagation of edge fracture in the rheometric gap is far too complicated (Datta *et al.* 2021), nevertheless generic criteria have been established (McKinley *et al.* 1996) . Early work supported the argument that the relation of N_1 to the measured shear stress can provide criteria for the onset of edge fracture (Kulicke and Wallbaum 1985). However, later it was found that local shear stress gradients along with N_2 are important and rendered predictions more complicated (Hemingway and Fielding 2019). For simplicity, in our entangled polymeric liquids study, we consider criteria based on continuum analysis where the potential molecular origin of edge distortion is ignored. To this end, N_{2c} calculated from Eq. (6.1) is considered as a rough estimate of the onset of edge fracture. As we shall see, this is lower than the range of $|N_2|$ of our samples inferring that edge effects come into play for the rates tested. Based on observations by shear-induced polarized light imaging (Parisi *et al.* 2021) and modeling (Hemingway and Fielding 2019) it was confirmed that edge facture can occur even at low Wi, of order unity, severely affecting the N_1, N_2 measurements.

An efficient strategy to delay edge effects is based on the use of cone partition plate fixture (CPP), pioneered by Meissner (Meissner *et al.* 1989) and further developed by (Schweizer 2002) and (Snijkers and Vlassopoulos 2011) . The CPP consists of an inner circular (plate) connected to the transducer (thus, it is sensing normal and shear stresses) and an external inert corona, fixed on the rheometer's upper stage. The sole purpose of this inert corona is to postpone edge fracture by accommodating excess amount of sample (beyond the measuring volume). The outer surface inevitably suffers from edge fracture which propagates without affecting the shear measurement until it reaches the inner tool region. This is the simplest version that we refer to CPP2 as it involves two surfaces, the measuring inner disk and one inert partition. A big advantage of this setup (Costanzo *et al.* 2016, Costanzo *et al.* 2018) is its compactness. The tool can fit in the ARES convection oven. This setup allowed the measurement of N_1,N_2 but required at least two loadings with two different plate sizes (Costanzo, Ianniruberto, Marrucci and Vlassopoulos 2018, Schweizer 2002) which introduces errors. We name this method CPP2 (R_1,R_2). To overcome this limitation (Schweizer and Schmidheiny 2013) developed the CPP3version with three geometries, two sensing and one inert, thus allowing the determination of N_1,N_2 with data acquired in a single experiment, simultaneously. Despite its novelty, this setup proved bulky, difficult to use and the external temperature control was not optimal due to required long equilibration times and small temperature range.

In this work we report the design and construction of an improved CPP3 fixture, the CPP3+ with two normal force sensors: the instrument's transducer and a piezoelectric ceramic sensor. Contrary to

CPP3, the CPP3+ is a compact tool able to fit to the ARES oven. The piezoelectric sensor compliance and response time is superior to the strain gauge based one, which was used in CPP3. The background on the CPP and related nomenclature are summarized in table 6.1. There are many strategies to extract N_1, N_2 in steady shear. For instance by measuring F_N or the resulting normal stress N with different sample radii, different cone-plate gap or even by pressure transducer's embedded on the standing tool (Baek and Magda 2003, Gauthier *et al.* 2021). The merits and disadvantages of the different strategies followed by different authors to tackle this cumbersome measurement are reviewed elsewhere (Costanzo, Ianniruberto, Marrucci and Vlassopoulos 2018, Maklad and Poole 2021) . Here, we focus on normal stress differences measurements based on the CPP fixture.

Table 6.1 A summary of the Cone Partitioned Plate fixture evolution and relevant nomenclature. Commercially available CPP (TA, Anton Paar) are not included.

	Fixtures	**Comments**	**References**
CPP single partition	2 (disk and one inert corona)	Not connected with commercial rheometer* Required modification in ARES oven+	*(Meissner, Garbella and Hostettler 1989) +(Snijkers and Vlassopoulos 2011)
CPP2 single partition	2 (disk and one inert corona)	Compatible with ARES oven.	(Costanzo, Ianniruberto, Marrucci and Vlassopoulos 2018, Schweizer 2002)
CPP3 double partition,	3 (disk, a sensing and an inert corona)	Bulky, requires custom made temperature control	(Schweizer *et al.* 2008)
CPP3+ double partition	3 (disk, a sensing and an inert corona)	Compatible with ARES oven. Fast response	Present work

6.2 Determination of N_1 and N_2

We turn our attention to the origin of N_1, N_2 for linear chains. Considering entangled polymers, as time progresses in a shear start-up experiment, more and more chains are oriented and more entanglements are annihilated (while others are formed) due to the nonaffine stretch of the molecules the so-called convective constrain release (CCR)(Ianniruberto and Marrucci 1996). This loss of topological

constrains leads to a reduced density of entanglements (Baig *et al.* 2010, Ianniruberto and Marrucci 2014) that becomes important at rates > $1/\tau_d$. At faster rates, past the inverse of Rouse time, chains will be stretched on average and contribute to shear thinning, modeled by the so-called friction-coefficient reduction (Ianniruberto *et al.* 2012). The resulting microstructural anisotropy alters the refractive index tensor and this change is measurable by birefringence where the total stress tensor can be extracted from the stress-optical rule (Kalogrianitis and van Egmond 1997). Whether oriented or stretched, chains tend to revert to their equilibrium configuration, via relaxation. This manifestation of nonlinear elasticity, responsible for the positive N_1, creates an extra tension along the curved streamlines (of the CP geometry), resulting in a hoop stress that thrusts the plate apart. In open geometries rod climbing, or rod dipping for a dense suspension exhibiting positive N_2, is exhibited (Boyer *et al.* 2011). Tension along vorticity lines σ_{22}, responsible for the non-zero N_2, contributes as well to this total normal force F_N. This F_N is normalized by the plate surface to yield the global average normal stress N that the rheometer measures. On the other hand, the normal stress profile, i.e., the local normal stress (N_{local}) as a function of radial coordinate r, can be calculated from momentum balance (Bird *et al.* 1987):

$$N_{local}(\mathbf{r}) = -(\mathbf{N_1} + 2N_2)\ln\left(\frac{r}{R_s}\right) - \mathbf{N_2} \tag{6.2}$$

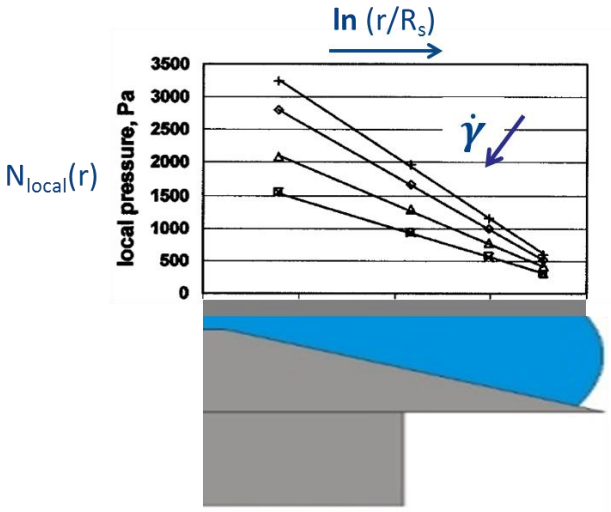

Figure 6.1 The normal stress profile in the cone plate rheometric gap as a function of the logarithm of the radial coordinate over the total sample radius R. Symbols are data measured by capacitive local pressure sensors at rates of 150, 120, 80, and 50s^{-1}. Sample is a reference polymer NIST SRM-1490. Linear profiles confirm the logarithmic dependence of N on r/R consistent with Eq.(6.2). Graph taken from (Baek and Magda 2003).

The logarithmic dependence of N on r/R_s, visualized in Figure 6.1 for various shear rates of deformation, implies that the local normal stress measured at any point of the geometry depends on the total sample radius R_s. The two major experimental challenges, mentioned above are now evident: a) both N_1 and N_2 contributions are contained in N hence it is difficult to decouple them especially for polymers where $|N_2$

|<< $|N_1|$. b) the normal stress distribution in the gap, hence N, depends on the flow conditions at every point of the geometry even at the inert outer corona of the CPP. By integrating Eq.(6.2) over r we get an expression connecting the observable N with the two unknown material properties N_1, N_2:

$$N = N_1 + 2(N_1 + 2N_2)\ln(R_s/R_{xducer}) \quad (6.3)$$

where N is the average normal stress exerted on the inner part of the disk with radius R_{xducer} smaller than the total one R_s. Therefore to obtain N_1 and N_2 we need at least two independent measurements of N from two different geometries, i.e., either two CPP2 experiments with different radii (Costanzo, Ianniruberto, Marrucci and Vlassopoulos 2018, Schweizer 2002) or a single CPP3+ experiment in the spirit of (Schweizer, Hostettler and Mettler 2008) . Obviously the former requires two loadings, more time and is prone to trimming errors.

6.3 Experimental setup

All experiments were conducted on an ARES, a separated motor transducer rheometer. The modified CPP3+ measuring geometry is depicted in Figure 6.2. All metallic components are fabricated of stainless steel alloy.

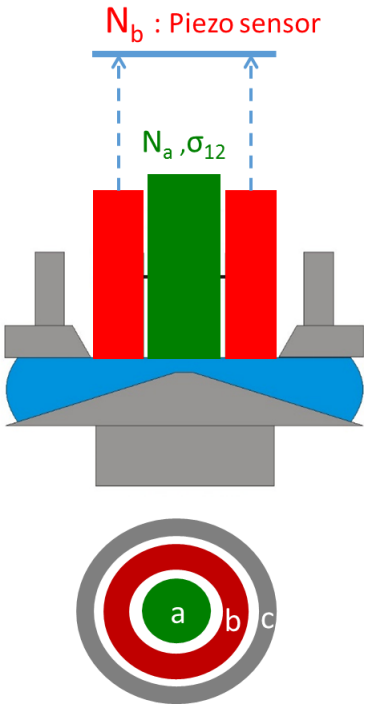

Figure 6.2 Cartoon of CPP3+ showing the side view (top) and the partitioned upper geometry (bottom). The inner disk surface "a" ($R_{\_xducer}$) depicted in green, is mechanically connected to the ARES transducer capable of measuring shear and normal stresses. Surface "b" comprises the first partition (corona) and is connected to the piezoelectric normal force sensor depicted in red. Similar color coding applies to the corresponding data. The outer (inert) corona is surface "c" (R_s) depicted in gray. The sample area is denoted in blue.

The lower part of the geometry depicted in grey, consists of a cone with 25mm radius. We utilized two angles, 0.1 rad and 0.04 rad. Larger angles are preferred, as they will mitigate the effects of the instrument's axial compliance (Hansen and Nazem 1975) trading off an earlier onset of edge fracture (Keentok and Xue 1999). The upper part of the geometry consists of: a) a 6mm inner disk, labeled "a" which is mechanically connected to the instrument's force rebalanced transducer (2kFRT-N1). Shear and normal stress N_a can be sensed b) the first partition, surface "b", mounted (glued) to the ring-shaped piezoelectric sensor's lower end. The other end is fixed to the instrument's upper stage, decoupled from the transducer. The mean normal stress on this surface (N_b) can be sensed via the piezoelectric ceramic c) the "inert" outer partition, surface "c" with the sole purpose to delay edge fracture effects as described above. Further details are shown in the schematic in A.6 nevertheless different diameters can be used.

The piezoelectric ceramic is used as sensor on the principle of the direct piezoelectric effect. The normal force excreted by the sample will slightly deform the crystalline lattice of the sensor leading to the generation of electric charge. The resulting current is integrated over time by means of a charge amplifier (5015A, Kistler Switzerland) and converted to a proportional voltage waveform. During a shear start-up experiment, both the piezoelectric and the ARES raw normal force signals, are recorded and observed in an oscilloscope (Picoscope 3000, Pico technologies UK). Hence, this setup yields two normal force signals F_{N_a} and F_{N_b} that are converted to the equivalent normal stresses N_a and N_b applied on the two surfaces "a" and "b" respectively. As it will become clear later, these are the averaged stress values. Details about the signal processing are discussed in the calibration section.

The sensor consists of three piezoelectric ceramic disks sintered together by the manufacturer (PI Ceramic GmbH, Germany). Although already calibrated piezo-electric based force sensors are available (Naue *et al.* 2018), we opted for PI PD150.3 ceramic based on certain characteristics. Primarily concerns were: a) shape and dimensions restricted by its ability of fitting-in the existing ARES oven and its mechanical compatibility with the tool, b) adequate sensitivity and range for the given surface of the measuring geometry c) minimal axial compliance in order to avoid force rebalancing feed-back loops d) sufficient temperature range. ARES convection oven can reach temperatures around 250 ^{0}C, therefore the limits of the piezoelectric sensor and the used heat resistant epoxy glue were considered. A safe temperature for the sensor and the epoxy glue would be 80°C. Since the piezo ceramic is positioned outside the oven, a cooling jet of gas can be applied extending the temperature range. We limited the experiments for now to 100 ^{0}C. Drift may become chaotic during temperature equilibration and this should be also accounted. An image of the sensor and CPP3+ design details can be found in the appendix in Figure A.5 and Figure A.6.

6.4 Data extraction and calibration

The raw signals are voltage waveforms proportional to the applied normal stresses on surfaces "a" and "b", therefore a conversion factor was applied. For the ARES rheometer according to specifications, the conversion from Volts to force is 400 grf/V. Given the tool surface area of 28.26 10^{-6} m^2, this translates to a normal stress coefficient of 138,712 Pa/V. For the piezoelectric sensor, one can either calculate the conversion factor based on the piezoelectric coefficient, the amplifier's gain and the tool's surface or determine it experimentally. For simplicity and accuracy, i.e., ruling out imperfections in the piezo ceramic and tool, we chose the latter. By hanging different standardized weights on surface "b" and by logging the amplifier's output, we have constructed the static calibration plot (Figure 6.3). The linear dependence of the signal on the weight, verifies the linear response of our sensor and the voltage to force conversion is determined from the slope of the line. Since F_{N_b} and response are determined the effective normal stress, N_b can be calculated by dividing with surface "b" area, leading to a coefficient of 182,528 Pa/V.

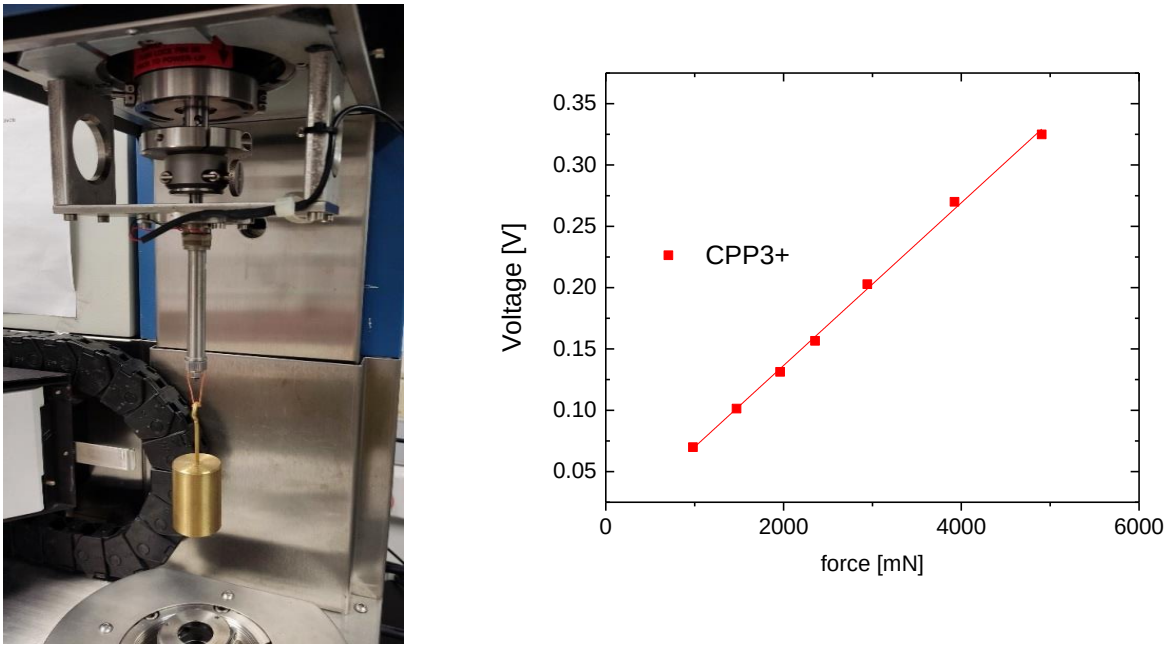

Figure 6.3 Static calibration of the piezoelectric sensor of CPP3+. The photograph shows the fixture with its outer corona and lower cone removed. A standardized weight emulates the normal force. Graph depicts the response for different values of static normal force (weights). The ordinate is the voltage at the charge amplifier output logged by the Picoscope.

While this static calibration might suffice for a simple sensor, this is not the case for piezoelectric sensors with inherent limitations. The major one for our application is the charge leakage. The piezoelectric sensor can be modeled as a charge source in parallel with a capacitor that stores the charge and a resistor that inevitably will leak the charge to the ground after some time thus compromising the measurement in

long times Figure 6.4(a). Additionally the voltage sensing device that we use will also drain some charge. To compensate for this gradual decay of the signal in the static mode special type charge amplifiers are used (Cudney *et al.* 1972). The basic principle is shown in Figure 6.4(b).The operational amplifier output is used to charge a capacitor C_F connected to its inverting input. This basic circuitry is a current integrator (Horowitz *et al.* 1989, Starecki 2014) hence the name charge amplifier. Resistor R_F is used to dissipate the energy stored on the integrating capacitor C_F. This is the working principle of the charge amplifier we utilized, the Kistler 5015A (Switzerland). When the amplifier is set to the "long" mode, meaning huge time constant corresponding to large R_F and large capacity C_F, the output is proportional to all charges generated since measurement commenced.

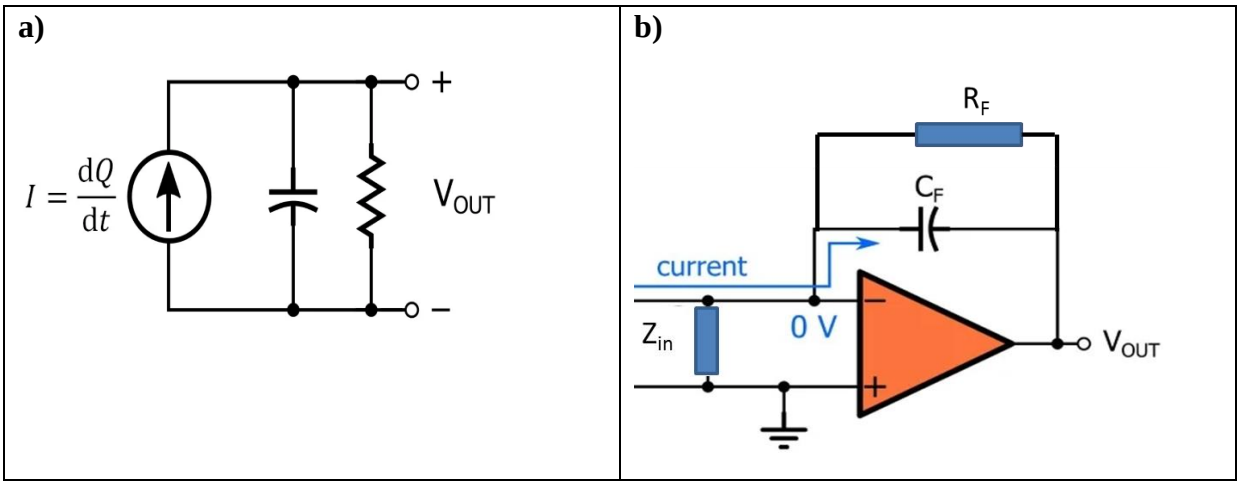

Figure 6.4 Charge generation and signal conditioning in a typical piezoelectric sensor setup; a) model of a piezoelectric sensor consisting of (starting from left) a charge source, a capacitor that holds the charges and a resistor for charge leakage; b) charge amplifier basic circuit consisting of an operational amplifier (denoted in triangle shape) and the capacitor C_F and the resistor R_F that govern the time constant. Cartoons adapted from www.allaboutcircuits.com

In this mode of operation (long) normal stress measurements for longer than few seconds are possible. However, cumulative summing will eventually lead to signal drift until the amplifier overloads. To prevent this, the capacitor should be manually discharged (zeroed) before each measurement and the drift needs to be determined and subtracted from the raw signal. During all the measurements the charge amplifier, was set to long mode and the capacitors charge was zeroed just before start. This, along with the huge input impedance Z_{in} of this device allowed performing measurements in the so called quasi-static mode. As mentioned, quasi-static mode comes along with drift that is compensated by various methods (Kos *et al.* 2019) . We have not observed any drift due to the amplifier itself, but a significant one

stemming from the electrostatic interference of the sensor with the environment, and this will be discussed below.

Considering these inherent limitations of piezoelectric sensors a dynamic calibration validation is needed. To this end, we constructed a simple tool, which is shown in Figure 6.5. A 1mm thick PDMS membrane constituted the upper part (diaphragm) of a metallic (aluminium alloy) airtight cylindrical chamber, where pressure could be altered by introducing water via a hand pump. The lower tool (cone) was replaced by this fixture, allowing the diaphragm to exert on both sensing geometries the same normal stress. We varied the internal pressure in such a way as to emulate the signal in a real shear start-up experiment. Data from this dynamic calibration test are shown in Figure 6.5. ARES raw signal (blue curve) after correction for the baseline offset leads to the green curve that collapses nicely to the piezoelectric signal. In a conventional measurement the baseline offset (drift) is accounted for by the instruments software so the user will not see it unless the raw signal is examined. For the data of Figure 6.5 we used the conversion factors derived from static calibration therefore normal stress values (in Pa) rather than voltage is depicted for both geometries. The time lag of N_a signal is reminiscent of the moderate response time of 2kFRT-N1 transducer (around 100ms) compared to the almost instantaneous (order of μs) response of the piezo ceramic sensor. Drift should be assessed for the piezo signal, as the electrostatic interference with the environment generates charge that eventually will add up to the final N_b signal. Two characteristic examples of drift of N_a and N_b signals are shown in Figure 6.6 at two shear rates of 0.5 s^{-1} and 2s^{-1}.

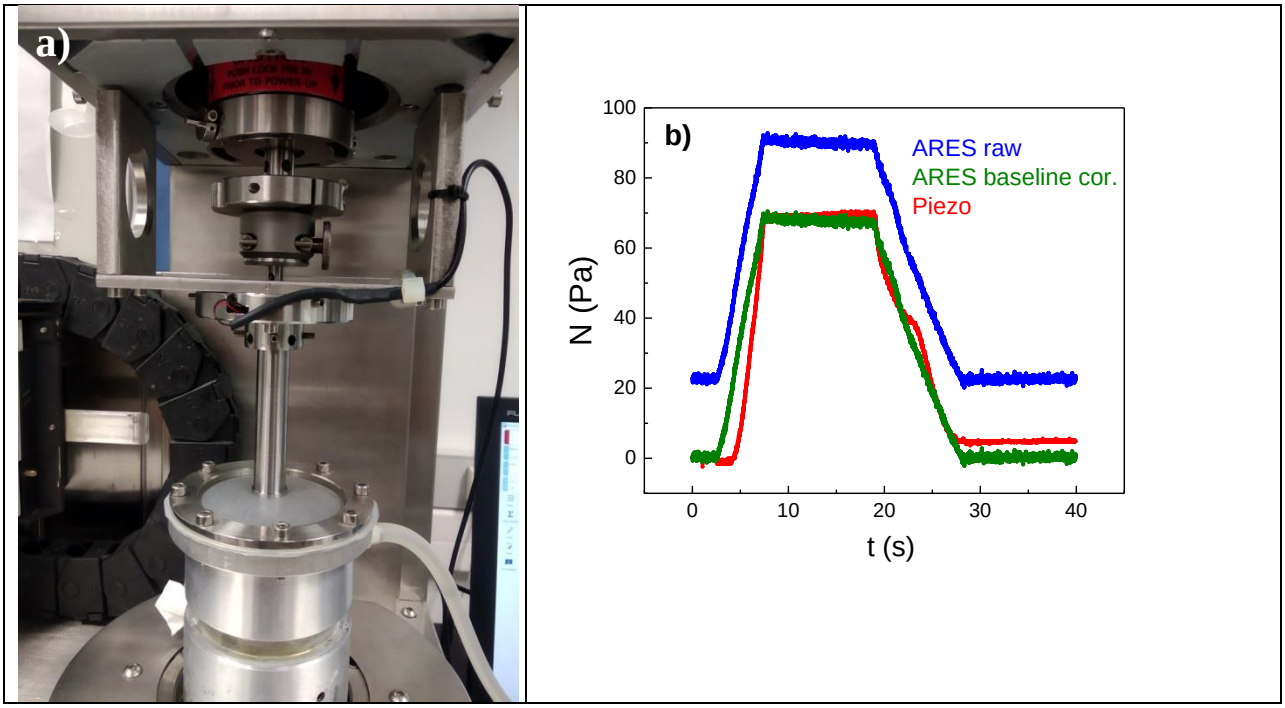

Figure 6.5 Dynamic calibration of CPP3+. a) The photograph shows the upper geometry in contact with a membrane, part of an airtight chamber where pressure is controlled by means of a manually operated valve. b) Normal stress signals under dynamic test. Blue curve is ARES raw normal stress signal, green is the same corrected for drift of baseline and red the piezoelectric sensor signal. All data are shown in stress units (Pa).

The ARES drift is constant over time but has a different value for each measurement. This value must be subtracted from the raw data of N_a (green) to correct for the offset of the baseline. This is executed by the rheometer's software (Orchestrator), for instance in the data of Figure 6.8, or manually when raw data of N_a are considered. On the other hand, the origin of the drift in N_b is very different. The charge amplifier integrates all charges generated during the measuring period hence, all electrostatic interference of the sensor with the environment. In contrast to $N_a(t)$, drift of $N_b(t)$ is not a constant value but a function of time. Fortunately, in most cases where sufficient time was allowed for temperature equilibration, this drift was found to be a linear function of time which can easily be analyzed. The piezoelectric drift in Figure 6.6 is the dashed line, derived from fitting the part of the signal before shear commences, i.e., with zero normal force. As a consistency check, the fit collapses nicely with the "new zero baseline" of the signal (red) after the flow cessation. By subtracting this drift contribution from the raw (red) signal we get the corrected signal (magenta). This is illustrated for two characteristic cases of minor and moderate drift in Figure 6.6. The abscissa is the elapsed time from the moment the data acquisition started and not the onset of shear flow. We have found that the drift varies with environmental conditions in the lab such as relative humidity and draughts while it is enhanced during temperature changes (possibly due to expansion) or when gas flow is directed to the sensor area. Now the steady state values can be extracted from both the ARES (green) and the Piezo (magenta). With this method, we end up with two normal stress values: N_a corresponding to the inner tool of radius say 3 mm (corresponds to R_{xducer}) and $N_a + N_b$, corresponding to plate radius 3+2=5mm. (corresponds to R_s). From these values the calculation of N_1, N_2 is possible via the evaluation of the Eq. (6.3) for the two cases R=5 and R=2 with a single measurement.

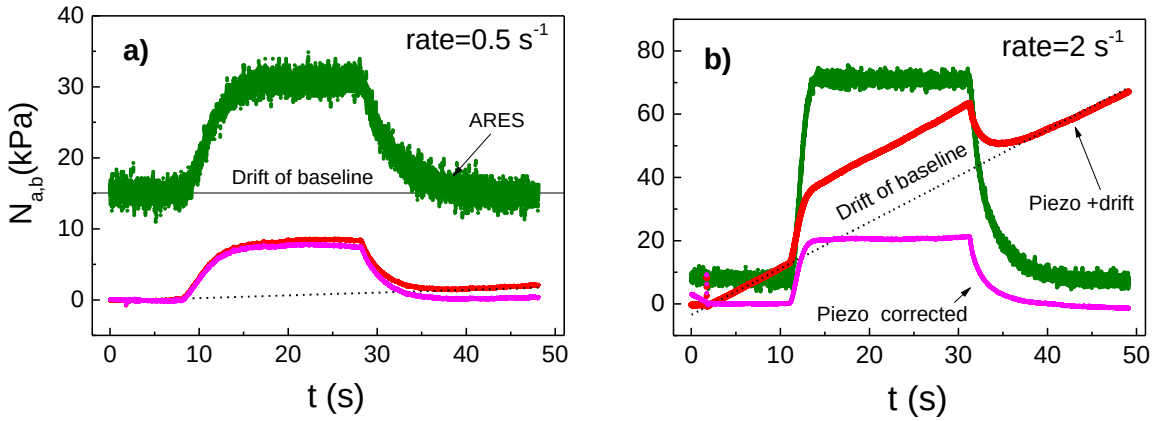

Figure 6.6 CPP3+ N_a and N_b raw data acquired by Picoscope. Two characteristic cases of a) minor and b) moderate drift of $N_b(t)$ baseline are shown. The raw time signal normalized in stress units is depicted in red. The magenta curve depicts the corrected signal after subtraction of the drift (short dashed line). $N_a(t)$ also is shown (green curve) where it exhibits significant but constant drift of 15kPa at the rate of $0.5s^{-1}$The abscissa is the elapsed time from the moment the data acquisition started.

6.5 Application to an entangled polymeric melt and solution.

We tested the calibrated CPP3+ with two polymeric samples. The first is a solution of polystyrene of M_W=160kg/mol diluted in dioctyl phthalate (DOP) at a weight concentration of 50%. Theta solvency conditions for DOP are met at 22°C (Inoue *et al.* 2002) therefore our measuring temperatures of 40, 60°C correspond to good solvent conditions. The second is poly n-butyl acrylate (PnBA) melt with M_W=166kg/mol and T_g= -49 °C, allowing measurements at room temperature. PnBA was kindly provided by E. van Ruymbeke of Université catholique de Louvain. Both polymers have low polydispersity (PS M_w/M_n=1.05, PnBA M_w/M_n=1.22) and are moderately entangled, exhibiting 4 and 9 entanglements per chain, respectively. The entanglement molecular weight for the PS solution $M_e(\varphi) = M_e(1)\,\varphi^{-1.3}$ (Van Ruymbeke *et al.* 2012) where $M_e(1)$, corresponds to the melt. The $M_e(1)$ for PS and PnBA was taken 17 kg/mol and 36kg/mol (Jullian *et al.* 2010), respectively.

First, we discuss the rheology of the PS solution. The LVE spectrum in Figure A.1 in the appendix indicates a terminal time of 1.35s and 0.185s at 40, 60°C respectively. Start-up tests were performed at various shear rates with CPP2 and two different radii, 6 and 10mm, to study the sample behavior and ensure that the signal strength is adequate. The shear stress growth coefficient during shear start-up is depicted in Figure 6.7(a). This is a typical response of linear entangled polymers. At the lower rate of $0.5s^{-1}$ the η^+ overshoot is weak, while at higher rates it increases as the chain deviate more from their equilibrium conformation. An undershoot, attributed to tumbling, starts to emerge at the rate of $2s^{-1}$ and becomes prominent at the rates of 5 and $10s^{-1}$. Evidently, the rates tested fall in the shear thinning

regime with an exponent of 0.66 consistent with similar studies (Costanzo, Huang, Ianniruberto, Marrucci, Hassager and Vlassopoulos 2016, Moldenaers *et al.* 1993, Xu *et al.* 2014). The LVE envelope denoted with star symbols, is calculated from dynamic complex viscosity, based on Cox Merz empirical rule in the spirit of (Snijkers and Vlassopoulos 2014) and validates the steady shear data.

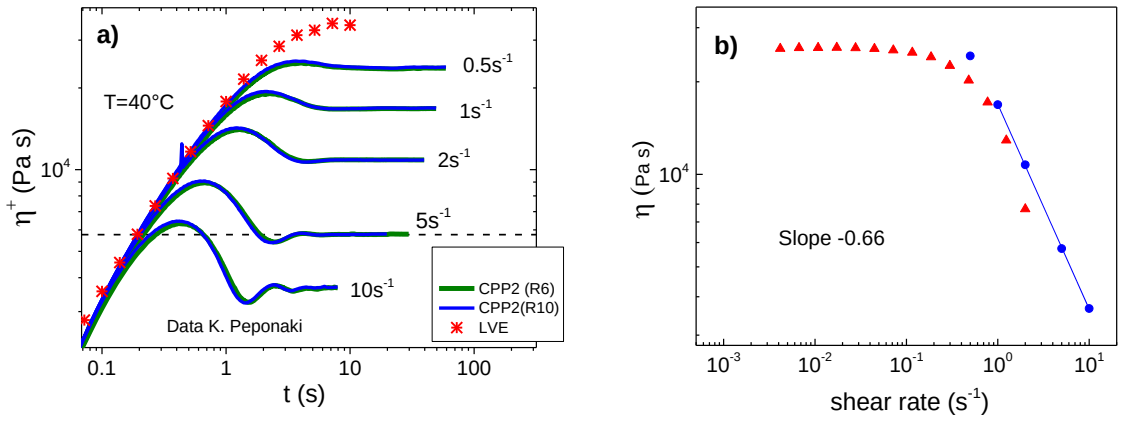

Figure 6.7 Shear start-up response of PS (M_W=160kg/mol) solution in DOP 50% wt. a) Shear stress growth coefficient at different rates. The blue curve measured with CPP2(R=10mm) and the green CPP2(R=6) collapse nicely. The dashed line is drawn to help discerning the undeshoot at $5s^{-1}$. The red symbols denote the LVE envelope b) Shear thinning behavior of steady state viscocity. Red symbols are measurements with ARES CPP2. Blue symbols denote mesurements with a CP8mm in Anton Paar MCR702. The discrepancy is attributed to onset of edge fracture in the CP8 geometry.

Importantly, with shear stress measurements, the N_{local} distribution is affected by the edge fracture, even when the latter did not propagate up to the measuring surface, due to effective sample radius reduction (see Eq 6.3). The normal stress signal exhibits fluctuations earlier and at lower rates compared to the shear stress signal. This is clearly shown in Figure 6.8 where at rates 5, 10 and 20 s^{-1} the shear stress does not fluctuate as the outer corona "shields" the sensor from edge effects. On the contrary the normal stress starts fluctuating at $10s^{-1}$ due to edge instabilities whereas at $50s^{-1}$ both shear and normal stress (N_a) signals fluctuate because the instability propagated to inner surface "a". Other phenomena such as wall slip and secondary flows are also contributing to signal fluctuation.

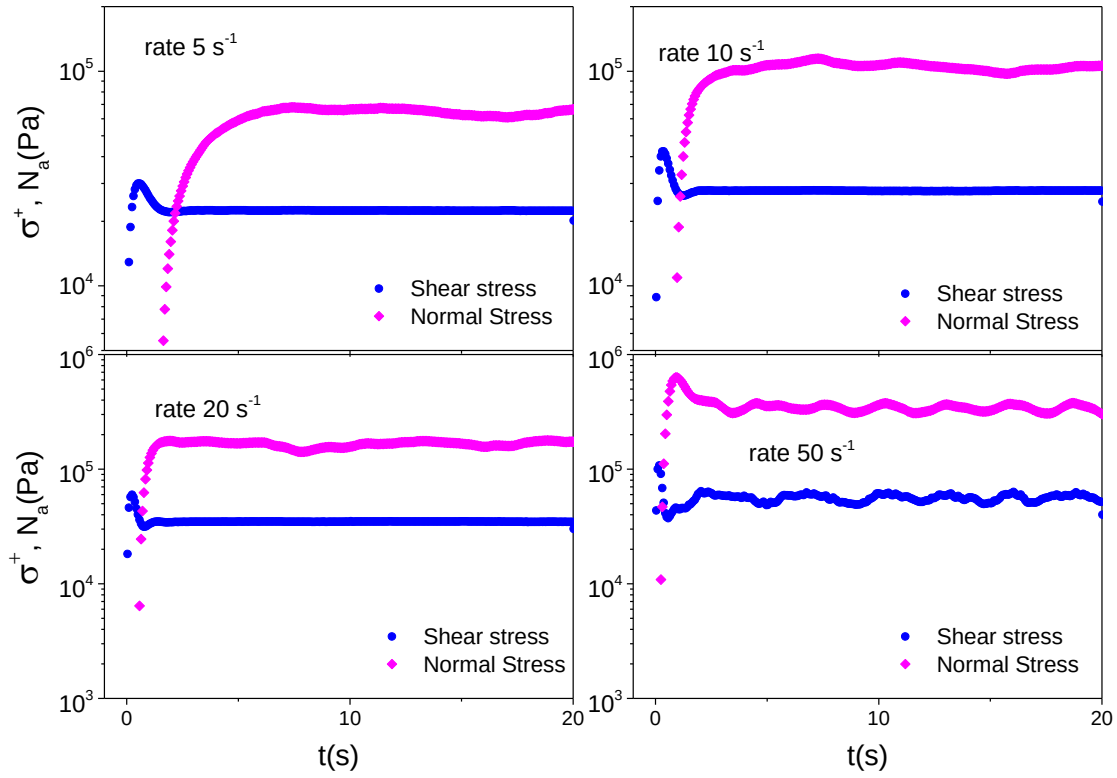

Figure 6.8 Experimental data of σ(t) and N_a(t) with CPP3+ fixture. Only ARES transducer is utilized while data are processed via instruments software (Orchestrator). Shear start-up experiment is performed at various rates. Sample is PS/DOP solution at 40 °C. The early onset of N_a (t) fluctuations at a shear rate of $5s^{-1}$ is evident even on the log scale. Shear stress does not fluctuate up to the rate of 20 s^{-1}

Fluctuations are also present in the N_b signals of Figure 6.9. These are raw signals acquired by the Picoscope where the onset of fluctuations is observed at $5s^{-1}$ and beyond. Stress values are lower that the N_a values at equivalent rates (Figure 6.8), as the stress profile of Figure 6.1 dictates. Fluctuations in N_b at the rate of $10s^{-1}$seem to be larger than in N_a (Figure 6.8) as the latter is possibly smoothed by ARES software and due to logarithmic scale. Based on CPP3+ measurements the N_1, N_2 for the PS solution where calculated via the method described above and are shown in Figure 6.10. First we focus on low Weissenberg number regime ($Wi_d = \dot{\gamma}\,\tau_d$) were both N_1 and N_2 exhibit a linear dependence on Wi_d or shear rate. As a further consistency check, the same sample was measured with CPP2 using the method requiring two different loadings (Costanzo, Ianniruberto, Marrucci and Vlassopoulos 2018). For this reason, two CPP2(R=3mm) and CPP2(R=5mm) fixtures were used. Measurements were performed by K. Peponaki. The respective N_1 and N_2 data are depicted as star shaped symbols.

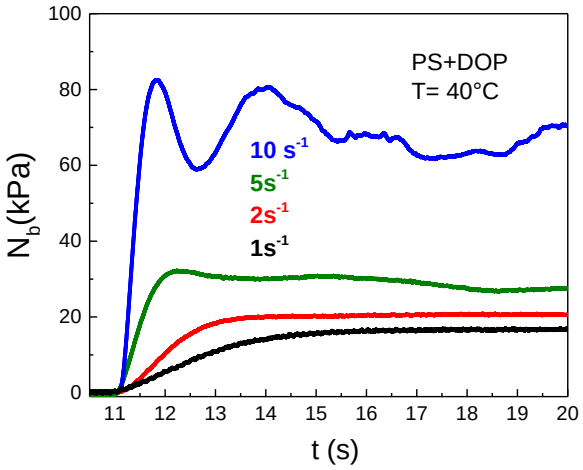

Figure 6.9 Raw N_b signals from piezoelectric sensor of the inner surface. Shear start-up measurements were performed at 1, 2, 5 and 10 s^{-1} with CPP3+ for PS/DOP solution at 40°C. Abscissa is the elapsed time from the moment the data acquisition started. Drift has been subtracted.

The agreement with CPP3+(R6) data is satisfactory, given the challenges associated with this type of measurement. This further validates the already discussed calibration of the setup, as well as the whole procedure. Moving on to higher rates (yellow shaded area in Figure 6.10) $|N_2|$ drops significantly faster than N_1 and finally N_2 becomes positive, an unphysical behavior. This is undoubtedly an artifact. Similar behavior we observe for PnBA melt in Figure 6.10(b).

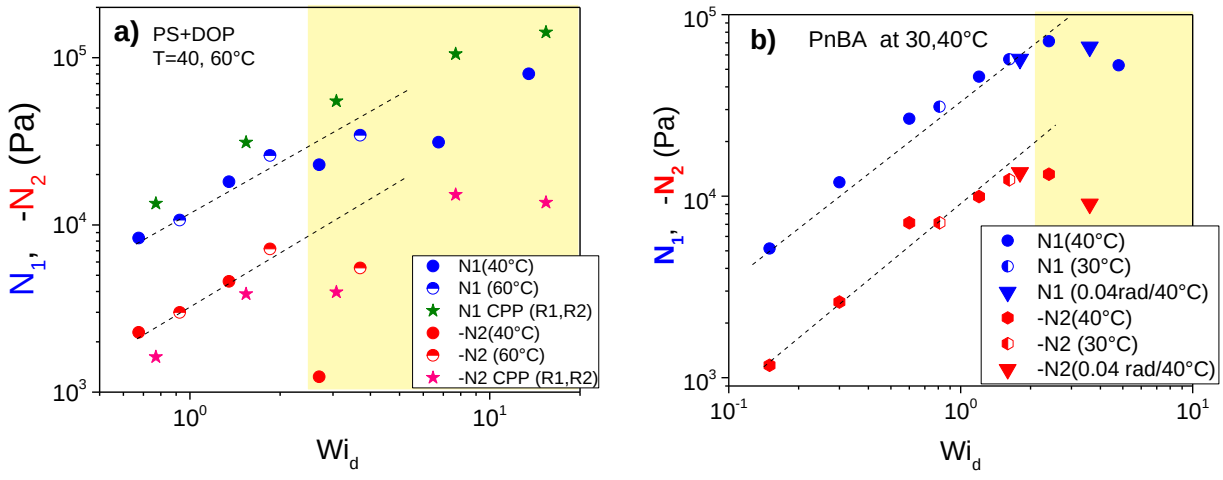

Figure 6.10 N_1,N_2 (steady state) values for PS/DOP solution and PnBA melt measured with CPP3+ and cone angle 0.1 rad (circles). a) Data for PS solution are compared with measurements performed with CPP2(R1,R2), i.e., with two different diameters and loadings , denoted with star symbols. b) PnBA was measured with cone angle of 0.1 rad as PS/DOP and 0.04rad as indicated in the legend. Dashed lines are guides to the eye with a slope of 1, and yellow shaded areas indicate the onset of instabilities.

To identify the origin of this artifact, we need to consider the flow conditions in the rheometric gap. N_2 controls edge fracture with the later commencing when $|N_2|$ exceeds a critical value that can be calculated from Eq. (6.1). By approximating the polymer's surface tension as 31mN/m (Wu 1970) and a=h/2, we obtain $N_{2c} \approx 51$ Pa for a cone with an angle of 0.1 rad and R= 8mm, implying that we have exceeded by far the limit of edge fracture even at $Wi_d < 1$. This is consistent with other studies (Hemingway and Fielding 2019), where the stable and unstable region was defined, based on simulations with a Giesekus fluid (Vlassopoulos and Hatzikiriakos 1995), and by considering the shear rate gradient as an additional parameter for the onset of instabilities. Notably, the indentation of the sample at the interface may propagate further inside the geometry breaking down the hypothesis of constant shear rate. There are two consequences of this effect. Firstly, the fracture will distort the spherical shape of the interface (Venerus 2007) and reduce the effective total sample radius (R_s), therefore alter the pressure gradient in the gap. This will in turn reduce the normal stress signal N_a and N_b. Secondly, when the instability reaches surface "b" then definitely N_b will be underestimated considerably. In this case N_2 will falsely drop faster than N_1 - see error analysis in the appendix- shifting to positive values as observed in Figure 6.10. Before this point, a pseudo shear thinning of $-N_2/N_1$ is observed. The effect of the underestimation of N_b on N_2 is discussed in appendix A6.2. N_2 is indeed very sensitive. For example a 20% underestimation of N_b will reduce dramatically |N2| or even drive N_2 to positive values which is definitely an artifact. On the other hand, shear measurements will be compromised only when the instability reaches the inner surface "a". This explains why the ratio $-N_2/N_1$ in Figure 6.11 for both PS/DOP solution and PnBA melt thins in an unphysical way at higher Wi_d. Therefore, the true onset of thinning is hardly discerned. We note here that this consensus is based on the assumption that a propagating edge fracture is the only type of instability present.

The two main features of the data are now discussed in more detail and with reference to literature: the linear dependence on shear rate and the early onset of edge fracture at $Wi_d \sim 1$ and its consequences.

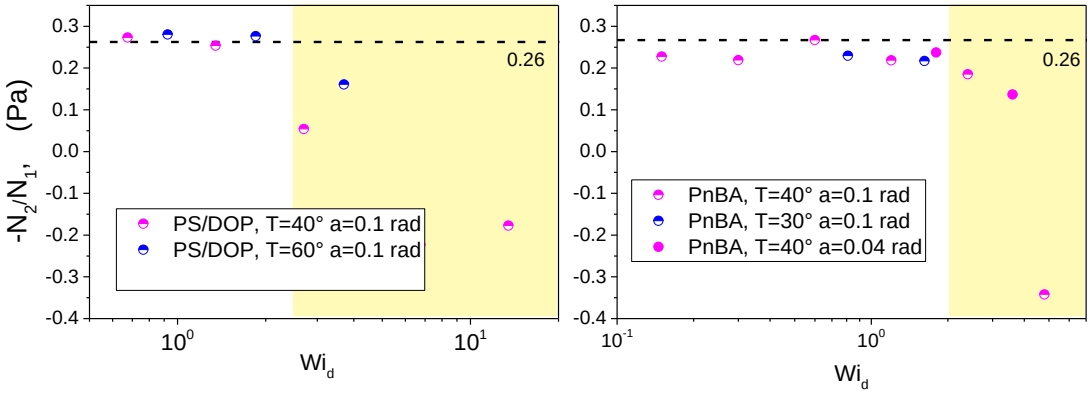

Figure 6.11 Normal stress differences ratio for PS solution and PnBA melt as a function of the Weissenberg number. The latter is calculated based on terminal time obtained from LVE data. Yellow shaded area denotes the area where instabilities affect the measurement giving the false impression of significant shear thinning. Dashed line is a visual guide. PS/DOP solution is measured with 0.1 rad cone angle, while PnBA melt with both 0.1 and 0.04 rad as indicated in the legend.

6.5.1 N_1, N_2 shear rate dependence.

In general viscoelastic materials exhibit weakly nonlinear second order fluid (Coleman and Noll 1960) behavior at low shear rates, regime I of Figure 6.12, where shear viscosity is constant and N_1, $|N_2|$ has quadratic dependence on rate (Coleman and Markovitz 1964). Contrary to shear stress, both N_1, N_2 do not change sign when flow is reversed as they are even functions of rate (Graessley 2008). In this regime the departure from Newtonian behavior is marginal.

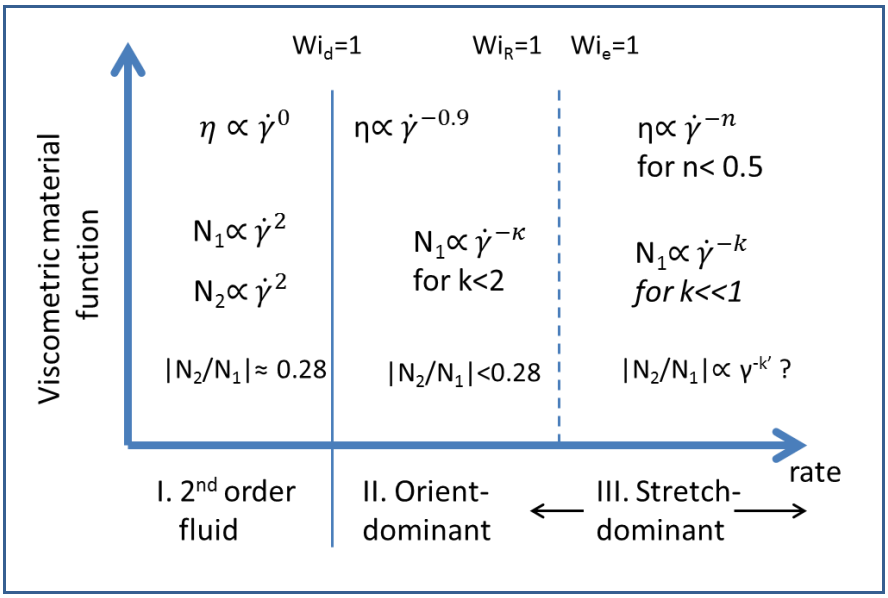

Figure 6.12 Illustration of the trend of material properties of linear entangled polymers as a function of the shear rate.

This quadratic dependence of N_1 on shear rate can be predicted from LVE when it is expressed as a power-law series, where the first odd term (quadratic) provides a sufficient approximation. The Doi and Edwards (DE) model also predicts N_1,N_2 quadratic dependence at small shear rates (Bird, Armstrong and Hassager 1987), while at increased values, the predicted dependence changes, i.e., slopes of 0 and -0.5 for N_1 and N_2, respectively. This can be attributed to the fact that the model ignores CCR and primitive path fluctuations concepts. Recent work, based on CCR and a finitely extensible version of the Rolie–Poly model predicted a behavior consistent with experiments where N_1 and N_2 attain slopes of ~ 0.5 and 0.7 respectively at high rates (Dolata and Olmsted 2023). Experimentally the N_1 slope was also found to decrease with increasing shear rate reaching values as low as 0.5 (Menezes and Graessley 1980). Similar behavior was reported by many authors who performed rheo-optical experiments (Kalogrianitis and van Egmond 1997), single DNA molecule experiments (Schroeder *et al.* 2005) and simulations (Xu, Chen and An 2014). Our N_1, N_2 data of Figure 6.10 correspond to the viscosity (see Figure 6.7) thinning regime II of Figure 6.12 and exhibit a slope of 1 consistent with the above. Access to higher shear rates should lead to weaker dependence on shear rate. This trend is also depicted in Figure 6.13 where predictions of the Corotational Maxwell (CRM) model for η, N_1, N_2 are presented. This is a simple generic model based on Oldroyd's equations under the requirement that constitutive equations obey frame invariance within the continuum framework (Bird *et al.* 1987, Larson 2013). The calculations are based on η_0=20700 Pa s and τ_d =1.35s values that correspond to the PS/DOP solution at 40°C. Remarkably, CPP3+ N_1 data exhibit a satisfactory agreement with the model despite its continuum nature. N_2 is only plotted to highlight the sensitivity to edge fracture, (see last data point at shear rate of $2s^{-1}$). CRM predicts $-N_2/N_1$=0.5 which is different from the DE predictions as well as the experimental data. Nevertheless, the purpose of this graph is to indicate that the experimental shear rates correspond to the onset of the shear thinning regime II of Figure 6.12, i.e., the transition of the rate dependence from quadratic to rate independent regime which justifies the experimental slope of 1 in Figure 6.10.

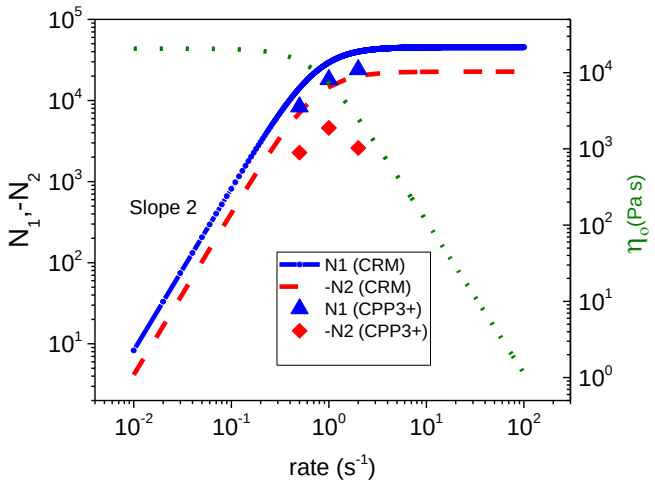

Figure 6.13 Predictions of the CRM model for η, N_1,N_2 as a function of shear rate for a linear polymer (PS/DOP) solution with η_0=20700 Pa s and τ_d =1.35s . Lines are predictions and symbols experimental data of N_1 (triangles) and N_2 (diamonds) for PS/DOP.

6.5.2 -N_2/N_1 thinning and the effects of edge fracture.

Based on molecular theory the DE model predicts $-N_2/N_1$ to be 0.28 for low rates (Larson 2013) whereas it weakly shear thins at higher ones (Figure 6.12) and this trend is again confirmed experimentally (Costanzo *et al.* 2018, Magda and Baek 1994). Ironically, the value of 0.28 is predicted when the independent chain alignment approximation is invoked, i.e., the chain orientation due to retraction in the tube is neglected. Instabilities and in particular edge fracture seems to affect more $|N_2|$ rather than N_1 (see Figure A6.2) leading to the artifact of a pseudo thinning behavior. Our inability to reach the thinning regime for $-N_2/N_1$ with this concentrated solution, appears to be consistent with the work of (Magda and Baek 1994), who reported that edge fracture affected the measurement before -N_2/N_1 reached the shear thinning regime. Earlier work also support this finding as the authors suggested that flow-induced concentration fluctuations resulted in $-N_2/N_1$ thinning, in PS solutions in DOP (Moldenaers *et al.* 1993). The more concentrated the solution (larger Z) the smaller the Wi where edge fracture affects the experiment as depicted in Figure 6.14 where "X" indicate the limit of measurement due to edge fracture for various concentrations of PS solutions in good solvent, n-butylbenzene. For the 88kg/m^3 solution the measurement could not exceed Wi_d~1. Our PS/DOP solution concentration is 500 kg/m^3, i.e., 5 times larger. The authors measured the N_{local} with 4 pressure sensors embedded in the CP74mm (0.04 rad) geometry at different radial positions, with the outer one being 0.25 mm from the edge. The propensity for edge fracture was higher due to lager h, yet comparable with the CPP3+ where the "b" surface is shielded by the 0.22mm outer corona ("c"). Therefore, the conclusion that edge fracture occurs before $-N_2/N_1$ thins, seems applicable for our study as well.

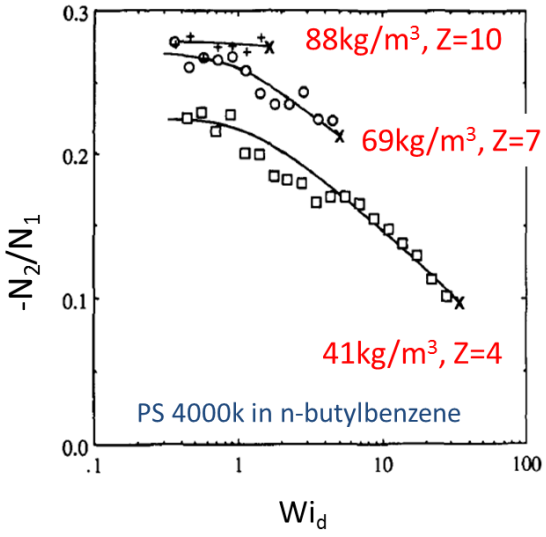

Figure 6.14 Dependence of $-N_2/N_1$ on Wi_d for solutions of PS4000 in n-butylbenzene at various concentrations. The symbol 'x' denotes the onset of the predominance of edge fracture instability where the measurement has to stop. Measurement was performed with CP74mm geometry and small cone angle (0.04rad). From (Magda and Baek 1994).

In the discussion so far we have considered the propagating edge fracture as the sole instability. Nevertheless, the onset of instabilities is hard to predict for polymer melts and solutions. From the material's properties perspective, neither t_d (related to Wi_d) nor Z are the sole instability governing quantities. CCR suggests that under flow the entanglement density decreases (Ianniruberto and Marrucci 2014), hence so does the associated relaxation time. Therefore, the material should be considered as being in a new steady state with a reduced effective Z and altered relaxation spectrum. In our view this should be considered for proper scaling of the onset of instabilities with W_d. This scaling assumes that Z is the only control parameter, which is a reasonable assumption for polymeric melts. On the other hand, in polymer solutions the flow-concentration coupling parameter $E = \frac{G'(\varphi)}{x^{-1}\varphi^2}$ where χ^{-1} is the osmotic susceptibility (Cromer *et al.* 2013) and G′(φ) the concentration dependent elastic modulus, seem to show the propensity for the so- called shear induced demixing of polymer and solvent, i.e., during flow gradients form in polymer concentration on macroscopic length scales (Burroughs *et al.* 2023). The authors demonstrated that shear-induced demixing in entangled polymer solutions results in gradients of both concentration and shear rate associated with unstable flow. Further analysis is necessary in future work to conclude how these findings are related to the onset of edge fracture.

As a final test of the presented measurements it is tempting to compare the data with Laun's rule. Given that N_1 originates from elasticity, Laun's semi-empirical formula infers N_1 from LVE spectrum (Laun 1986) :

$$N_{1\_Laun}(\dot{\gamma})|_{\omega=\dot{\gamma}} = 2\,G'(\omega)\left(1+\left(\frac{G'(\omega)}{G''(\omega)}\right)^2\right)^a \tag{6.4}$$

This is valid however only for low shear rates in regime I of Figure 6.12, at the onset of nonlinearity. In the original Laun's publication the exponent was a=0.7. At higher rates, Laun's rule overestimates N_1 as we depart from $\dot{\gamma} = \omega$ corresponding to the terminal regime (Menezes and Graessley 1980).

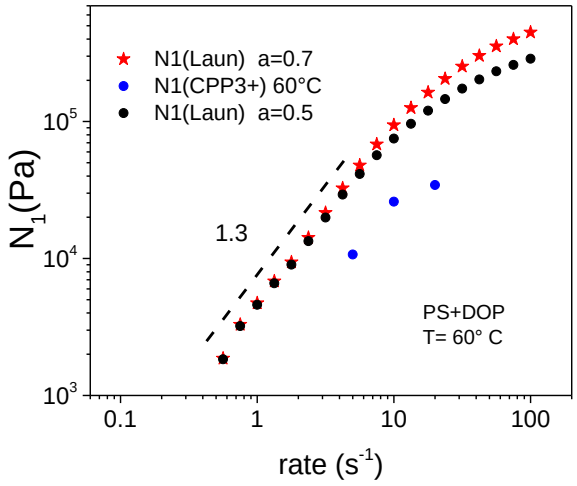

Figure 6.15 Comparison of N_1 CPP3+ measurement and predictions of Laun's rule from Eq. (6.4) for two exponent values a=0.7 and 0.5. LVE data of Figure S1 were utilized.

In a more recent work, the exponent of 0.5 (and even lower values) was found to describe better the data of monodisperse polymers at higher rates (Wen *et al.* 2004). To this end, Eq. (6.4) was evaluated for exponents 0.7 and 0.5, where the latter seems to exhibit better agreement with experimental data (Figure 6.15). Interestingly, the slope of 1.3 of the calculated N_1, exhibited at shear rates up to $10s^{-1}$, is in reasonable agreement with the slope of the experimental data. At higher rates the slope decreases for both experimental data and Laun's rule predictions in agreement with the argument that the tested shear rates falls in regime the II of Figure 6.12. Unfortunately there is not such a prediction for N_2.

6.6 Comments on transient response

The main thrust of this work concerns the measurements of the steady state values of N_1 and N_2. The fast response of our piezoelectric sensor, is a key feature to capture the transient response N(t). Note for example that during start-up shear at $4s^{-1}$ N_a (t) is lagging 0.37 s from the N_b (t) piezo signal. This proves the suitability of the sensor for capturing transient signals. Relaxation of N_b(t) upon flow cessation is also nicely captured. Hence a further development of the CPP3+ would make feasible the measurement

with two sensors both based on piezoelectric ceramics (the CPP3++ fixture) , with the same time constant and completely independent from the force rebalancing of the rheometer's transducer and its associated response delays. This will give the ability to accurately determine the fast transients of N_1 and N_2 which is vital for reasons discussed below.

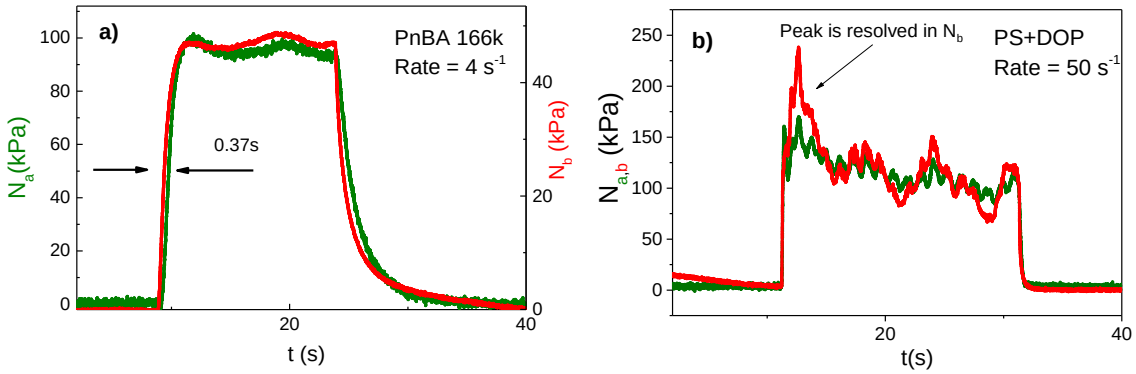

Figure 6.16 Time signals of normal stresses $N_a(t)$ and $N_b(t)$ in shear start-up at low and high shear rates a) $N_a(t)$ lags behind $N_b(t)$ by 0.37s as indicated by the arrows. Fluctuations seem present in both signals (ARES, Piezo) at the shear rate of $4s^{-1}$. b) Strong fluctuations are present in both signals at $50s^{-1}$. N_b is scaled down to match N_a amplitude, for comparison.

In shear start-up experiments, the early response $N_1(t)$ provides insight on the first departure from linearity described as "first effects of finite elasticity" (Graessley 2008). This onset of nonlinearity should be measurable at short times, before the shear stress departs from the LVE envelope, as constituted based on the Cox Merz rule. In this early regime, the material behaves as a second order fluid (in analogy with regime I in Figure 6.12) and N_1 can be linked to LVE with the Coleman Markovitz relation (Coleman and Markovitz 1964, Menezes and Graessley 1982) :

$$\lim_{\dot{\gamma}\to 0} \frac{N_1(\dot{\gamma})}{\dot{\gamma}^2} = 2 \lim_{\omega\to 0} \frac{G'(\omega)}{\omega^2} \tag{6.5}$$

In shear start-up experiments of higher rates the departure from regime I will result in $N_1(t)$ overshoot due the chain stretching (Pearson *et al.* 1991) and this can certainly be resolved with the fasts CPP3+ transducer. On the other hand, to the best of our knowledge there is little work reported on N_2 transient behavior. These experiments thought require appropriate sample (Mw and concentration) selection to obtain sufficient strong signal and on the same time avoid stress localization effects (Marrucci and Grizzuti 1983) which are prenominal in stress relaxation experiments. In addition to the above the normal stress transients provide a useful test of constitutive relationships

Another interesting possibility is to perform a nonlinear step strain test and probe the $N_1(t)$ relaxation that should lead to the calculation of the damping function $h(\gamma)$ for cases where time and strain seperability holds (Laun 1978) :

$$N_{1\,(t,\gamma)} = \gamma^2 h(\gamma) G(t) \tag{6.6}$$

The latter is a sensitive measure of nonlinearity and helps assessing constitutive models. Last but not least, we note the importance of the study of the onset and the spatial propagation of instabilities triggered by shear-concentration coupling as frequently observed in polymeric melts (Burroughs *et al.* 2021). More generally, coupling between flow and microstructure at high shear rates leads to spatiotemporal rheochaotic flows with dominant oscillations (Hilliou and Vlassopoulos 2002) or irregular fluctuations (Fielding and Olmsted 2004). The strength of this coupling depends on the solvent quality and the number of entanglements (Burroughs *et al.* 2023). Since $N_a(t)$ and $N_b(t)$ signals correspond to different radial positions, they reflect the presence of instabilities at different regimes. Clues can be obtained by analyzing the fluctuations of these two signals as shown for example in Figure 6.16(b) where the normal stress signals of PS/DOP at $50s^{-1}$ are captured. The ARES transducer failed to resolve the stress peak in Figure 6.16(b). Hence a two piezo CPP3++ fixture would be appropriate. It would exhibit the required short time response without the interference of the force rebalancing mechanism of the rheometer.

6.7 Conclusions and perspectives

We discussed the design and implementation of CPP3+, a simple and robust tool capable of measuring normal stress differences in cone-plate rheometry with a single loading. The CPP3+ is compact enough to be accommodated in the rheometer's oven. Results for entangled polymer solutions and melts are in satisfactory agreement with other established methods and theoretical predictions. We have also shown the sensitivity of the measurement to instabilities and in particular to edge fracture. A two piezo CPP3++ fixture would be appropriate to capture transient normal stress signals without the interference of the force rebalancing mechanism of the rheometer. Beyond macromolecules, $|N_2|$ is not always small. The N_2 magnitude appears to be dominant in the flow of concentrated non-Brownian suspensions (Dai *et al.* 2013, Denn and Morris 2014) while the algebraic sign of N_1 (as a function of volume fraction) is still a subject of debate. The different origin of N_2, due to particle collisions, calls for further investigation where CPP3++ could play a primary role. There is also a growing interest to explore N_1, N_2 in yield stress fluids (De Cagny *et al.* 2019, Venerus *et al.* 2022) where time resolution capabilities are important. Certainly, the acquisition of normal stress in two surfaces simultaneously and the short time response are features of the CPP3+ that can be further exploited in many soft materials.

Appendix A.6

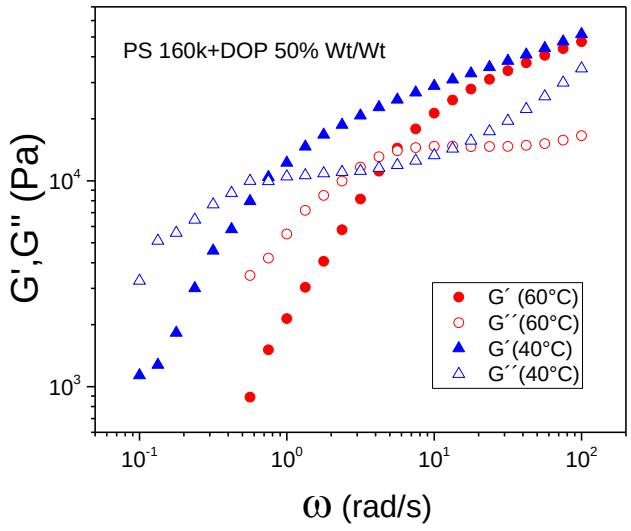

Figure A.1 LVE spectra of PS solution in DOP measured with the CPP3+ installed on the ARES

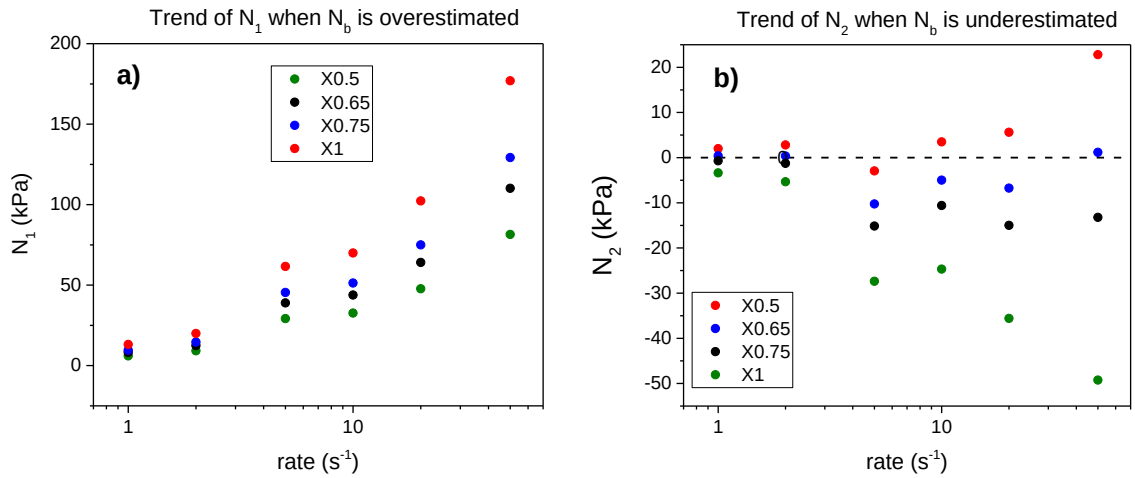

Figure A.2 N_1 and N_2 real data calculated when N_b is deliberately underestimated by the factor indicated in the legend. a) The N_1 error , proportional to N_b error, will hide in log-log plot. b) N_2 is severely affected even for the 0.25% reduction of N_b and eventually will change sign. $|N_2/N_1|$ will show apparent thinning behavior.

Figure A.2 emulates the case where instabilities have reached N_b resulting in underestimation of its value.

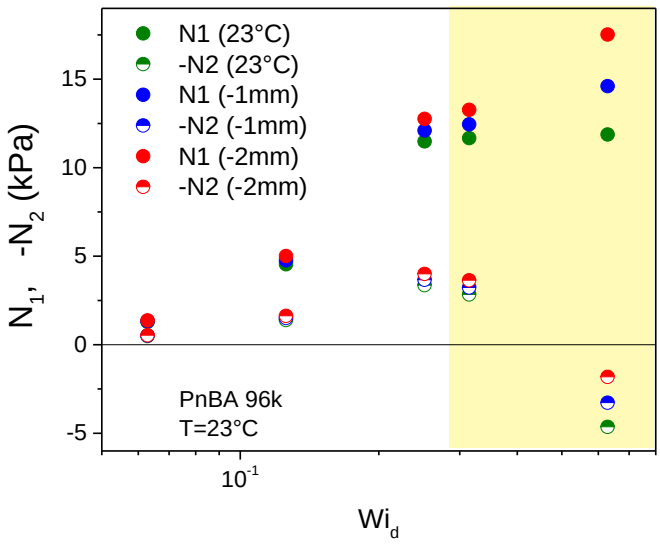

Figure A.3 N_1, N_2 calculated for reduced geometry. Based on real data from experiments with the PnBA melt

Let's hypothetically consider that edge fracture occurred during the measurement and has propagated by 1 or 2 mm while no other instability is present. We also assume that fracture has not reached piezo (surface "b"). Figure A.3 shows the effect of the reduction of the total sample radius. N_1 and N_2 here are calculated from real N_a, N_b data by solving the two equations with two unknowns with reduced values of R_s ,i.e., by 1 or 2 mm as indicated. The error is substantial and increases with N_1, N_2 absolute value.

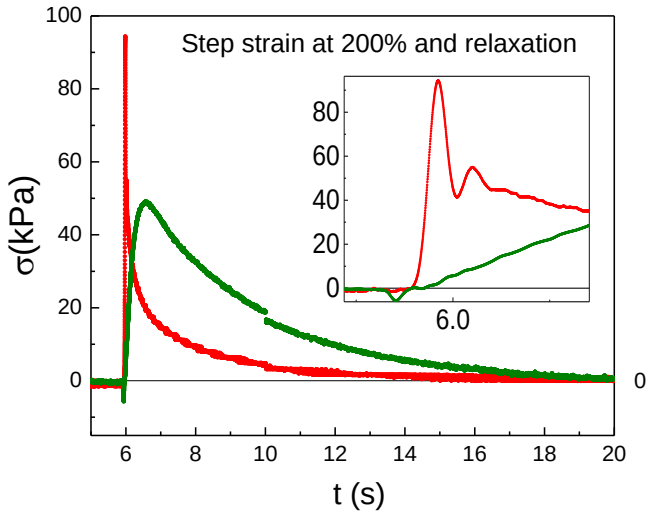

Figure A.4 Normal force raw signal N_a, N_b during step-strain at 200% and relaxation for the PS/DOP solution. The step-strain commenced at t~6s (see N_b at the expanded graph in the inset). The slow Na apparent relaxation is clearly an artifact as it is considerably slower compared to G(t). We attribute it to the slow ARES transducer response. The second peak in N_b can be attributed to ARES rebalancing. These are preliminary data.

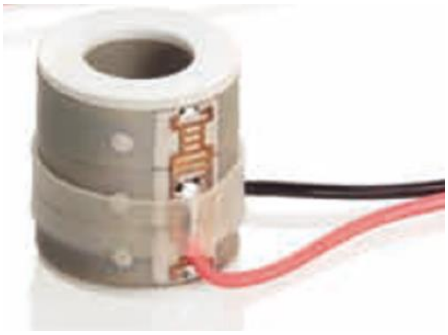

Figure A.5 The piezoelectric sensor consisting of 3 piezo ceramic rings PD150.3 sintered together. Dimensions : ID 9mm,

OD 15mm , Height (2x3)+1=7 mm

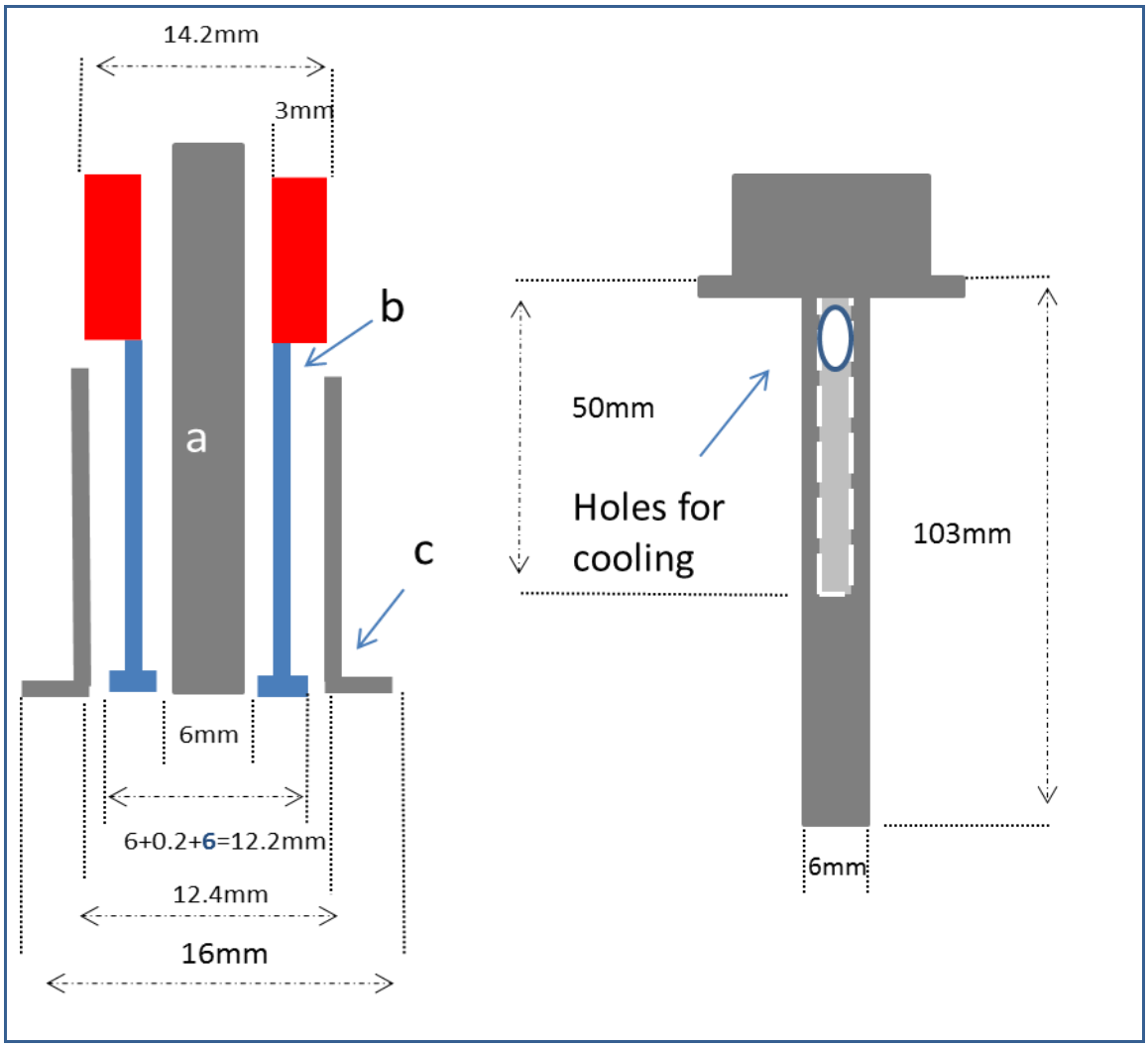

Figure A.6 Side view of the CPP3+ upper geometry with dimensions. Red color indicates the piezo ceramic sensor and letters a, b, c label the tool surfaces, i.e., the inner disk, the corona connected to piezo electric sensor and the outer inert corona, respectively. The whole inner tool (corresponding to surface "a") is shown separately.

References

Baek, S.-G., and Magda, J. J., ‘‘Monolithic rheometer plate fabricated using silicon micromachining technology and containing miniature pressure sensors for N_1 and N_2 measurements,’’ Journal of Rheology 47, 1249-1260 (2003).

Baig, C., Mavrantzas, V. G., and Kroger, M., ‘‘Flow effects on melt structure and entanglement network of linear polymers: Results from a nonequilibrium molecular dynamics simulation study of a polyethylene melt in steady shear,’’ Macromolecules 43, 6886-6902 (2010).

Bird, R. B., Armstrong, R. C., and Hassager, O., ‘‘Dynamics of polymeric liquids. Volume 1: fluid mechanics,’’ A Wiley-Interscience Publication, John Wiley & Sons (1987).

Boyer, F., Pouliquen, O., and Guazzelli, É., ‘‘Dense suspensions in rotating-rod flows: normal stresses and particle migration,’’ Journal of Fluid Mechanics 686, 5-25 (2011).

Burroughs, M. C., Zhang, Y., Shetty, A., Bates, C. M., Helgeson, M. E., and Leal, L. G., ‘‘Flow-concentration coupling determines features of nonhomogeneous flow and shear banding in entangled polymer solutions,’’ Journal of Rheology 67, 219-239 (2023).

Burroughs, M. C., Zhang, Y., Shetty, A. M., Bates, C. M., Leal, L. G., and Helgeson, M. E., ‘‘Flow-induced concentration nonuniformity and shear banding in entangled polymer solutions,’’ Physical Review Letters 126, 207801 (2021).

Coleman, B. D., and Markovitz, H., ‘‘Normal Stress Effects in Second‐Order Fluids,’’ Journal of Applied Physics 35, 1-9 (1964).

Coleman, B. D., and Noll, W., “An approximation theorem for functionals, with applications in continuum mechanics.” *The foundations of mechanics and thermodynamics* (Springer, 1960).

Costanzo, S., Huang, Q., Ianniruberto, G., Marrucci, G., Hassager, O., and Vlassopoulos, D., ‘‘Shear and extensional rheology of polystyrene melts and solutions with the same number of entanglements,’’ Macromolecules 49, 3925-3935 (2016).

Costanzo, S., Ianniruberto, G., Marrucci, G., and Vlassopoulos, D., ‘‘Measuring and assessing first and second normal stress differences of polymeric fluids with a modular cone-partitioned plate geometry,’’ Rheologica Acta 57, 363-376 (2018).

Cromer, M., Villet, M. C., Fredrickson, G. H., and Leal, L. G., ‘‘Shear banding in polymer solutions,’’ Physics of Fluids 25, 051703 (2013).

Cudney, R., Phelps, C., and Barreto, E., ‘‘An ungrounded electronic field meter,’’ Review of Scientific Instruments 43, 1372-1373 (1972).

Dai, S.-C., Bertevas, E., Qi, F., and Tanner, R. I., ‘‘Viscometric functions for noncolloidal sphere suspensions with Newtonian matrices,’’ Journal of Rheology 57, 493-510 (2013).

Datta, S. S., Ardekani, A. M., Arratia, P. E., Beris, A. N., Bischofberger, I., Eggers, J. G., López-Aguilar, J. E., Fielding, S. M., Frishman, A., and Graham, M. D., ‘‘Perspectives on viscoelastic flow instabilities and elastic turbulence,’’ arXiv preprint arXiv:2108.09841 (2021).

De Cagny, H., Fazilati, M., Habibi, M., Denn, M. M., and Bonn, D., ‘‘The yield normal stress,’’ Journal of Rheology 63, 285-290 (2019).

Denn, M. M., and Morris, J. F., ‘‘Rheology of non-Brownian suspensions,’’ Annual review of chemical and biomolecular engineering 5, 203-228 (2014).

Dolata, B. E., and Olmsted, P. D., ‘‘A thermodynamically consistent constitutive equation describing polymer disentanglement under flow,’’ Journal of Rheology 67, 269-292 (2023).

Fielding, S. M., and Olmsted, P. D., ‘‘Spatiotemporal oscillations and rheochaos in a simple model of shear banding,’’ Physical review letters 92, 084502 (2004).

Gauthier, A., Pruvost, M., Gamache, O., and Colin, A., ‘‘A new pressure sensor array for normal stress measurement in complex fluids,’’ Journal of Rheology 65, 583-594 (2021).

Graessley, W. W., *Polymeric liquids and networks: dynamics and rheology* (Garland Science, 2008).

Hansen, M., and Nazem, F., ‘‘Transient normal force transducer response in a modified Weissenberg rheogoniometer,’’ Transactions of the Society of Rheology 19, 21-36 (1975).

Hemingway, E. J., and Fielding, S. M., ‘‘Edge fracture instability in sheared complex fluids: Onset criterion and possible mitigation strategy,’’ Journal of Rheology 63, 735-750 (2019).

Hilliou, L., and Vlassopoulos, D., ‘‘Time-periodic structures and instabilities in shear-thickening polymer solutions,’’ Industrial & engineering chemistry research 41, 6246-6255 (2002).

Horowitz, P., Hill, W., and Robinson, I., *The art of electronics Vol. 2* (Cambridge university press Cambridge, 1989).

Huang, D. C., and White, J. L., ‘‘Extrudate swell from slit and capillary dies: an experimental and theoretical study,’’ Polymer Engineering & Science 19, 609-616 (1979).

Hutton, J., ‘‘Fracture and secondary flow of elastic liquids,’’ Rheologica Acta 8, 54-59 (1969).

Ianniruberto, G., Brasiello, A., and Marrucci, G., ‘‘Simulations of fast shear flows of PS oligomers confirm monomeric friction reduction in fast elongational flows of monodisperse PS melts as indicated by rheooptical data,’’ Macromolecules 45, 8058-8066 (2012).

Ianniruberto, G., and Marrucci, G., ‘‘On compatibility of the Cox-Merz rule with the model of Doi and Edwards,’’ Journal of Non-Newtonian fluid mechanics 65, 241-246 (1996).

Ianniruberto, G., and Marrucci, G., ‘‘Convective constraint release (CCR) revisited,’’ Journal of Rheology 58, 89-102 (2014).

Inoue, T., Yamashita, Y., and Osaki, K., ‘‘Viscoelasticity of Polymers in ϑ Solvents around the Semidilute Regime,’’ Macromolecules 35, 9169-9175 (2002).

Jullian, N., Leonardi, F., Grassl, B., Peyrelasse, J., and Derail, C., ‘‘Rheological characterization and molecular modeling of poly (n-butyl acrylate),’’ Applied Rheology 20 (2010).

Kalogrianitis, S. G., and van Egmond, J. W., ‘‘Full tensor optical rheometry of polymer fluids,’’ Journal of Rheology 41, 343-364 (1997).

Keentok, M., and Xue, S.-C., ‘‘Edge fracture in cone-plate and parallel plate flows,’’ Rheologica acta 38, 321-348 (1999).

Kos, T., Rojac, T., Petrovčič, J., and Vrančić, D., ‘‘Control system for automated drift compensation of the stand-alone charge amplifier used for low-frequency measurement,’’ AIP Advances 9, 035133 (2019).

Kulicke, W.-M., and Wallbaum, U., ‘‘Determination of first and second normal stress differences in polymer solutions in steady shear flow and limitations caused by flow irregularities,’’ Chemical engineering science 40, 961-972 (1985).

Larson, R. G., ‘‘Instabilities in viscoelastic flows,’’ Rheologica Acta 31, 213-263 (1992).

Larson, R. G., *Constitutive equations for polymer melts and solutions: Butterworths series in chemical engineering* (Butterworth-Heinemann, 2013).

Larson, R. G., and Desai, P. S., ‘‘Modeling the rheology of polymer melts and solutions,’’ Annual Review of Fluid Mechanics 47, 47-65 (2015).

Laun, H., ‘‘Description of the non-linear shear behaviour of a low density polyethylene melt by means of an experimentally determined strain dependent memory function,’’ Rheologica Acta 17, 1-15 (1978).

Laun, H., ‘‘Prediction of elastic strains of polymer melts in shear and elongation,’’ Journal of Rheology 30, 459-501 (1986).

Macosko, C. W., *Rheology: principles, measurements, and applications* (Wiley-vch, 1994).

Magda, J., and Baek, S., ‘‘Concentrated entangled and semidilute entangled polystyrene solutions and the second normal stress difference,’’ Polymer 35, 1187-1194 (1994).

Maklad, O., and Poole, R., ‘‘A review of the second normal-stress difference; its importance in various flows, measurement techniques, results for various complex fluids and theoretical predictions,’’ Journal of Non-Newtonian Fluid Mechanics 292, 104522 (2021).

Marrucci, G., and Grizzuti, N., “The Free Energy Function of the Doi‐Edwards Theory: Analysis of the Instabilities in Stress Relaxation,’’ Journal of Rheology 27, 433-450 (1983).

McKinley, G. H., Pakdel, P., and Öztekin, A., ‘‘Rheological and geometric scaling of purely elastic flow instabilities,’’ Journal of Non-Newtonian Fluid Mechanics 67, 19-47 (1996).

Meissner, J., Garbella, R., and Hostettler, J., ‘‘Measuring normal stress differences in polymer melt shear flow,’’ Journal of Rheology 33, 843-864 (1989).

Menezes, E., and Graessley, W., ‘‘Study of the nonlinear response of a polymer solution to various uniaxial shear flow histories,’’ Rheologica Acta 19, 38-50 (1980).

Menezes, E., and Graessley, W., “Nonlinear rheological behavior of polymer systems for several shear‐flow histories,” Journal of Polymer Science: Polymer Physics Edition 20, 1817-1833 (1982).

Moldenaers, P., Yanase, H., Mewis, J., Fuller, G., Lee, C., and Magda, J., ‘‘Flow-induced concentration fluctuations in polymer solutions: Structure/property relationships,’’ Rheologica acta 32, 1-8 (1993).

Naue, I. F., Kádár, R., and Wilhelm, M., ‘‘High sensitivity measurements of normal force under large amplitude oscillatory shear,’’ Rheologica Acta 57, 757-770 (2018).

Parisi, D., Han, A., Seo, J., and Colby, R. H., ‘‘Rheological response of entangled isotactic polypropylene melts in strong shear flows: Edge fracture, flow curves, and normal stresses,’’ Journal of Rheology 65, 605-616 (2021).

Pearson, D., Herbolzheimer, E., Grizzuti, N., and Marrucci, G., ‘‘Transient behavior of entangled polymers at high shear rates,’’ Journal of Polymer Science Part B: Polymer Physics 29, 1589-1597 (1991).

Poynting, J. H., ‘‘On pressure perpendicular to the shear planes in finite pure shears, and on the lengthening of loaded wires when twisted,’’ Proceedings of the Royal Society of London. Series A, Containing Papers of a Mathematical and Physical Character 82, 546-559 (1909).

Schroeder, C. M., Teixeira, R. E., Shaqfeh, E. S., and Chu, S., ‘‘Dynamics of DNA in the flow-gradient plane of steady shear flow: Observations and simulations,’’ Macromolecules 38, 1967-1978 (2005).

Schweizer, T., ‘‘Measurement of the first and second normal stress differences in a polystyrene melt with a cone and partitioned plate tool,’’ Rheologica acta 41, 337-344 (2002).

Schweizer, T., Hostettler, J., and Mettler, F., ‘‘A shear rheometer for measuring shear stress and both normal stress differences in polymer melts simultaneously: the MTR 25,’’ Rheologica acta 47, 943-957 (2008).

Schweizer, T., and Schmidheiny, W., ‘‘A cone-partitioned plate rheometer cell with three partitions (CPP3) to determine shear stress and both normal stress differences for small quantities of polymeric fluids,’’ Journal of Rheology 57, 841-856 (2013).

Snijkers, F., and Vlassopoulos, D., ‘‘Cone-partitioned-plate geometry for the ARES rheometer with temperature control,’’ Journal of Rheology 55, 1167-1186 (2011).

Snijkers, F., and Vlassopoulos, D., ‘‘Appraisal of the Cox-Merz rule for well-characterized entangled linear and branched polymers,’’ Rheologica Acta 53, 935-946 (2014).

Starecki, T., ‘‘Analog front-end circuitry in piezoelectric and microphone detection of photoacoustic signals,’’ International Journal of Thermophysics 35, 2124-2139 (2014).

Tanner, R., and Keentok, M., “Shear fracture in cone-plate rheometry” Journal of Rheology 27, 47-57 (1983).

Van Ruymbeke, E., Masubuchi, Y., and Watanabe, H., ‘‘Effective value of the dynamic dilution exponent in bidisperse linear polymers: From 1 to 4/3,’’ Macromolecules 45, 2085-2098 (2012).

Venerus, D. C., ‘‘Free surface effects on normal stress measurements in cone and plate flow,’’ Applied rheology 17, 36494-1-36494-6 (2007).

Venerus, D. C., Machabeli, O., Bushiri, D., and Arzideh, S. M., ‘‘Evidence for Chaotic Behavior during the Yielding of a Soft Particle Glass,’’ Physical Review Letters 129, 068002 (2022).

Vlassopoulos, D., and Hatzikiriakos, S. G., ‘‘A generalized Giesekus constitutive model with retardation time and its association to the spurt effect,’’ Journal of non-newtonian fluid mechanics 57, 119-136 (1995).

Wen, Y. H., Lin, H. C., Li, C. H., and Hua, C. C., ‘‘An experimental appraisal of the Cox–Merz rule and Laun's rule based on bidisperse entangled polystyrene solutions,’’ Polymer 45, 8551-8559 (2004).

Wu, S., ‘‘Surface and interfacial tensions of polymer melts. II. Poly (methyl methacrylate), poly (n-butyl methacrylate), and polystyrene,’’ The Journal of Physical Chemistry 74, 632-638 (1970).

Xu, X., Chen, J., and An, L., ‘‘Shear thinning behavior of linear polymer melts under shear flow via nonequilibrium molecular dynamics,’’ The Journal of chemical physics 140, 174902 (2014).

Epilogue

The development of tools and protocols has always been a central research aim in rheology, and this is reflected in the number of devices and protocols described in classic textbooks (Ferry 1980, Collyer 1993, Macosko 1994). In accord with this aim, the conclusions listed at every Chapter of this thesis point to the necessity for the expansion of the current rheometric capabilities. On the one hand, from a technical point of view we can improve conventional rheometry by taking advantage of recent developments in other fields such as mechanical engineering and signal processing. This path was followed in this thesis in order to; i) extend the SAOS range to higher frequencies with modern piezoelectric sensors and actuators; ii) utilize frequency modulated signals (chirps) for LVE interrogation; iii) incorporate piezoelectric sensors in the CPP fixture to reduce tool bulkiness and improve versatility and time response. On the other hand, the rheometric data interpretation methods must be in phase with material properties including structural and dynamic insights. This remains a crucial element in material science. Under this concept we also discussed; i) the often overlooked high frequency crossover in LVE spectra of colloidal glasses; ii) the structure and yielding of an amphiphilic hydrogel, as well as its long-lived structural memory; iii) a mechanical annealing protocol tailored to a hydrogel with weak residual stresses; iv) the suggestion of the modulus of resilience as a measure of structural memory.

All protocols are unavoidably associated with limitations that in many cases derive from fundamentals of materials physics or instrumental design. In certain studies these limitations are unimportant and naturally overlooked. However, there are cases where these limitations affect the data or their interpretation. Limitations discussed here are; i) sample inertia (gap loading limit) that sets a physical limit to the upper frequency of SAOS measurement; ii) residual stresses that affect nonlinear response in many materials such our amphiphilic hydrogel; iii) high-shear rate rejuvenation protocol ; iv) sensitivity of N1 and N2 measurement to edge effects.

More generally, the results of this work indicate that to advance the present state-of-the-art, a way forward is blending conventional rheometry with other fields such as signal processing and mechanics of solids. Putting emphasis on fast response and stiffness of transducers and actuators holds the promise for further developments that will allow probing materials (particularly metastable and thixotropic) with a wide range of structural and dynamic responses from ultrasoft to hard.

References

Collyer, A. A., Techniques in rheological measurement, 2nd ed. (Springer, 1993)

Ferry, J. D., Viscoelastic properties of polymers, 3rd ed. (Wiley, 1980)

Macosko, C. W., Rheology: principles, measurements, and applications (Wiley, 1994)